

PHD THESIS

LASER STABILIZATION
WITH LASER COOLED
STRONTIUM



BJARKE TAKASHI RØJLE CHRISTENSEN

ONE MAN'S NOISE
IS ANOTHER MAN'S DATA.

- BJARKE TAKASHI RØJLE CHRISTENSEN

LASER STABILIZATION WITH LASER COOLED STRONTIUM

Author Bjarke Takashi Røjle Christensen
Advisor Jan Westenkær Thomsen



PhD thesis

Group 12, Niels Bohr Institute
Ultra Cold Atoms and Quantum Optics

Submitted to the University of Copenhagen
April 29, 2016

ACKNOWLEDGEMENTS

This thesis presents the results of the work I carried out during my PhD program from March 2013 to April 2016 at the group for **Precision Measurements with Ultracold Atoms** at The Niels Bohr Institute, University of Copenhagen. During this work, I received indispensable support from a great number of people who helped me to complete this PhD program, and I wish to thank all of them here.

First of all, I would like to thank Jan W. Thomsen for being my supervisor for six years, more or less. I first met you when I chose your classical optics class, mostly because the time table of the course fit the rest of my course time table by coincidence. I was inspired by your enthusiasm, and I somehow managed to convinced you to let me work in your lab for my bachelor's thesis, not least because I thought the magneto-optical trap was the coolest thing I had ever seen (It still is.). Later, you were my *Skype-supervisor* during my studies in Japan, and finally I had the great pleasure of working under your supervision as a PhD student. I admire your understanding and awareness of the physical world around you (like when you spotted a 20,000 kr diamond among gravel on the ground) and just *how* much you can calculate during your "*30 minutes last night*". You have taught me a great amount of physics, but you have also taught me about many other important things in life and given me valuable advice regarding career, private life and Champagne. I am sure all of this will benefit me in my path after the PhD program.

I would also like to thank Philip G. Westergaard who initiated most of the experimental setup presented in this work. It is still a mystery to me how you managed to construct such a reliable experiment in just two years. I still occasionally find brilliant details which you implemented in the experiment. I would not have been able to achieve half of what I achieved without your thorough prior work.

In the theoretical work, we received great help from David Tieri, John Cooper and Murray Holland from **JILA**, University of Colorado, Denver. It was great have discussions with you during our visits to JILA and I

would like to thank you for taking our *back-of-the-envelope* semi-classical calculations out of our dirty experimental hands and developing a proper quantum mechanical model.

I also wish to thank Jun Ye and his group members at JILA. Jun Ye's advices have been priceless during both our experimental work as well as the writing process of our papers, and the members of his group have generously shared their experimental know-how with us. I would also like to thank James K. Thomsen and his group members who are similarly affiliated at JILA. James K. Thomsen and his group members have been great discussion partners during this work, although we were constantly caught short of breath by their incredible progress.

I had the pleasure of staying for two months (Oct-Dec 2015) at The Optical Frequency Metrology Group at **SYRTE, Paris Observatory** during this PhD program. It was a great experience to work hands-on with a state-of-the-art atomic clock experiment, and it was nice to experience how I was able to contribute in other labs. I would like to thank Rodolphe Le Targat, Jérôme Lodewyck, Eva Bookjans and Slawomir Bilicki for letting me join your group and for letting me accompany your coffee breaks.

I would not have been able to realize half of the work presented in this thesis without the support from my amazing co-PhD students Stefan Schäffer and Martin Henriksen. My first year as a PhD student was very lonely since I was the only regular member of the group besides Jan, but both Stefan and Martin joined the group very soon as master students. It was clear already during their master programs that they both possessed abilities that I did not have. Much of the outcome of this work would not have been realized without Martin's great technical skills and Stefan's deeply analytical and forward thinking mindset. I had the pleasure to attend conferences in Germany, Colorado and France together with Stefan and Martin and it has been a pleasure to experience your unique interplay. I will look forward to join future harvest celebrations at Martin's home and to meet Stefan and Turi's forthcoming daughter. I wish to thank both of you and I wish you all the best in the future.

I also had the great pleasure to be '*rusvejleder*' (introductory tutor) for Sigrid Adsersen and Stefan Rathmann in 2010, and to have both of them to join our group as master students 4–5 years later. I would like to thank Sigrid for having a meal rhythm completely synchronized with my own rhythm and Stefan for enduring my well-intentioned but occasionally hard advice in the last months of my PhD.

The electronic- and mechanical technicians, Axel Boisen, Jimmi Hansen, Bent Neumann, Erik Grønbæk and Michael Bernt have provided priceless technical help, gossip, jokes and cake, which in combination pushed our

work far forward. I was always in awe of the great effort you put into our work, and I would like to thank you all.

I was fortunate to have a task-force for correcting all the chapters of this work. This task-force consisted of Anine Borger, Amalie Christensen, Jan Thomsen, Jens Christian Hillerup, Martin Henriksen, Sigrid Adsersen, Sofie Hansen, Stefan Rathmann and Stefan Schäffer. I would like to thank all of you for your great help.

I would also like to thank my family for supporting me and for shaping the man I am today. My father showed me to have passion and dedication for one's profession. It is both a gift and a burden. My mother taught me to be ambitious and to make a difference for other people. It is... also both a gift and a burden. My grandfather (farfar) set my academic standards and knew what is best for me long before I even knew it. Both my late grandmothers taught me the pride and joy in being a good teacher, which I will bring along in my future profession.

... and now I would like to thank some wonderful friends for being a part of my life during my PhD years:

- Wagner, Jens Christian and Smed for our career and life discussions, and the rest of '*Amok*' for making me laugh every day.
- Malene Pontoppidan for growing into a L^AT_EX expert and making me proud.
- Universitetskoret LilleMuko for giving me a weekly break from the PhD life and for giving me a feeling of taking part in and contributing to a culture.
- Fondation Danoise and its residents for giving me optimal living conditions during my stay in Paris. I learned a lot during my stay and I will always bring with me the unforgettable long night in the common room after the terror attacks on November 13th 2016.
- The Øland family for being truly amazing and for accepting me into your lives. You are my role models and I look up to everything you do.
- All friends and former teachers from my old primary school, JIYU Gakuen, for laying the foundation of my character and my education, and for maintaining the contact after all these years.

- Fysikrevy™, medrusvejledere (co-tutors), fellow students, lecturers, staff and everybody from The Niels Bohr Institute for enriching my life during all my years at the institute.
- Satosan and the citizens of Higashimatsushima in the Northern Japan for being so friendly and unshakable despite the circumstances of life. I am honored to be allowed to be a part of your lives.
- Asbjørn Arvad for following my footsteps and maintaining the good relationship between the Niels Bohr Institute and the amazing **The Katori Quantum Metrology Laboratory**.
- Veronika and Torbjørn for making the best possible home base for three far too busy cellists in '*Cellogrotten*'. It has truly been an era.

Til sidst vil jeg gerne takke Karen, og det bliver nødt til at være på dansk. Tak fordi du har været en del af mit liv under det meste af min ph.d. De sidste 2–3 år har helt sikkert ikke været de nemmeste år af mit liv at være sammen med mig, men jeg ville aldrig kunne have klaret det uden dig. De vigtigste ting, jeg har lært under ph.d'en, har jeg lært af dig. Jeg har meget at lære endnu, men jeg arbejder på det, og jeg håber, at vi kan gå mange flere ture ved vandet sammen. Du er det vigtigste i mit liv.

CONTENTS

1	Introduction	1
1.1	Characterization of frequency standards	4
1.2	Optical Atomic clocks	9
1.3	Ultra stable lasers	13
1.3.1	Strategies for improvement	14
2	Active standards	17
2.1	Laser stabilization on atomic systems	19
2.2	Active light sources	21
3	Finite temperature systems	25
3.1	Velocity dependent many-atom theory	26
3.2	Cavity transmission	33
3.2.1	Cavity transmission in terms of classical dispersion	35
3.3	What is all this nonlinearity about?	39
3.3.1	Velocity dependent multiphoton scatterings	42
3.4	Shot noise limited laser linewidth	46
3.4.1	Calculation of the shot noise limited laser stabilization	46
3.4.2	Evaluation of the shot noise limited laser linewidth	50
4	Experimental techniques	57
4.1	Optical cavities	57
4.2	External Cavity Diode laser	59
4.3	Second Harmonic Generation	61
4.4	Magneto-Optical Trap	64
4.5	Laser stabilization	66
4.5.1	Hänsch-Couillaud	66
4.5.2	Pound-Drever-Hall	68
4.6	NICE-OHMS	71
4.6.1	Modifications of the transmission coefficient	74

5 Experimental systems	83
5.1 Laser systems	83
5.1.1 The 689 nm probe laser	85
5.1.2 The 461 nm cooling laser	95
5.1.3 The 707 nm & 679 nm repumping lasers	106
5.2 Main Experiment	108
5.2.1 Trapping of strontium 88	109
5.2.2 Low finesse cavity	112
5.2.3 Vacuum cavity	118
6 Nonlinear spectroscopy for laser stabilization	127
6.1 Spectroscopy with low finesse	128
6.1.1 Absorption spectroscopy	131
6.1.2 Demodulation spectroscopy	135
6.1.3 Atom number dependency	144
6.1.4 Input power dependency	146
6.2 Other spectroscopic techniques	150
6.2.1 Sideband probing	150
6.2.2 Multi photon recoils	153
6.3 Spectroscopy with high finesse	159
6.4 Outlook	163
7 Collective spontaneous emission	165
7.1 Super radiance, Super Fluorescence and Amplified Spontaneous Emission	166
7.1.1 Characteristic time scales	168
7.2 Experimental investigations	170
7.2.1 Dynamics of the collectively enhanced transmission	175
8 Outlook	187
8.1 This work	187
8.1.1 Other similar works	189
8.1.2 Future studies	190
8.2 On the horizon	191
A Appendix	195
A.1 Vacuum chamber mounts	195
A.2 Modulation index for fiber EOM	198
A.3 Outgassing of viton	199
A.4 Vacuum cavity drawing	199
A.5 Servo circuit for vacuum cavity	201

A.6	Simultaneous NICEOHMS	202
B	Main publications	203
B.1	Non-linear Spectroscopy of Sr Atoms in an Optical Cavity for Laser Stabilization	203
B.2	Laser stabilization using saturated absorption in a cavity- QED system	211
B.3	Observation of Motion-Dependent Nonlinear Dispersion with Narrow-Linewidth Atoms in an Optical Cavity	219
	Bibliography	225

LIST OF FIGURES

1.1	Photo of Marine Clock No.1, 1760 by Ferdinand Berthoud.	2
1.2	Illustration of the frequency standards in GPS satellites	2
1.3	A part of [Bohr, 1913] By Niels Bohr.	3
1.4	Illustration of the basic principle of an atomic clock.	5
1.5	Accuracy and precision illustrated by bullet holes on a target.	7
1.6	From [Takamoto et al., 2015]: Allan deviations for comparisons of different optical lattice clocks.	8
1.7	From [Kessler et al., 2012a]: Allan deviation showing the instability of ultra stable reference cavities.	8
1.8	From [Chou et al., 2010b]: Frequency differences for two ion clocks with different relative heights.	11
1.9	From [Abgrall et al., 2015]: The fractional variation of the ratio of two atomic transitions measured for 14 years.	11
1.10	From [Predehl et al., 2012]: Map of fiber link for long distance frequency comparison.	12
1.11	From [Riehle, 2015]: Picture of a transportable optical lattice clock.	13
1.12	Photo of an ULE cavity inside a vacuum system.	13
2.1	Illustrations of the good and bad cavity limit.	18

2.2	Schematics of stabilization of a probe laser on an atom-cavity system.	20
2.3	Schematics of collective emission from a beam of atoms coupled to an optical cavity.	21
3.1	Normalized optical cavity output power as function of optical cavity input power.	33
3.2	Illustration of vacuum Rabi splitting	35
3.3	Theoretical transmission and dispersion lineshapes for the system studied in this work.	36
3.4	Illustration of the non-linear scaling of the transmission and dispersion lineshapes studied in this work.	40
3.5	The dispersion slope at resonance for different number of intra-cavity atoms.	41
3.6	The dispersion slope at resonance for different input probe powers.	43
3.7	Illustration of doppleron multiphoton scatterings.	44
3.8	Illustration of the level scheme for doppleron multiphoton scatterings.	44
3.9	Theoretical predictions of the near resonant transmission and dispersion lineshapes with and without doppleron scatterings.	45
3.10	The dynamics of the dispersion lineshape, dispersion slope at resonance and ideal shot-noise limited linewidth for different temperatures of the atoms.	54
4.1	Illustration of a ring cavity.	58
4.2	Illustration of the gain lineshapes relevant for an ECDL.	60
4.3	Illustration of the <i>Littrow</i> and <i>Littman-Metcalf</i> ECDL configurations	60
4.4	Illustration of cavity enhanced SHG.	62
4.5	1D schematic of a MOT.	64
4.6	Picture of a MOT with trapped ^{88}Sr atoms.	64
4.7	Illustration of the Hänsch-Couillaud scheme.	67
4.8	Illustration of the Pound-Drever-Hall scheme.	69
4.9	Illustration of the general concepts of the NICE-OHMS technique	72
4.10	Spectral components relevant for the NICE-OHMS technique.	73
4.11	Illustration of the corrections of the NICE-OHMS signal imposed by the cavity servo system.	80
5.1	Electronic level scheme for ^{88}Sr	84
5.2	Overview of the probe laser system.	87

5.3	Detailed overview of the <i>probe laser</i> breadboard.	88
5.4	PDH error signal and cavity transmission during scan of laser frequency.	89
5.5	Error signal and Allan deviasion of the probe laser during frequency stabilization.	90
5.6	Output characteristics of the 689 nm ECDL.	91
5.7	Detailed overview of the <i>slave laser</i> system.	93
5.8	Output power plateau of the injection locked slave diode. . . .	94
5.9	Pictures of optical systems for generating light at 461 nm. . . .	95
5.10	Overview of the realized laser system for generating light at 461 nm.	97
5.11	Output characteristics of the 922 nm ECDL.	98
5.12	Output characteristics of the MOPA system.	99
5.13	Frequency scans of the 461 nm cooling laser.	101
5.14	102
5.15	Overview of the atomic reference oven construction.	103
5.16	Fluorescence and lock-in signal from the reference oven during frequency scan of the cooling laser.	104
5.17	Overview of the setup for frequency stabilization of the cooling laser.	105
5.18	Overview of the detunings of the cooling laser.	106
5.19	Picture of one of the Littman-Metcalf type ECDL developed for the repumping lasers.	107
5.20	Output characteristics of the two repumping lasers.	108
5.21	Overview of the main setup for trapping neutral ^{88}Sr in a MOT.	110
5.22	Dynamics of the realized MOT.	111
5.23	Overview of the low finesse cavity system.	113
5.24	Transmission spectrum of the low finesse cavity during scan of cavity length.	115
5.25	Bode plot of the serve circuit used for stabilizing the low finesse cavity.	116
5.26	Illustrations of the vacuum cavity spacer.	119
5.27	Overview of the vacuum finesse cavity system.	120
5.28	Transmission and reflection spectra of the vacuum cavity. . . .	121
5.29	Error signal of the vacuum cavity.	122
5.30	Bode plot of the servo circuit used for stabilizing the vacuum cavity.	124
6.1	Overview of experiment for cavity enhanced spectroscopy of laser cooled ^{88}Sr atoms.	129
6.2	The cavity transmission as function os probe laser detunings. .	132

6.3	Theoretical values of the transmission coefficient modified by the cavity servo system.	136
6.4	Illustration of the spectral components relevant for the NICE-OHMS technique.	137
6.5	Broad scans of NICE-OHHMS signal for demodulation at $1 \times \text{FSR}$ and $2 \times \text{FSR}$	140
6.6	Example of cavity transmission used for determining the modulation index.	142
6.7	Atom number dependency of the narrow dispersion feature. .	145
6.8	Near resonant phase dispersion lineshapes for different probe input powers.	147
6.9	Input probe power dependencies of the dispersion slope and the ideal shot-noise limited linewidth.	148
6.10	Relation between the spectral components relevant for the sideband probing.	151
6.11	Overview of the AOM configuration for sideband probing. .	153
6.12	Phase dispersion measurements of the main atom-cavity system by sideband probing.	154
6.13	Illustration of the multi-photon recoil shift δ_p	154
6.14	Illustration of the setup for measuring recoil shifts.	156
6.15	Measured signal from demodulation of the cavity transmitted light.	157
6.16	Theoretically predicted lineshape of the signal acquired by demodulating the cavity transmitted light.	158
6.17	Picture of a MOT inside the cavity structure inside the main vacuum chamber.	159
6.18	Frequency scan of the absorption and shape shift of the light transmitted by the vacuum cavity.	161
7.1	Illustration of superradiance (SR), superfluorescence (SF) and amplified spontaneous emission (ASE).	167
7.2	Experimental overview for pulse experiments.	170
7.3	MOT fluorescence before and after excitation by a resonant pulse.	173
7.4	Illustration of the experimental sequences presented in Chap. 7.	174
7.5	Illustration of the spatial overlap of the pulse mode, cavity mode and the MOT volume.	175
7.6	Transmission signal of the vacuum cavity during the pulse sequence illustrated in Fig. 7.4b).	176
7.7	Experimental and theoretical shape of the flash of collective emission.	178
7.8	Atom number dependency of the flash of collective emission.	179

7.9	Pulse power dependency of the flash of collective emission.	181
7.10	Pulse detuning dependency of the flash of collective emission.	183
7.11	The cavity transmitted flash measured by detecting the direct transmission power and by the NICE-OHMS technique.	183
7.12	Flash lineshapes for different intra cavity seed powers.	184
8.1	Pictures of the new generation of laser stabilization systems inspired by this work.	192
A.1	Technical drawing of the mounting structure used to fix the output mirror of the low finesse cavity described in Sec. 5.2.2.	196
A.2	Technical drawing of the mounting structure used to fix the input mirror of the low finesse mirror cavity in Sec. 5.2.2.	197
A.3	Dependency of sideband generation for different phase modulation powers in terms of dBm.	198
A.4	Pressure level and temperature of the test vacuum chamber during the outgassing process of Viton strips.	199
A.5	Technical drawings of the cavity spacer for the vacuum cavity described in Sec. 5.2.3.	200
A.6	Picture and circuit diagram of the servo circuit used for stabilizing the length of the vacuum cavity described in Sec. 5.2.3.	201
A.7	Simultaneous measurements of the NICE-OHMS signals for demodulation at 1FSR or 2FSR.	202

LIST OF TABLES

3.1	Shot noise limited linewidths estimated theoretically for different alkali metals.	55
6.1	Multi-photon recoil shifts.	155

LIST OF ABBREVIATIONS

AOM	Acousto Optical Modulator
APD	Avalanche Photo Detector
ASE	Amplified Spontaneous Emission
BS	(non-polarisation dependent) Beam Splitter
DBM	Double Balanced Mixer
ECDL	External Cavity Diode Laser
EOM	Electro Optical Modulator
FM	Frequency Modulation
FP cavity	Fabry Perot cavity
FSR	Free Spectral Range
HC scheme	Hänsch-Couillaud scheme
IF filter	Interference filter
MOPA	Master Oscillator Power Amplifier
MOT	Magneto-Optical Trap
NICE-OHMS	Noise Immune Cavity Enhanced Optical Heterodyne Molecular Spectroscopy
PBS	Polarisation Beam Splitter
PDH scheme	Pound-Drever-Hall scheme
PM	Polarization Maintaining
PPKTP	Periodically Poled Potassium Titanyl Phosphate

RAM	Residual Amplitude Modulation
RF	Radio Frequency
SF	Superfluorescence
SHG	Second Harmonic Generation
SR	Superradiance
ULE	Ultra Low Expansion
VCO	Voltage Controlled Oscillator

ENGLISH ABSTRACT

The frequency stability of current state-of-the-art stabilized clock lasers are limited by thermal fluctuations of the ultra-stable optical reference cavities used for their frequency stabilization. In this work, we study the possibilities for surpassing this thermal limit by exploiting the nonlinear effects from coupling of an optical cavity to laser cooled atoms having a narrow transition linewidth. Here, we have realized such a system where a thermal sample of laser cooled ^{88}Sr atoms are coupled to an optical cavity. The ^{88}Sr atoms were probed on the narrow $^1\text{S}_0 \rightarrow ^3\text{P}_1$ intercombination line at 689 nm in a strongly saturated regime. The dynamics of the atomic induced phase shift and absorption of the probe light were experimentally studied in details with the purpose of applications to laser stabilization. The atomic sample temperature was in the mK range which brought this system out of the domains described by previous theoretical works. A new theoretical cavity-QED model, which took into account the effects of finite atomic velocities, was developed and the theoretical predictions showed great agreement with the experimental observations. It was predicted by the experimental and theoretical studies, that an increase of the cavity finesse would bring the studied system into an interesting domain, where laser stabilization performance may compete with the current state-of-the-art stable laser systems. A new vacuum cavity system with increased finesse was hence realized. This vacuum cavity also brought the system into a new domain where collective emission processes were observed. Collective emission processes can potentially be exploited as active light sources with unprecedented spectral purity and preliminary investigations of this collective emission process were carried out. The studies presented in this work open novel possibilities for alternative and simple strategies for surpassing the state-of-the-art laser stabilization and for realizing active light sources involving collective emission from narrow-line atoms.

DANSK SAMMENFATNING

Frekvensstabiliteten af de mest stabile clocklasere tilgængelige i dag er begrænsede af termiske fluktuationer af de ultrapræcise optiske referencenkaviteter, som bruges i frekvensstabilisationsprocessen. I dette værk studeres mulighederne for at overkomme denne termiske grænse ved at udnytte de ikke-lineære effekter, som forekommer, når en optisk kavitet kobles til laserkølede atomer med smalle atomare overgange.

Her har vi realiseret et sådant system, hvor en termisk samling af laserkølede ^{88}Sr -atomer er koblede til en optisk kavitet.

^{88}Sr -atomernes smalle $^1\text{S}_0 \rightarrow ^3\text{P}_1$ interkonbinationsovergang ved 689 nm var probet i et stærkt mættet regime. Fasen og absorptionen, som atomerne påførte probelyset, blev undersøgt eksperimentelt i detaljer med henblik på anvendelse til laserstabilisation.

Temperaturen af de undersøgte atomer var i mK-intervallet, hvilket bragte dette system ud af det parameterdomæne, som tidligere teoretiske studier har beskrevet. En ny teoretisk model, som tog højde for effekterne af atomernes endelige hastigheder, blev udviklet. Denne teoretiske models forudsigelser viste god overensstemmelse med de eksperimentelle målinger. De teoretiske og eksperimentelle studier forudså, at en forøgelse af kavitetens finesse ville bringe systemet ind i et nyt interessant parameterdomæne, hvor systemets ydeevne for laserstabilisation muligvis kunne konkurrere med de mest stabile lasersystemer tilgængelige i dag. Et nyt kavitetssystem med forøget finesse blev derfor realiseret inde i vakuum.

Dette vakuumkavitet bragte også systemet ind i et domæne, hvor kollektive emissionsprocesser blev observeret. Kollektive emissionsprocesser kan potentielt anvendes som aktive lyskilder med enestående spektral renhed. Indledende undersøgelser af denne kollektive emissionsproces blev derfor udført. Undersøgelserne præsenteret i dette værk åbner op for nye alternative strategier for at overgå stabilitetsniveauet af de mest stabile lasersystemer tilgængelige i dag og for at realisere aktive lyskilder med kollektiv emission fra atomer med smalle overgange.

PREFACE AND PUBLICATIONS

The main focus of this work is the study of the possibilities for using laser cooled strontium atoms coupled to an optical cavity for laser stabilization.

The chapters of this work are structures such that Chap. 1–2 and Chap. 4 introduce the basic concepts and experimental techniques relevant for the field of frequency standards and ultra stable lasers. The results of the theoretical and experimental studies carried out in this work are presented in Chap. 3 and 5–7.

The author of this work sincerely hopes, that Chap. 1–2 and 4 can work as an introduction to the field of frequency standards for future bachelor (undergraduate) students in the same way as past phd-theses such as [Boyd, 2007] gave a similar introduction for the author of this work.

The studies presented in this work were carried out from March 2013 to April 2016 at the group for **Precision Measurements with Ultracold Atoms** at The Niels Bohr Institute, University of Copenhagen. The author of this work contributed to the following scientific publications:

Journal publications

1. Bjarke T. R. Christensen, Martin R. Henriksen, Stefan A. Schäffer, Philip G. Westergaard, Jun Ye, Murray J. Holland & Jan W. Thomsen, *Non-linear Spectroscopy of Sr Atoms in an Optical Cavity for Laser Stabilization*, *Phys. Rev. A*, **92**, 053820 (2015).
2. David A. Tieri, John Cooper, Bjarke T. R. Christensen, Jan W. Thomsen, & Murray J. Holland, *Laser stabilization using saturated absorption in a cavity-QED system*, *Phys. Rev. A*, **92**, 013817 (2015).
3. Philip G. Westergaard, Bjarke T. R. Christensen, David A. Tieri, Rastin Matin, John Cooper, Murray J. Holland, Jun Ye & Jan W. Thomsen, *Observation of Motion-Dependent Nonlinear Dispersion with Narrow-Linewidth Atoms in an Optical Cavity*, *Phys. Rev. Lett.* **114**, 093002 (2015).

Conference proceedings

4. Bjarke T. R. Christensen, Stefan A. Schäffer , Martin R. Henriksen, Philip G. Westergaard, Jun Ye & Jan W. Thomsen, *Laser Stabilization on Velocity Dependent Nonlinear Dispersion of Sr Atoms in an Optical Cavity*, *proceedings of the joint conference of IEEE IFCS and EFTF*, 357-362 (2015).
5. Stefan A. Schäffer, Sigrid S. Adsersen, Bjarke T. R. Christensen, Martin R. Henriksen, & Jan W. Thomsen, *Large Waist Cavity for Ultra Narrow Transition Spectroscopy*, *proceedings of IEEE IFCS and EFTF*, 625-629 (2015).
6. Bjarke T. R. Christensen, Martin R. Henriksen, Philip G. Westergaard, Jun Ye & Jan W. Thomsen, *Prospects for Frequency Stabilization Using Collective Effects of Strontium Atoms in an Optical Cavity*, *proceedings of IEEE IFCS*, 239 (2014).

The main topics presented and discussed in this work cover the results reported in publication 1.–4. and 6. presented above

INTRODUCTION

Frequency is the one measurable quantity we can determine with the highest precision and accuracy with the current technology. These precise frequency measurements are performed by comparing the frequency under test with an other known ultra precise frequency provided by a reference oscillator. The well known frequency of an reference oscillator with a great level of precision an accuracy can be applied as a time keeping pendulum in ultra precise clocks, which keep the time for a wide range of applications around the world. Precise frequency measurements are hence equivalent with precise measurements of time. The current state-of-the-art research groups have realized atomic clocks with astonishing precision and accuracy down to the 1×10^{-18} fractional level [[Chou et al., 2010a](#), [Hinkley et al., 2013](#), [Nicholson et al., 2015](#), [Ushijima et al., 2015](#)]. This corresponds to a clock which losses only one second in 30 billion years! The research field is however not yet satisfied with this breathtaking stability and researchers around the world is currently aiming for the 1×10^{-19} fractional precision level. This work is just one of many contributions to push this precision forward.

Precision of such orders of magnitude might seem obsolete at first sight, however, developments of this kind only occur, if it is driven by great technological and scientific motivations. This following chapter will present the many motivations that drives the research of precision clocks and outline the state-of-the art and trends within the research field. When this is presented, the current obstacles limiting the progress of this research field will become apparent, and the reader will be introduced to the details of the contributions of this work. Hopefully, the main objective and the



Figure 1.1: Private photo: Marine Clock No.1, 1760 by Ferdinand Berthoud exhibited at Musée des Arts et Métiers, Paris.

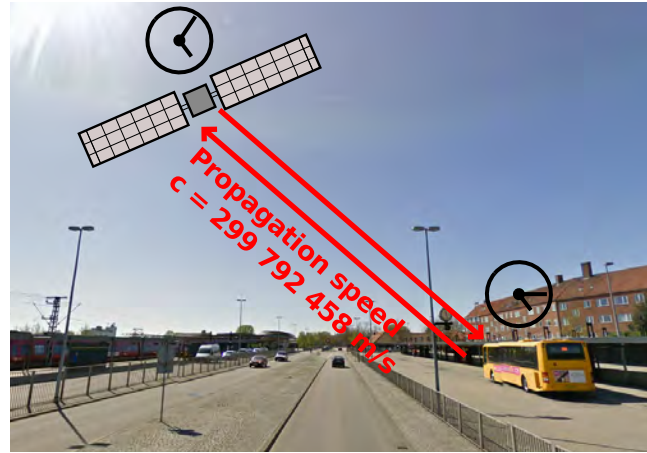


Figure 1.2: All GPS satellites are equipped with frequency standards in order to localize the GPS receivers through the propagation time of the GPS signal and to correct the time delays predicted by the general and special relativity.

possible implications of this work will be apparent after this chapter.

History of clocks

A part of the motivation for improving the precision of clocks becomes clear when realizing, that the majority of the measurable quantities are measured relative to *time*. In the 17'th century, the leaders of the empires around the world wished supremacy on the sea and a precise determination of positions on the sea was crucial for achieving this. The celestial objects were the only reliable references on the open waters and the latitude could be determined by measuring the height of the celestial objects relative to the horizon. The longitude on the other hand could only be determined by simultaneous measurements of the height of the sun relative to the horizon and the *time*. Precise measurements of time were hence made possible by developing mechanical pendulum clocks with great stability and accuracy. Figure 1.1 shows such a clock.

In the 20'th century, the improvement of the clocks sped up by the development of quartz crystals and microwave oscillators. SI units such as the meter was now defined relative to the speed of light in vacuum $c = 299792458 \text{ m/s}$ and *the second* and *time* was once again the main quantity of interest. We still benefit from time measurements for navigation as navigation systems such as the *Global Positioning System* (GPS) determine

the position of a GPS-receiver by analyzing the propagation *time* of a signal from the GPS satellites. This is illustrated in Fig. 1.2.

One corner stone of precision measurement of any observable is that all measurements are *comparisons* of two quantities. These measurements can never be more precise than the *least* precise quantity out of the two. Consider an example, where a research group develops a precise clock with a precision of ± 1 min and an other research group develops a less precise clock with a precision of only ± 30 min. A detailed comparison of these two clocks over time will reveal that the two clocks have a relative deviation of ± 30 min and it will not be possible to determine, which clock caused the deviation. Consequently, only appointments with precision of ± 30 min can be arranged between these two research groups.

A device capable of producing reliable and well known frequencies are hence needed as a reference for any frequency (and time) measurements. Such devices are called *frequency standards*. One of the most important frequency standards is the Caesium atomic clock, which currently defines the second.

An atomic clock is a frequency standard which exploits the discrete nature of atomic transitions described among many others by the Danish Nobel laureate physicist Niels Bohr [Bohr, 1913]. See Fig. 1.3. The frequency corresponding to a photon emitted or absorbed by an atomic transition is used as a frequency reference. An atomic transition is particularly suited as a frequency standard, as two atoms of same species are exactly identical anywhere in the universe according to the conventional understanding of quantum mechanics. The transition frequencies will hence also be identical provided that the surrounding environments are identical.

The International Committee for Weights and Measures (CIPM) has since 1967 defined the second to be 9 192 631 770 periods of the *microwave* radiation corresponding to the energy difference between the two hyperfine ground state levels of the ^{133}Cs atom. The precision of this definition

§ 2. Emission of Line-spectra.

Spectrum of Hydrogen.—General evidence indicates that an atom of hydrogen consists simply of a single electron rotating round a positive nucleus of charge e^+ . The reformation of a hydrogen atom, when the electron has been removed to great distances away from the nucleus—*e. g.*, by the effect of electrical discharge in a vacuum tube—will accordingly correspond to the binding of an electron by a positive nucleus considered on p. 5. If in (3) we put $E = e$, we get for the total amount of energy radiated out by the formation of one of the stationary states,

$$W_\tau = \frac{2\pi^2 me^4}{h^5 \tau^3}.$$

The amount of energy emitted by the passing of the system from a state corresponding to $\tau = \tau_1$ to one corresponding to $\tau = \tau_2$, is consequently

$$W_{\tau_2} - W_{\tau_1} = \frac{2\pi^2 me^4}{h^5} \left(\frac{1}{\tau_2^3} - \frac{1}{\tau_1^3} \right).$$

Figure 1.3: A part of the original article by Niels Bohr [Bohr, 1913] describing the absorption and emission of photons by discrete atomic transitions. The equation in the red box describes the energy difference of two stationary states of an electron in Hydrogen.

has reached a fractional level in the order of- or just below 1×10^{-15} [Bureau International des Poids et Measures, 2014].

In the 21st century, the frequency standards based on atomic transitions in the *optical* frequencies have been realized to a wide extend. The stability of those optical frequency standards has surpassed the stability of the ^{133}Cs atom clocks by two orders of magnitude [Chou et al., 2010a, Hinkley et al., 2013, Ushijima et al., 2015, Nicholson et al., 2015] and the huge task of redefining the second seems realizable in the future. The many motivations driving the improvements towards the 1×10^{-19} fractional stability level are diverse. Some of the scientific motivations are: measurements of relativistic effects due to gravitational potential changes [Bondarescu et al., 2012], simulations of many-body systems with cold atoms [Martin et al., 2013], investigations of potential drifts of fundamental physical constants [Rosenband et al., 2008] and detailed studies of the future promising field of gravitational astronomy after the recently confirmed detection of gravitational waves [Abbott et al., 2016]. Furthermore persistent efforts are put into the development of more compact systems in order to bring these stunning stability levels into the research fields located outside the laboratory environments.

The development of the optical frequency standards does not seem to slow down and the current state-of-the-art presented in this work will most likely be outdated just few years after its submission (April 2016). The reason for this extreme rapid development can perhaps be found in the fact, that studies of previously inaccessible physical effects are made possible every time an additional digit gets available for measurement. These new effects might also be the new limitation for further improvements of the precision.

During the years of this work, this striving for precision has been justified by the group members of the Ultra Cold Atoms Group at the Niels Bohr Institute by the following formulation:

One man's noise is another man's data.

1.1 Characterization of frequency standards

All clocks consist essentially of two components: an *oscillator* and a *counter*. The oscillator provides a well known frequency and the counter count the oscillations. The elapsed time is then recorded in terms of numbers of oscillations. For example, the recurrences of day and night is an oscillation

and the mankind has counted this oscillation to keep track of the calendar throughout human history.

An atomic clock can divide the time into much smaller intervals than day and night and even provide much better stability than the revolution of the Earth. The oscillator of an atomic clock is a laser which is stabilized to a well defined frequency. Narrow line atomic transitions such as the ground state hyperfine transition in the Caesium atom are used as references in atomic clocks. This basic concept of an atomic clock is illustrated in Fig. 1.4.

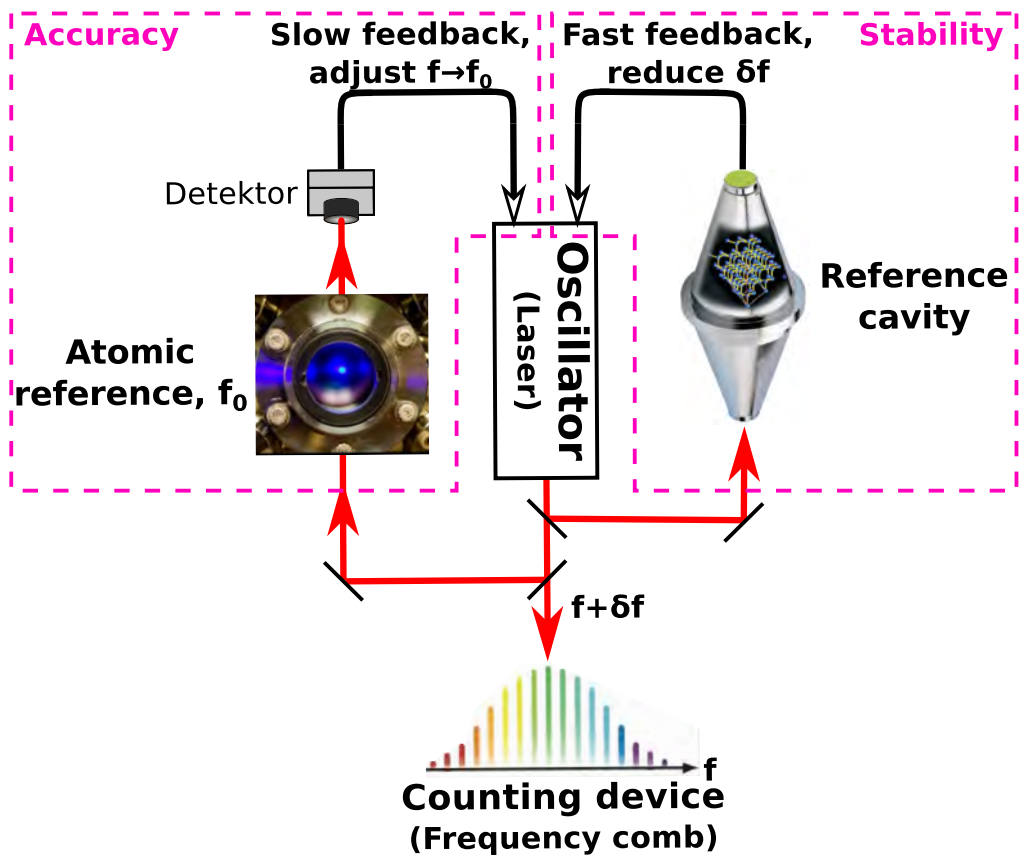


Figure 1.4: Illustration of the basic principle of an atomic clock. A local oscillator oscillating at a frequency f is stabilized through a feedback loop to a frequency f_0 corresponding to an atomic transition energy. Furthermore the local oscillator frequency f is stabilized to a reference cavity such that the frequency noise δf is reduced.

Frequency standards such as the atomic clocks are characterized in

terms of two quantities: *Accuracy* and *stability/precision*.

Accuracy is a measure of the deviation and uncertainty of a frequency relative to a reference frequency. This reference frequency is the frequency corresponding to the transition energy of an atomic transition in the case of an atomic clock. Accuracy is secured by adjusting the oscillator frequency to match the atomic transition frequency. See Fig. 1.4. This transition frequency can be considered as a target scale and the accuracy is then a measure for how *accurate* this transition frequency can be reproduced. Fig. 1.5a) and c) illustrates accurate frequency reproductions (red dots) relative to the reference frequency (the center of the target). Fig. 1.5b) and d) on the other hand are inaccurate reproductions relative to the reference frequency.

Stability is a measure of the frequency variation in time. The term *precision* is also covering the same property. It is necessary to repeat the measurement of the transition frequency in the case of an atomic clock, as atomic transitions have intrinsic fundamental uncertainties due to non-zero transition linewidths. Fig. 1.5a) and b) illustrates stable frequency reproductions (red dots) which reproduce the frequency to a great extent. Fig. 1.5c) and d) on the other hand are instable measurements where the frequency vary from measurement to measurement.

A measure for stability can be calculated based on repeated measurements. A widely used measure for the stability is the Allan variance σ^2 , which is the variance calculated for two subsequently measured values $\bar{y}_1(\tau)$ and $\bar{y}_2(\tau)$ with the same averaging time τ [Riehle, 2004, p. 51]:

$$\sigma^2(\tau) = \left\langle \sum_{i=1}^2 \left(\underbrace{\bar{y}_i(\tau)}_{\text{Measurement } i} - \underbrace{\frac{1}{2} \sum_{j=1}^2 \bar{y}_j(\tau)}_{\text{2-sample average}} \right)^2 \right\rangle. \quad (1.1)$$

The Allan variance σ^2 describes the stability of a frequency standard in more detail than just a single value representing the uncertainty of a frequency. The square root of the Allan variance, the Allan deviation σ , is often preferred when evaluating the stability of a frequency standard.

The stability for different averaging timescales can be illustrated in a Allan deviation plot. An example from [Takamoto et al., 2015] is shown in Fig. 1.6 where the Allan deviation is shown for frequency comparisons of three different optical atomic clocks (Sr/Sr, Yb/Sr and Hg/Sr) for averaging times up to $\tau = 10000$ s. It can be seen in Fig. 1.6 that the Allan deviation declines for longer integration times τ for clocks with great long-term

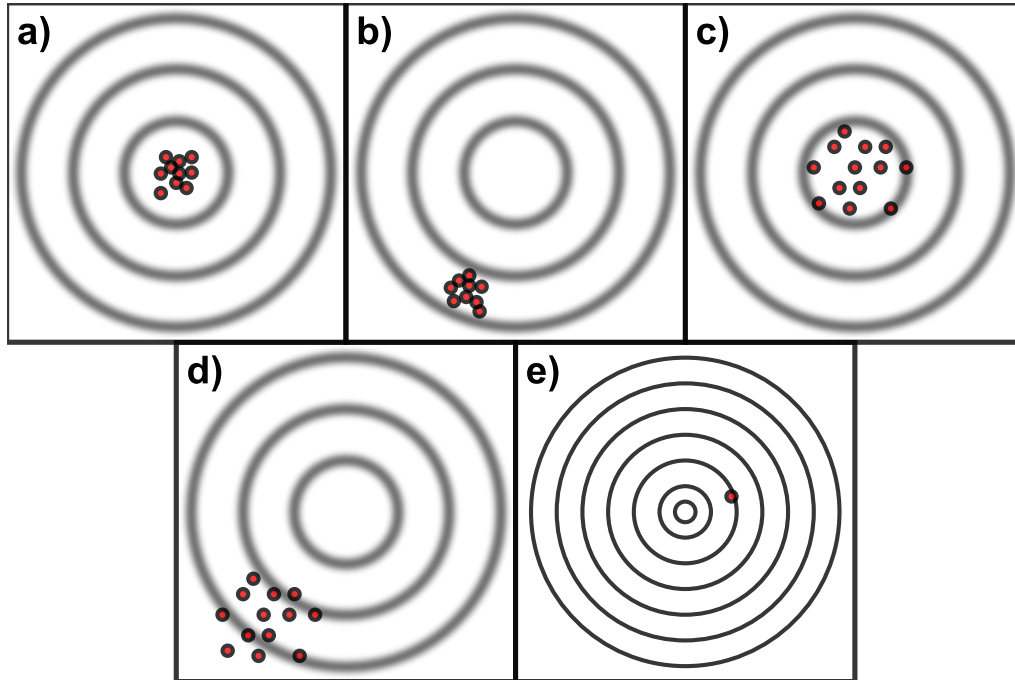


Figure 1.5: *Accuracy and precision illustrated by bullet holes on a target.* a) Precise and accurate. b) Precise but inaccurate. c) Accurate but not precise. d) Inaccurate and not precise. e) Target with improved resolution allowing more detailed determination of precision and accuracy.

stability. On the other hand, a slow drift of the measured quantity is reflected as an increase of the Allan deviation for longer τ as seen in Fig. 1.7 [Kessler et al., 2012a]. The time characteristics of the disturbances of the system can hence be derived from an Allan deviation plot.

The data shown in Fig. 1.6 and Fig. 1.7 are experimentally determined Allan deviations. The dynamics of the Allan deviation for an atomic clock is governed by a few key physical quantities:

$$\sigma \propto \frac{1}{Q} \frac{1}{S/N} \sqrt{\frac{T_c}{\tau}} \propto \frac{1}{Q} \frac{1}{\sqrt{N}} \sqrt{\frac{T_c}{\tau}}, \quad (1.2)$$

where, T_c is the measurement cycle time representing the duration of one measurement where data is acquired for the averaging time τ^i . Here, S/N is the signal-to-noise ratio during the frequency measurement. The last

ⁱThe maximum possible value for $\frac{\tau}{T_c}$ is of course 1.

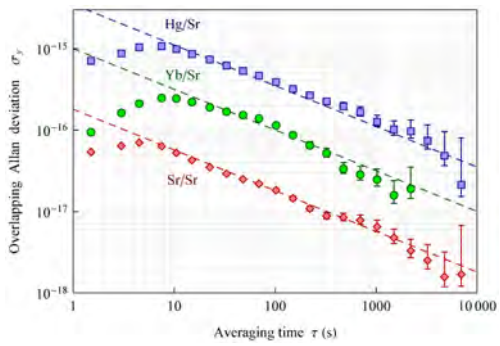


Figure 1.6: From [Takamoto et al., 2015]: Allan deviations illustrating the relative frequency instabilities for comparison of different optical lattice clocks. Sr/Sr, Yb/Sr and Hg/Sr comparison are shown here.

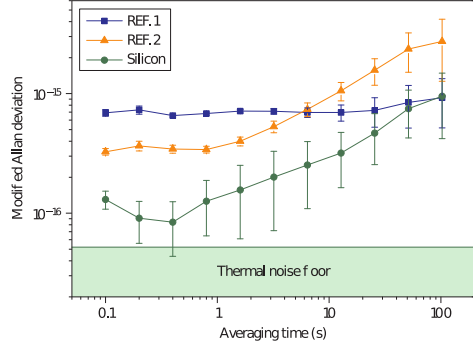


Figure 1.7: From [Kessler et al., 2012a]: Allan deviation showing the average instability of three reference cavities used for laser stabilization. Ref.1 and Ref.2 are conventional cavities, while the third cavity is made of mono-crystalline silicon.

rewriting in Eq. (1.2) exploits that this S/N ratio scales with the square root of the number of measured atoms for quantum projection noise limited measurements [Boyd, 2007, p.7]. The parameter $Q = v_0/\Delta\nu$ is the so-called quality factor denoting the experimentally determinable ratio of the atomic transition frequency v_0 and the transition linewidth $\Delta\nu$. The atomic transitions used in atomic clocks can ideally yield very high Q -factors and these transitions are often denoted *clock transitions*.

It can be seen from Eq. (1.2) that the Allan deviation is reduced for longer averaging time τ . This is illustrated by the dashed prediction lines in Fig. 1.6. It can also be seen that the Allan deviation can be reduced further by choosing an atomic transition with very high Q -factor and number of atoms N . The Q -factor is $\sim 2 \times 10^{10}$ for the hyperfine ground state transition of ^{133}Cs . However, the clock transitions of the optical atomic clock candidates yield Q -factors in the $10^{16} - 10^{17}$ -level due to the high optical frequencies in the ~ 100 THz-level and sub-Hz transition linewidths. Clearly, the optical atomic clocks have the potential to surpass the stability of the clocks operating in the microwave frequencies.

In fact, the state-of-the-art optical atomic clocks have in the recent years surpassed the precision level of the definition of the second [Chou et al., 2010a, Hinkley et al., 2013, Nicholson et al., 2015, Ushijima et al., 2015, Le Targat et al., 2013]. This makes the precision evaluation of such state-of-the-art optical clocks difficult, since the accuracy and stability of a frequency can only be evaluated relative to some reference frequency. All

stability evaluations of optical atomic clocks are hence relative evaluations performed by comparison of *two* systems with similar stability levels. The data shown previously in Fig. 1.6 are also acquired by comparing several optical atomic clock systems. Whereas stability measurements surpassing the definition of the second can be performed by comparison of two optical atomic clocks, nothing can per definition be more accurate than the definition of the second. A redefinition of the second seems to be inevitable in the future. Such a redefinition would correspond to improving the resolution of the scale of the target as shown in Fig. 1.5e) and allow even more detailed determination of the stability and accuracy of frequency measurements.

1.2 Optical Atomic clocks

It is suggested from Eq. (1.2) that precision levels surpassing the microwave clocks can be achieved by employing optical transitions with high Q -factor values. Precise measurements of the atomic transitions need reduction of the motional effects of the atomic transitions. Tight confinement of the atoms are hence needed. In general, two different trap schemes have been pursued for tight atom confinements in atomic clocks: *ion clocks* which exploit the long trapping times of a single ion in time-varying electric quadrupole potentials and *optical lattice clocks* which exploit the trapping of a large number of neutral atoms in a dipole trap operating at a so-called *magic wavelength* which cause equal AC Stark shifts on the both upper and lower levels of the clock transition [Katori, 2001]. Both ion clocks and optical lattice clocks have reached amazing precision and accuracy levels by imposing rigorous control of the systematic errors and shifts caused by the system environments.

The invention of the so-called frequency comb has allowed the comparisons of optical frequencies with other optical or microwave frequency standards [Diddams et al., 2000] and both absolute (relative to the current definition of the second, [Le Targat et al., 2013, Tyumenev et al., 2016]) and relative measurements of the different optical atomic clocks have been realized [Yamanaka et al., 2015, Tyumenev et al., 2016, Nemitz et al., 2016]. The frequency comb has had an essential impact on the research in the field of precision physics and it was awarded with the Nobel prize in 2006 [Hänsch and Hall, 2006]. Fractional instabilities in the 10^{-18} levels have been realized for both ion clocks ([Chou et al., 2010a, Huntemann et al., 2016]) and optical lattice clocks [Nicholson et al., 2015, Ushijima et al., 2015, Le Targat et al., 2013]. However, the optical lattice clocks have the

possibility to realize this stability level for much shorter averaging time τ as the large number of trapped atoms N in optical lattice clocks yield a lower Allan deviation in Eq. (1.2).

A selection of the current research topics within optical atomic clocks are mentioned in the following section. These topics are presented here to give the reader a general idea of the broad range of research topics which will benefit from improvements of the optical atomic clocks. Readers familiar with the main research topics in the field of optical atomic clocks can skip ahead to Sec. 1.3 where the current limitations of the optical atomic clocks and the main scope of this work is presented.

Gravitational sensing

One of the consequences of Einsteins General relativity is that time runs differently for different gravitational potentials. Consequently, the clock laser frequencies of two optical atomic clocks will oscillate differently if the two clocks are separated in different gravitational fields. This has been detected by comparing two optical $^{27}\text{Al}^+$ -based ion clocks based positioned with a relative height difference of 33 cm [Chou et al., 2010b]. See Fig. 1.8. Similar effects have also been detected by comparing two optical lattice clocks [Yamaguchi et al., 2011].

This sensitivity to changes in gravitational potentials opens the prospects for applying optical atomic clocks to relativistic geodesy [Baudouin et al., 2013] or for contribute [Graham et al., 2013] to the future studies of the newly discovered gravitational waves [Abbott et al., 2016].

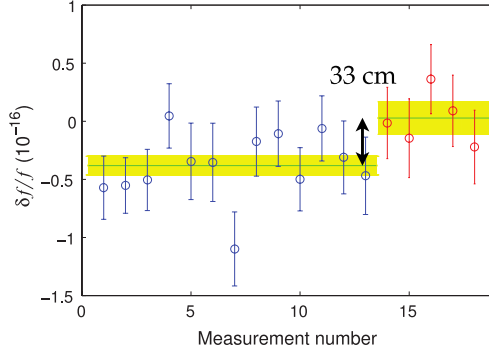


Figure 1.8: From [Chou et al., 2010b]: The fractional frequency differences for two $^{27}\text{Al}^+$ -based optical ion clocks has been demonstrated to change for different relative heights.

Variation of fundamental constants

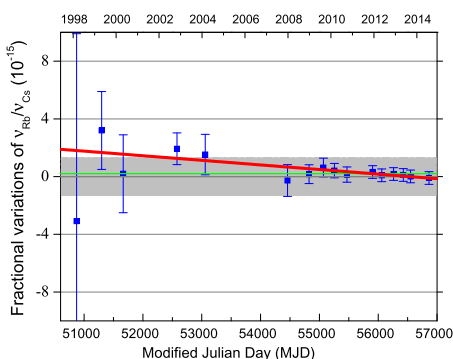


Figure 1.9: From [Abgrall et al., 2015]: The fractional variation of the ratio of the ground state hyperfine splitting for ^{87}Rb and ^{133}Cs , $\nu_{\text{Rb}}/\nu_{\text{Cs}}$, has been measured for 14 years. A drift might be indicated in this figure, however no significant drift has yet been confirmed.

The transition frequency of an atomic transition depends on the atomic number Z and the fine structure constant α_{fine} . Potential time variations of the fine structure constant can thus be studied by comparing two optical atomic clocks based on two different elements with different sensitivity to variations of the fine structure constant. Such studies have been performed both by comparing microwave clocks [Guéna et al., 2012] and by comparing optical ion clocks [Rosenband et al., 2008, Godun et al., 2014]. No clear drift of α_{fine} has yet been detected but an

upper limit of the time variation $\dot{\alpha}_{\text{fine}}/\alpha_{\text{fine}} = -(0.7 \pm 2.1) \times 10^{-17} \text{ year}^{-1}$ has been reported [Godun et al., 2014]. See Fig. 1.9.

Fiber links

A redefinition of the second will require a mature infrastructure of optical atomic clocks for comparing clocks around the world. Unfortunately, the most precise optical atomic clocks require advanced laboratory environments and are not yet transportable. While microwave clocks can compare frequencies using global satellite systems such as the GPS, a satellite based frequency comparison of two optical atomic clocks would be limited by the uncertainties caused by the atmospheric disturbances. Hence, fiber optical links over several hundred kilometers have been realized across international borders [Predehl et al., 2012, Lisdat et al., 2015]. Figure 1.10 illustrates one of these fiber optical links. Recently, frequency transfer with fractional instability in the 10^{-17} level has been reported [Lisdat et al., 2015], which evokes the possibilities for distributing the stabilities of the optical atomic clocks around the world.



Figure 1.10: From [Predehl et al., 2012]: Map of a 920 km fiber link for frequency comparison realized between München and Braunschweig in Germany.

Transportable optical clocks

An other strategy to distribute the supreme stabilities of the optical atomic clocks is to develop compact and energy efficient clocks systems. See Fig. 1.11. Staggering efforts have also been put into the development of space atomic clocks as PHARAOⁱⁱ and the Space Optical Clocks (SOC) project [Bongs et al., 2015], for improving the stability of satellite based frequency comparisons. The development of compact optical clock systems stabilized on narrow molecular transitions are also pursued [Castagna et al., 2013]. It should be mentioned that the technology for microwave clocks is in many ways more mature and several compact microwave clock

ⁱⁱPHARAO is in fact a microwave clock, but it will improve both the stability and accuracy level currently available in space.

systems have shown impressive stability and accuracy levels [Prestage et al., 2008, Schwindt et al., 2015].



Figure 1.11: From [Riehle, 2015]: A picture of a transportable optical lattice clock, which fits inside a truck.

work is improvements of the current state-of-the-art stabilized lasers.

Many of the above mentioned applications of optical atomic clocks are currently limited by the stability of the ultra stable clock lasers used for interrogation of the clock transmissions. A significant improvement of the stability of those clock laser would hence lead to advances for all above mentioned applications. Motivated by this demand, the main scope of this work is improvements of the current state-of-the-art stabilized lasers.

1.3 Ultra stable lasers

As mentioned previously, the state-of-the-art optical lattice clocks have achieved stabilities down to the 1×10^{-18} level. However, this requires averaging times in the order of $\tau = 10000$ s (about 3 hours). Ideally, the same stability level is desired for much shorter averaging time. It can be seen in Eq. (1.2) that the integration time τ can be reduced if the Q -factor or the number of atoms N could be increased. Only limited improvement of stability can be expected from increasing N as Eq. (1.2) scales as $N^{-1/2}$.

On the other hand, a significant improvement of the Q -factor can be expected, as the ultra high Q -factor are not fully exploited for the clock

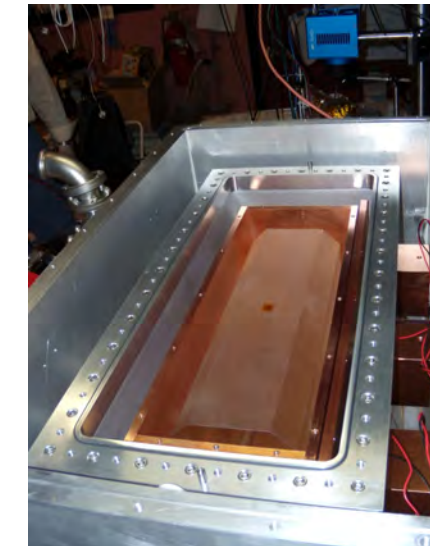


Figure 1.12: Private photo: The 40 cm ULE cavity inside a 3 layer vacuum system. Described in details in [Bishof et al., 2013, Bloom et al., 2014].

transitions of the optical lattice clock candidates. The current state-of-the-art stabilized lasers reaches fractional instabilities in the low 10^{-16} level corresponding to a linewidth in the order of 20 – 50 mHz [Bishof et al., 2013, Kessler et al., 2012a, Häfner et al., 2015]. This linewidth level is

still too large to resolve the natural linewidths $\Delta\nu$ of the clock transitions for the optical lattice clock systems where stability in the 10^{-18} level has already been achieved ($\Delta\nu = 1 \text{ mHz}$ for ^{87}Sr and $\Delta\nu = 10 \text{ mHz}$ for ^{171}Yb (CITE Ludlow review)). The Q -factor is hence limited by the linewidths of the lasers interrogating these clock transitions. These lasers are often denoted as *clock lasers*.

Current state-of-the-art clock lasers achieve these stability levels by locking the laser to an ultra stable passive optical cavity. These reference cavities are very complex and expensive cavity systems with high Q -factors. Figure 1.12 shows one of these ultra stable cavity systems consisting of *Ultra-Low Expansion* (ULE) glass cavity spacers placed under noise isolated environments. However, the stability of the current state-of-the-art clock lasers are currently limited by the thermal Brownian motions of the cavity mirrors [Kessler et al., 2012b, Cole et al., 2013]. This has already been indicated in Fig. 1.7, where the Allan deviation of an ultra stable laser is forced above a certain thermal noise floor for all integration times. New strategies and technologies seems necessary if further improvements are to be achieved and if the costs for these improvements are to be reduced.

1.3.1 Strategies for improvement

A variety of different strategies are investigated in order to surpass the limitations forced by the thermal noise. One conceptually straight forward strategy is to cool the optical cavity down to cryogenic temperatures. Ultra stable reference cavities composed of mono-crystalline silicon cavity spacers have been realized at 124 K temperatureⁱⁱⁱ and a linewidth of 40 mHz has been reported [Kessler et al., 2012a]. Such elaborate systems technically highly complex and expensive and not yet widely accessible.

Another conceptually simple strategy is to apply longer reference cavities. As the fractional frequency instability $\delta\nu/\nu_0$ scales proportionally with the stability of the cavity length $\delta L/L_0$. This fractional instability may potentially be reduced by increasing the cavity length L_0 . However, the use of longer and heavier cavities complicates the vibration suppression and uniform temperature control. Long term fractional instabilities in the low 10^{-16} and even short term fractional instabilities in the high 10^{-17} level has been reported [Häfner et al., 2015].

Another more complex strategy with great prospects is to apply crystalline mirror coatings consisting of monocrystalline multi-layers

ⁱⁱⁱ124 K is the zero crossing temperature of the thermal expansion coefficient of the mono-crystalline silicon spacers.

instead of the conventional dielectric multilayers for mirror coatings. Optical cavities with such crystalline coatings has been realized and a reduction of the thermal noise floor with an order of magnitude has been reported [Cole et al., 2013]. This strategy can potentially be combined with the conventional reference cavity technologies. Crystalline coatings can hence potentially push the entire research field forward if the technology matures and becomes widely accessible.

The last strategy to be mentioned here is to apply narrow line atomic transitions as a quantum mechanical frequency discriminator for laser stabilization. Recent proposals suggest to trap atoms with narrow transitions inside an optical cavity and probe the combined atom-cavity system [Martin et al., 2011, Chen, 2009]. The optical cavity serve primarily to enhance the atom-light interactions. The atomic linewidth will then dominate the linewidth of the combined system if the cavity linewidth is much greater than the atomic linewidth. One variation of this strategy is to realize so-called *active* frequency standards which directly emit radiation with a given frequency determined by the properties of the atoms. It has been proposed that active standards in the so-called *bad cavity* regime has prospects of reaching linewidths in the mHz range [Meiser et al., 2009, Chen, 2009]. The main topic of this work is to investigate the prospects for experimental realization of such atom-cavity systems for laser stabilization.

The above mentioned strategies are just a limited selection of the many current efforts around the world for improving the forefront of laser stabilization. The incredible development of the laser technology since its invention can be felt by reading the following quote from 1988 by Peter W. Milonni and Joseph H. Eberly in [Milonni and Eberly, 1988, p.363] regarding the realizable values for the *finesse*^{iv} of an Fabry-Perot optical cavity:

Practical difficulties, such as surface roughness of the Fabry-Perot plates, place a normal upper limit of around 30 on the finesse, tough values in the range $F \approx 100$ can be achieved under special circumstances.

The finesse is a quantity, which reflects the quality of an cavity as a frequency discriminator and despite this above mentioned claim from 1988, Finesses in the $\times 10^5$ level are widely achievable today [Kessler et al., 2012a, Häfner et al., 2015]. This improvement has only been possible due to a generation of material scientists and optical physicists who has

^{iv}Described in more details in Sec. 4.1.

pursued a vast number of strategies for improvements. This work will present just one more effort in the quest for ultimate precision.

CHAPTER

2

ACTIVE FREQUENCY STANDARDS

It was introduced in the previous chapter that the current state-of-the-art optical atomic clocks are limited by the instability of the clock lasers used in the atomic clocks. This work studies the prospect for exploiting narrow atomic transitions in order to surpass the current stability limits of these clock lasers.

Two main strategies are studied in this work: *laser stabilization on atomic systems*, and *active light sources*. The main concepts of these two strategies are presented briefly in the following sections before more detailed studies are presented from Chapter 3 and onwards.

Good and bad cavity limits

Most conventional lasers operate in the so-called *good cavity limit*. In this *good cavity limit*, lasing is realized for an atomic gain profile with linewidth Γ and optical cavity linewidth κ which relate to each other as $\kappa \ll \Gamma$, see Fig. 2.1. Shawlow and Townes originally predicted [Schawlow and Townes, 1958] the ideal linewidth $\Delta\nu_{\text{Good}}$ of a laser operating in the good cavity limit and only limited by the phase noise due to spontaneous emissionⁱ:

$$\Delta\nu_{\text{Good}} = \frac{\hbar\nu}{4\pi} \frac{\kappa^2}{P_{\text{out}}}, \quad (2.1)$$

ⁱ $\Delta\nu_{\text{Good}}$ is a linewidth in units of Hz while κ and Γ are in angular frequencies.

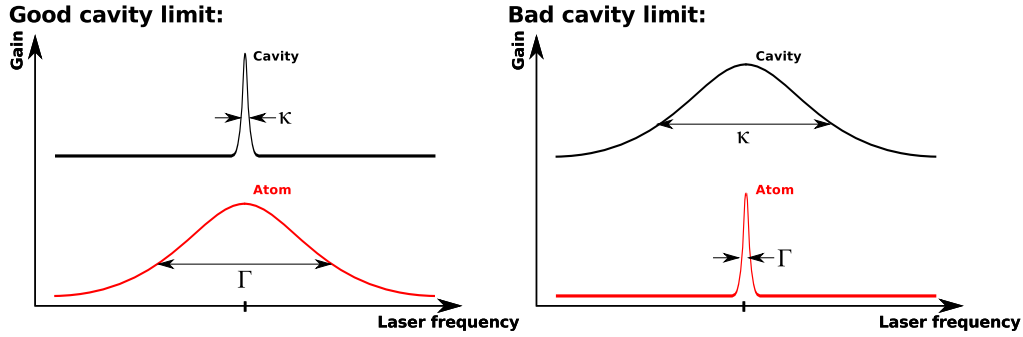


Figure 2.1: Illustrations of the relation between the cavity linewidth κ and atomic linewidth Γ for in the good cavity limit (left) and the bad cavity limit (right).

where P_{out} is the laser output power. It is assumed in Eq. (2.1), that the center frequencies of the atomic and cavity gain profiles coincide and that the laser is operating at steady state.

Equation (2.1) can yield remarkably narrow linewidths by realizing a narrow cavity linewidth κ and by operating at a high output power P_{out} . However, Eq. (2.1) do not take into account phase noise contributions such as fluctuations of the cavity length. The linewidths of the current state of the art laser systems are thus not limited by the Shawlow-Townes limit. They are instead limited by thermal noise in the entire reference cavity ensemble used for frequency stabilization [Kessler et al., 2012a, Cole et al., 2013].

A great number of strategies are being pursued to push laser stabilities beyond the thermal noise induced limitations as already discussed in Sec. 1.3.1. One strategy is to apply atom-cavity systems in the *bad cavity limit* where $\kappa \gg \Gamma$. Shawlow and Townes' linewidth limit in the good cavity limit described in Eq. (2.1) can be modified to an expression for a generalized linewidth limit $\Delta\nu_{\text{General}}$ [Kuppens et al., 1994]:

$$\Delta\nu_{\text{General}} = \frac{h\nu}{4\pi P_{\text{out}}} \frac{\kappa^2}{(\Gamma + \kappa)} \left(\frac{\Gamma}{\Gamma + \kappa} \right)^2. \quad (2.2)$$

Equation (2.2) reduces to Eq. (2.1) in the good cavity limit ($\kappa \ll \Gamma$). The latter factor $\frac{\Gamma}{\Gamma + \kappa}$ decreases in the bad cavity limit ($\kappa \gg \Gamma$) and the linewidth limit $\Delta\nu_{\text{Bad}}$ is:

$$\Delta\nu_{\text{Bad}} = \frac{h\nu}{4\pi P_{\text{out}}} \frac{\Gamma^2}{\Gamma + \kappa}. \quad (2.3)$$

This linewidth limit is dominated by the width of the atomic gain profile. $\Delta\nu_{\text{Bad}}$ can potentially surpass the good cavity limit (Eq. (2.1)) as atomic linewidths can be much narrower ($\Gamma \sim m\text{Hz}$) than the practically realizable linewidths for an optical cavity ($\kappa \sim 10 \text{ kHz}$).

An atom-cavity system in the bad cavity limit is also much less sensitive to the fluctuations of the cavity length. An atom-cavity system will have a combined average lasing frequency $\nu_{\text{avg}} = (\Gamma\nu_c + \kappa\nu_a)/(\Gamma + \kappa)$ when the atomic and cavity resonance frequencies ν_a and ν_c are not identical. Changes in the cavity length will cause the cavity resonance frequency ν_c to change and result in modifications of the combined resonance frequency ν_{avg} of the atom-cavity system. This effect is called *cavity pulling*. Fluctuations in cavity length will hence be manifested in fluctuations in the combined lasing frequency. The sensitivity P to this cavity pulling can be expressed as:

$$P = \frac{d\nu_{\text{avg}}}{d\nu_c} = \frac{\Gamma}{\Gamma + \kappa}. \quad (2.4)$$

Equation (2.4) shows, that the lasing frequency in the bad cavity limit is much more insensitive to fluctuations in the cavity frequency, as $P \approx 1$ in the good cavity limit, while $P \ll 1$ in the bad cavity limit.

Two strategies are studied in this work in order to improve laser stabilization by using systems in the bad cavity limit: *Laser stabilization on atomic systems* where a laser is stabilized in a feedback system with an atomic transition as a frequency discriminator, and *active light sources* where spectrally pure radiation is emitted directly and collectively from a narrow atomic transition. The main concepts of these two strategies are described below.

2.1 Laser stabilization on atomic systems

Recent studies have proposed to apply laser cooled atoms with ultra narrow transitions inside an optical cavity for laser stabilization [Martin et al., 2011]. Figure 2.2 illustrate the main concept, where the atom induced phase dispersion is used as an error signal for laser stabilization. An ultra narrow transition such as the ${}^1\text{S}_0 \rightarrow {}^3\text{P}_0$ transition in neutral strontium can provide a frequency discriminator with a linewidth in the order of mHz. Such ultra narrow transitions are very insensitive to external perturbations and the effect of the external perturbations are very well characterized in optical clock experiments [Riehle, 2015].

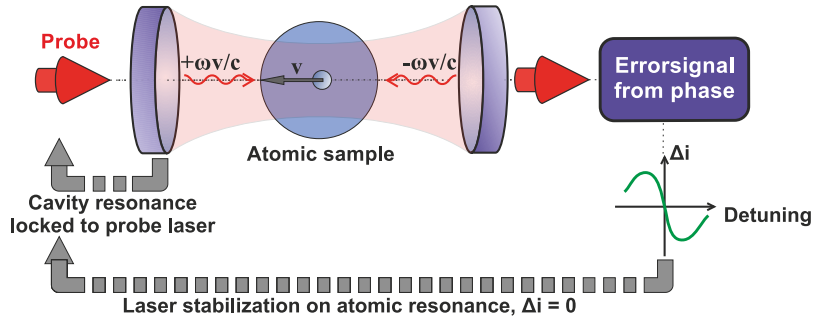


Figure 2.2: Schematics of stabilization of a probe laser on an atom-cavity system. The atom induced phase shift on the cavity transmitted field is detected and converted to a photocurrent Δi . This photo current serves as an error signal for a feedback loop that stabilized the probe laser frequency on the atomic resonance. In this work, the cavity resonance frequency v_c is required to be on resonance with the probe laser. This requirement is described in details later in Sec. 3.

Ultra narrow transitions are easily strongly saturated and this causes the system dynamics to become highly nonlinear and nontrivial. Furthermore, narrow transitions interact only very weakly with light and sufficient optical depths are not available in free space for current experimental systems. The interrogation of the atoms are hence cavity enhanced by placing the atoms inside an optical cavity. The first proposals have studied the highly non-linear dynamics of such atom-cavity systems with atomic temperatures equivalent to zero degree Kelvin [Martin et al., 2011]. In this work, these studies are extended by theoretical studies of the dynamics of a similar system with finite atomic sample temperatures. The ideal achievable linewidths are also predicted theoretically for laser stabilization on such systems. These theoretical studies are published in [Tieri et al., 2015] and discussed in details in Chap. 3. Two proof-of-concept experimental setups were also constructed during this work and the non-linear dynamics predicted in [Tieri et al., 2015] are investigated experimentally. The details of the experimental setups are described in Chap. 4–5, while the results of these experimental studies are published in [Westergaard et al., 2015, Christensen et al., 2015a] and presented in Sec. 6.

Finally, it should be mentioned that laser stabilization on optical transitions have been performed previously in several different systems [Cook et al., 2015, Fox et al., 2012]. These stabilization systems typically use stronger optical transitions, which are more sensitive to external perturbations. These transitions are hence not suited for improving the

current state-of-the-art laser stability.

2.2 Active light sources

Another approach is to let atom-cavity systems in the bad cavity limit to directly emit radiation with a spectral purity determined by the atomic transition linewidth Γ . This radiation is emitted collectively by the atoms inside the cavity. This collective emission is described in more details later in Sec. 7. The atomic transition will serve as a frequency filter and determine both the precision and accuracy of the system. The impact of the atomic transition can be seen in Eq. (2.3), where the lower limit of this bad cavity laser linewidth is dominated by the spontaneous emission rate Γ . $\Delta\nu_{\text{Bad}}$ in Eq. (2.3) can even be more narrow than the atomic transition Γ .

It has hence been proposed that extreme spectral purity can be achieved by applying ultra narrow transitionsⁱⁱ in such atom-cavity systems [Chen, 2009, Meiser et al., 2009]. These proposed active light sources are immune to thermal noise in the cavity frequency due to a vanishing pulling coefficient P (See Eq. (2.4)) and may pave the way to achieve laser stability levels below the thermal noise level. Excellent accuracy levels can also be achieved for such active light sources as the emitted optical frequency is determined by the atomic transition frequency.

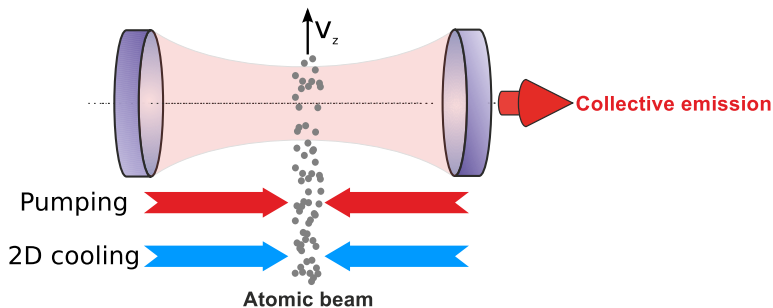


Figure 2.3: Schematics of collective emission from a beam of atoms coupled to an optical cavity. A beam of atoms are laser cooled in the directions relevant for the cavity. The atoms are pumped to the excited state before entering the cavity and emit radiation into the cavity mode.

Collective emission from narrow line transitions has been realized experimentally [Norcia and Thompson, 2016a, Norcia et al., 2016] and

ⁱⁱSuch as the 1 mHz $^1\text{S}_0 \rightarrow ^3\text{P}_0$ transition in neutral strontium.

laser linewidths narrower than the atomic transition linewidths have been observed for other systems [Bohnet et al., 2012, Zhi-Chao et al., 2015] with broader transition linewidths. Most of the mentioned collective emission experiments[Bohnet et al., 2012, Norcia and Thompson, 2016a, Norcia et al., 2016] are performed cyclically and the collective emission is only observed as pulses. Continuous operation is desired for clock purposes. This, however, requires a continuous and incoherent pumping of the upper excited state of the radiating transition. This may be achieved in 3- or 4-level systems [Zhi-Chao et al., 2015] or by coupling the cavity to a beam of atoms cooled in the relevant dimensions [Chen, 2009] where the intra cavity atoms are continuously replaced by new atoms in the beam. See Fig. 2.3. Such an atomic beam system can also be adapted for continuous laser stabilization described in Sec. 2.1.

Many experiments for studying collective emissions are performed with atomic samples trapped in optical lattices. In this work, preliminary studies are done for investigating the possibility of extracting spectrally narrow collective emission from laser cooled thermal atoms. These studies are presented in details in Sec. 7. The usage of thermal atoms simplifies the system and the complexity of the system is held low by avoiding more complex cooling techniques such as second stage cooling. The results from this work might thus prove valuable for more compact systems in the future.

Cooperativity

Both strategies presented in Sec. 2.1 and Sec. 2.2 depend greatly on a common unitless system parameter called the *cooperativity*. The single atom cooperativity is defined as $C_0 = 4g^2/\Gamma\kappa$, where g is the single atom-cavity coupling constant. The coefficient C_0 is a measure of how strong the coherent atom-cavity coupling is for a single atom inside the cavity mode. The *collective collectivity* $C = N_{\text{cav}}C_0$ is then a measure of how strong all the intra-cavity atoms are coupled to the cavity. Here, N_{cav} is the total number of intra-cavity atoms. Both the single atom- and collective cooperativity can *conceptually* be considered as a ratio between the rate of coherent scattering into the cavity mode and the rate of dissipation processes out of the cavity mode (shown for the collective cooperativity here):

$$C = N_{\text{cav}}C_0 = \frac{4g^2N_{\text{cav}}}{\Gamma\kappa} = \frac{\text{Coherent coupling}}{\text{dissipation}}. \quad (2.5)$$

Coherent collective emission can hence be built up inside the cavity when $C > 1$ (Coherent coupling>dissipation). A high value of the collective

cooperativity C is also beneficial for laser stabilization on an atom-cavity system, as the slope of the atom induced phase dispersion $\frac{\partial\varphi}{\partial\nu}$ is later shown to increase with C . $C = N_{\text{cav}}C_0$ can be increased by increasing the intra-cavity atom number or the cavity finesse. A natural upper limit of the collective cooperativity is however set as the number of atoms are often limited by technical limitations and the cavity finesse can only be increased in an extend where the bad cavity condition ($\kappa \gg \Gamma$) is maintained.

Outlook

This chapter has presented two promising strategies for pushing the stability of laser systems beyond the limitations induced by thermal noise. Both of these strategies operates in the bad cavity limit where strongly non-linear dynamics can be expected due to the easily saturated ultra narrow transitions used in these strategies.

The main focus in this work is laser stabilization on a system consisting of thermal atoms coupled to an optical cavity as described in Sec. 2.1. However, previous theoretical works have only described laser stabilization on atoms with temperatures equivalent to zero degree Kelvin [Martin et al., 2011]. A theoretical model for thermal atoms coupled to an optical cavity was hence developed in order to study the expected non-linear dynamics. The following chapter presents this theoretical model and investigates the non-linear dynamics relevant for laser stabilization.

CHAPTER



FINITE TEMPERATURE SYSTEMS FOR LASER STABILIZATION

It has been presented previously in Sec. 2.1 that laser stabilization on intra-cavity narrow line atomic systems show prospects for overcoming the limitations of the conventional laser stabilization techniques. In this work, theoretical and experimental studies have been done on laser stabilization using a thermal sample of laser cooled atomic systems with narrow line transitions. Laser cooled atoms exhibits larger temperatures than atoms tightly trapped in optical lattices, and this high temperature yields Doppler broadening of the transition, which might degrade the system's performance as a frequency discriminator. Nevertheless, a thermal sample was chosen as subject for this work for investigating the prospects for developing more simple and compact systems.

The structure of this chapter is organized as follows: The current state of the art of laser stabilization on atomic systems are described briefly below. Then, Sec. 3.1 describes the theoretical model developed in this work for describing the proof-of-concept experimental systems presented later in Sec. 4–6. The system dynamics and the implications for laser stabilization are then discussed in Sec. 3.2–3.4 based on this theoretical model.

Prior to this work, laser stabilization on atomic systems have been realized for a number of experimental systems which exploits atomic transitions in the $\sim 100\text{ Hz}$ level [Cook et al., 2015, Fox et al., 2012]. The advantages by applying the ultra narrow forbidden transitions ($\sim \text{mHz}$) in the alkali-earth metals are alluring. It has been predicted that laser

linewidths in the $\sim \mu\text{Hz}$ level can be achieved by applying ultra narrow optical transitions of atoms coupled to an optical cavity as frequency references for laser stabilization [Martin et al., 2011].

The theoretical work in [Martin et al., 2011] considers atoms trapped in a magic wavelength optical lattice. These trapped atoms are then placed inside an optical cavity, where the atomic transition is resonant with the cavity resonance. The optical cavity considered here in [Martin et al., 2011] has a relatively high finesse in the $\sim 10^4$ level. In this system, the atomic temperature corresponds essentially to $T = 0\text{ K}$, as the atoms are cooled down to the vibrational ground state in the optical lattice such that Doppler broadening and dissipation effects can be neglected. The design of such a system is complicated by the requirements of preparing an optical lattice inside a high finesse optical cavity resonant with the atomic transition. Furthermore, some of the essential technologies required in [Martin et al., 2011] are: magic wavelength optical lattice and pre-stabilized laser with a precision in the current state-of-the-art level. Both of these mentioned technologies are expensive technologies that are possessed primarily by state-of-the-art optical frequency standards laboratories.

In this work, theoretical studies have been done on the laser stabilization prospects of laser cooled thermal atoms ($T > 0\text{ K}$) coupled to an optical cavity in order to develop a simple alternative to the $T = 0\text{ K}$ -system. The complexity of this finite temperature system is greatly reduced by using laser cooled thermal atoms without an optical lattice and by choosing broader transitions in the $\sim \text{kHz}$ level. This theoretical work was developed by David Tieri, Murray Holland et al. from JILA, University of Colorado, in collaboration with the author of this thesis and it was published in Physical Review A 92, 053820 (2015) [Tieri et al., 2015].

3.1 Velocity dependent many-atom theory

The following section describes the theoretical model developed for this work. The above mentioned sample of laser cooled thermal atoms coupled to an optical cavity is treated as a cavity QED system, while a semi-classical interpretation is also discussed later in Sec. 3.2.1. The main scope of this section is to derive an expression for the cavity transmitted field, as this is the most accessible observable, which can be exploited in a feedback loop for laser stabilization as illustrated in Fig. 2.2.

The studied system was modeled as an ensemble of N two-level atoms coupled to a single mode of an optical cavity. Laser cooled neutral alkali atoms can be approximated as such a system. The following general

Born-Markov master equation [Meystre et al., 2007, p. 428] was used to model the open quantum system consisting of a statistical ensemble of the two-level atoms described by the density matrix $\hat{\rho}$:

$$\frac{d\hat{\rho}}{dt} = \frac{1}{i\hbar} [\hat{H}, \hat{\rho}] + \hat{\mathcal{L}}[\hat{\rho}], \quad (3.1)$$

where the coherent evolution of the system is described by the commutator term and the Liouvillian $\hat{\mathcal{L}}$ describes the dissipation of the system. The Hamiltonian \hat{H} of the coupled atom cavity system is:

$$\hat{H} = \hbar\Theta\hat{a}^\dagger\hat{a} + \frac{\hbar\Delta}{2} \sum_{j=1}^N \hat{\sigma}_j^z + \hbar\eta(\hat{a}^\dagger + \hat{a}) + \hbar \sum_{j=1}^N g_j (\hat{a}^\dagger \hat{\sigma}_j^- + \hat{\sigma}_j^+ \hat{a}), \quad (3.2)$$

where $\Theta = \omega_c - \omega_l$ is the detuning between the cavity and a probing laser, \hat{a} (\hat{a}^\dagger) is the annihilation (creation) operator of the cavity mode, $\Delta = \omega_a - \omega_l$ is the atom-laser detuning, $\hat{\sigma}_j^+$, $\hat{\sigma}_j^-$ and $\hat{\sigma}_j^z$ are Pauli spin matrices for the atoms and g_j is the atom-cavity coupling rate for the j 'th atom. The rate at which photons from the probe laser couples into the cavity is described by the so-called classical drive amplitude η , which is described as:

$$\eta = \sqrt{\frac{2\pi\kappa P_{\text{in}}}{\hbar\omega_c}}. \quad (3.3)$$

Here, κ is the cavity decay rate, P_{in} is the input optical power and ω_c is the resonance frequency of the cavity mode.

The parameters in Eq. (3.2) need to be specified to match the system studied in this work. The criterion $\Theta = \omega_c - \omega_l = 0$ was chosen, corresponding to a system where the empty cavity resonance is forced to be on resonance with the probe laser. This criterion is similar to the criterion also chosen in [Martin et al., 2011]. However, it turned out later, that this criteria differs slightly from the experimental system described in this work (described in Chap. 5), where the cavity mode modified by the atomic induced phase shift is forced to be on-resonance with the probing laser. This causes a standing wave to be present in the cavity at all times. It is shown later in Chap. 6, that this experimental criteria in this work modifies the experimental observables substantially compared to the theoretical results presented in this chapter. All atoms were also attributed finite velocities from a Maxwell-Boltzmann velocity distribution

and the spatial extent of the cavity field is also taken into account. The atom-cavity coupling rates are described as $g_j(t) = g_0 \frac{1}{2\pi w_0^2} e^{-r_j^2/w_0^2} \cos(\delta_j t)$, where g_0 is the maximum coupling amplitude, r_j is the radial position of the j 'th atom relative to the cavity axis, w_0 is the cavity waist radius, $\delta_j = k \cdot v_j$ is the Doppler shift for the j 'th atom with the velocity v_j and k is the wavenumber of the probe laser. The final Hamiltonian used in this model is then:

$$\hat{H} = \underbrace{\frac{\hbar\Delta}{2} \sum_{j=1}^N \hat{\sigma}_j^z}_{\text{Atomic excitation}} + \underbrace{\overbrace{\hbar\eta(\hat{a}^\dagger + \hat{a})}^{\text{Cavity photons}} + \hbar g_0 \frac{1}{s\pi w_0^2} \sum_{j=1}^N e^{-r_j^2/w_0^2} \cos(\delta_j t) (\hat{a}^\dagger \hat{\sigma}_j^- + \hat{\sigma}_j^+ \hat{a})}_{\text{Atom-cavity coupling}}. \quad (3.4)$$

The incoherent evolution of the evolution is described by the Liouvillian, $\hat{\mathcal{L}}[\hat{\rho}]$, in the second term of Eq. 3.1. The Liouvillian describes the decoherence contributions from the different dissipation channels in the system:

$$\begin{aligned} \hat{\mathcal{L}}[\hat{\rho}] &= \underbrace{-\frac{\kappa}{2}(\hat{a}^\dagger \hat{a} \hat{\rho} + \hat{\rho} \hat{a}^\dagger \hat{a} - 2\hat{a} \hat{\rho} \hat{a}^\dagger)}_{\text{Cavity dissipation}} \\ &\quad - \underbrace{\frac{\Gamma}{2} \sum_{j=1}^N (\hat{\sigma}_j^+ \hat{\sigma}_j^- \hat{\rho} + \hat{\rho} \hat{\sigma}_j^+ \hat{\sigma}_j^- - 2\hat{\sigma}_j^- \hat{\rho} \hat{\sigma}_j^+)}_{\text{Atomic decay}} \\ &\quad + \underbrace{\frac{\Gamma_p}{2} \sum_{j=1}^N (\hat{\sigma}_j^z \hat{\rho} \hat{\sigma}_j^z - \hat{\rho})}_{\text{External decoherence}}, \end{aligned} \quad (3.5)$$

where Γ is the spontaneous decay rate of the atomic transition and $\Gamma_p = \Gamma/2 + \Gamma_{\text{dec}}$ is the total decay rate of the atomic dipole including the external decoherence rate Γ_{dec} .

The equations of motion for the expectation values of the field operator $\langle \hat{a} \rangle = \alpha$ and the atomic operators $\langle \hat{\sigma}_j^\pm \rangle = \sigma_j^\pm$ and $\langle \hat{\sigma}_j^z \rangle = \sigma_j^z$ can be derived using Equation (Eq. 3.1–3.5):

$$\dot{\alpha} = -\kappa\alpha + \eta + \sum_{j=1}^N g_j(r_j, t)\sigma_j^-, \quad (3.6)$$

$$\dot{\sigma}_j^- = -(\Gamma_p + i\Delta)\sigma_j^- + g_j(r_j, t)\alpha\sigma_j^z, \quad (3.7)$$

$$\dot{\sigma}_j^z = -\Gamma(\sigma_j^z + 1) - 2g_j(r_j, t)(\alpha^*\sigma_j^- + \alpha\sigma_j^+). \quad (3.8)$$

Here we have introduced a semi-classical approximation, where both the atom number N and the cavity field drive is sufficiently large, and thus making the atoms and the cavity field, uncorrelated, $\langle \hat{a}^\dagger \hat{\sigma}_j^- \rangle \approx \langle \hat{a}^\dagger \rangle \langle \hat{\sigma}_j^- \rangle$. The dynamics of the system is described by Eq. (3.6)-(3.8) and the cavity transmission spectrum can be calculated through the intra cavity photon number $|\alpha|^2 = \langle \hat{a}^\dagger \hat{a} \rangle$. Solutions for α are of particular interest as mentioned previously, as the cavity transmitted field is the most accessible observable in the experimental systems studied in this work.

Equation (3.6)–(3.8) can be approximated to take the Doppler shift $\delta_j = kv_j$ into account:

$$\dot{\alpha} = -\kappa\alpha + \eta + \tilde{g}_0 N \int P(\delta) \cos(\delta t) \sigma^- d\delta, \quad (3.9)$$

$$\dot{\sigma}^- = -(\Gamma_p + i\Delta)\sigma^- + \tilde{g}_0 \cos(\delta t) \alpha \sigma^z, \quad (3.10)$$

$$\dot{\sigma}^z = -\Gamma(\sigma^z + 1) - 2\tilde{g}_0 \cos(\delta t)(\alpha^*\sigma^- + \alpha\sigma^+). \quad (3.11)$$

Here, $\delta = kv$ is a continuous variable and $P(\delta)$ is the Maxwell-Boltzmann velocity distribution with width δ_0 . This parameter δ_0 is related to the atomic sample temperature trough:

$$\delta_0 = \sqrt{\frac{k_B T}{mk^2}}. \quad (3.12)$$

The index j are gone in Eq. (3.9)–(3.11) as the atomic velocities are taken into account through the Maxwell-Boltzmann distribution instead of treating all N atoms individually. The spatial distribution of the cavity field is taken into account similarly through the Gaussian distribution of the intra-cavity field. The intra-cavity position of the atoms are independent of their velocities, so this spatial distribution of the cavity field was averaged and yields an effective atom-coupling rate $\tilde{g}_0 = g_0 \frac{1}{w_0^2} \int_0^\infty r e^{-r^2/w_0^2} \rho_{\text{MOT}}(r) dr$

in Eq. (3.9)-(3.11). Here, $\rho_{\text{MOT}}(r)$ is a uniformⁱ and normalized density distribution of the intra-cavity atoms.

A first approach would be to solve Eq. (3.9)-(3.11) by numerical integration of the integral while dividing the integral into finite-sized velocity bins. A second approach is however used for the theoretical studies presented in the rest of this section, as this approach illustrates the underlying physics more intuitively. The results of the two approaches do, however, show excellent agreement as long as the resolution of the velocity bins are high enough [Tieri et al., 2015].

In this second approach, σ^\pm and σ_z are expanded in terms of their Fourier components:

$$\sigma^- = \sum_l e^{il\delta t} x_1^{(l)}, \quad (3.13)$$

$$\sigma^+ = \sum_l e^{il\delta t} x_2^{(l)}, \quad (3.14)$$

$$\sigma^z = \sum_l e^{il\delta t} x_3^{(l)}, \quad (3.15)$$

where $x_1^{(l)}$, $x_2^{(l)}$ and $x_3^{(l)}$ are the complex amplitudes of the l 'th Fourier component. This expansion separates the slow evolution of the system (contained in $x_{1,2,3}^{(l)}$) and the fast evolution with frequencies $l \cdot \delta$.

The fast evolution with the frequencies $l \cdot \delta$ ($l \neq 0$) govern so-called doppleron resonances, which are multi-photon scatterings which can occur for atomic systems exposed to counter-propagating radiation with two different wavelengths [Tallet, 1994, Ficek and Freedhoff, 1993, Kyrölä and Stenholm, 1977]. In the system considered here, the bi-chromatic radiation is the Doppler shifted cavity light seen in the frame of the moving atoms. The fundamental process of these doppleron resonances are described in more details in the following Sec. 3.3.1. The contributions of the doppleron resonances are represented by the higher order Fourier components ($l \neq 0$). It is hence also possible to study the behavior of the system without doppleron resonances by only inserting only the $l = 0$ components of Eq. (3.13)-(3.15) into Eq. (3.9)-(3.11).

Equation (3.13)-(3.15) are inserted in Eq. (3.9)-(3.11) and the following equations of motion are found:

ⁱThis assumption of uniform spatial distribution of the atoms is valid for a magneto-optical trap (MOT) with high optical depth [Dinneen et al., 1999].

$$\dot{x}_1^{(l)} = -\left(i(\Delta + l\delta) + \Gamma_p\right)x_1^{(l)} + \frac{\tilde{g}_0\alpha}{2}\left(x_3^{(l+1)} + x_3^{(l-1)}\right), \quad (3.16)$$

$$\dot{x}_2^{(l)} = \left(i(\Delta + l\delta) - \Gamma_p\right)x_2^{(l)} + \frac{\tilde{g}_0\alpha^*}{2}\left(x_3^{(l+1)} + x_3^{(l-1)}\right), \quad (3.17)$$

$$\begin{aligned} \dot{x}_3^{(l)} &= -\Gamma\delta_{(l,0)} - (il\delta + \Gamma)x_2^{(l)} \\ &\quad - \tilde{g}_0\left(\alpha x_2^{(l+1)} + \alpha^* x_1^{(l+1)} + \alpha x_2^{(l-1)} + \alpha^* x_1^{(l-1)}\right). \end{aligned} \quad (3.18)$$

Higher order time derivations of the complex amplitudes $x_{1,2,3}^l$ were neglected during the derivation of Eq.(3.16)–(3.18) by performing a slowly varying amplitude approximation, as the evolution due to the Doppler shift is far faster than the conventional evolution of the systemⁱⁱ.

The steady state situation is studied by setting the time derivatives to zero in Eq.(3.16)–(3.18). Equation (3.16)–(3.17) are now substituted into Eq. 3.18 and the following expression can be found:

$$0 = \Gamma\delta_{(l,0)} + a_l x_3^{(l)} + d_l x_3^{(l+2)} + b_l x_3^{(l-2)}. \quad (3.19)$$

Here, $\delta_{(l,0)}$ is the Kronecker delta and a number of definitions are introduced for simplicity:

$$\begin{aligned} a_l &\equiv il\delta + \Gamma + \frac{\tilde{g}_0^2|\alpha|^2}{2}\left(\frac{1}{Q_{l+1}} + \frac{1}{P_{l+1}} + \frac{1}{Q_{l-1}} + \frac{1}{P_{l-1}}\right), \\ b_l = d_{l-2} &\equiv \frac{\tilde{g}_0^2|\alpha|^2}{2}\left(\frac{1}{Q_{l-1}} + \frac{1}{P_{l-1}}\right), \\ P_l &= i(l\delta + \Delta) + \Gamma_p, \\ Q_l &= i(l\delta - \Delta) + \Gamma_p. \end{aligned}$$

We can now return to Eq. (3.9) in steady state and insert the Fourier expansion Eq. (3.13):

$$\alpha = \frac{\eta}{\kappa} + \frac{\tilde{g}_0 N}{2\kappa} \int P(\delta)\cos(\delta t) \sum_l e^{il\delta t} x_1^{(l)} d\delta. \quad (3.20)$$

ⁱⁱFor the parameters of the experimental systems described in Sec. 5, the $l = 0$ terms in Eq. (3.13)–(3.15) develop with a frequency of the order of $\delta/2\pi = \langle v \rangle k/2\pi \sim 1$ MHz, while the evolution of the complex amplitude $x_{1,2,3}^l$ is in the order of the Rabi-frequency $\Omega_{\text{Rabi}} \sim 100$ kHz.

Only the components with $l = \pm 1$ in the integral of Eq. (3.20) contribute with non-oscillating values, when the expression inside the integral is calculated. Equation (3.20) can hence be simplified to the following expression, if only the steady state solution is of interest:

$$\alpha = \frac{\eta}{\kappa} + \frac{\tilde{g}_0 N}{2\kappa} \int P(\delta) (x_1^{(-1)} + x_1^{(1)}) d\delta. \quad (3.21)$$

The steady expression for the main observable of interest, α , can now be achieved by inserting steady state case of Eq. (3.16) ($\dot{x}_1^{(l)} = 0$) into Eq. (3.21):

$$\alpha = \frac{\eta}{\kappa} + \frac{\tilde{g}_0 N}{2\kappa} \int P(\delta) \frac{\tilde{g}_0 \alpha}{2} \left(\frac{x_3^{(0)} + x_3^{(-2)}}{P_{-1}} + \frac{x_3^{(0)} + x_3^{(2)}}{P_1} \right) d\delta. \quad (3.22)$$

Note that $x_3^{(0)}$ and $x_3^{(\pm 2)}$ in Eq. (3.22) depend cumulatively on all even orders of l according to Eq. (3.19). Equation (3.19) is hence a $\frac{l}{2} \times \frac{l}{2}$ -dimensional tridiagonal linear system of equations due to this cumulative dependency:

$$\begin{bmatrix} \vdots \\ 0 \\ -\Gamma \\ 0 \\ \vdots \end{bmatrix} = \begin{bmatrix} \ddots & & & & \\ 0 & d_2 & a_2 & b_2 & 0 \\ & 0 & d_0 & a_0 & b_0 & 0 \\ & & 0 & d_{-2} & a_{-2} & b_{-2} & 0 \\ & & & & \ddots & & \end{bmatrix} \begin{bmatrix} x_3^{(2)} \\ x_3^{(0)} \\ x_3^{(-2)} \\ \vdots \end{bmatrix}. \quad (3.23)$$

Equation (3.22) can be solved for a given value of α and when finite orders of l are included. We solved this efficiently by using the so-called Thomas algorithm. The components with even values of l correspond to the contributions from evolution with frequencies $2\delta, 4\delta, \dots$, which represents the contributions from the $p = l/2$ 'th doppleron resonance orderⁱⁱⁱ [Tallet, 1994]. We can now finally substitute the solutions of Eq. (3.23) into Eq. (3.22) and numerically solve this equation for the field amplitude α using Newton's method for root finding. The solutions for σ^\pm and σ^z can also be derived from Eq. (3.10) and (3.11) with similar procedures.

We have now established a velocity dependent cavity QED model for thermal atoms coupled to an optical cavity, and we have derived

ⁱⁱⁱThis is described in more details later in Sec. 3.3.1.

Eq. (3.22), which allows us to calculate the steady state solutions for the field amplitude α . As mentioned before, the solutions for the field amplitude α are of particular interest, as the field amplitude relates to the cavity transmitted field, which is an accessible observable in the experimental systems studied throughout this work. The characteristics and dynamics of this cavity transmitted field is hence studied in the following section.

3.2 Cavity transmission

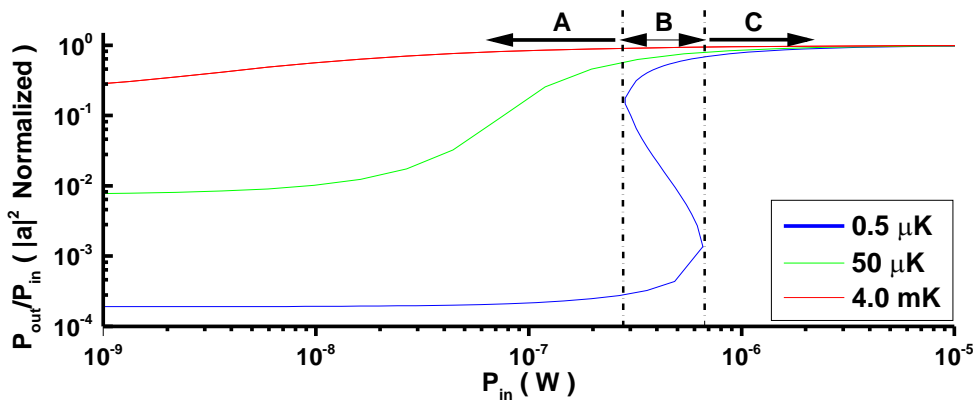


Figure 3.1: Normalized optical cavity output power ($|\alpha|^2$) as function of optical cavity input power when the probe laser frequency is on resonance with the atomic transition ($\Delta = \omega_a - \omega_l = 0$). Several solutions exist for an intermediate input power regime (marked as B) when the atomic temperature is sufficiently low.

It was argued in the previous section, that Eq. (3.6)-(3.8) describe the dynamics of the cavity QED systems^{iv} studied in this work. Furthermore, the cavity transmission can be calculated numerically in the steady state case through Eq. (3.22) as α represents the intra cavity photon number, $|\alpha|^2 = \langle \hat{a}^\dagger \hat{a} \rangle$. The spectroscopic lineshapes and the dynamics of this cavity transmission are investigated in details in the following sections.

The input power dependency of $|\alpha|^2$ is illustrated in Fig. 3.1 for three different atomic temperatures. The system parameters chosen for the theoretical calculations in Fig. 3.1 correspond to parameters from the

^{iv}Note, that these systems will also be called *atom-cavity systems*, when they are considered semi-classically throughout this work.

experimental system described in Sec. 5.2.2 with the exception of the temperature. Furthermore, the probe laser frequency is on resonance with the atomic transition ($\Delta = \omega_a - \omega_l = 0$). The solid blue line shows the case for near zero temperatures ($T = 0.5 \mu\text{K}$), which exhibits three different behaviors in three regions separated with dashed lines: For low input powers ($< 200 \text{nW} > 600 \text{nW}$, marked as A in Fig. 3.1) and high input powers ($> 600 \text{nW}$, marked as C in Fig. 3.1), the output optical power depends linearly on the input power. However, a different behavior emerges for intermediate input powers. Three different solutions are found for $|\alpha|^2$ in this intermediate regime (marked as B in Fig. 3.1). This nonlinear behavior is called *optical bistability* which also appears for $T = 0 \text{ K}$ systems [Martin et al., 2011]. Theoretical studies in [Martin et al., 2011] predict, that optimal input power for laser stabilization on similar cavity QED systems is within this bistable region. However, laser stabilization in this region is not feasible as the system will be unstable. Consequently, laser stabilization is constrained to be operated outside this region where the laser stabilization performance is orders of magnitude worse than the optimal input power region. Nevertheless, the predicted ideal shot-noise limited linewidth is in the very promising $\sim \text{mHz}$ level, even when operating above this bistability region [Martin et al., 2011].

Whereas bistability seems to limit the laser stabilization performance of $T = 0 \text{ K}$ -systems, this bistability disappears for thermal systems with much warmer temperatures. See red and green plots in Fig. 3.1. These thermal systems can hence operate stably in this bistability region, which was predicted to be the optimal region for laser stabilization. In addition, such systems will not need complex cooling and trapping techniques such as optical lattices operating at the magic wavelength. Consequently, laser stabilization in a favorable parameter regime can be performed in a much simpler experimental systems. This seems very promising but the laser stabilization performance of such systems needs to be studied thoroughly in order to evaluate, whether these thermal systems are competitive with the $T = 0 \text{ K}$ -systems. Such studies are presented later in Sec. 3.4.

Detailed understanding of the spectral lineshapes of the cavity transmitted light have to be established in order to understand why the cavity QED system studied here is suited for laser stabilization. Many previous works have described cavity QED systems with Hamiltonians similar to Eq. (3.2) with frequency relations as $\Delta = \Theta$ which corresponds to an optical cavity resonance locked on the atomic transition frequency ($\omega_c = \omega_a$). With such frequency relations, the cavity transmission spectrum reveals a splitting of the cavity transmission as a function of laser frequency ω_l . See Fig. 3.2. This splitting is the so-called *Vacuum Rabi splitting*, which is

often considered as a fingerprint of a strongly coupled cavity QED system [Tanji-Suzuki et al., 2011]. However, keep in mind that the frequency relations in the system studied here is $\Theta = \omega_c - \omega_l = 0$. This frequency relation yields a cavity transmission spectrum, which differ significantly from the Rabi splitting spectrum shown in Fig. 3.2. This alternative cavity transmission spectrum exhibits features, which can be most intuitively understood by considering the system semi-classically. The following section will hence present a semi-classical interpretation of this cavity transmission spectrum.

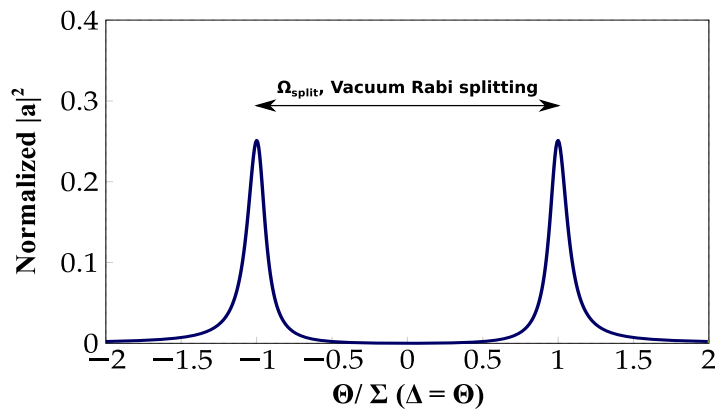


Figure 3.2: From [Matin, 2013]: Normalized optical cavity output power ($|\alpha|^2$) as function of probe laser detuning $\Delta = \omega_a - \omega_l$ relative to the atomic resonance. The cavity resonance and atomic resonance are kept equal in this case ($\omega_c = \omega_a$ and thus $\Theta = \Delta$). The splitting (in frequency) is to a good approximation proportional with the collective coupling parameter $g = g_0 \sqrt{N}$ [Tanji-Suzuki et al., 2011].

3.2.1 Cavity transmission in terms of classical dispersion

A semi-classical picture proves to be useful when considering the transmission characteristics of the main system of this work studied theoretically in Sec. 3.1 and 3.2. In this section, The vacuum Rabi splitting, which was presented quantum mechanically in the most recent Section, will be described semi-classically at first. This semi-classical description will then be applied for interpreting the transmission features, which are predicted by the theoretical model.

Vacuum Rabi Splitting can also be described classically. An electromagnetic field transmitted through an optical cavity is modified by the

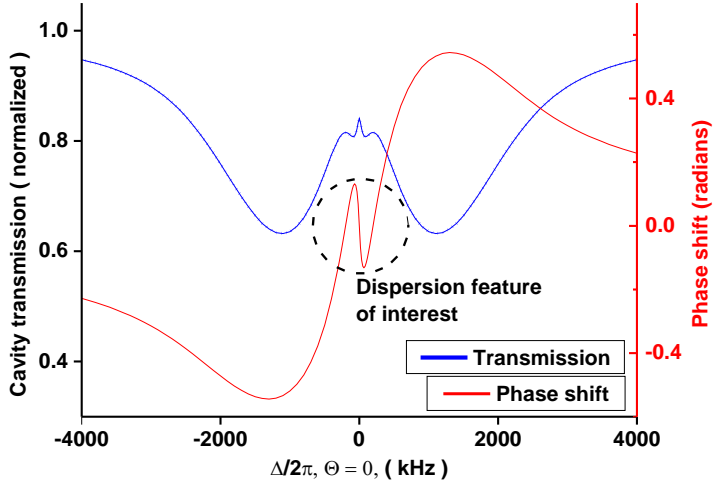


Figure 3.3: Blue line: Normalized optical cavity output power. Red line: Atom induced phase shift of the cavity transmitted field. Both the transmission and phase shift values are shown as function of probe laser detuning $\Delta = \omega_a - \omega_l$ where $\omega_c = \omega_l$ and thus $\Theta = 0$. The black dashed circle marks a narrow dispersion feature, which is of particular interest as an error signal for laser stabilization.

cavity according to the following transmission coefficient [Riehle, 2004, p.101],

$$E_{\text{out}} = \frac{Te^{i\varphi}}{1 - Re^{i2\varphi}} E_{\text{in}}, \quad (3.24)$$

where T (R) is the power transmission (reflection) coefficient of the cavity mirrors, φ is the single round-trip complex phase picked up by the intra-cavity field and E_{in} (E_{out}) is the cavity input (output) electromagnetic field. This single round-trip phase can be expressed in the presence of atoms inside the cavity as:

$$\varphi = \phi_{\text{cavity}} + \beta_D + i\beta_A, \quad (3.25)$$

where β_D and β_A denotes the single pass dispersion (β_D) and absorption (β_A) due to the atoms present in the cavity, and ϕ_{cavity} is the this single round-trip phase contribution from the cavity itself (cavity length, cavity servo etc.). Both β_D and β_A can be calculated by treating the atoms as classical dipoles. A classical explanation of Vacuum Rabi splitting can be

obtained from this picture. We assume in the following that the atomic resonance ω_a and the cavity resonance ω_c are kept equal, corresponding to the system requirements $\Delta = \Theta$ as in Fig. 3.2. For high atomic densities (corresponding to strong coupling) and for weak driving the atomic absorption β_A eliminates the cavity transmission peak. However the phase shift β_D shifts the transmission peak to two transmission peaks located symmetrically about the empty cavity resonance (as shown in Fig. 3.2) and these new peaks are located where the atomic phase shift $\beta_D = 0$. As β_D and β_A can be expressed fully analytically in the semi-classic model, the splitting Ω_{split} of the two transmission peaks can be expressed as following [Zhu et al., 1990]:

$$\Omega_{\text{split}} = \left(\frac{F\beta_{A0}L_0}{\pi} \Gamma \kappa - \frac{(\Gamma - \kappa)^2}{4} \right)^{1/2} \propto \sqrt{N}, \quad (3.26)$$

where F is the cavity finesse and L_0 is the length through the atomic ensemble. The parameter $\beta_{A0} = \frac{2f_0BNe^2}{m_e c \delta_a}$ is the single pass atomic absorption at resonance, where f_0 is the dipole oscillator strength and e (m_e) is the electron charge (mass). The splitting Ω_{split} is proportional with \sqrt{N} in this classical description. This $\Omega_{\text{split}} \propto \sqrt{N}$ dependency is also predicted in the quantum mechanical description of the vacuum rabi splitting [Tanj-Suzuki et al., 2011]. It should be noted that only linear absorption and dispersion terms are included in this classical model. If non-linear terms are included, which arise in strongly saturated systems, non-linear effects such as bistability appears [Martin et al., 2011].

As mentioned before, this classical picture proves to be useful for interpreting the transmission spectrum of the system studied theoretically in Sec. 3.1 and 3.2. Figure 3.3 shows the transmission and phase dispersion spectrum of this system. Remind that the empty cavity length of this system is controlled such that the a standing wave would be present at all times in the empty cavity mode. This criterion corresponds to $\omega_c = \omega_l$ and $\Theta = 0$ in Eq. (3.2). The blue plot in Fig. 3.3 shows the transmission spectrum for this criterion calculated through Eq. (3.22). This criterion modifies the transmission spectrum, which does not resemble the transmission shown in Fig. 3.2 and no apparent Rabi splitting is observed. Whereas Fig. 3.2 shows zero transmission for most detuning values, the Fig. 3.3 shows near total transmission for large detuning values. The near total transmission occurs because the optical cavity is forced on resonance with the probe laser for all detuning values. The atomic phase dispersion is also shown in Fig. 3.3 (red line), because this dispersion

can explain the origin of, three distinct features seen in the transmission spectrum in Fig. 3.3: First, a sharp increase in the transmission is seen in the most central region. This increase in transmission is due to the Doppler-free saturated absorption caused by the bi-directional intra-cavity field. A narrow phase dispersion feature corresponding to this saturated absorption is also seen in the dispersion lineshape near resonance. It is shown later in Sec. 3.3.1, that the strength of this saturated absorption is reduced slightly by the doppleron resonances. Secondly, a small reduction of the transmission, a *dip*, occurs for small detunings on both sides of the central narrow saturation peak. This reductions of transmission is caused by the atom-induced near resonant phase dispersion mentioned above, which shifts the probe laser out of resonance with the cavity and reduces the transmission. Finally, the transmission is greatly reduced for larger detuning. This is caused by the broad phase dispersion (~ 1.5 MHz wide) due to the Doppler phase dispersion. This large phase shift also shifts the probe laser out of resonance and the transmission is greatly reduced. These transmission and dispersion lineshapes shown in Fig. 3.3 are investigated experimentally in this work by employing the so-called *Noise Immune Cavity Enhanced Optical Heterodyne Molecular Spectroscopy* [Ye et al., 1998, Ma et al., 1999] (NICE-OHMS, see Sec. 4.6 for details). The results of these measurements are presented in Sec. 6, and it turns out that the measured transmission and dispersion lineshapes are modified further by the NICE-OHMS technique and the doppleron resonances.

So far the main focus has been on the transmission lineshape, however the narrow phase dispersion feature at resonance may be used as an error signal for laser stabilization. The slope of this dispersion feature is steep at resonance making it sensitive to detuning fluctuation and the dispersion has a zero-crossing at resonance allowing it discriminate the sign of the detuning. Hence, this dispersion feature seems suited as an error signal. The prospect for laser stabilization on this narrow phase dispersion are investigated theoretically in Sec. 3.4 and experimentally in Chap. 6.

The bistability and the highly detailed transmission and dispersion lineshapes illustrate, that the atom-cavity system studied here exhibits non-linear and complex dynamics. It turns out that non-linear dynamics are also present for the phase dispersion lineshape. Details of this non-linear dynamics of the phase dispersion need to be understood in order to identify the optimal parameters for laser stabilization. The following section uses the theoretical model developed in Sec. 3.1 to investigate this non-linear phase dynamics.

3.3 What is all this nonlinearity about?

It was shown in the previous section, that the phase dispersion lineshape shown in Fig. 3.3 (red line) is suited as an error signal for laser stabilization. Understanding the non-linear dynamics of this lineshape is however important to identify the optimal parameters for laser stabilization with this system as a reference.

An example of the non-linear dynamics is shown in Fig. 3.4. Here, the transmission and dispersion lineshape are shown for the total intra cavity atom number $N_{\text{cav}} = 2.5 \times 10^7$ and for $N_{\text{cav}} = 0.5 \times 10^7$. The absorption and dispersion is scaled 5 times up in the case for $N = 1.0 \times 10^8$ in order to simulate a linear scaling of the absorption and dispersion. However, it is apparent from the disagreement of the blue and red lineshapes, that the lineshapes do not follow a linear scaling as function of N . This disagreement is most evident for large detunings and it is in fact negligible for the dispersion feature near resonance. Hence, the nonlinear atom number scaling for large detunings do not affect the dynamics of laser stabilization with the central dispersion feature as an error signal. However, the dynamics for both small and large detuning are studied experimentally later in this work (see Chap. 6) in order to validate the theoretical model derived in earlier in Sec. 3.1 for all relevant parameter regions.

The dispersion slope at resonance is one of the most essential parameters for laser stabilization. An atom-cavity system with a steep dispersion slope at resonance provides a large phase shift on the cavity transmitted light for very small frequency fluctuations (detunings). This large phase shift represents a frequency detuning and can be measured and implemented in a feedback loop to minimize the phase shift as illustrated previously in Fig. 2.2. The lineshape dynamics shown in Fig. 3.4 implies a linear atom number scaling of the dispersion slope at resonance. The atom number dependency of the dispersion slope is shown in more details in Fig. 3.5. The theoretical resonance slopes of the dispersion is shown for two different cavity finesse^v for different total atom numbers up to $N = 80 \times 10^9$. Note, that distinction is drawn between the total number of atoms inside the cavity mode N_{cav} and the total number of laser cooled atoms N^{vi} . Most of the total atom numbers shown in Fig. 3.5 are far above atom number values reported for single stage MOT trapping of ^{88}Sr [Yang

^vCorresponding to the finesse of the optical cavities studied in Sec. 6

^{vi}The total atom number N is the total number of trapped atoms of which only a fraction constitutes the intra-cavity number of atoms, N_{cav} . N_{cav}/N is determined by the geometry of the cavity mode and the trapped atomic sample.

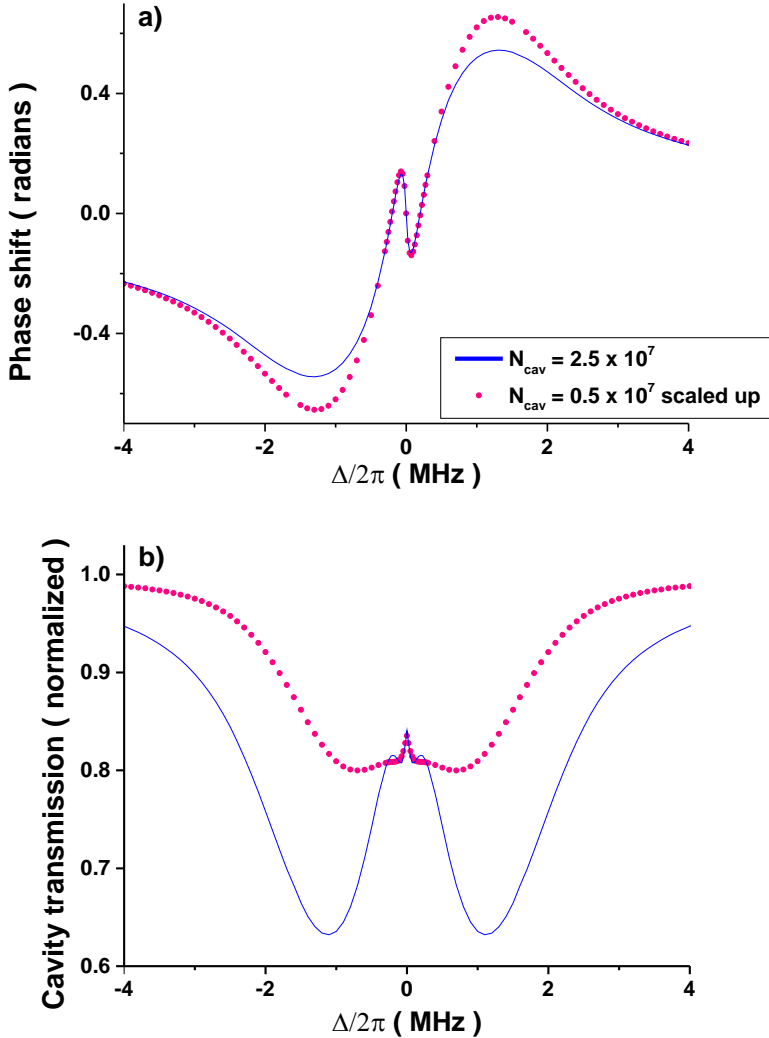


Figure 3.4: *Theoretical predictions of transmission and dispersion lineshapes for a sample of laser cooled ^{88}Sr with temperature $T = 4.0\text{ mK}$ probed with $P_{in} = 100\text{ nW}$ optical power. The solid blue lines show predicted values for $N_{cav} = 2.5 \times 10^7$ atoms inside the cavity. The dashed red lines show predicted values for $N_{cav} = 0.5 \times 10^7$ atoms inside the cavity. These values for $N_{cav} = 0.5 \times 10^7$ intra cavity atoms are scaled 5 times up to match the values for $N_{cav} = 2.5 \times 10^7$ in order to simulate a linear scaling.*

et al., 2015]. Whereas Fig. 3.5 shows evident nonlinear dynamics, the relevant experimentally achievable atom numbers are in the $< 1 \times 10^9$ region

(marked with a dashed line in Fig. 3.5), where the dynamics appears to be linear. It follows from Fig. 3.5, that the highest possible atom numbers are preferred for laser stabilization within this linear region. It is also evident, that high cavity finesse is preferred as long as the system remains in the bad-cavity regime as described previously in Chap. 2.

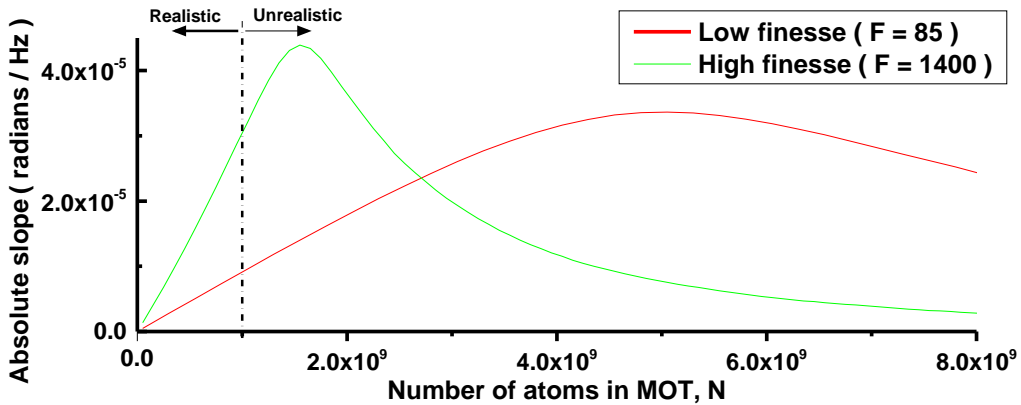


Figure 3.5: The dispersion slope at resonance ($\Delta = 0$) for different number of trapped atoms. The optical probe input power is kept constant at $P_{in} = 100 \text{ nW}$. Values for unrealistically large numbers of trapped atoms are shown in order to illustrate the nonlinear dynamics.

Increasing the number of intra cavity atoms experimentally within the linear regime is straight forward and the highest possible value is determined by technical limitations. However, the phase dispersion slope depends nonlinearly on other experimental parameters, which makes the optimal choice of parameters for laser stabilization nontrivial. One of those parameters is the optical intracavity power. The dispersion slope at resonance as function of the optical input power is shown in Fig. 3.6. It is apparent from Fig. 3.6 that an input power exists where the absolute value of the dispersion slope is maximal. A steep slope yields a high sensitivity to frequency fluctuations and the optimal input power is hence around this maximal phase dispersion. The dynamics of this phase slope is hence essential to take into consideration, when optimizing the laser stabilization performance of an atom-cavity system. This laser stabilization performance studied in details later in Sec. 3.4.2.

Figure 3.6 shows three different parameter regimes: High optical input power, intermediate optical input power and near zero input power. The transmission lineshape in the high optical input regime (see inset A in

Fig. 3.6) is similar to the spectrum shown in Fig. 3.4b). The absolute phase dispersion slope is reduced for higher input powers, because the saturated absorption peak is power broadened. The slope is increased when the optical input power is reduced and the system enters the regime with intermediate optical input power (see inset B in Fig. 3.6). Here, the power broadening is reduced and the maximum phase dispersion slope is found. Furthermore the transmission lineshape is no longer modified by the broad thermal dispersion. Finally, the slope value is reduced again for even lower optical input powers (see inset C in Fig. 3.6) despite further reduction of the power broadening. This reduction of dispersion slope is caused by reduction of the saturation parameter and the magnitude of the saturated absorption peak is reduced. The saturation peak even disappears for very low input powers. This is reflected in Fig. 3.6, as the slope changes sign for very low input powers. A sign change might seem as a spectacular nonlinear behavior, but there is in fact a simple explanation. The central dispersion feature disappears when the saturation peak disappears and only the broad thermal background dispersion is left. The slope sign of this thermal dispersion is the reverse of the saturation dispersion and hence the sign is changed for near zero input powers in Fig. 3.6.

The sample temperature is one final system parameter, which can be varied experimentally to some extend. Small changes of sample temperature can be achieved by changing the detuning of the cooling lasers relative to the transition used for laser cooling [Xu et al., 2003b]. Large temperature changes require different cooling and trapping schemes, which inevitably have an effect on the total number of trapped atoms. Isolated control the sample temperature is hence hard to achieve. The temperature dynamics of the parameters relevant for laser stabilization is nevertheless investigated later in Sec. 3.4.2.

The phase dispersion slope has been shown in this section to depend non-linearly on the experimentally controllable parameters. The consequences of this non-linear dynamics on the laser stabilization performance are investigated theoretically in Sec. 3.4. Multiphoton scatterings are described briefly before Sec. 3.4, as these scattering processes can possibly modify the phase dispersion lineshape.

3.3.1 Velocity dependent multiphoton scatterings

Multiphoton scattering processes also known as dopplerons can occur when atoms with non-zero velocities are strongly driven by counter propagating fields [Tallet, 1994, Kyrölä and Stenholm, 1977]. The following section describes briefly the doppleron scattering process and investi-

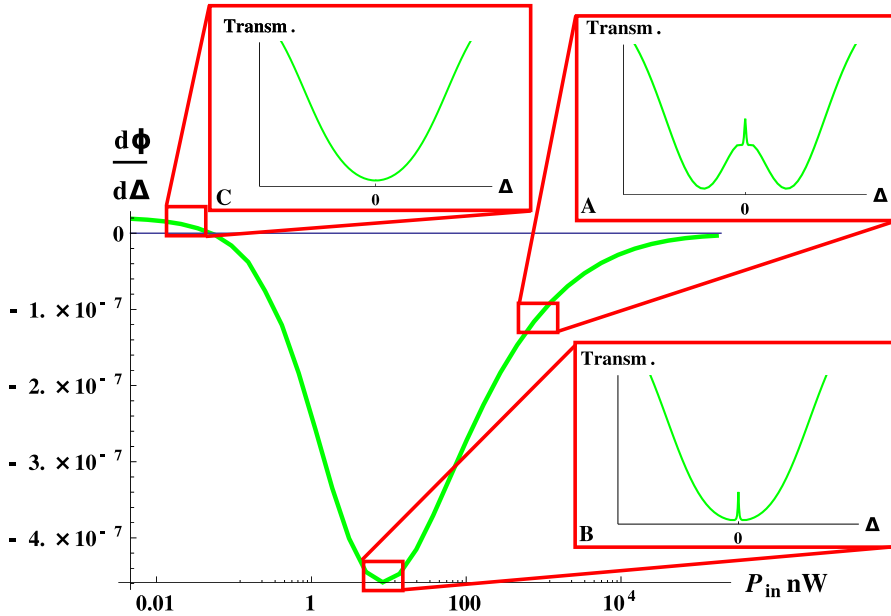


Figure 3.6: Dispersion slope $2\pi \frac{d\phi}{d\Delta}$ at resonance (Vertical axis, in units of radians/Hz) as function of input power P_{in} of the probe laser (Horizontal axis, in units of nW). Note that the slope values are mostly negative, while only the absolute value of the slope $2\pi \left| \frac{d\phi}{d\Delta} \right|$ is the main interest for laser stabilization. A maximum absolute value of the slope $2\pi \left| \frac{d\phi}{d\Delta} \right|$ is seen around $P_{in} = 2 \text{ nW}$, while a sign change is seen around $P_{in} = 0.02 \text{ nW}$. The insets show the transmission lineshapes for the corresponding input powers.

gates whether these doppleron scatterings modify the phase dispersion lineshape relevant for laser stabilization.

The extent of the energy scale studied in this work is determined by the sample temperature in the mK level. This temperature results in a Doppler broadened spectrum with a width in the MHz level. See for example Fig. 3.3. The probed atomic transition has a natural linewidth in the kHz level. The Doppler broadened spectrum in this system is hence several orders of magnitude broader than the natural linewidth of the narrow atomic transition. Multiphoton resonances, called dopplerons [Tallet, 1994, Kyrölä and Stenholm, 1977], are present if such a system is probed by counter-propagating beams. A moving atom coupled to the optical cavity experiences the intra cavity standing wave field as a bichromatic field in the rest frame of the atom. The frequencies of this bichromatic

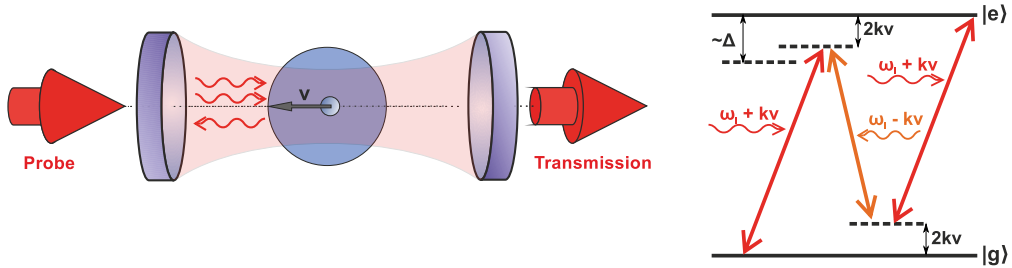


Figure 3.7: Illustration of doppleron multiphoton scatterings. An atom with a velocity v parallel with the cavity axis absorbs $p + 1$ ($p + 1 = 3$ in figure) photons and emits p photons in the opposite direction. Note, that doppleron scatterings can occur in both directions of the cavity axis.

Figure 3.8: Illustration of the level scheme for excitation through the 1st order doppleron scattering ($p = 1$ in Eq. (3.27)).

field are given by $\omega_{\pm} = \omega_l \pm kv$. Here, ω_l is the probe laser frequency, k is the wave number of the probe light and v is the atomic velocity parallel with the cavity mode. Hence, $\delta = kv$ corresponds to the Doppler shift due to the no-zero velocity of the atom. Doppleron scattering is a Raman-like multiphoton scattering event for a given detuning $\Delta = \omega_l - \omega_a$ where $p + 1$ detuned photons from one direction are absorbed and p photons are emitted in the opposite direction, while the atom is left in the excited state. This scattering process is illustrated in Fig. 3.7 and 3.8. Energy conservation requires the following resonance condition [Tallet, 1994]:

$$kv = \frac{\pm \sqrt{\Delta^2 + 2g_0^2}}{2p + 1}, \quad (3.27)$$

where p is the order of doppleron resonances and g_0 is the single-atom-cavity coupling (also presented in Sec. 3.1) and Δ is the laser detuning relative to the atomic transition. The doppleron resonances depend on the Doppler shift $\delta = kv$ and are described by the Fourier components in Eq. (3.13)–(3.15), where all even orders of l correspond to the contributions from the $l/2 = p$ 'th order doppleron resonance.

The doppleron scatterings do not modify the transmission and dispersion lineshapes for most detuning values as the doppleron scatterings occur in both directions due to the symmetrical atomic velocity distribution. However, the doppleron scatterings do reduce the central saturated absorption peak and the amplitude of the corresponding phase dispersion

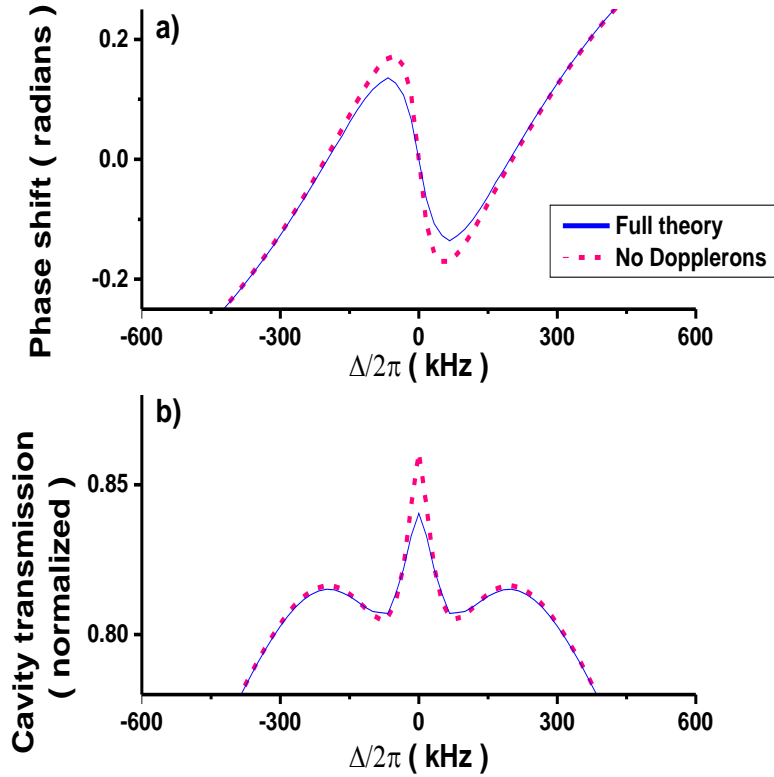


Figure 3.9: *Theoretical predictions of the near resonant transmission and dispersion lineshapes. The solid blue lines are theoretical predictions were the contributions from doppleron resonances are included. The dashed red lines show the theoretical predictions without the doppleron resonances.*

is also reduced. This can be seen by comparing the theoretical transmission and dispersion lineshapes including higher order Fourier components ($0 < l$) and without higher order Fourier components (only $l = 0$) in Eq. (3.13)-(3.15). See Fig. 3.9. This reduction might possibly degrade the prospects of applying this phase dispersion as a frequency discriminator, as the slope at resonance is also reduced. The laser stabilization performance of this reduced phase dispersion is investigated in details in the following section in order to evaluate whether the doppleron resonances degrades the laser stabilization performance significantly.

3.4 Shot noise limited laser linewidth

With the understanding of the dynamics of an atom-cavity system described in the previous sections (sec. 3.1-3.3), it is now possible to theoretically evaluate the ideally achievable quantum shot noise limited spectral linewidth of a laser stabilized to such an atom-cavity system. This will hence be the topic of this section. Much focus has been on the slope of the phase dispersion so far, but the ideal shot noise limited linewidth, $\Delta\nu_{\text{SNL}}$, do also depend on the signal-to-noise ratio governed by the optical power of the probe carrier, P_c , and the sidebands, P_s . An ideal linewidth only limited by shot noise can be calculated by assuming a perfect feedback system with infinite control bandwidth for laser locking and a unity quantum efficiency of the photo detector for measuring the cavity transmission:

$$\boxed{\Delta\nu_{\text{SNL}} = \frac{\pi h\nu}{2\left(\frac{\partial\varphi}{\partial\nu}\right)^2} \left(\frac{1}{P_c} + \frac{1}{2P_s} \right).} \quad (3.28)$$

Equation (3.28) is derived in the following Sec. 3.4.1. The procedure followed in Sec. 3.4.1 is similar to [Riehle, 2004, Sec. 3.4] and [Martin et al., 2011, Appendix A] but it is adjusted to suit a laser stabilization system with a NICE-OHMS detection scheme. Section 3.4.1 concludes with Eq. (3.43) which corresponds to the above mentioned expression for the shot noise limited linewidth, Eq. (3.28).

Sections 3.4.1-3.4.2 are arranged such as the reader can skip ahead to Sec. 3.4.2 for a discussion of the laser stabilization performance with an atom-cavity system, if the theoretical derivation is not of interest.

3.4.1 Calculation of the shot noise limited laser stabilization

We consider a system consisting of laser cooled atoms with narrow line transitions coupled to an optical cavity. The narrow line transition is probed by a laser with carrier frequency^{vii} ν_l and two symmetrically applied sidebands with frequencies $\nu_- \pm \text{FSR}$, where FSR is the *free spectral range* of the cavity. The two sidebands are off-resonant with the atomic transition. The cavity transmitted probe carrier and sidebands are detected by a photo detector. The atom-induced phase shift on the probe carrier is measured by frequency mixing the photo detector signal with mixing

^{vii} ν_l is in units of Hz.

frequency $\nu_m = \text{FSR}$. See Fig. (4.10). The photocurrent after the frequency mixing is given as:

$$\Delta i(t) = \frac{e\eta_{qe}}{hv} \sqrt{2P_c P_s} (\Delta\varphi + \phi_{\text{mix}}) + \delta i(t). \quad (3.29)$$

Here, η_{qe} is the quantum efficiency of the photo detector, $\Delta\varphi$ is the atom induced phase shift on the probe carrier with cavity transmission optical power P_c , P_s is the cavity transmitted optical power for each of the two sidebands, ϕ_{mix} is the mixing phase, which can be set to $\phi_{\text{mix}} = 0$ in experiments and $\delta i(t)$ is the stochastically fluctuating white noise contribution to the photo current due to shot noise^{viii}. The detuning $\Delta\nu$ of the probe carrier from the atomic resonance is represented by the photo current $\Delta i(t)$ as illustrated in Fig. 2.2. Equation (3.29) can be expanded as function of the detuning $\Delta\nu$ by approximating the phase dispersion to be linear around resonance:

$$\Delta i(t) = \frac{e\eta_{qe}}{hv} \sqrt{2P_c P_s} \frac{\partial\varphi}{\partial\nu} \Delta\nu + \delta i(t). \quad (3.30)$$

A servo system seeks to reduce $\Delta i(t)$ to zero by controlling the probe carrier frequency, when the probe carrier is locked on the atom-cavity resonance. The photo current is hence reduced to $\Delta i(t) = 0$ when assuming a perfect servo system. Equation 3.30 can then be rewritten to describe the frequency error $\Delta\nu_{\text{err}}(t)$:

$$\Delta\nu_{\text{err}}(t) = \frac{\delta i(t)}{\frac{2e\eta_{qe}}{hv} \sqrt{2P_c P_s} \frac{\partial\varphi}{\partial\nu}}. \quad (3.31)$$

It can be seen in Eq. (3.31) that the shot noise contribution $\delta i(t)$ causes frequency noise even in this ideal case. It is possible to achieve the power spectral density $S_{\Delta\nu_{\text{err}}}(f)$ of the locked laser by applying the so-called Wiener-Khinchin theorem [Riehle, 2004, p.56]:

$$S_{\Delta\nu_{\text{err}}}(f) = \int_{-\infty}^{\infty} \langle \Delta\nu_{\text{err}}(t) \Delta\nu_{\text{err}}(t + \tau) \rangle e^{-i2\pi f\tau} dt. \quad (3.32)$$

^{viii}A similar noise component is already found on the signal from the photo detector before mixing. However, the power spectral density of white noise is uniform for all frequencies[Riehle, 2004, Table 3.1], and hence frequency mixing will also yield uniformly distributed noise components for all frequencies.

Here, the spectral density function $S_{\Delta\nu_{\text{err}}}(f)$ for a frequency component f is determined by Fourier transforming the time domain auto correlation function $\langle \Delta\nu_{\text{err}}(t)\Delta\nu_{\text{err}}(t+\tau) \rangle$, where τ is the time displacement of the correlation. Equation (3.32) can be rewritten by considering the autocorrelation function of $\delta i(t)$ [Martin et al., 2011]:

$$\langle \delta i(t)\delta i(t+\tau) \rangle = \frac{e^2\eta_{qe}}{h\nu}(P_c + 2P_s)\delta(t), \quad (3.33)$$

where $\delta(t)$ is the Dirac delta function. Equation (3.33) shows that the shot noise is a memoryless noise, which only correlate for $\tau = 0$. The autocorrelation function in Eq. 3.32, $\langle \Delta\nu_{\text{err}}(t)\Delta\nu_{\text{err}}(t+\tau) \rangle$, can now be rewritten by inserting Eq. 3.33:

$$\begin{aligned} \langle \Delta\nu_{\text{err}}(t)\Delta\nu_{\text{err}}(t+\tau) \rangle &= \frac{\langle \delta i(t)\delta i(t+\tau) \rangle}{\frac{4e^2\eta_{qe}^2}{h^2\nu^2}2P_cP_s\left(\frac{\partial\varphi}{\partial\nu}\right)^2} \\ &= \frac{\delta(\tau)h\nu}{4\eta_{qe}\left(\frac{\partial\varphi}{\partial\nu}\right)^2} \cdot \left(\frac{1}{P_c} + \frac{1}{2P_s}\right). \end{aligned} \quad (3.34)$$

The power spectral density of the ideally stabilized laser can now be found by inserting Eq. (3.34) in Eq. (3.32):

$$S_{\Delta\nu_{\text{err}}}(f) = \frac{h\nu}{4\eta_{qe}\left(\frac{\partial\varphi}{\partial\nu}\right)^2} \cdot \left(\frac{1}{P_c} + \frac{1}{2P_s}\right). \quad (3.35)$$

This noise spectral density in Eq. (3.35) can be applied to determine the stabilized laser spectral linewidth in the carrier frequency domain. This linewidth is determined by starting by looking at the probe laser carrier in the time-domain described as:

$$E(t) = E_0 e^{i2\pi\nu_0 t + i\delta\phi(t)},$$

where ν_0 is the carrier frequency and $\delta\phi(t)$ is the phase error. The frequency domain spectral lineshape of this carrier field can be achieved by using the Wiener-Khinchin theorem (see Eq. (3.32)) once again. To do so, the autocorrelation function of the carrier field is needed:

$$\langle E(t)E^*(t+\tau) \rangle = |E|^2 e^{i2\pi\nu_0\tau} \langle e^{i(\delta\phi(t)-\delta\phi(t+\tau))} \rangle. \quad (3.36)$$

The last term in Eq. (3.36) can be rewritten by assuming a Gaussian probability distribution of the phase error^{ix}:

$$\begin{aligned}\langle e^{i(\delta\phi(t)-\delta\phi(t+\tau))} \rangle &= e^{-\langle(\delta\phi(t)-\delta\phi(t+\tau))^2\rangle/2} \\ &= e^{-(2\langle\delta\phi(t)\rangle^2-2\langle\delta\phi(t+\tau)\rangle^2)/2}.\end{aligned}\quad (3.37)$$

The Wiener-Khinchin theorem can then be applied to rewrite Eq. (3.37) in terms of phase noise power spectral density, $S_{\delta\phi}$:

$$\begin{aligned}\langle(\delta\phi(t)-\delta\phi(t+\tau))^2\rangle &= 2 \int_{-\infty}^{\infty} S_{\delta\phi}(f)(1-e^{i2\pi f\tau}) df \\ &= 2 \int_{-\infty}^{\infty} \frac{S_{\Delta\nu_{\text{err}}}(f)}{f^2}(1-e^{i2\pi f\tau}) df.\end{aligned}\quad (3.38)$$

The phase noise power spectral density $S_{\delta\phi}(f)$ was rewritten in terms of the frequency noise power spectral density $S_{\Delta\nu_{\text{err}}}$ in the last line of Eq. (3.38). The simple relation between $S_{\delta\phi}(f)$ and $S_{\Delta\nu_{\text{err}}}(f)$ is described in [Riehle, 2004, Table 3.1]. Equation (3.38) can be even further rewritten by inserting the frequency noise spectral density from Eq. (3.35) and by taking the real part:

$$\begin{aligned}\langle(\delta\phi(t)-\delta\phi(t+\tau))^2\rangle &= 2 \cdot 2 \int_0^{\infty} \frac{b_0}{4f^2} \cdot (1 - \cos(2\pi f\tau)) df \\ &= b_0 \pi^2 \tau,\end{aligned}\quad (3.39)$$

where,

$$b_0 = \frac{h\nu}{\eta_{qe} \left(\frac{\partial\phi}{\partial\nu}\right)^2} \cdot \left(\frac{1}{P_c} + \frac{1}{2P_s}\right).\quad (3.40)$$

With Eq. (3.39) in hand, the autocorrelation function of the electric field (Eq. (3.36)) can be rewritten as:

^{ix}This assumption is valid for a large number of uncorrelated phase shifts due to the central limit theorem. [Riehle, 2004, p.65][Martin et al., 2011, Appendix A]

$$\langle E(t)E^*(t + \tau) \rangle = |E|^2 e^{i2\pi\nu_0\tau} e^{-b_0\pi^2\tau/2}. \quad (3.41)$$

The spectral lineshape of the electric field can now be expressed analytically by applying the Wiener-Khinchin theorem one final time and by keeping the real parts on Eq. (3.41):

$$\begin{aligned} S_E(\nu - \nu_0) &= 2|E|^2 \int_0^\infty \cos(2\pi\nu_0\tau) e^{-b_0\pi^2\tau/2} d\tau \\ &= 2|E_0|^2 \frac{b_0\pi^2/2}{(b_0\pi^2/2)^2 + 4\pi^2(\nu - \nu_0)^2} \\ &= 2|E_0|^2 \frac{\gamma/2}{(\gamma/2)^2 + 4\pi^2(\nu - \nu_0)^2}. \end{aligned} \quad (3.42)$$

The spectral lineshape in Eq. (3.42) is a Lorentzian profile and the ideal shot noise limited full width at half maximum (FWHM), $\Delta\nu_{\text{SNL}} = \frac{\gamma}{2\pi}$, can finally be described:

$$\boxed{\Delta\nu_{\text{SNL}} = \frac{\pi h\nu}{2\eta_{qe} \left(\frac{\partial\varphi}{\partial\nu}\right)^2} \left(\frac{1}{P_c} + \frac{1}{2P_s} \right)}. \quad (3.43)$$

3.4.2 Evaluation of the shot noise limited laser linewidth

Equation (3.43) (or Eq. (3.28)) describing the ideal shot noise limited linewidth was developed in Sec. 3.4.1. This allows us to study the dynamics of the ideal shot noise limited linewidth in this section.

It was assumed during the derivation of Eq. (3.43) that the detection is only limited by the quantum shot noise. This is not an unrealistic assumption, if the error detection is moved up to very high radio frequency levels (> 300 MHz) as white frequency noise dominates these frequency regimes. The NICE-OHMS detection scheme (described later in Sec. 4.6) is one possible technique to move this detection up to these frequency regimes. Furthermore, the feedback system for laser stabilization was assumed to be a perfect feedback system with infinite bandwidth. A feedback system with infinite bandwidth is of course unphysical and feedback systems with finite bandwidths in the 200 kHz \sim 1 MHz are usually used in the current state of the art laser stabilization systems [Kessler et al., 2012a, Häfner et al., 2015]. Whereas these reported bandwidths covers

most of the technical noise spectrum, a more thorough study of the effects of such a finite bandwidth on the derivation in Sec. 3.4.1 is needed. An unity quantum efficiency $\eta_{qe} = 1$ was also assumed in Eq (3.28). This assumption is to some extent unrealistic. However, photo detectors with quantum efficiencies in the $\eta_{qe} > 0.5$ range are commercially available and quantum efficiencies in this range will not degrade the calculated limited linewidth crucially in Eq. (3.43).

The dynamics of an atom-cavity system described in the previous sections (Sec. 3.1–3.3) showed strongly nonlinear behavior and nonlinear dynamics can also be expected from the ideal stabilized laser linewidth. Figure 3.10 shows the atom sample temperature dependencies of the dispersion lineshape, dispersion slope at resonance and the ideal shot noise limited linewidth calculated using Eq. (3.43).

Figure 3.10a) shows the atom induced phase dispersion of the cavity transmitted for three different temperatures. All three dispersion line-shapes are for input power of $P_{in} = 100 \text{ nW}$. It appears that the Doppler broadened background dispersion is narrowed for lower sample temperatures. The inset in Fig. 3.10a) shows that the central narrow dispersion have nearly the same slope for sample temperatures of $400 \mu\text{K}$ and $40 \mu\text{K}$. This is a less intuitive behavior and it could appear as if the gain from further cooling of the atoms is small considering the additional technical difficulties for further cooling. However, it was seen in Fig. 3.6 that the dispersion slope depend strongly on the input power. Figure 3.10b) shows that the maximum absolute slope occur for different optical input powers, when the temperature is changed. This can explain the apparent less intuitive temperature dependency shown in the inset of Fig. 3.10a). Figure 3.10c) shows the ideal shot noise limited linewidths corresponding to the slope values shown in Fig. 3.10b). All values in Fig. 3.10c) are calculated with Eq. (3.28). The advantages of lower temperatures are more clear here. The minimum shot noise linewidths are $\sim 600 \text{ mHz}$ for $T = 4 \text{ mK}$, $\sim 100 \text{ mHz}$ for $T = 400 \mu\text{K}$ and $\sim 50 \text{ mHz}$ for $T = 40 \mu\text{K}$. However, note that the calculations presented in Fig. 3.10c) are performed for the same total number of trapped atoms^x, $N = 4.4 \times 10^8$, in all cases. This number of atoms is realistic for single stage laser cooling of alkali and alikali earth metal atoms. Sub-mK cooling of atoms will often require second stage cooling or other complex cooling schemes that would possibly reduce the atom number in the process. The calculated shot noise limited linewidths in Fig. 3.10c) are hence promising but possibly inaccessible

^xNote, that this total number of trapped atoms is not identical with the number of intra-cavity atoms, N_{cav} .

for sample temperatures of $T = 400 \mu\text{K}$ and $T = 40 \mu\text{K}$. However, this sub-Hz linewidth for $T = 4 \text{ mK}$ atomic samples are already close to be comparable with the linewidths of the clock lasers used in the current state-of-the art atomic clocks [Nicholson et al., 2015, Ushijima et al., 2015, ?]. The prospects of reaching sub-Hz linewidths with relatively hot atomic temperatures in the mK-level are hence very alluring. A proof-of-concept experiment consisting of optical cavities coupled to laser cooled ^{88}Sr atoms with temperatures in the mK-level has been realized in this work. Detailed studies of the dynamics of this proof-of-concept system are presented later in Sec. 6.

The shot noise limited linewidths were estimated using Eq. (3.28) for a number of different atomic isotopes. The minimum obtainable shot noise limited linewidths and the input optical powers corresponding to these linewidths are shown in Table 3.1 for each element. Each isotope was assumed to be cooled down to temperatures near the Doppler limit reported in [Westergaard et al., 2015, Riedmann et al., 2012, Kohno et al., 2009, Dammalapati et al., 2009]. These temperatures are all in a high temperature regime where the bistability does not occur^{xi}. A realistic atom number overlapping the cavity mode was estimated to be $N_{\text{cav}} = 2.5 \cdot 10^7$ for all the elements. This estimate of the atom number is conservative to some extend, as larger atom numbers have been reported in the literature [Yang et al., 2015]. The cavity waist diameter is chosen to 1.0 mm, which corresponds to the experimental value described in Sec. 5 and in [Westergaard et al., 2015]. The empty cavity finesse was set to $F = 250$ and $F = 1000$, corresponding to an empty cavity decay rate of $\kappa/2\pi = 2.0 \cdot 10^6 \text{ Hz}$ and $\kappa/2\pi = 0.5 \cdot 10^6 \text{ Hz}$. In each case the probe laser decoherence has been assumed to be $\gamma_{\text{laser}} = 2\pi \cdot 2.0 \text{ kHz}$ throughout all the calculations in order to specify an order of magnitude.

The atomic isotopes shown in Table 3.1 were isotopes with a suited $^1\text{S}_0 \rightarrow ^3\text{P}_1$ transition chosen among the isotopes often applied in optical frequency standard experiments. Especially, the possibility of exploiting laser cooled strontium isotopes for optical frequency standard experiments have been studied extensively (ref, Bloom, LeTargat, Ushijima). The stabilization of a probe laser on the $^1\text{S}_0 \rightarrow ^3\text{P}_1$ transition of ^{88}Sr with cavity finesse $F = 250$ and intra cavity atom number $N_{\text{cav}} = 2.5 \cdot 10^7$ predicts an ideal shot noise limited linewidth of 107 mHz. This linewidth is already comparable with the linewidths of the current state-of-the-art frequency stabilized lasers [Kessler et al., 2012a, Bishof et al., 2013, Häfner et al., 2015]. The shot noise limited linewidth may be reduced even further

^{xi}See Sec. 3.3 for a description of bistability.

by increasing the atom number or the cavity finesse, corresponding to increasing the collective cooperativity $C = NC_0$. This dependency can be seen in Eq. (3.28), as the phase slope at resonance, $\frac{\partial\phi}{\partial\Delta}$, depends linearly on the atom number N (see Fig. 3.5). A similar linear scaling of $\frac{\partial\phi}{\partial\Delta}$ occurs when increasing the finesse while keeping the drive amplitude η constant. The laser linewidth may even be reduced to $\Delta\nu = 6.8$ mHz by only increasing the cavity finesse to $F = 1000$ and increasing the intra cavity atom number to $N_{\text{cav}} = 5.0 \cdot 10^7$. These slightly increased cavity finesse and atom numbers are experimentally achievable [Yang et al., 2015, Norcia and Thompson, 2016c].

Outlook

A theoretical model was developed in this chapter for a thermal atomic sample with a narrow line transition coupled to an optical cavity. The cavity transmitted field of this modeled system was investigated in details and strongly non-linear dynamics were identified. The studies of this non-linear dynamics proved to be valuable, as optimal system parameters (number of atoms, input power and temperature) were discussed. Finally, the ideal shot-noise-limited linewidths of such systems were evaluated and very promising sub 10 mHz linewidths were predicted for experimentally accessible system parameters.

Of course, it is questionable whether such ideal shot-noise-limited linewidths in the mHz-level are experimentally realizable. This is experimentally studied by realization of a proof-of-concept experimental system, which will be described in the following chapters.

Finally, it is worth mentioning, that the analysis which led to the predicted ideal linewidths was performed following the same procedures as in [Martin et al., 2011], which also predicts a shot-noise-limited linewidth in the mHz-level for a sample of ^{87}Sr trapped in an optical lattice and probed with realistic decoherence rates on the ultra narrow ${}^1\text{S}_0 \rightarrow {}^3\text{P}_0$ transition ^{xii} [Martin et al., 2011, Table I]. Hence, the system studied in this work predicts a similar laser stabilization performance as the system studied in [Martin et al., 2011] with a much more simple and robust system consisting of thermal laser cooled atoms and a much broader transition.

^{xii}The predicted ultimate shot-noise limited linewidth is $0.74 \mu\text{Hz}$ without any external decoherence.

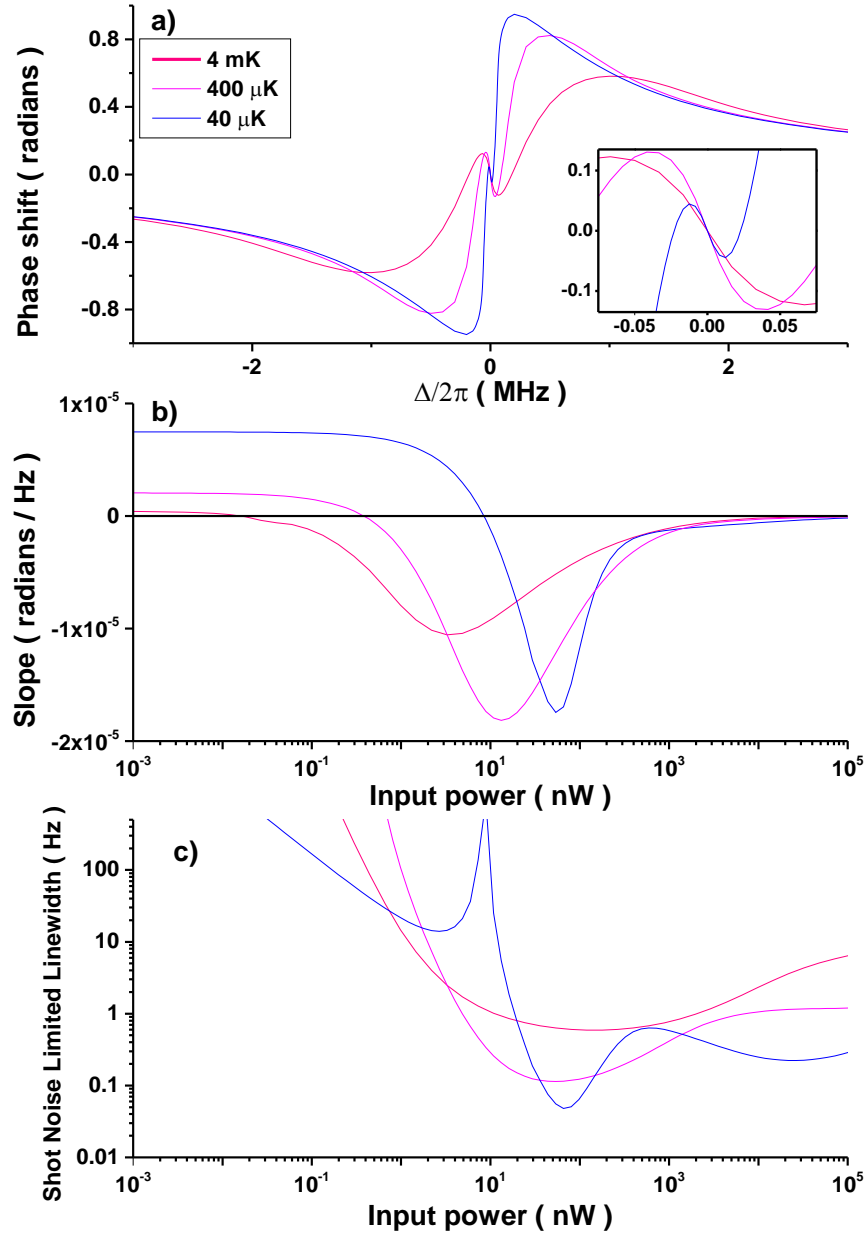


Figure 3.10: *Theoretical plots illustrating the dynamics of the dispersion lineshape, dispersion slope at resonance and ideal shot-noise limited linewidth for different temperatures of the atoms. The temperature $T = 4$ mK corresponds to a typical experimental situation in this work. a) The dispersion lineshapes for three different atomic temperatures. The inset shows a zoom on the central part of the plot with the same units on the axes. b) The dispersion slope at resonance as function of the probe laser input power. It is seen, that the maximum absolute slope value is not necessarily optimal for the lowest temperature.c) The ideal shot-noise-limited linewidth values calculated by using Eq. (3.43) for the dispersion slopes values shown in b).*

Transition	λ	$\gamma/2\pi$	F	N_{cav}	T	$P_{\text{in,optimal}}$	$\Delta\nu$
$^{171}\text{Yb } ^1\text{S}_0 \rightarrow ^3\text{P}_1$	556 nm	182 kHz	250 1000	$2.5 \cdot 10^7$ $5.0 \cdot 10^7$	6.5 mK	128 μW 312 μW	3.3 Hz 207 mHz
$^{40}\text{Ca } ^1\text{S}_0 \rightarrow ^3\text{P}_1$	657 nm	400 Hz	250 1000	$2.5 \cdot 10^7$ $5.0 \cdot 10^7$	1.7 mK	5.5 nW 2.2 nW	322 mHz 20 mHz
$^{24}\text{Mg } ^1\text{S}_0 \rightarrow ^3\text{P}_1$	457 nm	34 Hz	250 1000	$2.5 \cdot 10^7$ $5.0 \cdot 10^7$	3.0 mK	0.5 nW 0.2 nW	8.1 Hz 500 mHz
$^{88}\text{Sr } ^1\text{S}_0 \rightarrow ^3\text{P}_1$	689 nm	7.6 kHz	250 1000	$2.5 \cdot 10^7$ $5.0 \cdot 10^7$	3.0 mK	47 nW 84 nW	102 mHz 6.8 mHz

Table 3.1: From [Tieri et al., 2015]. Shot noise limited linewidths $\Delta\nu$ estimated theoretically for a number of $^1\text{S}_0 \rightarrow ^3\text{P}_1$ intercombination lines at experimentally realizable parameters: transition wavelength λ , natural linewidth γ , atomic sample temperature T as reported in literature [Westergaard et al., 2015, Riedmann et al., 2012, Kohno et al., 2009, Dammalapati et al., 2009] and optimal cavity input power $P_{\text{in,optimal}}$. The ratio of the carrier and sideband power is chosen to $\frac{P_{\text{sig}}}{2P_{\text{sideband}}} = 1$ in all cases. A prestabilized probe laser decoherence of $\gamma_{\text{laser}}/2\pi = 2.0 \text{ kHz}$ was assumed throughout all the calculations. The shot noise limited linewidths are calculated for systems with empty cavity finesse of $F = 250$ and $N_{\text{cav}} = 2.5 \cdot 10^7$ atoms overlapping the cavity mode, and a improved system with $F = 1000$ and $N_{\text{cav}} = 5.0 \cdot 10^7$.

CHAPTER



EXPERIMENTAL TECHNIQUES

Two proof-of-concept experimental systems were realized in this work in order to study the dynamics of strontium atoms coupled to an optical cavity. These dynamics were predicted by the theoretical model presented in Chap. 3. The following section describes in brief terms the relevant experimental techniques used for realizing these proof-of-concept experimental systems. The intention of the following sections is to introduce basic experimental concepts for readers who are new to the field of atomic and optical physics. Experienced readers can hence move on to the descriptions of the realized experimental systems in Chap. 5. However, it is recommended to get familiarized with the *Noise Immune Cavity Enhanced Optical Heterodyne Molecular Spectroscopy* (NICE-OHMS) technique described in Sec. 4.6, as the details of this technique are essential for the main spectroscopic experiments described in Chap. 6.

4.1 Optical cavities

Optical cavities (or resonators) play several essential roles in this work, and they are for example used for laser mode selection in laser systems and for enhancement of non-linear frequency conversion processes. Optical cavities are also used as frequency references for laser stabilization, and for enhancing the interaction (optical depth) of an atomic sample and the intra cavity field. The relevant properties of optical cavities are presented below.

Optical cavities consist of at least two reflecting surfaces establishing

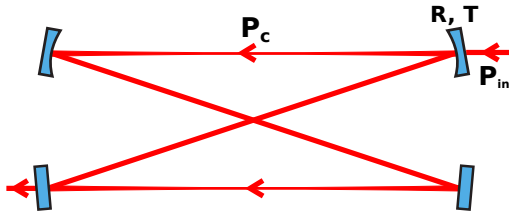


Figure 4.1: Illustration of a ring cavity. Note, that the light only propagates in one direction. P_{in} (P_c) is the input (intra-cavity) optical power and R (T) is the power reflection (transmission) coefficient of the input mirror. The enhancement P_c is described in Eq. (4.3).

an optical path which is traversed repeatedly. Optical cavity designs exist in a wide variety. Two types of optical cavities are used in this work: *Fabry Perot cavity* and *ring cavity*. A *Fabry Perot cavity* (FP cavity) consists of only two mirrors facing each other. The intra-cavity light propagates in both directions in a FP cavity, while the light will only propagate in one direction in a so-called *ring cavity*. See Fig. 4.1.

Monochromatic radiation inside an optical cavity can make standing waves by being reflected at the mirrors and repeat the same optical path inside the cavity. However, a condition for this standing wave is that the intra cavity field undergo a round trip phase shift corresponding to an integer number of 2π . This condition will only be fulfilled for certain resonance frequencies and certain spatial mode dimensions of the radiation. An optical cavity with fixed dimensions can hence be used as a frequency reference and for filtering spatial radiation modes. Two cavity parameters essential for this work are described in the following.

The first parameter is the so-called *Free Spectral Range* (FSR), which describes the frequency spacing between two resonance frequencies of the same transverse mode of an optical cavity. This FSR depends on the cavity dimensions such as the length L of the cavity and can be described as:

$$\text{FSR} \equiv \frac{c}{2nL}, \quad (4.1)$$

where c is the speed of light in vacuum and n is the index of refraction inside the cavity. Note, that this expression for FSR in Eq. (4.1) is only valid for a FP cavity and differs from the FSR for a ring cavity (shown in Fig. 4.1).

A second essential parameter is the so-called cavity finesse, F , which is a measure of how many round-trips the intra cavity field completes before leaving the cavity:

$$F = \frac{\pi}{T + \mathcal{L}_{\text{tot}}}. \quad (4.2)$$

Here, T is the power transmission coefficient of the output cavity mirror and \mathcal{L}_{tot} is the total power loss per round-trip. Eq. (4.2) is only valid in the limit where \mathcal{L}_{tot} is very small. The finesse can also be expressed as the ratio of the FSR and the resonance linewidth of the cavity, $\delta\nu_{\text{cav}}$: $F = \text{FSR}/\delta\nu_{\text{cav}}$. A high finesse will thus often yield a narrow resonance linewidth, which can be exploited as a frequency reference for laser stabilization. Furthermore, high finesse also implies long lifetime of the intra cavity field. This leads to a significant enhancement of the optical power P_c inside the cavity. This intra cavity power can be expressed as the following for a ring cavity illustrated in Fig. 4.1 [Bergquist et al., 1982]:

$$\frac{P_c}{P_{\text{in}}} = \frac{(1 - R)}{1 - \sqrt{R(1 - \mathcal{L}_{\text{tot}})}} \cdot \kappa_{00}, \quad (4.3)$$

where P_{in} is the input power, R is the power reflection coefficient of the input coupler, and κ_{00} is the fraction of the input light which is coupling to the fundamental transversal electromagnetic mode (TEM_{00} mode) of the cavity. This build up of optical power can be exploited for enhancing the efficiency of *Second Harmonic Generation* as described in Sec. 4.3.

4.2 External Cavity Diode laser

The lasing frequency and spatial modes of a diode laser is typically determined by the internal cavity constituted by the reflection from the diode surfaces. The mode stability, tunability and spectral linewidth of a diode laser is often insufficient for spectroscopy of narrow atomic and molecular transitions. Hence, the diode laser is often developed into an *external cavity diode laser* (ECDL) to meet the requirements of spectroscopy experiments. Two different ECDL designs are used in this work and the basic concepts of these two different ECDL systems are presented in this section.

An ECDL is a diode laser which is extended by a wavelength selecting external cavity. The output surface of the diode laser is typically anti-reflection coated but internal cavity modes are still constituted by the diode surfaces. Hence, the ECDL system is composed of several components each with their own gain lineshape shown in Fig. 4.2. An ECDL tends to lase at a frequency ν_0 and spatial mode with greatest net gain, i.e. when the maxima of the gain spectra overlap. The lasing frequency can be tuned

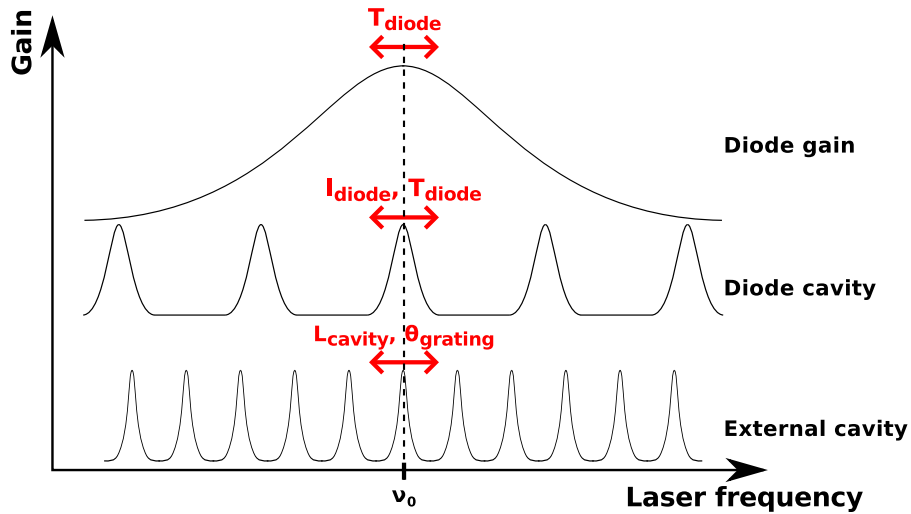


Figure 4.2: Illustration of the gain lineshapes relevant for an ECDL. The diode gain depends on the diode temperature T_{diode} . The gain of the diode cavity depends on T_{diode} and the diode current I_{diode} . The gain of the external cavity depends on the cavity length L_{cavity} and the angle θ_{grating} of the diffraction grating used for the external cavity.

by adjusting different parameters to modify the different gain spectra. The diode temperature, diode current and the length of the external cavity are adjustable parameters often used for controlling the lasing frequency. The linewidths of ECDL systems are typically about few MHz if the external cavity includes a wavelength selecting filter such as a diffraction grating.

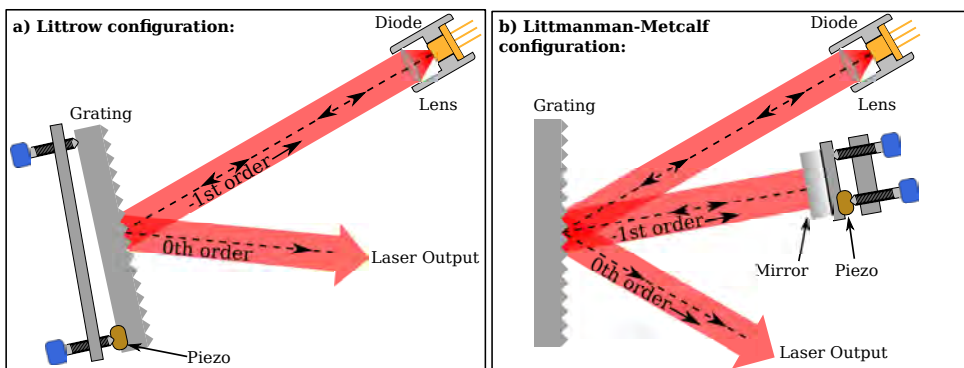


Figure 4.3: Illustration of two ECDL configurations: a) Littrow and b) Littman-Metcalf.

Two different ECDL configurations are used in this work: The *Littrow* and *Littman-Metcalf* configuration.

An ECDL in the *Littrow* configuration consists of a laser diode and an adjustable diffraction grating. Figure 4.3a) illustrates this configuration. The diffraction grating reflects a fraction of the incident light conventionally (0th order in Fig. 4.3a)) while another fraction is diffracted with a wavelength dependent diffraction angle (-1st order in Fig. 4.3a)). This -1st order diffraction can be redirected towards the laser diode and constitute an optical cavity with the back end surface of the laser diode as the second mirror surface. The diffraction grating serves as a wavelength selecting filter and the resonant frequencies of the external cavity can easily be tuned by rotating the grating about an axis. This can be done manually by fine-pitch screws or by implementing a piezo electric element. A minor inconvenience occurs when the lasing wavelength is tuned by adjusting the grating angle, as the output angle will change as well. This might cause unwanted changes in the output beam alignment.

An ECDL in the *Littman-Metcalf* configuration consists similarly of a laser diode, a fixed diffraction grating and an adjustable mirror. This configuration is illustrated in Fig. 4.3b). The diode laser beam is diffracted on the diffraction grating. The -1st order diffraction is directed towards the mirror and retro-reflected back to the grating. The new -1st diffraction of this reflection is then redirected towards the laser diode. The resonant frequencies of this external cavity is tuned by adjusting the mirror angle by fine-pitch screws or by a piezo electric element. The advantage of this configuration is that the output beam direction is unaffected by changes in the mirror angle. However, a smaller fraction of the diode output is diffracted back to the diode, as the light is diffracted twice. This can be compensated by choosing a diffraction grating with higher diffraction efficiency.

4.3 Second Harmonic Generation

Second Harmonic Generation (SHG) is a technique often used when a desired wavelength is not accessible through direct laser radiation. In this work, SHG is used for generating light at 461 nm for laser cooling of ^{88}Sr . This laser system for generating light at 461 nm is described later in Sec. 5.1.2.

SHG is a process where light with a frequency twice the input light is generated during propagation in a nonlinear medium. This frequency doubling is caused by a nonlinear susceptibility term of the nonlinear

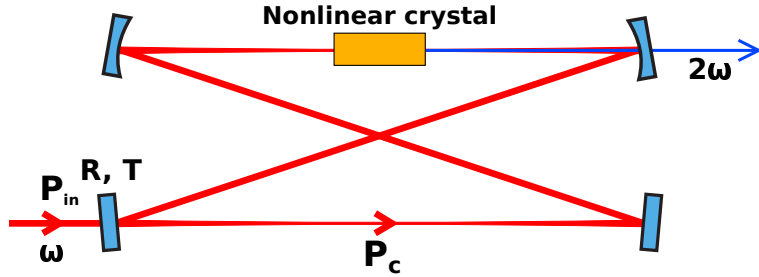
Cavity enhanced SHG:

Figure 4.4: Illustration of cavity enhanced SHG. SHG is often performed in a ring cavity such that the frequency doubled light will only propagate in one direction. The first mirror after the nonlinear crystal is anti-reflex coated such that the frequency doubled light is transmitted out of the cavity.

medium. This nonlinear susceptibility depends quadratically on the input field amplitude [Milonni and Eberly, 1988, p.631].

Figure 4.4 illustrates a beam with fundamental frequency ω sent through an optical ring cavity with an intra-cavity nonlinear crystal and a frequency component with twice the fundamental frequency 2ω is generated. The generated frequency doubled optical power $P_{2\omega}$ can be approximated as the following expression, when the fundamental light with optical power P_ω passes through the nonlinear crystal once [Nagourney, 2014, p.400]:

$$P_{2\omega} = \frac{1}{2} \left(\frac{\mu_0}{\epsilon_0} \right)^{3/2} \frac{\omega^2 d_{\text{eff}}^2 L^2 \sin^2(\Delta k L)}{n_\omega^2 n_{2\omega}} \frac{1}{A} P_\omega^2, \quad (4.4)$$

$$P_{2\omega} = \gamma P_\omega^2. \quad (4.5)$$

where d_{eff} is the effective second-order susceptibility of the nonlinear medium. μ_0 is the vacuum magnetic permeability and ϵ_0 is the vacuum electrical permittivity. n_ω and $n_{2\omega}$ are the respective index of refraction for the fundamental frequency ω and the doubled frequency 2ω . L is the length of the crystal, A is the area of the input beam profile and $\Delta k \equiv k_{2\omega} - 2k_\omega$ is the phase mismatch between the frequency doubled light and the fundamental input light.

A quadratic $P_{2\omega} \propto P_\omega^2$ dependency is evident in Eq. (4.4) and a single pass conversion efficiencyⁱ $\gamma = P_{2\omega}/P_\omega^2$ is defined in the rewriting from Eq. (4.4) to Eq. (4.5). This quadratic dependency is characteristic for

ⁱNote that the unit of this conversion efficiency γ is the possibly non-intuitive [%/W].

many SHG systems. However this approximation is only valid for low conversion efficiencies as the energy conservation would otherwise be violated for high values of P_ω . The net conversion efficiency will be limited for high P_ω as the fundamental optical power will be decreased for high conversion efficiency [Milonni and Eberly, 1988, p.637].

The conversion efficiency γ can be effectively enhanced by constructing an optical cavity around the non-linear crystal as an intra-cavity optical power $P_{\omega,\text{cavity}}$ is built up inside the cavity. Equation (4.3) can be applied to achieve an expression for the frequency doubled power $P_{2\omega,\text{cavity}}$ enhanced by a ring cavity:

$$\begin{aligned} P_{2\omega,\text{cavity}} &= \gamma P_{\omega,\text{cavity}}^2, \\ &= \gamma \left(\frac{\kappa_{00}(1-R)}{1 - \sqrt{1-\mathcal{L}}R} \right) P_\omega^2. \end{aligned} \quad (4.6)$$

Note, that Eq. (4.6) corresponds to a cavity enhanced version of Eq. (4.5), where the enhancement level depends on the cavity parameters.

The optical power of the frequency doubled component $P_{2\omega}$ in Eq. (4.4) yields the maximum value when the phase mismatch is $\Delta k = 0$. This phase matching condition does usually not occur naturally due to the dispersive behavior of the non-linear crystals. However, the non-linear crystals are often birefringent and phase matching can be optimized by adjusting the angle between the beam propagation and the optical axis of the non-linear crystal. The phase matching can also be optimized by adjusting the temperature of the crystal and exploit the non-trivial temperature dependency of the birefringence. Furthermore phase matching can be optimized by periodically changing the optical axis of the non-linear crystal during fabrication. All these above mentioned phase matching strategies are used for optimizing SHG conversion efficiency later in this work. This is described in Sec. 5.1.2.

Equation (4.4) suggests that the conversion efficiency γ can be increased unrestrictedly by simply extending the crystal length L and reduce the area of the fundamental beam. Equation (4.4) is, however, only an approximation for a beam with constant beam profile. The beam area will inevitably diverge due to the nature of Gaussian beams and the conversion efficiency will be limited. The optimal conversion efficiency is achieved when the ratio ζ of the crystal length L and the confocal length b of the fundamental Gaussian beam is $\zeta = L/b = 2.84$ [Boyd and Kleinman, 1968].

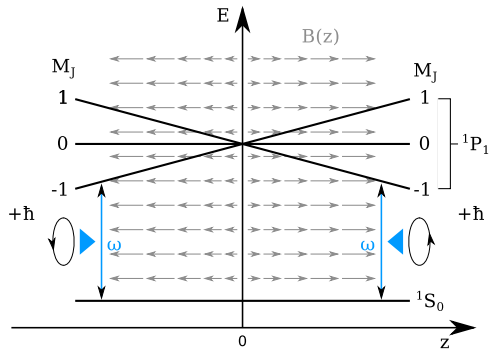


Figure 4.5: From [Schäffer, 2015]: 1D schematic of a MOT. The gray arrows illustrate the magnetic field strength which determines the Zeeman splitting.



Figure 4.6: Picture of a MOT with trapped ^{88}Sr atoms. The bright blue spot is the fluorescence from the trapped atoms.

4.4 Magneto-Optical Trap

A *Magneto-Optical Trap* (MOT) is a technique for cooling and trapping neutral atoms down to temperatures in the mK range. The MOT is a workhorse for a wide range of cold atom experiments and was rewarded with a Nobel prize in 1997 [Cohen-Tannoudji, 1998]. A MOT was also used in this work for trapping and cooling ^{88}Sr atoms for performing spectroscopy experiments. The MOT realized for this purpose is presented later in Sec. 5.2.1.

The principle of a MOT can be described by considering atoms with a ground state with a total angular momentum $J = 0$ ⁱⁱ. The $J = 1$ excited state has magnetic sub-levels with $M_J = 0, \pm 1$. The atoms are located in the center of a linearly increasing magnetic field in all three dimensions. This magnetic field is produced by two coaxial coils in the anti-Helmholz configuration, which to first order produces a linear field gradient in the center between the two coils. The $M_J = \pm 1$ states are shifted as illustrated in Fig. 4.5 by this magnetic field due to the Zeeman shift. The atoms are irradiated in all three dimensions by counter-propagating beams with circular polarization of opposite helicity. The frequency of these beams are red-detuned with respect to the unperturbed $\Delta_{M_J} = 0$ transition. We recall that the magnetic field modifies the resonance conditions for the $M_J = \pm 1$ states such that this red-detuned light is resonant for atoms in positions away from the center of the magnetic field ($z = 0$ in Fig. 4.5).

ⁱⁱNote, that the $J = 0 \rightarrow J = 1$ transition is used for a strontium MOT, while many other $J \rightarrow J + 1$ transitions are used for laser cooling of other elements.

The two different circular polarizations σ^\pm ensure furthermore that the transition is only excited to the lower Zeeman shifted level by the beam pointing towards the center of the system. A scattering force is thus yielded towards the center and the atoms are trapped. Figure 4.6 shows the MOT realized in this work. This realized MOT is described later in Sec. 5.2.1.

The mean velocity of the trapped atoms is also damped by the scattering force and the atoms are effectively cooled. The MOT temperatures are typically in the mK level (Some examples are shown in Table 3.1). This atomic temperature and the number of trapped atoms can be controlled to some extend by controlling the detuning and power of the trapping beams [Xu et al., 2003b]. The lower limit of the achievable temperature T_D is set by the natural linewidth of the transition Γ_{MOT} used for laser cooling:

$$T_D = \frac{\hbar\Gamma_{\text{MOT}}}{2k_B}. \quad (4.7)$$

Here, \hbar is the Planck constant and k_B is the Boltzmann constant. Sub-Doppler temperatures below T_D have been widely realized with cooling techniques exploiting the degeneracy of the atomic states involved in the laser cooling process [Xu et al., 2003a]. However, Sub-Doppler cooling was not employed in this work.

Zeeman slower

Another spatially varying magnetic field configuration is used in a *Zeeman slower*. A Zeeman slower is often used for 1 dimensional slowing of a beam of atoms from a source before trapping in a MOT. The beam of atoms is slowed by counter propagating resonant radiation. The resonance frequency of a moving atom in the laboratory frame of reference is shifted due to the Doppler effect. This means that the frequency shift of an atomic resonance depends on the velocity of the atom which will change during a cooling process. This change of resonance is counter-acted by a position dependent Zeeman shift imposed by a likewise position dependent magnetic field. The appropriate magnetic field $B(z)$ for a desired deceleration from an initial velocity v_i to a final velocity v_f along a z axis can be described as [Metcalf and van der Straten, 2001, p.77]:

$$B(z) = B_0 \sqrt{1 - z/z_0}. \quad (4.8)$$

B_0 is the appropriate overall magnetic field strength, which depends on the cooling transition properties and the initial velocity of the decelerated atoms. z_0 is the appropriate length of the Zeeman slower, which is

determined by the magnitude of the desired deceleration and the initial velocity. The optimal slowing of the atoms is hence not achieved by just designing the Zeeman slower as long as possible and with as strong magnetic field as possible. A wide variety of different Zeeman slower designs have been developed in other works in order to achieve some desired uniform deceleration of atoms.

4.5 Laser stabilization

Optical cavities can be used as local frequency references for laser stabilization. Both the transmission and reflection spectrum of an optical cavity are however symmetrical (even) and the sign of a laser detuning relative to the cavity resonance is not revealed. It is hence necessary to generate an anti-symmetric (odd) signal for a stabilization loop. Such an anti-symmetric signal is often referred to as an *error signal* (previously illustrated as the green line in Fig. 2.2). The following sections describe the two different techniques used for generating error signals in this work.

4.5.1 Hänch-Couillaud

One simple technique for generating a sign sensitive error signal is the *Hänch-Couillaud* (HC) laser stabilization scheme [Hansch and Couillaud, 1980]. The HC scheme utilizes birefringence in an optical cavity. This birefringence can be introduced by inserting a polarization selecting element such as a Brewster plate in the optical cavity as shown in Fig. 4.7. The birefringence results in different single-round-trip propagation phase shifts for intracavity light parallel E_{\parallel} or perpendicular E_{\perp} to the birefringence axis. The two polarization components are thus resonant with the optical cavity for different resonance frequencies. Consider the case where the parallel component E_{\parallel} is resonant with the optical cavity and standing waves of the E_{\parallel} component is present inside the cavity. Then, the perpendicular component E_{\perp} is not resonant with the cavity and standing waves of E_{\perp} is not present inside the cavity and the entire component is reflected by the in-coupling mirror of the cavity. The reflected E_{\perp} is linearly polarized, but it is converted to circular polarization by a $\lambda/4$ -plate and divided equally between the two output ports of a *polarisation beam splitter* (PBS). These two equally divided outputs are detected by their respective photo detector (PD) resulting in a signal proportional to the photo currents i_1 and i_2 shown in Fig. 4.7. The difference of these two photo detector signals $i_2 - i_1$ is generated with a differential amplifier. This signal will

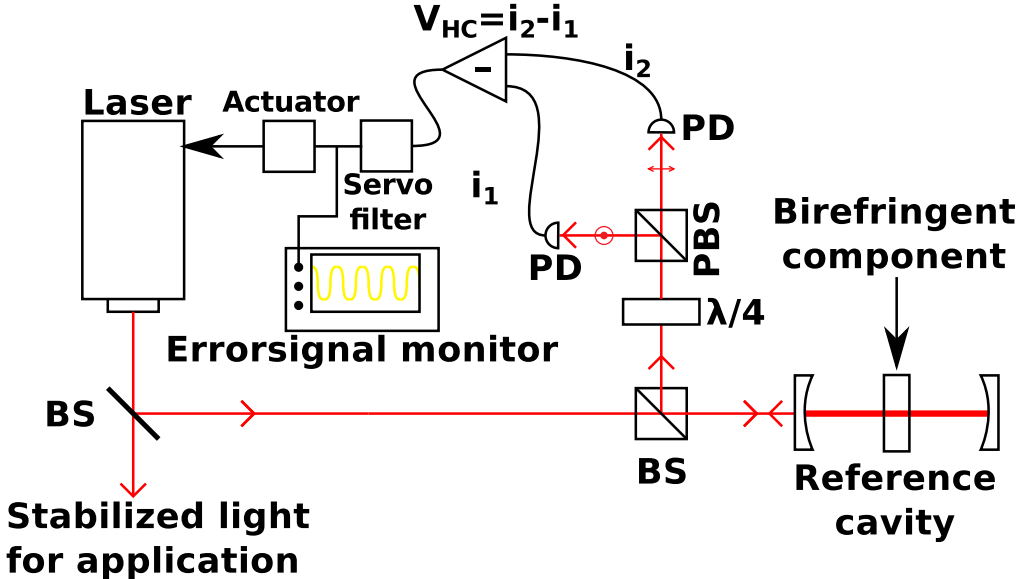


Figure 4.7: Block diagram illustrating the general concepts of a HC setup. Red lines are optical paths while black lines are electronic signal paths. Note, that the generated error signal is used for stabilizing a laser frequency in this figure, while the error signal can also be used to stabilize the length of the cavity. The HC scheme was mostly used for stabilizing cavity lengths in this work.

yield a zero value when only the E_{\perp} component is reflected and when the polarization of this reflected component is controlled such that the optical power of the reflected component is equally divided to the two photo detectors. However, a fraction of the parallel E_{\parallel} component is also reflected by the in-coupling cavity mirror. The phase of this reflected E_{\parallel} component depends sign sensitively on the cavity detuning [Riehle, 2004, p.105]. This causes ellipticity for the polarization of the total reflected field which results in non-zero values for the differential signal $i_2 - i_1$ [Riehle, 2004, p.270]:

$$i_2 - i_1 \propto 2\cos(\theta)\sin(\theta) \frac{TR\sin(2\Delta\omega L/c)}{(1 - R^2)^2 + 4R\sin^2(\Delta\omega L/c)}, \quad (4.9)$$

where θ is the angle between the input polarization and the birefringence axis and $\Delta\omega$ is the laser detuning with respect to the cavity resonance. Here, L is the cavity length and c is the speed of light. Equation (4.9) is valid for a symmetrical FP cavity with power reflection (transmission) coefficient of R (T).

The signal expressed in Eq. (4.9) can be used as an error signal, as it is sign sensitive around the cavity resonance ($\Delta\omega = 0$). This error signal can be used for stabilizing a laser to a stable reference cavity or to lock an adjustable cavity length to an input laser such that standing waves are kept inside the cavity at all times.

The HC scheme is particularly suited for cavity systems with intrinsic birefringent cavity components such as non-linear crystals for generation of higher order harmonics (see Sec. 4.3). The technique is simple and often relatively inexpensive. The error signal offset is however sensitive to drifts of the involved optical components and the error signal is affected by low frequent technical noise.

The HC locking scheme is used in this work for stabilizing an enhancement cavity for SHG and for stabilization of the atom-cavity system in the main experiment. An experimentally realized HC error signal is shown later in Fig. 5.13.

4.5.2 Pound-Drever-Hall

Another widely used technique for generating a sign sensitive error signal for laser stabilization is the *Pound-Drever-Hall* (PDH) scheme. The PDH technique applies a set of sidebands on the spectrum of a laser by applying a periodic phase modulation with modulation frequency ω_m on the electric field of the laser. This modulation frequency is typically in the range of $\omega_m/2\pi = 10 \sim 50$ MHz. The phase modulation is done by using an *Electro Optical Modulator* (EOM) as shown in Fig 4.8. The fundamental component of the laser before phase modulation is henceforth called the *carrier*. The laser with the sidebands is coupled into the reference cavity and a photodetector measures the reflected light consisting of both the reflection from the first and second mirror in the reference cavity. The basic principle of the PDH technique is to compare the phase of the reflected sideband components and the ontra-cavity collected phase of the carrier.

The total single cavity round-trip phase shift of the carrier field will be $q \cdot 2\pi$ if the carrier frequency is resonant with the cavity resonance, q is any integer. The sum of all round trip components inside the cavity will result in standing waves in this resonant case, while the reflected beam outside the cavity is canceled out by destructive interference. The carrier will on the other hand be reflected, if the carrier is not resonant with the cavity. This reflection acts hence as a frequency discriminator dependent on the laser detuning with respect to the cavity resonance. The detuning dependency of the reflected component is symmetric and does not depend on the sign of the detuning.

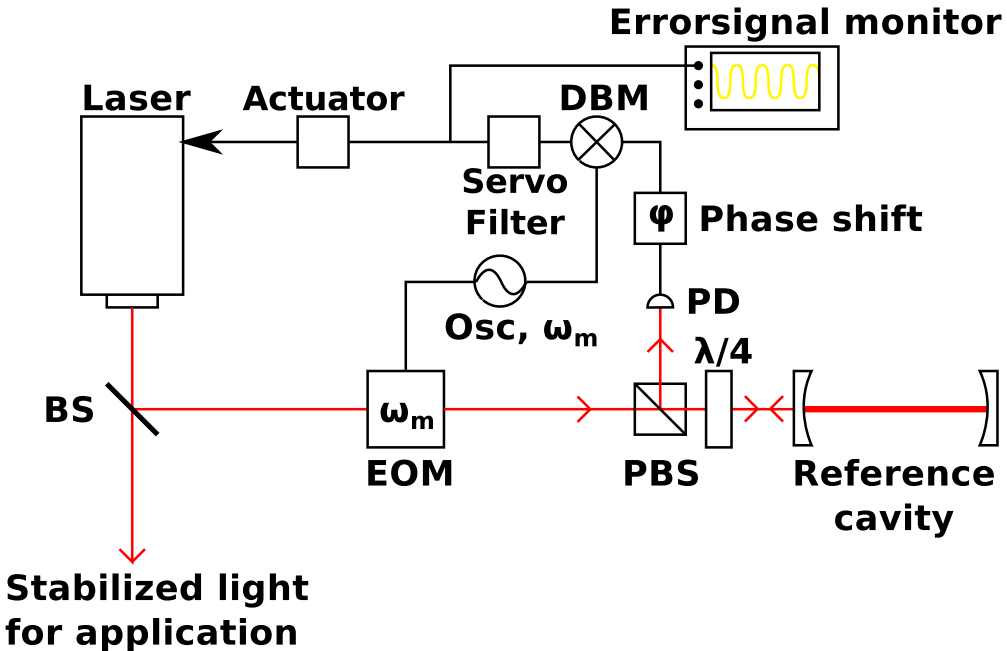


Figure 4.8: From [Christensen, 2012]: Block diagram illustrating the general concepts of a PDH setup. Red lines are optical paths while black lines are electronic signal paths.

The total reflected components can be detected by a photo detector and be sent into a *Double Balanced Mixer* (DBM or mixer) as illustrated in Fig. 4.8. The signal detected by the photo detector can be mixed together with the phase modulation frequency ω_m . This *mixed* signal $V_{PD}(\Delta f)$ corresponds to the product of the photo detector signal and the sinusoidal modulation signal. This $V_{PD}(\Delta f)$ signal forms the PDH error signal and it can be described as [Riehle, 2004, p.273]:

$$V_{PDH}(\Delta f) \propto -\frac{\omega_m^2 (\Delta\omega_c/2) \Delta\omega [(\Delta\omega_c/2)^2 - \Delta\omega^2 + \omega_m^2]}{[(\Delta\omega_c/2)^2 + \Delta\omega^2][((\Delta\omega - \omega_m)^2 + (\Delta\omega_c/2)^2)[(\Delta\omega + \omega_m)^2 + (\Delta\omega_c/2)^2]']}, \quad (4.10)$$

where $\Delta\omega_c/2\pi$ is the cavity linewidth and $\Delta\omega/2\pi$ is the frequency difference of the laser frequency ω and the cavity resonance frequency ω_c , $\Delta\omega = \omega - \omega_c$. This unitless coefficient in the right hand side of Eq. (4.10) forms the characteristic lineshape of the PDH error signal as a function of the detuning of the laser and the cavity resonance. An experientially realized PDH error signal is shown later in Fig. 5.4. The magnitude of this error

signal can be increased by introducing a $\lambda/4$ -plate before the reference cavity and by using a PBS for redirecting most of the reflected light to the photo detector as shown in Fig. 4.8. The total power of the reflected light reaching the photo detector is then optimized and the magnitude of the error signal will also be increased. The PDH technique can also be carried out with a *non-polarisation dependent beam splitter* (BS) and without a $\lambda/4$ -plate. This setup may be advantageous if the circular polarization caused by the $\lambda/4$ -plate is of some reason unwanted for the intra cavity light. However, the total reflected power detected by the photo detector will be lower in this case.

Equation (4.10) expresses the error signal for an optimized relative mixing phase φ . This phase is shown as a phase shift between the photo detector and the DBM mixer in Fig. 4.8. This phase can be optimized by adjusting cable lengths or by implementing voltage controllable RF phase shifter modules. Another quadrature with a different lineshape ([[Riehle, 2004, p.273](#)]) will be included and degrade the error signal if the relative mixing phase is not optimized.

The PDH technique is in this work for both locking a laser to a reference cavity (described in Sec. 5.1.1) and for stabilizing an adjustable cavity length on resonance with an input laser (described in Sec. 5.2.3). Figure 5.4 shows both a plot of an experimentally realized PDH error signal and a theoretical fit based on Eq. (4.10). The characteristic lineshape of the PDH error signal is clearly seen in Fig. 5.4. It is also evident, that the error signal is anti-symmetric, i.e it has different sign on both sides of the cavity resonance, which makes this signal suited as a frequency discriminator.

The PDH technique requires a slightly more complex setup than the HC technique (described in Sec. 4.5.1) and it requires potentially expensive components such as an EOM and high frequency *radio frequency* (RF) components. However, the technique has the advantage that the error detection can be shifted up to high RF frequencies by choosing a high modulation frequency ω_m . The error detection will then not be disturbed by low frequent technical noise. In such a case, laser stabilization with the PDH technique can be performed only limited by the photo detector shot-noise and by *residual amplitude modulation* (RAM) caused by disturbances in the EOM or other optical elements which can cause phase fluctuations [[Zhang et al., 2014](#)].

4.6 NICE-OHMS

The atomic absorption of resonant light can be measured conceptually simple by comparing the field power before and after the atomic interaction. On the other hand, measurements of the phase shift induced by the atoms requires slightly more complex techniques. One technique is to employ heterodyne detection [Riehle, 2004, p.71] by studying the relative phase between an electro magnetic field interacting with the atoms and a local field with no atomic interaction [Martin et al., 2011]. Heterodyne detection has proven to be effective in a large number of experiments, but requirements of relative phase stabilization of all involved oscillators increases the complexity of the system. One approach to reduce the complexity of the system and at the same time increase the noise immunity of the system is to apply the so-called *Noise Immune Cavity Enhanced Optical Heterodyne Molecular Spectroscopy* (NICE-OHMS) technique [Ye et al., 1998, Ma et al., 1999].

This NICE-OHMS technique constitutes a central part of the main experiments presented in this work and a description of the basic concepts are presented below. This description will be similar to the description for conventional free-space frequency modulation (FM) spectroscopy. However, the NICE-OHMS technique involves feedback control of a cavity to be on resonance with an input probe laser such that a standing wave of light will be present inside the cavity for all times. This turns out to result in significant changes in the observables of the system, and a direct comparison with the theoretical results derived in Chap. 3 is hampered. A more detailed description of the consequences of this feedback control is presented later in Chap. 6.

The experimental setup for the NICE-OHMS technique is presented in Fig. 4.9. An ensemble of two-level atoms or molecules is placed inside an optical cavity and the system is interrogated by a probe laser with laser frequency ω_l . Sidebands are applied to this probe laser spectrum by applying a periodic phase modulation [Riehle, 2004, p.25]. An EOM is employed to apply this phase modulation with a modulation frequency Ω , which is chosen such that it matches the FSR of the optical cavity, $\Omega/2\pi = \text{FSR}$. The frequencies of the sideband components are thus $\omega \pm 2\pi\text{FSR}$. In the following, the applied components will be called *sidebands* while the component with the original probe laser frequency ω_l will be called *the carrier*. Both the probe carrier and both sideband components will be on resonance with the optical cavity. The probe laser carrier can be assumed to be tunable and near resonant with the atomic transition and the cavity transmitted electromagnetic field E_{out} can be

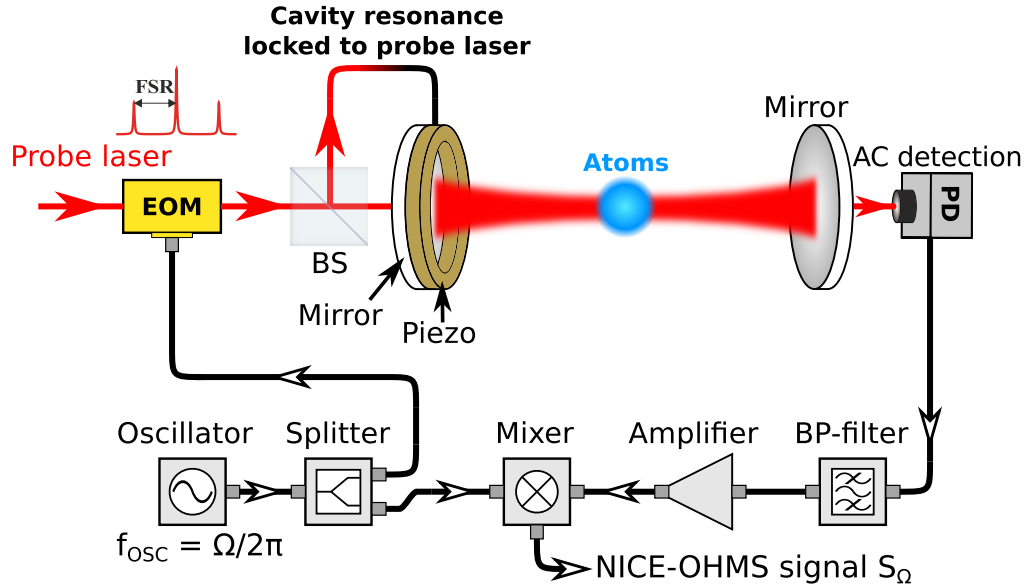


Figure 4.9: General concept of the NICE-OHMS technique. Sidebands are applied on a probe laser by periodic phase modulation with frequency $\Omega/2\pi$. All components of the probe laser are transmitted through the cavity, as they are all resonant. The phase shift induced by atoms inside the cavity can be measured by demodulating the transmission signal.

described as:

$$E_{\text{out}} = E_0 \left(J_0(x) e^{-\alpha} e^{i(\omega_l t + \varphi_a + \varphi_c)} + J_1(x) e^{i(\omega_l + \Omega)t + i\varphi_c} - J_1(x) e^{i(\omega_l - \Omega)t + i\varphi_c} \right). \quad (4.11)$$

Here $J_j(x)$ is the j 'th order regular Bessel function describing the amount of power transferred from the carrier to the j 'th order sideband when modulated by an EOM with modulation index x . This modulation index x depends on the phase modulation amplitude and governs the magnitude of the sideband components. The first component in Eq. (4.11) corresponds to the probe carrier, and this component is affected by an atomic absorption $e^{-\alpha}$ and a phase shift φ_a induced by the atomic dispersion. All components experience a common phase φ_c corresponding to the phase shift from propagation in the empty optical cavity. The relation of the different involved spectra are illustrated in Fig. 4.10. The optical power of the cavity

transmitted light can be detected by a photo detector and the measured signal current S_{PD} will have the following form:

$$\begin{aligned} S_{PD} \propto & E_0^2 (e^{-2\alpha} J_0(x)^2 + 2J_1(x)^2) \\ & + J_0(x) J_1(x) e^{-\alpha} (e^{i\varphi_a} - e^{-i\varphi_a}) (e^{i(\Omega t)} - e^{-i(\Omega t)}) \\ & - J_1(x)^2 (e^{i(2\Omega t)} + e^{-i(2\Omega t)}). \end{aligned} \quad (4.12)$$

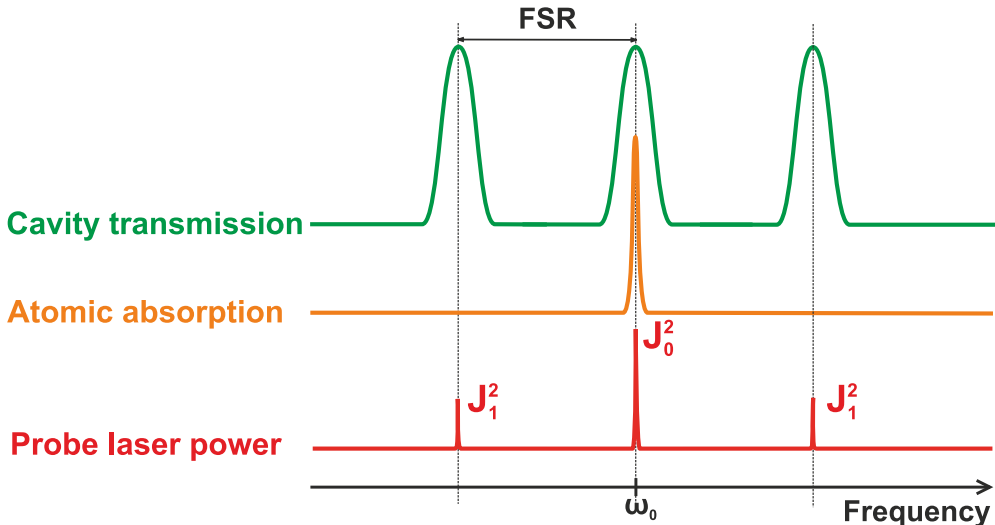


Figure 4.10: Relation between the spectral components relevant for the NICE-OHMS technique. J_j is the j 'th order regular Bessel function which illustrate the power ratio of the carrier and sideband components of the probe laser.

Equation (4.12) consists of three different frequency components: static (DC) components (first line in Eq. (4.12)), components oscillating at Ω (second line) and components oscillating at 2Ω (third line). Note that the empty cavity phase φ_c has been canceled for all terms. The DC components and the 2Ω components can be filtered away with a bandpass filter. The Ω part of the signal can hence be isolated and mixed with a sinusoidal signal $\sin(\Omega t) = \frac{1}{2} (e^{i\Omega t} - e^{-i\Omega t})$ and demodulated down to a DC signal, S_Ω :

$$S_\Omega \propto 4J_0(x) J_1(x) e^{-\alpha} \sin(\varphi_a). \quad (4.13)$$

This demodulation can be done experimentally by using a DBM. The demodulated signal in Eq. (4.13) can be approximated to scale linearly

with the atom induced phase shift $S_\Omega \propto \sin(\varphi_a) \approx \varphi_a$ for very small phase shifts $\varphi_a \ll 1$. Hence, this demodulation technique provides a static DC signal which is proportional with φ_a and the probe laser frequency (ω_l) dependency of the phase dispersion can be mapped out if $e^{-\alpha}$ is approximated to be constant. This approximation is definitely not valid when performing a frequency scan over a frequency range comparable with the absorption width, but it is a reasonable approximation for small scan regions near the center of the atomic resonance.

Equation (4.13) is an expression also seen in the litterature of FM spectroscopy without an optical cavity [Ye and Lynn, 2003]. The optical cavity enhances the achieved signal by increasing the effective interaction between the atoms and the intra-cavity photons. This optical cavity does not introduce additional mechanical noise as all probe laser components experience the same cavity phase φ_c , which was canceled out during detection (see Eq. (4.12)). In addition, the demodulation technique allows shifting the detection up to radio frequencies by designing an optical cavity with an FSR in the RF frequencies. This results in very noise immune detection as most of the mechanical and electric noise frequency components are found below the RF frequencies and only the white frequency noise is detected. The signal to noise ratio of this detection can be improved even further by applying very narrow banded bandpass filters for selecting out the Ω components in Eq. (4.12).

The signal achieved from the NICE-OHMS technique is described as in Eq. (4.13) in most of the litterature [Ye et al., 1998, Ma et al., 1999, Ye and Lynn, 2003]. However the requirement of having a standing wave inside the cavity for all times is significantly modifying the demodulated signal (described in Eq. (4.13)) in the experimental systems studied in this work. An extended description of the NICE-OHMS technique is presented in the following Sec. 4.6.1 by including the standing wave requirement. Two variations of the NICE-OHMS technique, *sideband probing* and the *overtone demodulation*, were also developed during this work. These two techniques are described in details later in Sec. 6.1.2 and Sec. 6.2.1 when presenting the results obtained with these techniques.

4.6.1 ***Modifications of the transmission coefficient***

The following section presents a detailed and slightly cumbersome description of the modifications of the NICE-OHMS signal caused by the requirement of having a standing wave inside the cavity at all times. These modifications apply mainly for large atomic induced phase shifts and will

mostly affect the NICE-OHMS signal for large detuning, when the phase shiftⁱⁱⁱ is measured for the main spectroscopic experiments in this work.

A general expression for describing the total input probe field is as follows, when sidebands are applied with a periodic phase modulation [Riehle, 2004, p.27]:

$$E_{\text{in}} = E_0 \sum_{j=-\infty}^{\infty} J_j(x) e^{i(\omega_c + j\Omega t)}. \quad (4.14)$$

Note that Eq. (4.14) includes all sideband orders, while the probe laser spectrum (described in Eq. (4.11)) treated in the previous section only included the first order sidebands. Each of the components described in Eq. (4.14) is modified by a transmission coefficient χ_j when transmitted through an optical cavity. Here, χ_j is the transmission coefficient for the j 'th sideband component. This transmission coefficient can be expressed analytically for each component in a semi-classical description [Riehle, 2004, p.101]:

$$E_{\text{out}} = \frac{Te^{i\varphi}}{1 - Re^{i2\varphi}} E_{\text{in}} = \chi E_{\text{in}}. \quad (4.15)$$

$E_{\text{in/out}}$ is the input/output field, T and R are the power transmission and reflection coefficient of the cavity mirrors, and φ is the single round-trip complex phase shift experienced by the intra-cavity field. The transmission coefficient χ_j is however not identical for all probe laser components, when the NICE-OHMS technique is applied. Very different behavior are found for the transmission coefficient χ_0 for the probe laser carrier ($j = 0$) component and χ_j for the j 'th order sideband.

The carrier component is resonant with the atomic transition. The single round-trip phase shift φ_0 experienced by the carrier includes contributions from the single pass atomic dispersion β_D , the atomic absorption β_A and the phase shift due to propagation in the empty cavity ϕ_{cavity} :

$$\varphi_0 = \phi_{\text{cavity}} + \beta_D + i\beta_A, \quad (4.16)$$

The j 'th order sideband component on the other hand experiences only the phase shift due to the empty cavity propagation, as it is off-resonant

ⁱⁱⁱThis phase shift is predicted in Fig. 3.3.

with the atomic transition and the single round-trip complex phase shift $\varphi_{\pm j}$ is:

$$\varphi_{\pm j} = \phi_{\text{cavity}} \pm j\pi. \quad (4.17)$$

Here, $\pm j\pi$ is added as the single round-trip phase shifts of neighboring longitudinal cavity modes differ with $\pm\Omega$. As mentioned earlier, the NICE-OHMS technique imposes a requirement that the combined cavity-atom system is forced to be on resonance with the probe laser such that a standing wave field is present during the whole experiment. This requirement is usually fulfilled by implementing a feedback loop (details regarding feedback systems are presented in Sec. 4.5) to control the cavity length by using a piezo element on the cavity mirror as an actuator [Ye et al., 1998, Westergaard et al., 2015, Christensen et al., 2015a, Dinesan et al., 2015]. This requirement modifies the single round-trip complex phase shifts described in Eq. (4.16) and (4.17). The real part of the complex single round-trip phase shift is modified as:

$$\text{Re}(\varphi_0) = \phi_{\text{cavity}} + \beta_D = m\pi, \quad (4.18)$$

where m is an integer. The complex single round-trip phase shift of the j 'th order sideband is modified according to Eq. (4.18), as all probe laser components experience the same single round-trip cavity phase shift φ_c :

$$\varphi_{\pm j} = \phi_{\text{cavity}} \pm j\pi = -\beta_D \pm j\pi. \quad (4.19)$$

These modified phase shifts have direct implications for the transmission coefficients for the different probe laser components. The transmission coefficient χ_0 for the carrier becomes purely real and it reflects only the absorptive part (β_A) of the atomic interaction:

$$\chi_0 = \frac{Te^{-\beta_A}}{1 - Re^{-2\beta_A}}. \quad (4.20)$$

The transmission coefficients $\chi_{\pm j}$ for the sideband components are complex and reflect only the dispersive part (β_D) of the atomic interaction:

$$\chi_{\pm j} = \frac{Te^{i(\pm j\pi - \beta_D)}}{1 - Re^{2i(\pm j\pi - \beta_D)}}. \quad (4.21)$$

These modifications of the transmission coefficients modifies the experimental observables substantially when performing spectroscopic

experiments with the NICE-OHMS technique. More intuitive interpretations of the observables are discussed later in Sec. 6.1.2 in comparison with experimentally observed quantities. The focus here will be the consequences for the NICE-OHMS signal.

The cavity transmitted field is no longer as described in Eq. (4.11) and the standing wave restrictions modifies the field as (here for sidebands up to second order):

$$\begin{aligned} E_{\text{out}} = & E_0 \left(J_0(x) \chi_0 e^{i\omega_l t} \right. \\ & + J_1(x) \chi_1 e^{i(\omega_l + \Omega)t} - J_1(x) \chi_{-1} e^{i(\omega_l - \Omega)t} \\ & \left. + J_2(x) \chi_2 e^{i(\omega_l + 2\Omega)t} + J_2(x) \chi_{-2} e^{i(\omega_l - 2\Omega)t} \right). \end{aligned} \quad (4.22)$$

Following the procedures followed from Eq. (4.11) to Eq. (4.13), the cavity transmitted field can be demodulated with demodulation frequency Ω and the resulting NICE-OHMS signal is:

$$\begin{aligned} S_\Omega \propto & J_0(x) J_1(x) \chi_0 \cdot \text{Im}(\chi_1) \\ & (+ J_1(x) J_2(x) (\chi_2 \chi_1^* - \chi_1 \chi_2^*) + J_2(x) J_3(x) (\chi_2^* \chi_3 - \chi_2 \chi_3^*)). \end{aligned} \quad (4.23)$$

The last terms inside the parenthesis in Eq. (4.23) are only small corrections. However, these corrections are important to establish a complete connection between the experimental data and the theoretically predicted values. The essential part here is the first term in Eq. (4.23). This first term $J_0(x) J_1(x) \chi_0 \cdot \text{Im}(\chi_1)$ corresponds to the conventional NICE-OHMS expression in Eq. (4.13). χ_0 describes as mentioned above the effect of the atomic absorption and corresponds to $e^{-\alpha}$ in Eq. (4.13). χ_1 describes the effect of the atomic dispersion and corresponds to $\sin(\phi_a)$ in Eq. (4.13). This first term of Eq. (4.23) is in fact reduced to an expression similar to the expression for the conventional FM demodulation $e^{-\beta_A} \sin(\beta_D)$ (described in Eq. (4.13)) in the limit of $R \rightarrow 0$. The exact expression for $\text{Im}(\chi_1)$ is as follows:

$$\text{Im}(\chi_1) = \underbrace{\frac{T \cdot e^{-\beta_A} (1 + R \cdot e^{-2\beta_A})}{1 + R^2 \cdot e^{-4\beta_A} - 2e^{-2R\beta_A} \cos(2\beta_D)}}_{\text{cavity enhancement}} \cdot \underbrace{\sin(\beta_D)}_{\text{phase shift}}. \quad (4.24)$$

This rather extensive expression in Eq. (4.24) can be approximated to $\text{Im}(\chi_1) \propto \beta_D$ if $\beta_D \ll 1$ and $e^{-\beta_A}$ is constant. These approximations

corresponds to the same approximations applied in order to let Eq. (4.13) scale linearly with the total atomic induced phase shift φ_a . Whereas $\sin(\beta_D) \approx \beta_D$ represents the single round-trip phase shift of the atoms, the rest of Eq. 4.24 represents the cavity enhancement of the dispersion yielding the total atomic induced phase shift φ_a . The NICE-OHMS signal described in Eq. (4.23) is hence effectively reduced to Eq. (4.13) for small atomic dispersion β_D and low modulation index x^{iv} .

The restrictions of forcing the combined cavity-atom system to be resonant with the probe carrier laser is different from the system considered in the theoretical model presented in Chap. 3. This theoretical model assumes the probe laser frequency ω_l to be resonant with the empty cavity resonance frequency ω_c at all times, $\omega_l - \omega_c = 0$. Furthermore, the main focus of the theoretical studies in Chap. 3 has been on the total cavity transmitted field calculated through the quantum mechanical creation and annihilation operators for the intra cavity photons^v $|\alpha|^2 = \langle \hat{a}^\dagger \hat{a} \rangle$. The cavity transmitted field is calculated numerically for a steady-state system through α (described in Eq. (3.22)). This do not take sidebands and the cavity servo system into account and the total atom induced absorption and dispersion is considered instead of the single round-trip absorption and dispersion. Hence, this cavity transmitted field calculated through α needs to be described in terms of single round-trip absorption and dispersion and to take the sidebands into account. This is done by expressing the cavity transmission coefficient χ in terms of α :

$$\frac{E_{\text{out}}}{E_{\text{in}}} = \chi = \frac{\kappa}{\eta} \alpha, \quad (4.25)$$

where κ is the cavity decay rate which is a measure of the rate the intra cavity photons decay in the empty cavity and η is the classical drive amplitude, which describes the rate at which photons from the probe laser couples into the cavity. A single round-trip atomic absorption β_A and dispersion β_D can now be evaluated by approximating the transmission coefficient described by α in Eq. (4.25) as a semi-classical transmission coefficient (see Eq. (4.15)):

^{iv}Corresponding to small higher order sidebands $J_2(x) \approx 0$ and $J_3(x) \approx 0$.

^vHere α represents the intra cavity field and α is *not* the same as the α representing the total atomic absorption in Eq. (4.11).

$$\frac{\kappa}{\eta} \operatorname{Re}(\alpha) = \operatorname{Re} \left(\frac{Te^{i(\beta_D+i\beta_A)}}{1 - Re^{i2(\beta_D+i\beta_A)}} \right). \quad (4.26)$$

$$\frac{\kappa}{\eta} \operatorname{Im}(\alpha) = \operatorname{Im} \left(\frac{Te^{i(\beta_D+i\beta_A)}}{1 - Re^{i2(\beta_D+i\beta_A)}} \right). \quad (4.27)$$

The single round-trip atomic absorption β_A and phase shift β_D can now be evaluated by solving the equation system Eq. (4.26)–(4.27). These values for β_A and β_D can then be inserted in the expressions for the transmission coefficients χ_j (shown in Eq. (4.20) and Eq. (4.21)) and the modified NICE-OHMS signal S_Ω can be calculated through Eq. (4.23).

Note that Eq. (4.26)–(4.27) are approximations. These approximations prove valuable for describing the NICE-OHMS signals for low-finesse cavity systems described later in Sec. 6.1, while some inconsistency are observed for high-finesse cavity systems described in Sec. 6.3. Thorough studies of the limitations of these approximations are hence still needed.

One other correction imposed by the cavity feedback system is the contributions on the error signal by the sidebands. The feedback systems are designed to provide a sign sensitive error system scaling with the cavity detuning of an input laser frequency. The atomic induced phase shift will shift the resonance frequency of the cavity mode by ω_m . This frequency shift depends on the total atom induced phase shift φ_a , $\omega_m = \frac{\kappa \tan(\varphi_a)}{2}$ [Ye and Lynn, 2003, p.22]. The feedback system will mainly control the cavity length such that the standing-wave criteria for the probe carrier is maintained as the optical power from the carrier will dominate the error signal for the feedback system. This brings all the sideband components out of resonance with their respective cavity resonances. The off-resonant sidebands will now contribute to the error signal and shift the cavity resonance frequency back in the opposite direction as the initial atomic induced cavity shift ω_m . The cavity and the carrier will hence be detuned with x_D . The atom induced shift of the cavity resonance ω_m and the detuning due to the error signal contributions of the sidebands x_D are illustrated in Fig. 4.11. The value of x_D correspond to the case where the error signal contribution from the carrier and all orders of sidebands are equal:

$$x_D \cdot J_0(x)^2 = 2(\omega_m - x_D) \cdot \left(\sum_{j=1}^{\infty} J_j(x)^2 \right). \quad (4.28)$$

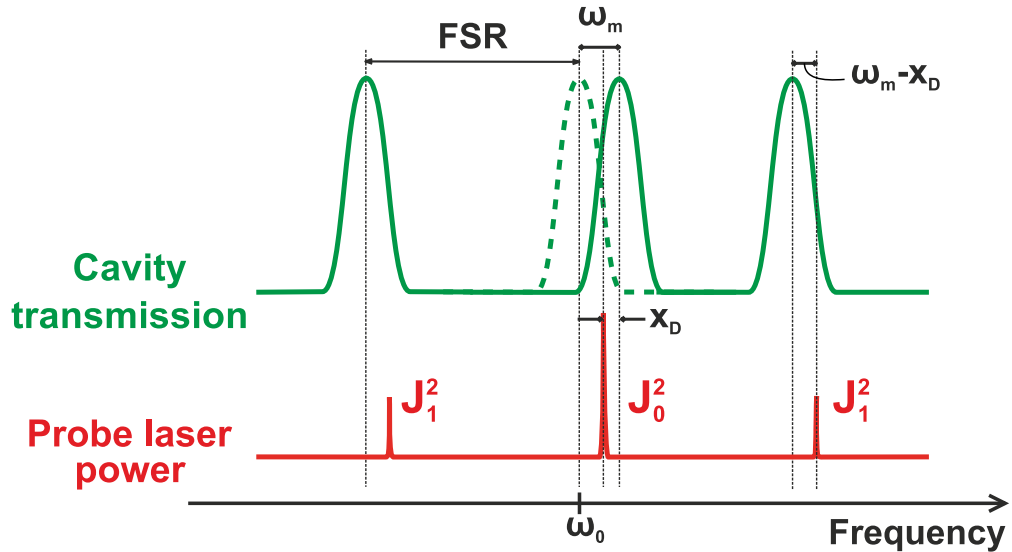


Figure 4.11: Illustration of the corrections imposed by the cavity servo system and the atom induced phase shift on the spectral components relevant for the NICE-OHMS technique. ω_m is the frequency shift of the cavity resonance induced by the atomic phase shift. Note, that only the cavity mode resonant with the atomic resonance is shifted by ω_m . x_D is the shift of all cavity modes due to contributions to the error signal caused by the off-resonant sidebands. Note, that x_D shifts in the opposite direction as ω_m .

It can be derived from Eq. (4.28) that the carrier-cavity detuning x_D due to the contributions from the sidebands is:

$$x_D = \kappa \cdot \tan(\varphi_a) \sum_{j=1}^{\infty} J_j(x)^2. \quad (4.29)$$

Note that the relation $J_0(x)^2 + 2 \sum_{j=1}^{\infty} J_j(x)^2 = 1$ was used to derive Eq. (4.29). The value of x_D is only of significance for very large modulation index x and for very large total atomic phase shifts φ_a . The total atomic phase shift is very small for the near resonance dispersion and this correction is hence not of importance in this near resonance detuning region which is the main focus of this work. The correction due to x_D is also very small for large detuning but the corrections are included for completeness in the analysis presented in Chap. 6.

Finally, it should be mentioned that different variations of the NICE-OHMS technique were developed during this work. These variations are presented later in Sec. 6.1.2 and Sec. 6.2.1.

Outlook

The most basic concepts of the experimental techniques used in this work have been presented in this chapter. A substantial emphasis has been put on a detailed description of the NICE-OHMS technique, as this technique constitutes an essential part of the main spectroscopic experiments described in Chap. 6.

These experimental techniques presented in this chapter will prove valuable in the following chapter, which presents the experimental systems developed for this work.

CHAPTER



EXPERIMENTAL SYSTEMS

This section presents the main experimental systems developed and used in this work in order to perform the non-linear spectroscopy experiments described in Chap. 6. Section 5.1 describes the developed laser systems, while Sec. 5.2 describes the trapping of ^{88}Sr atoms and the two cavity systems developed for cavity enhanced spectroscopy. Most of the basic experimental concepts presented in this chapter have been described in the previous Chap. 4. It is recommended to read this chapter if the reader is not familiar with some of the experimental concepts during the reading.

The majority of the systems described in Sec. 5.1–5.2.2 were developed or initiated by Philip G. Westergaardⁱ, while the finalization and operation were carried out in this work.

5.1 Laser systems

The main focus of this work is to study the dynamics of laser cooled ^{88}Sr atoms placed inside an optical cavity. All laser wavelengths required for these studies are in the visible range and direct lasing at these wavelengths are to some extend achievable with diode lasers. However, complete laser systems were either not commercially available or not available within the financial framework for this work and all laser systems were homemade. This following section presents these laser systems developed in this work.

ⁱCurrent affiliation: Danish Fundamental Metrology, Matematiktorvet 307, 1. sal, 2800 Kgs. Lyngby, Denmark

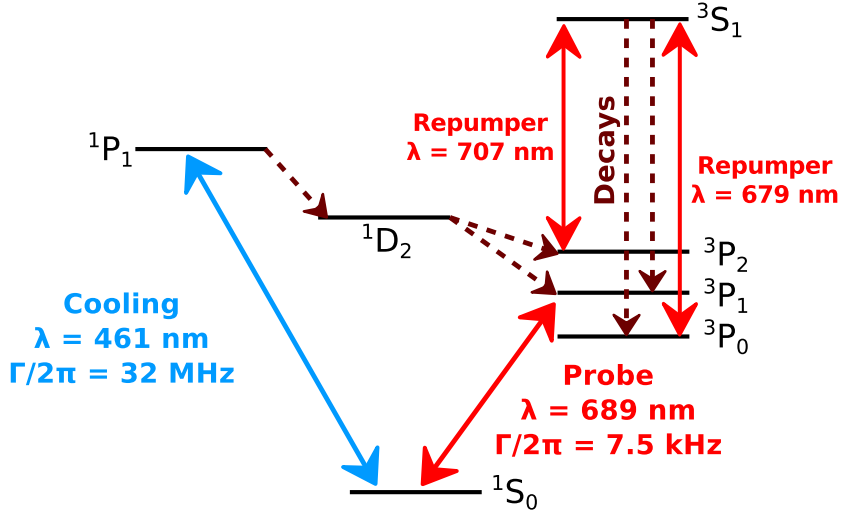


Figure 5.1: Electronic level scheme for ^{88}Sr showing the relevant transitions for this work. All arrows are transitions driven by lasers in the main experiment, while the dashed lines are decay channels.

Figure 5.1 shows the transitions of ^{88}Sr relevant for this work. The strong dipole-allowed $^1\text{S}_0 \rightarrow ^1\text{P}_0$ transition at 461 nm is used for laser cooling of the atoms in a MOT. However, this transition do not constitute a perfect two-level system as a minor decay channel to the $^1\text{D}_2$ state is present. The atoms may decay further from the $^1\text{D}_2$ state to the $^3\text{P}_1$ and $^3\text{P}_2$ states. The decay to the $^3\text{P}_1$ is not a problem, as this state decays further down to the ground state ($^1\text{S}_1$) with a relatively short life time of approximately 21 μs . Atoms decayed into the $^3\text{P}_2$ state on the other hand, will stay in this state for all relevant time scales, as the lifetime of the $^3\text{P}_2$ state is about 520 s [Yasuda and Katori, 2004]. This process is called *shelving* of atoms in the $^3\text{P}_2$ state as atoms are left in this state and lost from the MOT. Two repumping transitions can be exploited in order to reduce this shelving loss. The $^3\text{P}_2 \rightarrow ^3\text{S}_1$ transition at 707 nm can be used to excite the atoms in $^3\text{P}_2$ up to $^3\text{S}_1$. The atoms decay from here to the $^3\text{P}_1$ or $^3\text{P}_0$ state. The $^3\text{P}_1$ decays once again to the ground state, while the $^3\text{P}_0$ state is long lived. A second repumping transition, $^3\text{P}_0 \rightarrow ^3\text{S}_1$ at 679 nm can be applied to return the atom to the $^3\text{S}_1$ from where it can decay to the ground state. Note, that a repumping laser at 679 nm will only reduce the shelving loss, if another repumping laser at 707 nm is present.

The narrow ($\Gamma/2\pi = 7.5 \text{ kHz}$) $^1\text{S}_0 \rightarrow ^3\text{P}_1$ transition is the transition

of main interest in this work. This transition is coupled strongly to the fundamental mode of optical cavity systems and interrogated by a resonant intra-cavity field in the bad-cavity regimeⁱⁱ. The laser system for interrogating this transition is henceforth denoted *the clock laser* or the *the probe laser*. Note, that the ultranarrow $^1\text{S}_0 \rightarrow ^3\text{P}_0$ transition (transition linewidth: $\sim 1\text{ mHz}$, see Fig. 5.1) is used as the reference transition for conventional optical lattice clocks based on strontium atoms and the term *clock laser* is very often used for the 698 nm laser for interrogating this transition.

In conclusion, four laser systems were used for this work: a cooling laser at 461 nm, a laser system at 689 nm for interrogating the narrow $^1\text{S}_0 \rightarrow ^3\text{P}_1$ transition and two repumping lasers at 707 nm and 679 nm. The cooling laser and the clock laser are described in details in the following sections. After this, the repumping lasers are also described briefly.

It might be appropriate to consider Fig. 5.1 once more before venturing to the details of the laser systems. The unique feature of the level structure of strontiumⁱⁱⁱ is that the required wavelengths are to some extend commercially available. The other candidate elements for optical atomic clocks such as Hg [Yamanaka et al., 2015, ?], Yb [Hinkley et al., 2013, Nemitz et al., 2016] and Mg [Kulosa et al., 2015] all require less accessible wavelengths, which heighten the technological requirements. A great amount of strontium related knowhow and techniques have been developed [Norcia and Thompson, 2016b, Targat et al., 2005, Shimada et al., 2013]^{iv} around the world since the strontium based optical lattice clocks was proposed [Katori, 2001]. This availability and the maturing of the technology might be some of the arguments for a redefinition of the second based on strontium atoms in the future.

5.1.1 The 689 nm probe laser

A frequency stabilized *Littman-Metcalf* configuration external cavity diode laser (ECDL, described in Sec. 4.2) laser system was developed in order to probe the $^1\text{S}_0 \rightarrow ^3\text{P}_1$ transition shown in Fig. 5.2. The main task of the clock laser in our system is to perform cavity enhanced spectroscopy on the doppler broadened $^1\text{S}_0 \rightarrow ^3\text{P}_1$ transition and to resolve the central doppler free saturated absorption feature (marked with a dashed circle in Fig. 3.3).

ⁱⁱThis bad-cavity regime is described in details in Chap. 2.

ⁱⁱⁱThe level structure of the fermionic ^{87}Sr is slightly more complicated due to the nuclear spin.

^{iv}These cited works are only a small selection of technical papers relevant for experiments with ultracold strontium.

The spectral width of this saturation absorption feature can ultimately be in the same order as the natural linewidth of the interrogated transition. A clock laser linewidth narrower than this natural transition linewidth is hence desired. In addition, it was previously predicted in Sec. 3.4.2 that the probing powers in the 10–1000 nW range was optimal for laser stabilization. Based on this, it was evaluated that about $\sim 2\mu\text{W}$ probing power was required with the coupling efficiency of the cavity taken into account. The requirements for this laser system are hence:

- A spectral linewidth narrower than the natural linewidth of the $^1\text{S}_0 \rightarrow ^3\text{P}_1$ transition, $\Gamma/2\pi = 7.5 \text{ kHz}$.
- Lasing wavelength of 689 nm with tuning range of $\pm \sim 10 \text{ MHz}$ around the transition resonance.
- $2\mu\text{W}$ optical power coupled to the atom-cavity system.

Figure 5.2 shows the ECDL based laser system developed in order to fulfill the above mentioned requirements. The narrow linewidth is achieved by stabilizing the frequency of this laser system to an *Ultra Low Expansion* (ULE) cavity and the wavelength is controlled by a number of *Acousto Optical Modulators* (AOM) in order to achieve the resonance frequency of the investigated transition. In addition, the available optical power is amplified by injection locking a slave diode. These components of the total probe laser system are described in details in the following sections.

Frequency stabilization

The probe laser frequency was stabilized by using an ULE cavity as a stable frequency reference. This was done in order to achieve a laser linewidth, which was narrower than the natural linewidth of the probed transition ($\Gamma/2\pi = 7.5 \text{ kHz}$) such that the spectroscopic features studied in this work could be resolved. A typical temperature- and current stabilized ECDL system has a spectral linewidth in the order of few MHz. This linewidth was too broad for the spectroscopy experiments and the probe laser was frequency stabilized relative to the ULE cavity in order to reduce the linewidth down to $< 7.5 \text{ kHz}$.

The frequency stabilization was performed using the previously described *Pound-Drever-Hall* (PDH) laser stabilization technique (described in Sec. 4.5.2). The specific setup for this PDH stabilization is shown in Fig. 5.3. Two sidebands were applied to the probe laser spectrum by applying a periodic phase modulation with modulation frequency

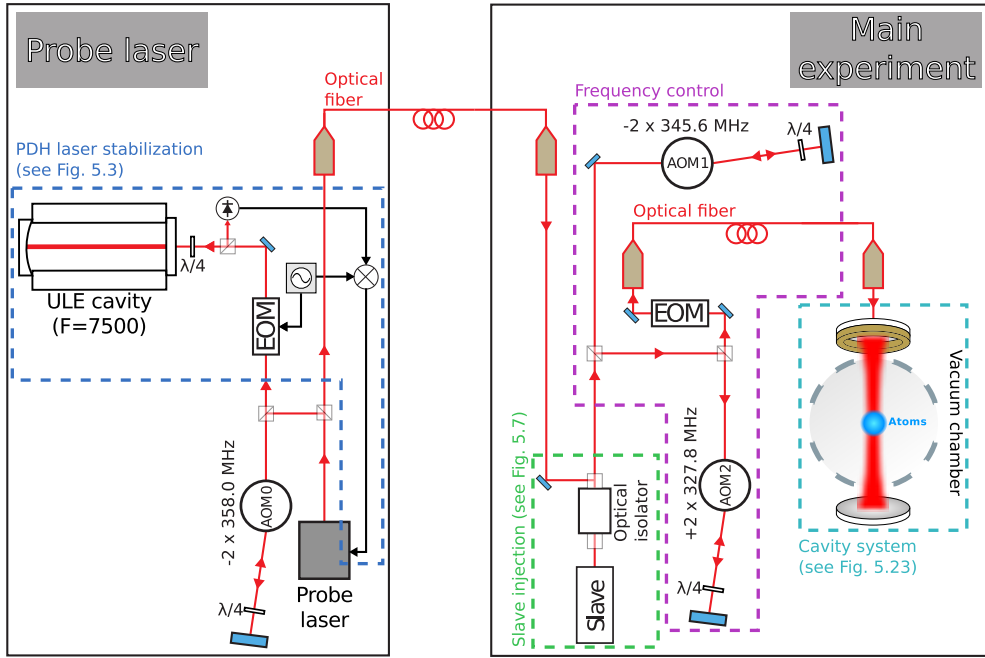


Figure 5.2: *Overview of the probe laser system. All free space optical paths are red, while electrical signal paths are black. The probe laser system is distributed over two optical breadboards illustrated by the black boxes (marked as Probe laser and Main experiment). AOM2 (AA Optoelectronic, MT330-B20A0,2-800) is an AOM with anti-reflect coating for 689 nm, while AOM0 and AOM1 are similar AOM models but with coatings not optimized for 689 nm. The AOM configuration on the Main experiment table is modified in some of the experiments described in Sec. 6 and 7.*

$\omega_{\text{mod}}/2\pi = 10 \text{ MHz}$. The initial frequency component of the clock laser is henceforth called *the carrier*. Figure 5.4b) shows the clock laser spectrum with the sidebands and the carrier. This light was coupled into an ULE cavity and the reflected light was detected by a photo detector. The carrier was only reflected and detected by the photo detector, when the probe laser was off-resonant with the ULE cavity. A $\lambda/4$ -plate was placed before the cavity, such that most of the reflected light was redirected to the photo detector through a *polarisation beam splitter* (PBS). This photo detector signal was mixed with the phase modulation frequency ω_{mod} through a *Double Balanced Mixer* (DBM or *mixer*). This mixed signal acted as an error signal for the laser stabilization of the probe laser. Figure 5.4a) shows a

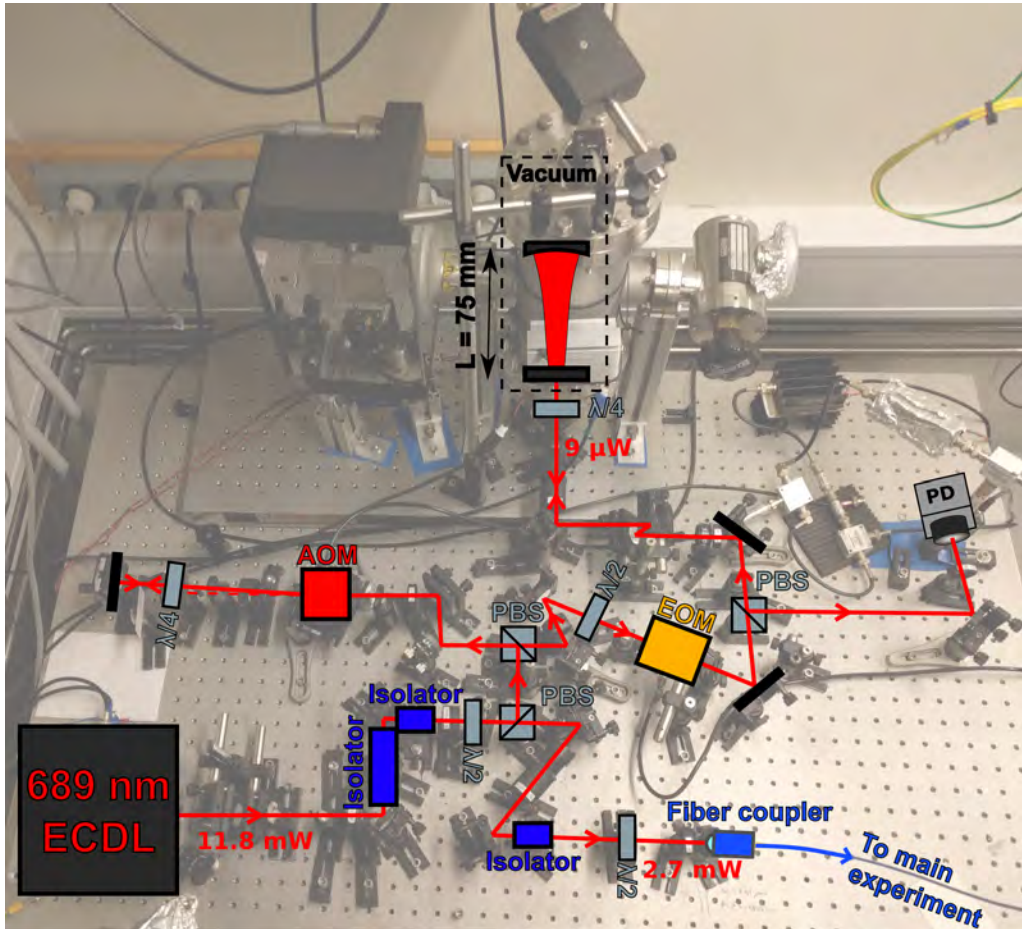


Figure 5.3: Detailed overview of the probe laser breadboard in Fig. 5.2. The background picture is a picture of the actual system. An ECDL based 689 nm master laser is frequency stabilized on a 75 mm long ULE cavity by using the PDH scheme (described in Sec. 4.5.2). About 2.7 mW stabilized light is sent through an optical fiber and about 1.3 mW light is received on the main experiment bread board.

frequency scan of this optimized error signal measured by scanning the probe laser frequency. The red solid line in Fig. 5.4a) is a theoretical fit based on Eq. (4.10) and it is clear that the characteristics of the error signal is as expected from the description in Sec. 4.5.2.

The ULE cavity was placed inside a temperature stabilized vacuum chamber and the entire clock laser system was placed on a separate vibration isolating air-supported bread board. This bread board is shown

in Fig. 5.3. These efforts are done as vibrations and mechanical drifts of the ULE cavity would be manifested as frequency errors in the error signal. The length of the ULE cavity is 75 mm yielding a *Free Spectral Range* (FSR) of $\text{FSR}=2.0\text{ GHz}$. The finesse of the cavity is $F = 7500$ corresponding to a cavity linewidth of about 270 kHz. A fraction of this linewidth can be expected for the linewidth of a laser stabilized to this cavity.

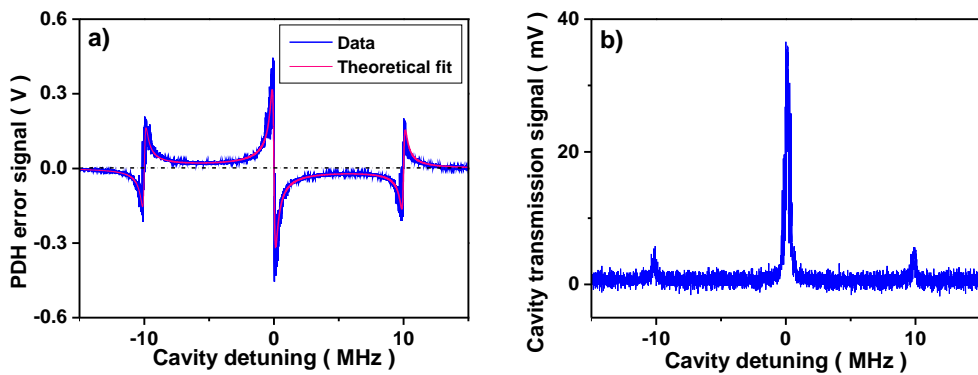


Figure 5.4: *PDH error signal and cavity transmission during scan of laser frequency. Blue solid lines are experimental data while the red solid line is an experimental fit. Sidebands are applied by periodic phase modulation at 10 MHz, which yield sidebands placed 10 MHz from the carrier frequency. The horizontal axis is calibrated by using this well known sideband spacing.*

Figure 5.5a) shows the PDH error signal during laser stabilization. Such an error signal is a measure of the frequency detuning of the clock laser relative to the ULE cavity resonance. This error signal is hence converting the frequency noise of the clock laser to a voltage signal. This frequency-to-voltage conversion factor was evaluated by determining the linear slope around resonance of the error signal in Fig. 5.4a). The horizontal axis in Fig. 5.4a) was needed to be calibrated to Hz for determining this slope. This was done by using the well known sideband spacings $\omega_{\text{mod}}/2\pi = 10\text{ MHz}$. This conversion factor was then applied to convert the vertical axis of Fig. 5.5a) to Hz, such that Fig. 5.5a) shows the probe laser frequency noise in time domain. This can be used to calculate the Allan deviation σ through Eq. (1.1). Figure 5.5b) shows this Allan deviation calculated for different integration times τ . This Allan deviation in Fig. 5.5b) shows, that a sub 10 Hz linewidth can be achieved for integration times below 1 s. The probe laser interrogates the atom-cavity system for about 100 μs in the main

spectroscopy experiments of this work described later in Sec. 6. Figure 5.5b) shows a probe laser linewidth of about 800 Hz for timescales relevant for the spectroscopy experiments. This linewidth is hence sufficient for resolving the spectroscopic details of the studied system as this linewidth is significantly narrower than the natural linewidth of the interrogated transition, $\Gamma/2\pi = 7.5$ kHz.

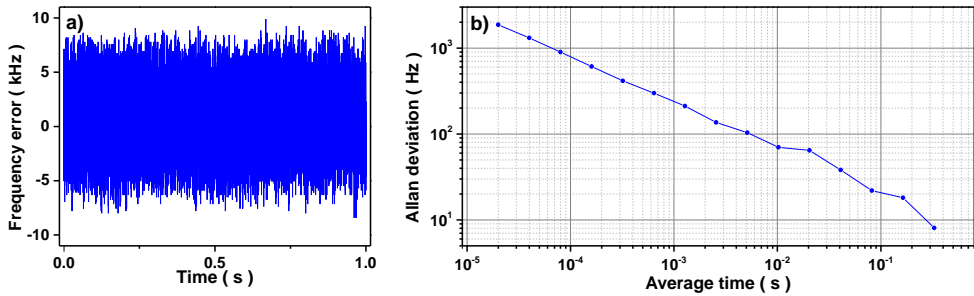


Figure 5.5: Same data also presented in [Henriksen, 2014]. a) Error signal during lock of probe laser on the ULE reference cavity. The vertical axis is calibrated to frequency error by assuming a linear slope around resonance for the error signal shown in Fig. 5.4a). b) Allan deviation for the probe laser based on the in-loop error signal during lock.

Frequency control

The frequency of the probe laser is stabilized as described in the above section by using an ULE cavity as a frequency reference. However, the ULE cavity is man-made and the resonance frequency is unlike the atomic transition frequencies not absolutely defined. The resonance frequency of an optical cavity with a fixed length is thus most likely not identical with the relevant atomic transition. In addition, the resonance frequency of the ULE cavity will drift in time due to aging effects. A system for controlling the clock laser frequency was hence needed.

The ULE cavity resonance frequency ω_{ULE} was detuned about -680.4 MHz from the ${}^1\text{S}_0 \rightarrow {}^3\text{P}_1$ transition frequency ω_0 , $\omega_{\text{ULE}} = \omega_0 - 2\pi \cdot 680.4$ MHz. The emission frequency ω_{probe} of the clock master laser is detuned 2×358 MHz from this cavity resonance by a double pass AOM setup as illustrated in the *Probe laser* part in Fig. 5.2. This laser frequency of the probe laser is hence $\omega_{\text{probe}} = \omega_0 + 2\pi \cdot (680.4 \text{ MHz} - 2 \times 358 \text{ MHz}) = \omega_0 + 2\pi \cdot 35.6 \text{ MHz}$, and this frequency is transferred over to the main experiment table though

an polarization maintaining (PM) optical fiber. Here, the transferred probe laser frequency is modulated further by two double pass AOM setups (AOM1 and AOM2 shown in Fig. 5.2) resulting in the final probe laser frequency $\omega_l = \omega_0 + 2\pi \cdot (35.6 \text{ MHz} - 2 \times 345.6 \text{ MHz} + 2 \times 327.8 \text{ MHz}) = \omega_0$. This probe laser frequency is now resonant with the $^1S_0 \rightarrow ^3P_1$ transition and the light is transferred to the main experiment through another PM fiber.

While the modulation frequencies and RF powers are held constant for AOM0 and AOM1 shown in Fig. 5.2, AOM2 is controlled by a computer and it is used for controlling the relative detuning of the probe laser frequency and the atomic resonance frequency. The RF modulation power of AOM2 is also controlled in order to keep the optical power constant in the main experiment as strain and temperature variations in the PM fiber before the main experiment can cause intensity fluctuations on the probing light.

Slave injection

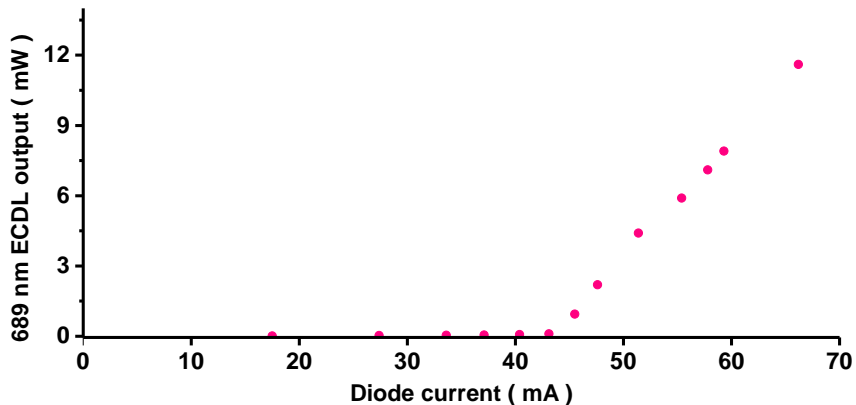


Figure 5.6: Output characteristics of the 689 nm probe laser ECDL.

The output characteristics of the clock master laser is shown in Fig. 5.6. The typical operation output power of the probe laser ECDL was about 11.8 mW. A fraction of this optical power was redirected for the PDH frequency stabilization. The rest of the optical power was coupled twice to optical fibers and frequency shifted twice in double pass AOM setups (AOM1 and AOM2 in Fig. 5.2). All these processes caused losses in optical power and the direct output of the probe laser ECDL was not sufficient for the power requirements of the main experiment.

This need for more optical power was overcome by *injection locking* of a slave laser with the stabilized clock master laser. A relatively weak master laser can be sent into an already lasing slave laser. The master laser will then be amplified by the gain medium of the slave laser if the master laser frequency is within the gain bandwidth of the slave laser and if the spatial beam mode of the injected master laser matches the lasing mode of the slave laser. The master laser frequency will then dominate the slave laser emission if the amplified master laser intensity exceeds the slave laser intensity [Nagourney, 2014, p.209]. The spectral properties of the master laser is for all relevant purposes copied exactly by the slave laser. A slave laser injection locked by the probe laser described in this section will hence keep the frequency stability of the probe laser as shown in Fig. 5.5b). Note that the achievable output power level for injection locking is limited by the maximum output power of the slave diode and it can not provide high power outputs (~ 1 W) as tapered amplifiers described later in Sec. 5.1.2.

About 1.3 mW of the stabilized probe laser is injected into a slave diode trough one of the polarization beam splitters of a Faraday isolator. This setup is shown in Fig. 5.7. The intrinsic spatial beam mode of the slave laser is elliptical, however circular Gaussian beam modes with long Rayleigh lengths are desired for the AOM configuration described previously in this section. The beam mode of the slave laser is hence corrected by a pair of cylindrical lenses. The spatial mode of the master laser beam is then matched to the corrected slave laser mode. It is assured that only the master laser frequency is directed to the main experiment by filtering the injected slave laser beam with an *interference filter* (IF filter), which transmits the master laser frequency and blocks the slave laser frequency^v. The gain spectrum of the slave laser diode, which depends on the diode current, needs to match the injected laser spectrum in order to achieve injection locking. Hence, the amplification of the injected probe laser dominated the entire slave laser emission for a span of the slave diode current. Figure 5.8 shows the IF filter transmitted slave laser output when the slave laser current is modulated periodically. A significant increase in the output power is observed when the master laser is injected and a flat *plateau* indicates that the gain medium of the slave laser is entirely dominated by the injected probe laser for slave diode current span within this plateau. A wide plateau will hence lead to stable operation of the injected slave laser. The width of this plateau was hence optimized by optimizing the mode overlap of the master- and slave laser

^vThis IF filter is in principle not necessary if the slave injection is conducted properly, but it is a great tool when constructing and optimizing the injection setup.

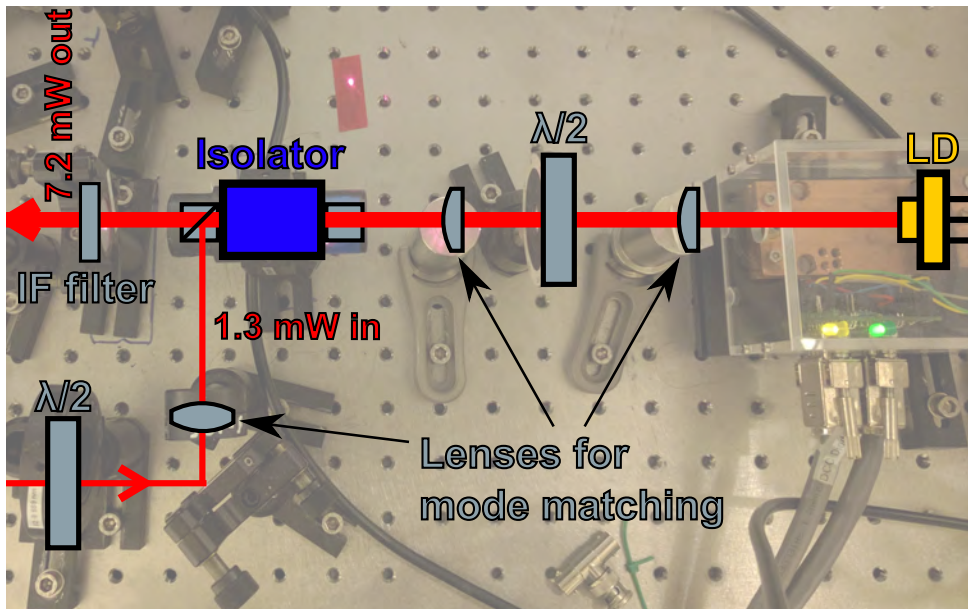


Figure 5.7: Detailed overview of the slave laser system (also shown in Fig. 5.2). The background picture is a picture of the actual system. About 1.3 mW of the frequency stabilized light from the master laser was injected into a slave diode through one of the PBS cubes of an Fararay optical isolator. The slave diode output was sent through an interference filter (IF filter) in order to filter out unwanted frequency components from the slave diode. The IF filter was convenient during optimization of a slave injection but it was in principle unnecessary if the injection is done properly.

and by optimizing system parameters such as slave diode current and temperature. Finally, a total injection locked slave laser output of 7.8 mW was obtained for the main experiment.

This injected slave laser output delivers ultimately $1 - 10 \mu\text{W}$ to the atom-cavity system, which is sufficient for the main experiment. The exact amount of optical power delivered to the cavity-atom system depends on the two different EOM configurations presented later in Sec. 5.2.2. A significant fraction of the optical power was however lost in the AOM setups shown in Fig. 5.2 due to insufficient correction of the slave laser beam shape. This has resulted in astigmatism which has limited the deflection efficiencies of the AOMs. Improvements of these AOM deflection efficiencies can be expected if the slave laser beam shape correction can be improved possibly by implementing a pair of anamorphic prisms for beam shaping instead of the pair of cylindrical lenses. Such interventions would

however require significant modifications of the entire AOM configuration for the main experiment.

It should also be noted that only AOM2 (shown in Fig. 5.2) is anti-reflect coated for 689 nm and some of the optical power loss might be attributed to the wrong coating on AOM0 and AOM1. However, this does most likely not change the fact, that the main reason for the low AOM efficiencies is attributed to the astigmatism.

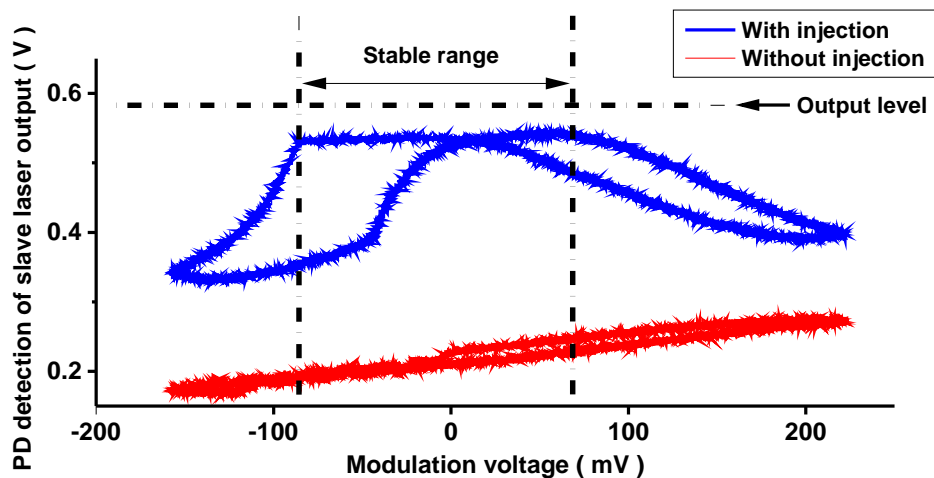


Figure 5.8: *Output power of the slave diode injected by the frequency stabilized probe master laser. The slave diode current was modulated by an external modulation signal. The horizontal axis shows this modulation signal. Hysteresis is observed during scan, however the slave laser output was stable roughly over the entire flat plateau, when the laser current was kept constant. Typical operation parameters are: $I_{\text{slave}} = 77 \text{ mA}$ and $T_{\text{slave}} = 22.7^\circ\text{C}$.*

In conclusion, an ECDL based probe laser system was developed. The lasing frequency of this probe laser system was controlled by a configuration of several AOMs leading to a tunable lasing frequency resonant with the ${}^1\text{S}_0 \rightarrow {}^3\text{P}_1$ transition of ${}^{88}\text{Sr}$. The probe laser system consists of an ECDL system and a spectral linewidth narrower than the natural linewidth of the ${}^1\text{S}_0 \rightarrow {}^3\text{P}_1$ transition was achieved by frequency stabilization with respect to an ULE reference cavity. Finally, the optical power of this clock laser system was increased to the required level by injection locking a slave laser.

5.1.2 The 461 nm cooling laser

The cooling and trapping of ^{88}Sr is performed in this work by realizing a *magneto-optical trap* (MOT) as described in Sec. 4.4. The strong $^1\text{S}_0 \rightarrow ^1\text{P}_1$ transition at 461 nm was used for this MOT. This following section describes the 461 nm cooling laser system developed for this purpose.

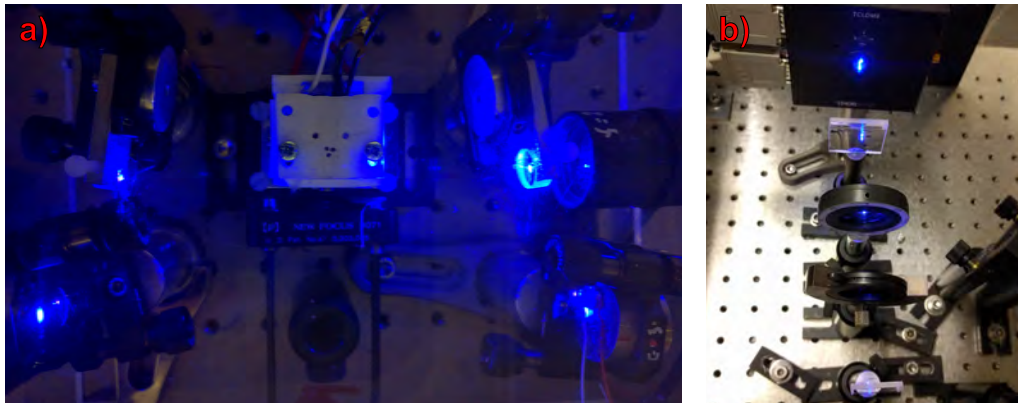


Figure 5.9: Pictures of optical systems for generating light at 461 nm for laser cooling. a): Ring cavity for cavity enhanced SHG of light at 922 nm to 461 nm. b): NICHIA NDB4216E laser diode at 461 nm for injection locking. This system is under preparation.

The linewidth of this transition is $\Gamma_{\text{MOT}} = 32$ MHz and the linewidth of the cooling laser is required to be narrower than Γ_{MOT} . This transition linewidth do also limit the lower temperature T_D achievable with a MOT to $T_D = 0.8$ mK following Eq. (4.7). Cooling and trapping with solely the $^1\text{S}_0 \rightarrow ^1\text{P}_1$ transition is often referred as *single stage cooling*, as temperatures below T_D can be achieved by performing a *second stage cooling* by extending the cooling scheme using the much narrower $^1\text{S}_0 \rightarrow ^3\text{P}_1$. Only the single stage cooling will be addressed in this work.

The transition wavelength of the single stage cooling on the $^1\text{S}_0 \rightarrow ^1\text{P}_1$ transition is 461 nm. Frequency doubling by SHG (described in Sec. 4.3) of a near infrared 922 nm laser has been a widely used technique in many previous works [Targat et al., 2005] for obtaining sufficient light at this wavelength. This technique was also used for generating the cooling light in this work. Figure 5.9a) shows a picture of the light at 461 nm generated by SHG.

Single mode blue laser diodes at 461 nm have nevertheless become commercially available the recent years. Injection locking of such diodes seems as a simple and promising alternative to the frequency doubling

[Shimada et al., 2013]. Injection locking of a blue laser diode is also under preparation for future experiments related to this work. Figure 5.9b) shows a picture of injection locking setup under preparation.

The requirements for the cooling laser linewidth are not as severe as for the clock laser (described in Sec. 5.1.1). However, the cooling laser frequency is required to be stable within the $^1S_0 \rightarrow ^1P_1$ cooling transition linewidth in order to keep the shot-to-shot number of trapped atoms stable. Furthermore at least about ~ 30 mW of the 461 nm cooling light has to reach the atoms in order to trap enough atoms for the main experiment. It is hence evaluated that generation of around 100 mW optical power of the 461 nm light will be convenient for the experiment. The requirements for this cooling laser system are hence:

- Lasing wavelength of 461 nm.
- A long term stability and accuracy of the laser frequency within the natural linewidth of the $^1S_0 \rightarrow ^1P_1$ transition, $\Gamma_{\text{MOT}}/2\pi = 32$ MHz.
- Generation of about 100 mW optical power at 461 nm.

Figure 5.10 shows the overview of the laser system for generating the cooling light at 461 nm and for fulfilling the above mentioned requirements. The 461 nm wavelength is achieved by frequency doubling and the optical power of the fundamental 922 nm light is amplified in a *Master Oscillator Power Amplifier* (MOPA). The long term stability is finally achieved by stabilizing the laser to a thermal strontium beam as reference. All mentioned components of this cooling laser system are described in details in the following sections.

The 922 nm light source

An *Littrow* configuration ECDL (described in Sec. 4.2) laser system was developed for lasing at 922 nm. The output characteristics of this 922 nm ECDL is shown in Fig. 5.11. The typical operation power output of this ECDL is about 17.5 mW. This output power is far below the required optical power for the MOT as the SHG efficiency is limited. This output power of the ECDL is limited by the damage threshold intensity of the small area active gain medium of the single mode diode (Eagleyard, EYR-RWE-980) used in the ECDL. The light emitted from the ECDL can however be amplified by sending the light through a *tapered diode* with a large gain area. This large area diode is anti-reflection coated at each end such that no unwanted lasing will occur, when no light is sent through the diode. The gain region of this diode is tapered such that the area of the

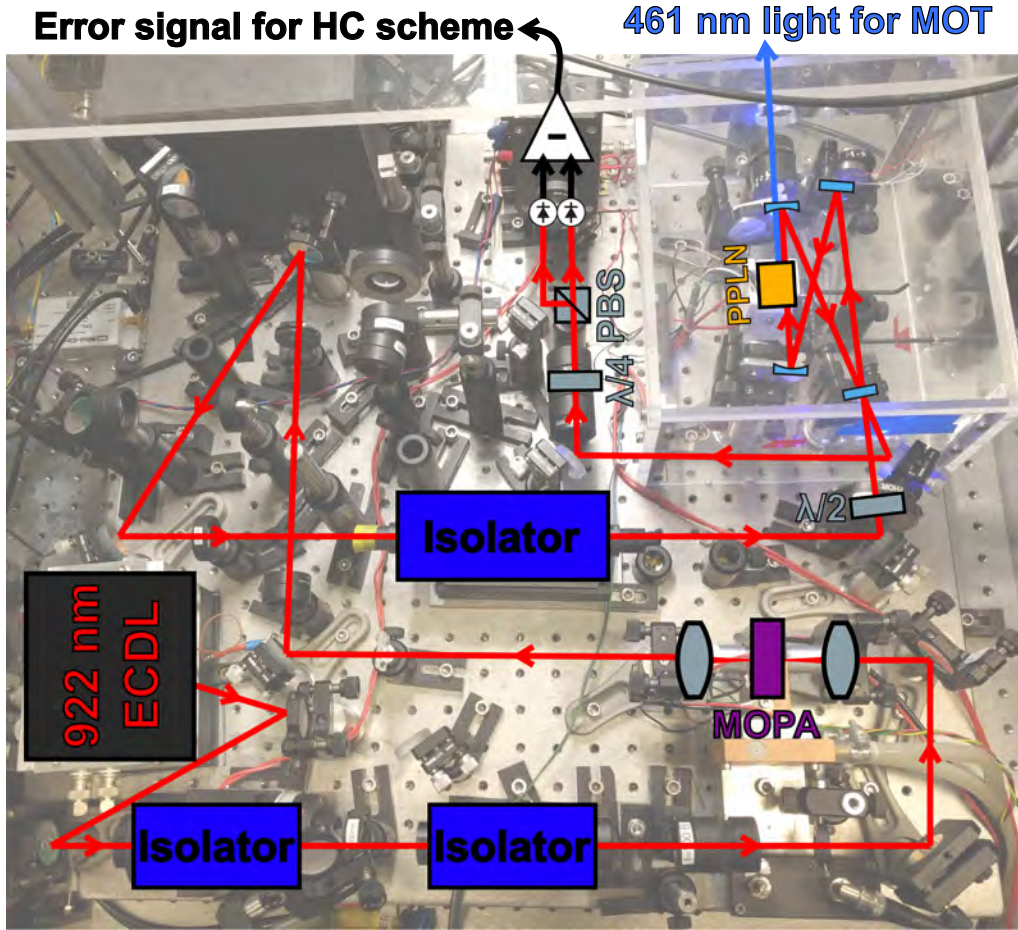


Figure 5.10: Detailed overview of the laser system for generating light at 461 nm for laser cooling. The background picture is a picture of the actual system. The output power of an ECDL system at 922 nm is amplified in a MOPA. The amplified light is frequency doubled to 461 nm by cavity enhanced SHG with a PPKTP crystal (delivered by Raicol Crystals) with anti reflect coated surfaces placed inside a ring cavity. The doubling cavity is kept on resonance with the input light by employing the HC locking scheme (described in Sec. 4.5.1) and by controlling the position of one of the cavity mirrors with an piezo electric element. About 78 mW light at 461 nm is typically generated. Typical operation parameters are: $I_{922\text{ nm, diode}} = 112.5\text{ mA}$, $T_{922\text{ nm, diode}} = 16.63^\circ\text{C}$, $T_{\text{ECDL mount}} = 22.55^\circ\text{C}$, $I_{\text{MOPA}} = 2600\text{ mA}$, $T_{\text{slave}} = 21.38^\circ\text{C}$ and $T_{\text{PPLN}} = 52.71^\circ\text{C}$.

gain region is adiabatically increased as the beam diverges and the optical power is amplified by the gain. The total optical power is increased but

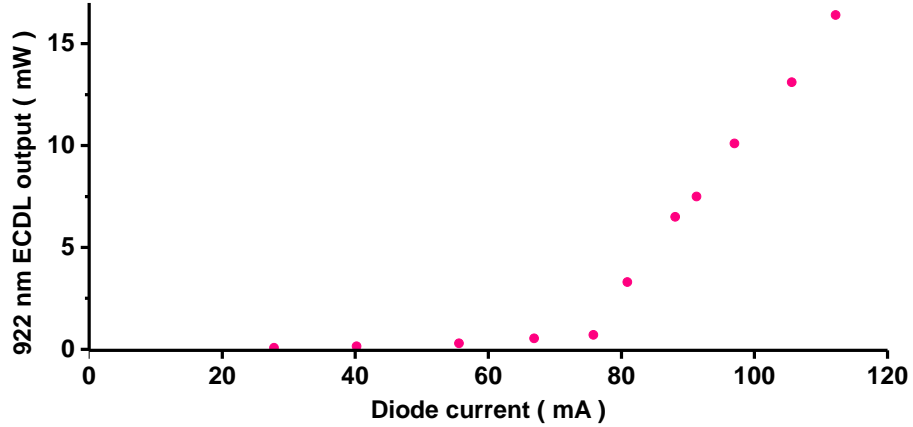


Figure 5.11: Output characteristics of the 922 nm ECDL.

the area of the beam profile is increased ensuring that the intensity will be below the damage threshold. A careful mode matching of the input beam mode and the shape of the tapered gain medium is essential for achieving optimal amplification. The output of this tapered diode will not be limited by the saturation of the active medium. The above mentioned properties allow the tapered diode to reach a higher output power than a small-area single mode laser diode [Nagourney, 2014, p.205].

The output of the realized 922 nm ECDL was focused down and mode matched to a tapered diode^{vi} as shown in Fig. 5.10. The output power characteristics of the tapered diode for 17.5 mW input power at 922 nm is shown in Fig. 5.12. The conversion efficiency from electrical to optical power is often limited for a MOPA system and heat will be dissipated in the tapered diode. The temperature T_{MOPA} of the tapered diode is hence cooled down to $T_{\text{MOPA}} = 21.38^\circ\text{C}$ by a peltier element. The heat from the hot side of the peltier element is conducted to a copper block and then guided away by a water based chiller system^{vii}. A stable power output of 930 mW was achieved for a tapered amplifier operation current of $I_{\text{MOPA}} = 2600 \text{ mA}$. See Fig. 5.12.

SHG Enhancement cavity

The 922 nm light amplified in the MOPA system was frequency doubled by SHG in a *Periodically Poled Potassium Titanyl Phosphate* (PPKTP) crystal.

^{vi}Eagleyard, EYP-TPA925

^{vii}Coherent, water chiller T251P

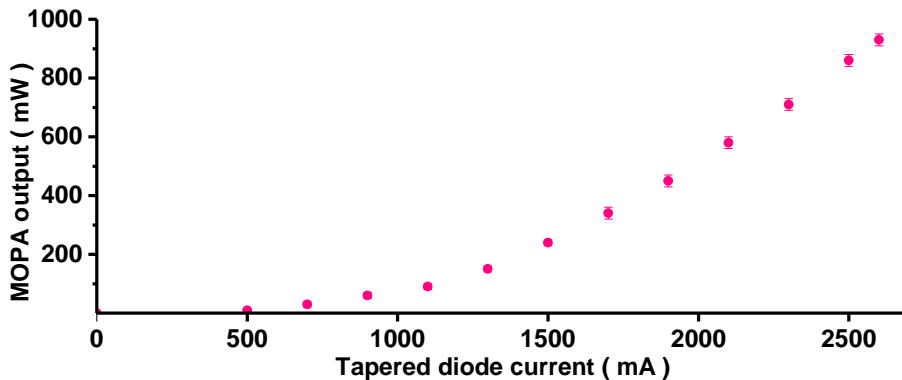


Figure 5.12: *Output characteristics of the MOPA system as function of the tapered diode current. The input power at 922 nm was 17.5 mW for all data points.*

The phase matching condition for the SHG was optimized in the PPKTP by periodical changes in the optical polarization axis of the PPKTP crystal. The single-pass SHG efficiency of this PPKTP is limited but the conversion efficiency was enhanced by placing the PPKTP crystal inside a ring cavity system as described in Eq. (4.6).

Figure 5.9a) shows a bow-tie ring cavity constructed for enhancing the SHG. This bow-tie cavity build up the intensity of the fundamental 922 nm light and increased the total frequency doubled optical power. The first cavity mirror after the PPKTP crystal was anti-reflect coated for 461 nm and the frequency doubled light was transmitted to the main experiment.

The dimensions of the bow-tie cavity were designed such that a mode waist was present inside the PPKTP crystal. The SHG efficiency was optimized by careful cavity mode matching of the in-coupled fundamental beam mode and optimization of the cavity finesse, such that the interaction of the fundamental light and the PPKTP crystal was enhanced. The phase matching was optimized by careful optimization of the relative angle between the optical axis of the PPKTP crystal and the polarization of the intra cavity fundamental light.

The phase matching condition was furthermore optimized by heating the PPKTP temperature to $T_{\text{PPKTP}} = 52.72^\circ\text{C}$. The PPKTP crystal was clamped on a heated aluminum mount, which was shielded by a teflon cover while keeping the cavity mode unblocked. This heating was carried out by a two-part temperature control system. Firstly, the PPKTP crystal mount was heated by a DC loaded heater. Secondly, the temperature

of the heated crystal mount was finely tuned and stabilized by a peltier element.

The cavity length needed to be stabilized in order to maintain the intensity build-up of the fundamental light and achieve a stable output from the cavity-enhanced SHG. The cavity length was controlled by a piezo-electric element mounted on one of the cavity mirrors and the HC stabilization scheme (described in Sec. 4.5.1) was used for this purpose. The PPKTP crystal is intrinsically birefringent and the cavity reflected light was hence suited for generating the polarization sensitive error signal in the HC scheme. Figure 5.13a) shows a clearly sign-sensitive HC error signal measured when the cavity length was scanned. A small fraction of the cavity transmitted frequency doubled light was monitored during the same scan and Fig. 5.13b) shows that this transmission power increases when the cavity resonance matches the input fundamental frequency.

External influences such as acoustic noise and air draft can disturb the stability of the cavity lock or ruin the phase matching condition by causing temperature instabilities. The bow-tie cavity was hence isolated from such external disturbances by being placed inside a plexiglass box. Efforts were furthermore put in the mirror mounting to increase the stability of the cavity lock by fixing the cavity mirrors on heavy copper mounts. These mounts are implemented as counter-weights to shift the mechanical resonance frequencies to higher frequencies, as mechanical resonances are ultimately limiting the bandwidth of the feedback system for cavity locking.

Figure 5.14 shows the output characteristics of the frequency doubled light at 461 nm. A quadratic conversion efficiency is observed as described in Sec. 4.3. An output power up to 78.4 mW of 461 nm light was achieved. This output power corresponds to a net conversion efficiency of about 10.5 %. Much higher conversion efficiencies have been reported [Targat et al., 2005] and improvements of the conversion efficiencies might possibly be expected by optimizations of the ratio ζ between the crystal length and the confocal length of the Gaussian cavity mode [Boyd and Kleinman, 1968]. Such an optimization procedure will, however, change the already established optical setup of the entire main experiment (described in Sec. 5.2) and must be conducted with care. The achieved output power is close to the desired power of ~ 100 mW, although room is left for improvement. It is described later in Sec. 5.2 that this amount of light at 461 nm is sufficient for performing spectroscopy experiments on the cavity-atom systems described theoretically in Chap. 3.

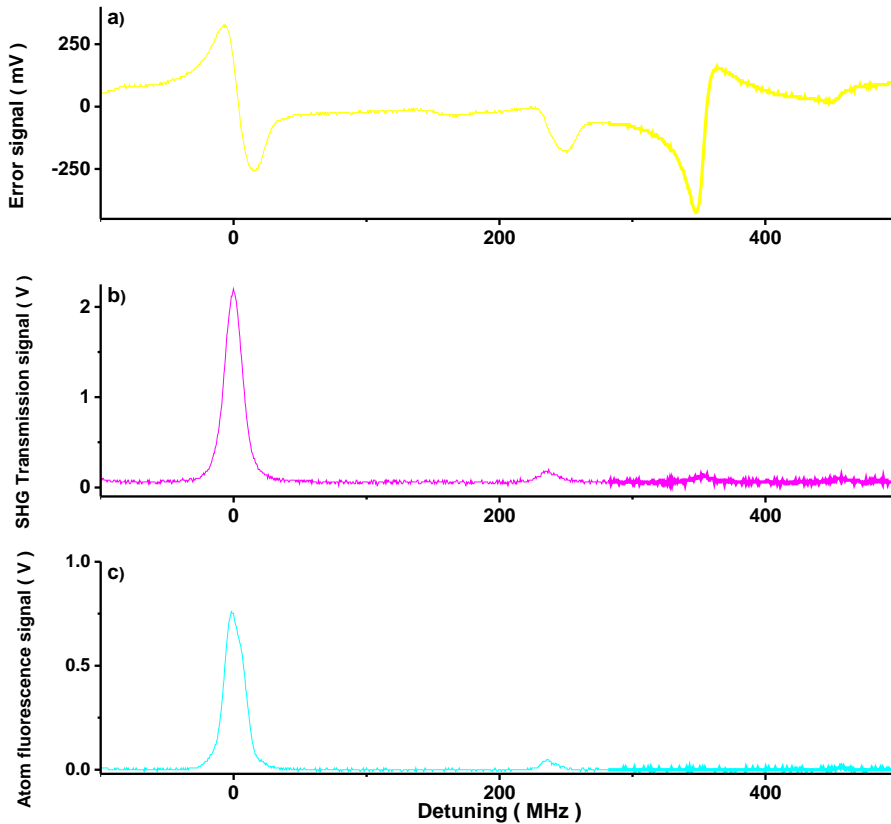


Figure 5.13: Relevant spectra for the 461 nm cooling laser during scan of the SHG cavity. The horizontal axis is calibrated by using the known FSR of the SHG cavity. a): error signal for the SHG cavity generated by using the HC stabilization scheme (described in Sec. 4.5.1). b): Output power of the SHG cavity detected by a photo detector. The small transmission peaks are due to imperfect mode matching of the input beam mode. c): Fluorescence signal from the reference oven (shown in Fig. 5.15). The 922 nm ECDL frequency was kept such that the light for probing the reference oven was near resonance of the $^1S_0 \rightarrow ^1P_1$ transition during the cavity scan.

Atomic reference

The final requirement for the cooling laser is a long term stability and accuracy of the laser frequency within the natural linewidth of the $^1S_0 \rightarrow ^1P_1$ transition, $\Gamma_{\text{MOT}}/2\pi = 32$ MHz. This requirement was fulfilled by locking the cooling laser frequency to an atomic reference. A thermal beam of Sr was prepared to $T = 520$ °C in an oven separated from the main

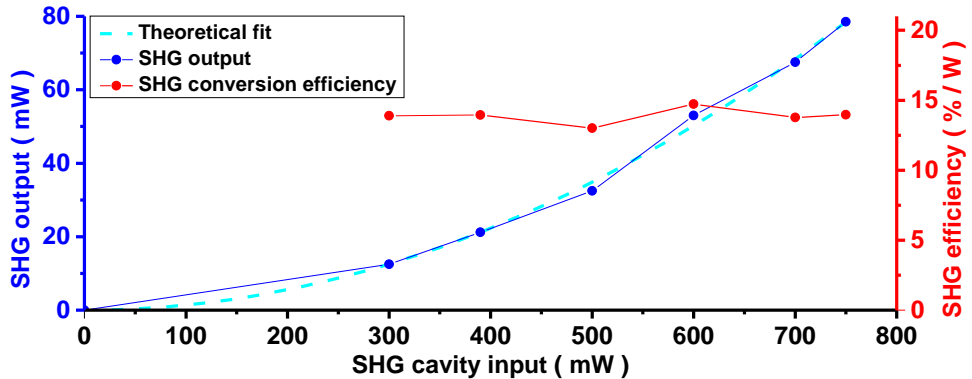


Figure 5.14: Blue: Output power at 461 nm as function of the input power at 922 nm. The dashed line is a quadratic fit, which confirms the quadratic behavior predicted in Eq (4.6). Red: Conversion efficiency as function of the input power. Note, that the conversion efficiency is shown in the units of %/W, which correspond to the units of the conversion efficiency γ in Eq (4.6).

experiment. The released thermal strontium gas was guided into a beam of Sr gas through $\varnothing 1 \sim 2$ mm pinholes. The schematic of this reference oven is shown in Fig. 5.15.

A fraction of the light at 461 nm (described previously in Sec. 5.1.2) was sent into this beam of strontium gas. This 461 nm light was aligned perpendicularly with the beam propagation axis and retro-reflected in order to enhance the interaction of the light and the atomic beam. The strontium atoms will spontaneously emit fluorescence at 461 nm if the input light is resonant with the $^1S_0 \rightarrow ^1P_1$ transition. This fluorescence was detected by focusing a fraction of the emitted fluorescence onto a *photo multiplier*. Figure 5.16a) shows the fluorescence signal measured for different detunings of the 461 nm light. Two distinguished peaks are visible in this fluorescence spectrum shown in Fig. 5.15a). The largest peak is due to the fluorescence of ^{88}Sr , while the minor peak is caused by ^{86}Sr . The emission lines of ^{87}Sr are located in between the two peaks. The fluorescence from these lines are however smaller due to the lower natural abundance and they are not straightforwardly visible in Fig. 5.16a). The frequency differences of the fluorescence from ^{88}Sr and ^{86}Sr is 124.8 MHz [Courtillot, 2003] and this value was used to calibrate the horizontal axes in Fig. 5.16.

The divergence of the strontium gas is kept down by the $\varnothing 1 \sim 2$ mm pinholes. The atomic velocity components are hence slowed down in the

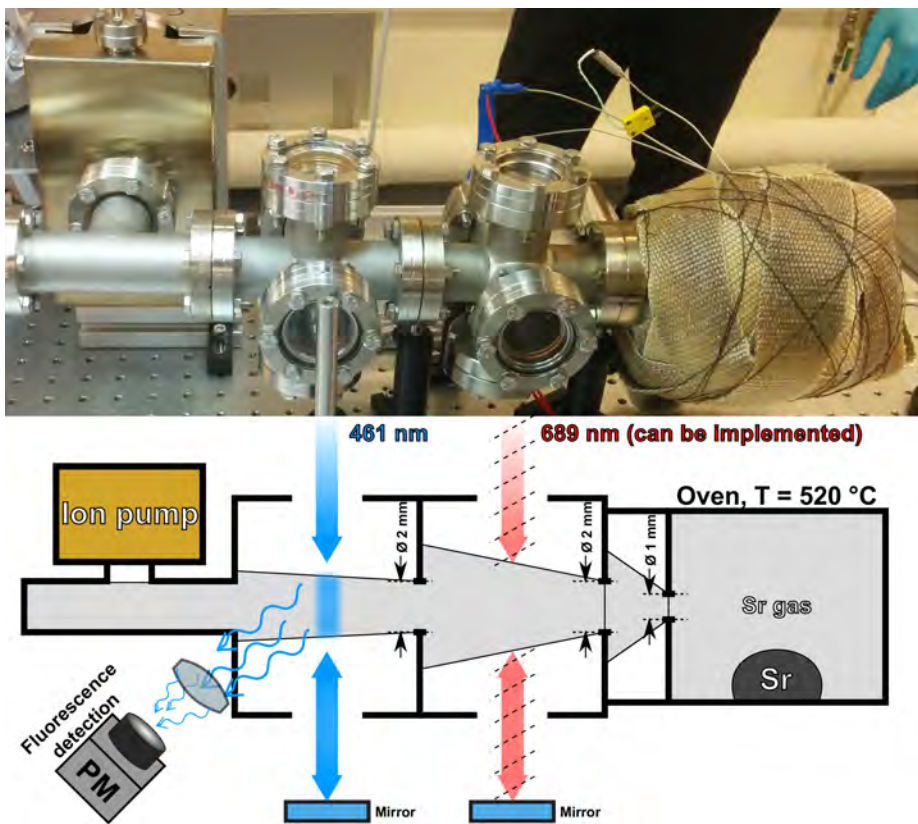


Figure 5.15: Top: Picture of the atomic reference oven. Bottom: Overview of the atomic reference oven construction. The individual parts of this setup are placed side by side the corresponding part on the picture above. View ports were also prepared for stabilization of the clock laser on the 689 nm $^1S_0 \rightarrow ^1P_3$ transition. This was used occasionally to confirm the clock laser frequency but it was not applied for frequency stabilization.

direction parallel with the 461 nm light. This results in a Doppler broadened fluorescence spectrum with a *Half Width Half maximum* (HWHM) below 50 MHz. This fluorescence spectrum can potentially serve as a reference for stabilizing the 461 nm laser within the natural linewidth ($\Gamma_{\text{MOT}}/2\pi = 32$ MHz) of the $^1S_0 \rightarrow ^1P_1$ transition.

A sign sensitive error signal was generated by using a lock-in amplifier. The lock-in amplifier applied a periodic modulation on the detuning of the 461 nm. The fluorescence was hence modulated too and detected by the photo multiplier. This fluorescence signal was then demodulated by the same modulation frequency and the resulting DC signal yielded a derivative-like lineshape shown in Fig. 5.16b). This signal can be used

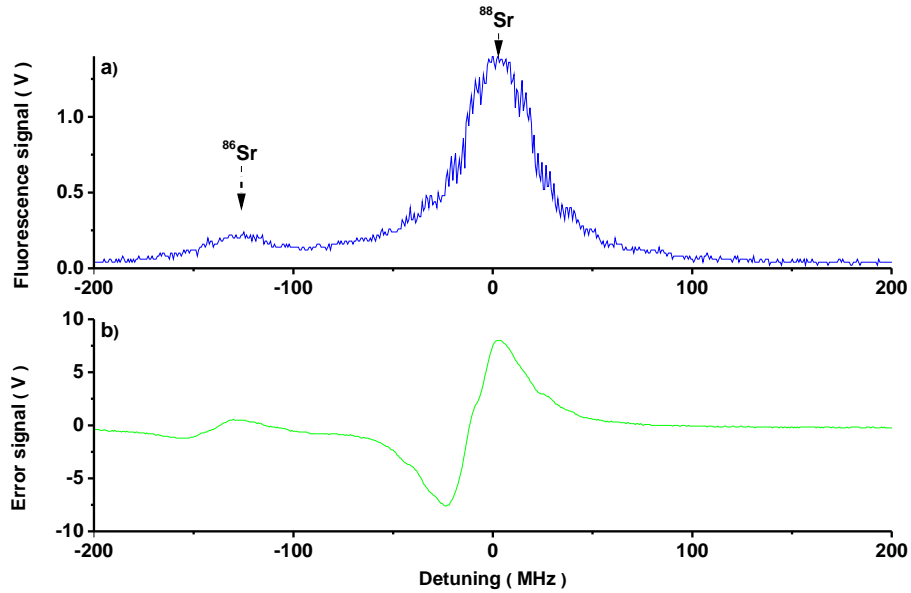


Figure 5.16: a): The fluorescence signal from the reference oven during frequency scan of the 461 nm cooling laser. Multiple fluorescence peaks are observed due to isotope shifts of the resonance frequencies for different isotopes of strontium. Frequency difference for the emission line of ^{88}Sr and ^{86}Sr has been used to calibrate the horizontal axes [Courillot, 2003]. b): Error signal generated by the lock-in amplifier for locking the cooling laser on the $^1\text{S}_0 \rightarrow ^1\text{P}_1$ transition. The signal-to-noise ratio of this signal is better than the fluorescence signal and some of the emission lines of ^{87}Sr might be weakly visible.

as an error signal. Note that the signal-to-noise ratio is clearly higher in Fig. 5.16b) compared to Fig. 5.16a). This is due to the bandpass filter in the lock-in amplifier which only allowed detection of noise components within a narrow bandwidth around the modulation frequency. Furthermore, the noise in this detection bandwidth was reduced by choosing a high modulation frequency as most technical noise spectrums decrease in amplitude for higher frequencies [Riehle, 2004, p.59]. The modulation frequency in this setup was 9.179 kHz.

A feedback loop was established to stabilize the cooling laser frequency by sending this error signal to the 922 nm master laser (described in Sec. 5.1.2). The diode current of the 922 nm ECDL was used as an actuator for frequency control in this case. Figure 5.17 shows the overview of this feedback system.

The cooling laser frequency was successfully locked uninterrupted for up to several hours by the above described feedback system. The

stabilized cooling laser was automatically near resonant with the cooling transition, as both the laser cooling and the frequency stabilization was performed on the ${}^1S_0 \rightarrow {}^1P_1$ transition.

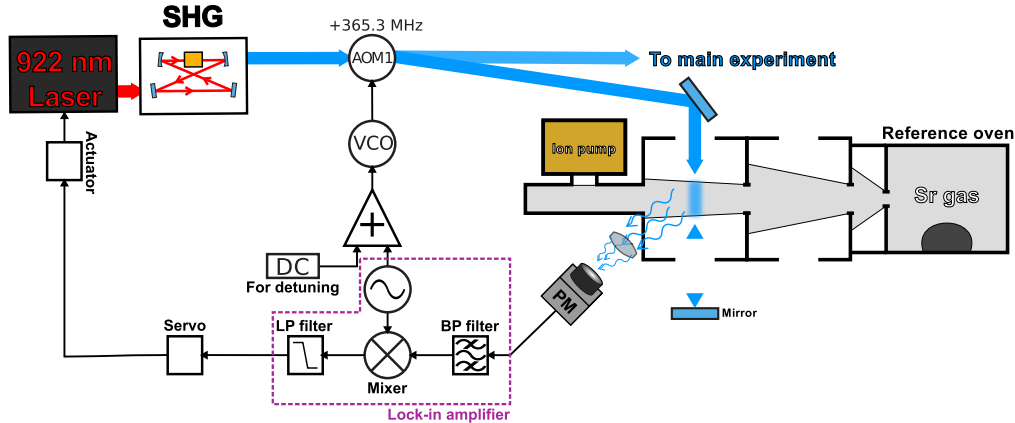


Figure 5.17: *Overview of the setup for frequency stabilization of the 461 nm cooling laser on the atomic reference oven. A lock-in amplifier is employed to generate an error signal. The output frequency of the cooling laser system is red-detuned 360 MHz with respect to the ${}^1S_0 \rightarrow {}^1P_1$ transition when the cooling laser is locked on the reference oven.*

The frequency shift of the AOM shown in Fig. 5.17 can be controlled by adjusting the DC signal to the *Voltage Controlled Oscillator* (VCO). The cooling laser detuning in the main experiment can be controlled by adjusting this AOM frequency for temperature control of the laser cooled atoms. This 461 nm beam and its retro-reflection was aligned perpendicular with the atomic beam. The fluorescence spectrum would be Doppler shifted if the angle between the 461 nm beam and the atomic beam is not perpendicular. This Doppler shift is caused by the velocity components in the direction of the beam propagation and this could result in uncontrolled detuning of the cooling laser. Great care was hence put into aligning the 461 nm light beam interrogating the reference atomic beam.

The direct output frequency from the SHG cavity was shifted by +365.3 MHz by AOM1 (shown in Fig. 5.17 and 5.18) before it is locked to the ${}^1S_0 \rightarrow {}^1P_1$ transition to the atomic reference. This setup is illustrated in Fig. 5.17. The non-deflected 0th order beam of this AOM1 is sent towards the main experiment. The frequency of this 0th order beam was hence detuned -365.3 MHz from the ${}^1S_0 \rightarrow {}^1P_1$ transition. This detuning

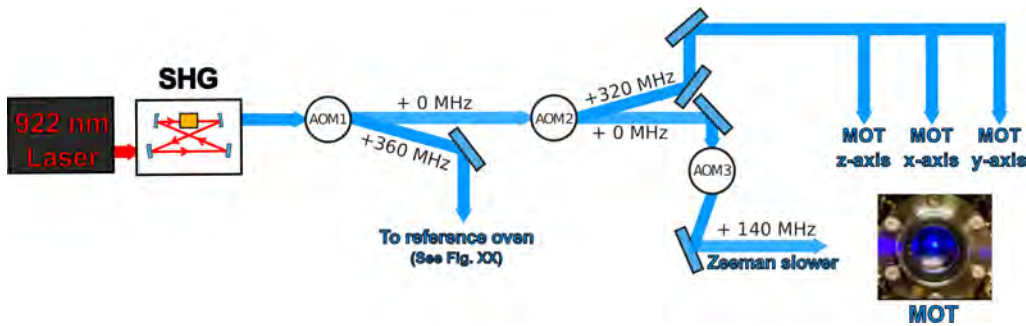


Figure 5.18: *Overview of the detunings of the 461 nm cooling laser. AOM2 was used as a shutter for switching the MOT on and off in the experimental sequences. See Fig. 6.1c).*

was partly corrected by a +328.3 MHz shift imposed by AOM2 (shown in Fig. 5.18) before the cooling light is sent to the three MOT axes. The frequency of the MOT beams were thus red detuned around -37 MHz from the ${}^1\text{S}_0 \rightarrow {}^1\text{P}_1$ transition. The temperature of the cooled atoms was expected to be about 4 mK for this detuning [Xu et al., 2003b, Fig.7]. This temperature was verified by time-of-flight measurements and by measuring the width of the doppler broadened absorption spectrum (shown later in Fig. 6.2). The 0th order of this second AOM2 is shifted +140 MHz and sent towards the Zeeman slower. The detuning of the MOT beams and the Zeeman beam can be controlled by adjusting the modulation frequency of AOM1. This method was used for controlling the MOT temperature without changing the deflection angles of AOM2 and AOM3.

5.1.3 The 707 nm & 679 nm repumping lasers

Decays from the ${}^1\text{P}_0$ state to the long lived ${}^3\text{P}_2$ state can cause shelving loss of the atoms trapped in the MOT. The relevant states are shown in Fig. 5.1. This shelving loss can however be eliminated by applying two repumping lasers at 707 nm and 679 nm. Two very similar ECDL systems in the Littman-Metcalf configuration (described in Sec. 4.2) were developed for this repumping purpose.

The ECDL components^{viii} were all fixed on a monolithic mount shown in Fig. 5.19. The lasing frequencies were adjusted to match the two

^{viii}Diode for 707 nm ECDL: Thorlabs, HL7001MG. Diode for 679 nm ECDL: Optica, LD-0675-0035-AR-1.

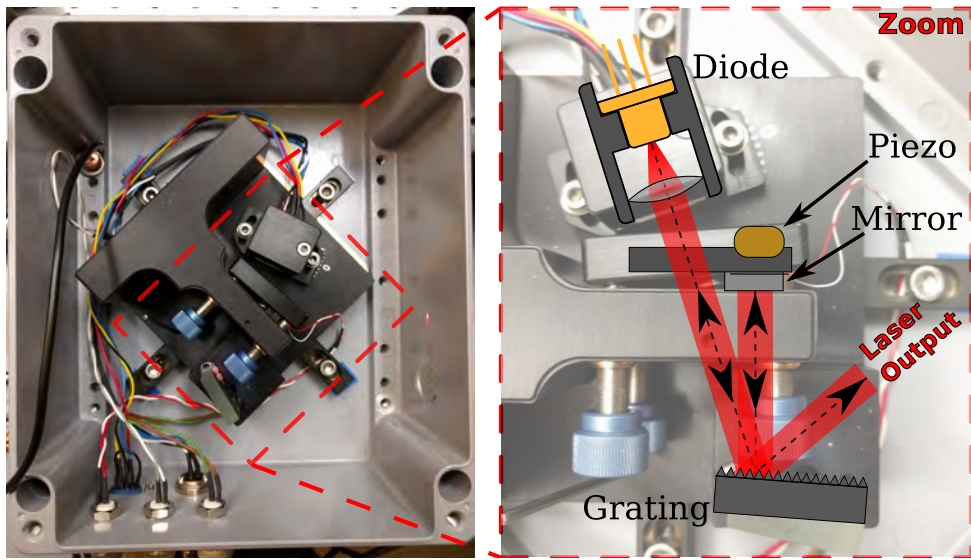


Figure 5.19: Picture of one of the Littman-Metcalf type ECDL developed for the repumping lasers. Left: All main components of the ECDL is mounted on a monolithic mount. The mount is temperature stabilized and the entire system is placed inside a sealed metal box. The ECDL output beam was transmitted out of the box through slightly angled windows with anti-reflect coating. Right: Zoom of the main components of the ECDL. Each component is indicated by figures for comparison with Fig. 4.4.

repumping transitions^{ix}. This was done by controlling the current and the temperature of the diode and the angle of the retro-reflection mirror. Lasing at the desired repumping wavelengths were thereby achieved and the output power characteristics of these repumping lasers are shown in Fig. 5.20. Both output power characteristics in Fig. 5.20 show characteristic threshold currents which confirm that lasing is achieved.

The lasing frequency of an ECDL is sensitive to temperature fluctuations as the laser diode gain spectrum and the internal cavity of the laser diode are temperature dependent. This is illustrated in Fig. 4.2. A two-stage active temperature control was hence implemented. Firstly, the laser diode temperature was stabilized by a peltier-element placed right below the laser diode. Secondly, the monolithic laser mount structure was temperature stabilized slightly above room temperature by employing a heating element. This second temperature stabilization was necessary as temperature drifts of this mount cause instabilities of the external cavity

^{ix} $^2P_0 \rightarrow ^3S_1$ transition at 707 nm and $^3P_0 \rightarrow ^3S_1$ transition at 679 nm.

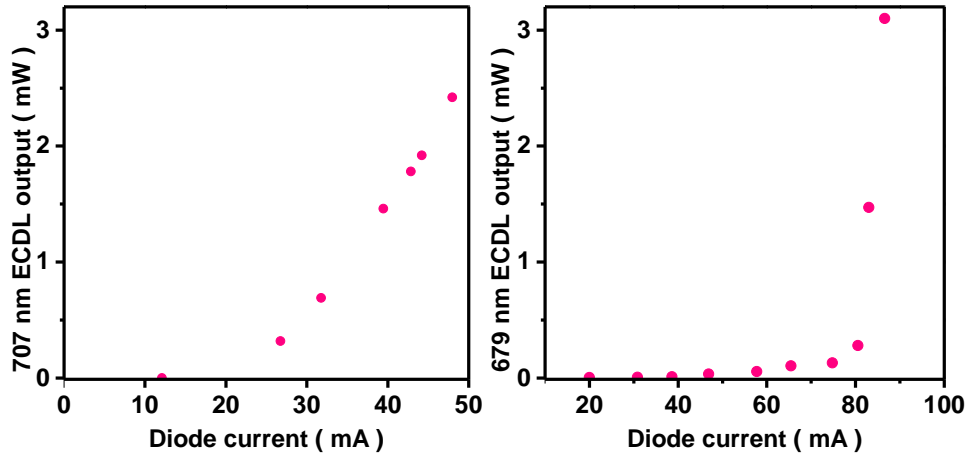


Figure 5.20: *Output characteristics of the two repumping lasers. Typical operation diode current $I_{707\text{ nm}}$ and thermistor resistance $R_{707\text{ nm}}$ for the temperature control system for the 707 nm ECDL: $I_{707\text{ nm}} \approx 50\text{ mA}$, $R_{707\text{ nm}} \approx 9.0\text{ k}\Omega$. Typical operation diode current $I_{679\text{ nm}}$ and thermistor resistance $R_{679\text{ nm}}$ for the temperature control system for the 679 nm ECDL: $I_{679\text{ nm}} \approx 81\text{ mA}$, $R_{679\text{ nm}} \approx 9.1\text{ k}\Omega$. These mentioned operation parameters are only approximate values, as these were optimized daily.*

dimensions due to thermal expansion of the mount. Passive temperature control were also imposed by placing both repumping ECDL systems inside sealed boxes. The output beams were transmitted out of the sealed boxes through slightly angled windows with anti-reflection coating. In conclusion, the lasing frequencies of the two repumping lasers were kept stable on time scales sufficient to perform the main experiments of this work.

5.2 Main Experiment

The laser systems described in Sec. 5.1 are developed with the main purpose of performing cavity enhanced non-linear spectroscopy on laser cooled strontium atoms for laser stabilization purposes. This was theoretically discussed in Chap. 3, but an experimental realization of a sample of laser cooled strontium atoms coupled to an optical cavity system is of course necessary. The overall overview of this main experimental system is presented in the following sections.

Firstly, laser cooling of ^{88}Sr in a MOT (described briefly in Sec. 4.4) was

realized inside a vacuum chamber and the performance of this system is presented in Sec. 5.2.1. Subsequently, two different cavity systems were developed. A low finesse cavity system was developed for performing proof-of-principle experiments presented later in Sec. 6. The cavity mirrors of this system were placed outside the vacuum chamber, which limited the coupling strength of the atoms and the intra-cavity field. A new cavity system was hence developed and placed inside the vacuum chamber. The coupling of the atoms to the cavity mode was improved with more than an order of magnitude, which allows non-linear spectroscopy experiments in an interesting regime for laser stabilization. Preliminary studies with this vacuum chamber is presented in Sec. 6.3. This improved vacuum cavity did also allow early studies of cavity enhanced collective emission processes with laser cooled ^{88}Sr . This is presented later in Sec. 7.

5.2.1 Trapping of strontium 88

Figure 5.21 gives a general overview of the main experimental system of this work. Solid strontium with natural isotopic composition was warmed up in an oven to a temperature $T = 520^\circ\text{C}$ and a beam of thermal strontium atoms diffused out of a 1.2 mm hole in the oven. This beam was sent through a Zeeman slower (described briefly in Sec. 4.4), where the beam of atoms was exposed to a 1 dimensional deceleration in the beam propagation direction due to radiative forces from counter propagating resonant radiation at 461 nm. The atomic resonance frequencies is however modified during the deceleration in a Zeeman slower, as the Doppler shift changes when the atomic velocity changes. A structure of electrically conductive coils provided a magnetic field with an appropriate gradient that exploits the Zeeman splitting to shift the atomic transition frequencies and keep the atoms resonant with the counter propagating light.

The Zeeman slower decelerated the atoms down to velocities around 30 cm/s [Matin, 2013], which was around the trapping velocity of the MOT. The slowed down atoms were then trapped in the MOT when entering the *main vacuum chamber* (marked with dashed blue lines in Fig. 5.21). The upper main part of the vacuum chamber consisted of a commercially available chamber structure (Kimball Physics Inc., MCF800-ExtOct-G2C8A16). The vacuum level was hence kept down by two ion pumps^x as the background pressure inside this main chamber would potentially limit the performance of the MOT. These two ion pumps

^xOne ion pump connected to the lower part of the main chamber and an other ion pump connected to the oven part of vacuum system.

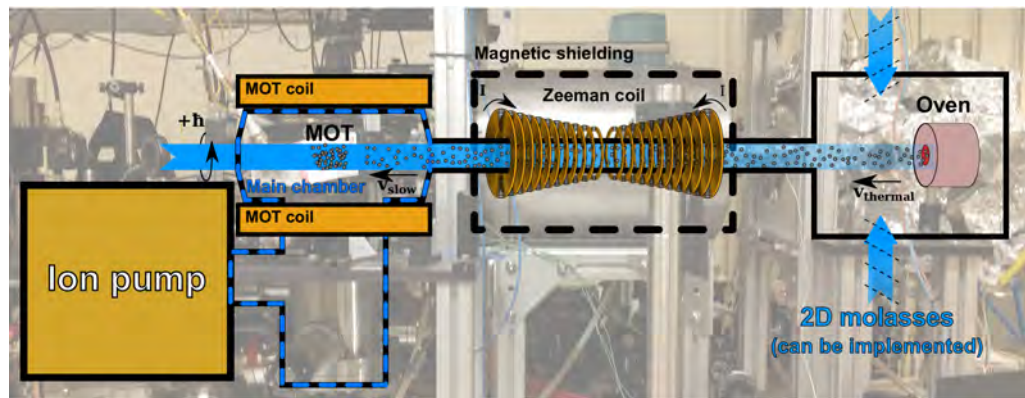


Figure 5.21: Overview of the main setup for trapping neutral ^{88}Sr in a MOT. A sample of strontium is warmed up to $T = 520^\circ\text{C}$ in an oven and a thermal beam of strontium with velocity v_{thermal} is sent out through a $\varnothing 1.2\text{ mm}$ pinhole in the oven. This beam is sent through a Zeeman slower (described in Sec. 4.4) and the velocity is slowed down to v_{thermal} in the propagation direction. The slowed atoms are now sent into the main chamber. Two MOT coils are placed above and below the main chamber creates a magnetic field in the anti-Helmholz required for a MOT (described in Fig. 4.5). The MOT coils current were around $I_{\text{Top}} = 58.2\text{ A}$ and $I_{\text{Bottom}} = 54.4\text{ A}$ but were adjusted every time the alignment of the MOT beams were optimized.

provided a pressure level of $5 \times 10^{-10}\text{ mBar}$ in the main chamber when the strontium oven is at room temperature and $6 \times 10^{-8}\text{ mBar}$ when the oven temperature is $T = 520^\circ\text{C}$.

Two coils were placed above and below the main vacuum chamber and constituted the anti-Helmholz coils in a MOT. Counter-propagating cooling beams at 461 nm were sent into the center of the MOT in all three orthogonal directions and a sample of ^{88}Sr was trapped in the center of the main vacuum chamber. A picture of the trapped atoms was shown previously in Fig. 4.6. The time dynamics of the trapped number of atoms $N(t)$ can be approximately described as:

$$N(t) = N_{\text{Max}} (1 - e^{-\alpha t}). \quad (5.1)$$

Here, α is the rate at which atoms are lost from the MOT. This can be caused by collisions with atoms from the background pressure and by so-called *shelving losses* where atoms are left in dark states due to the $^1\text{P}_1 \rightarrow ^1\text{D}_2 \rightarrow ^3\text{P}_2$ decay. Two-body losses due to collision processes are

neglected in Eq. (5.1). The number of trapped atoms will reach a steady state at N_{Max} according to Eq. (5.1). The MOT is in an equilibrium at this steady state where the loading rate L and the loss rate are equal and consequently, $N_{\text{Max}} = L/\alpha$.

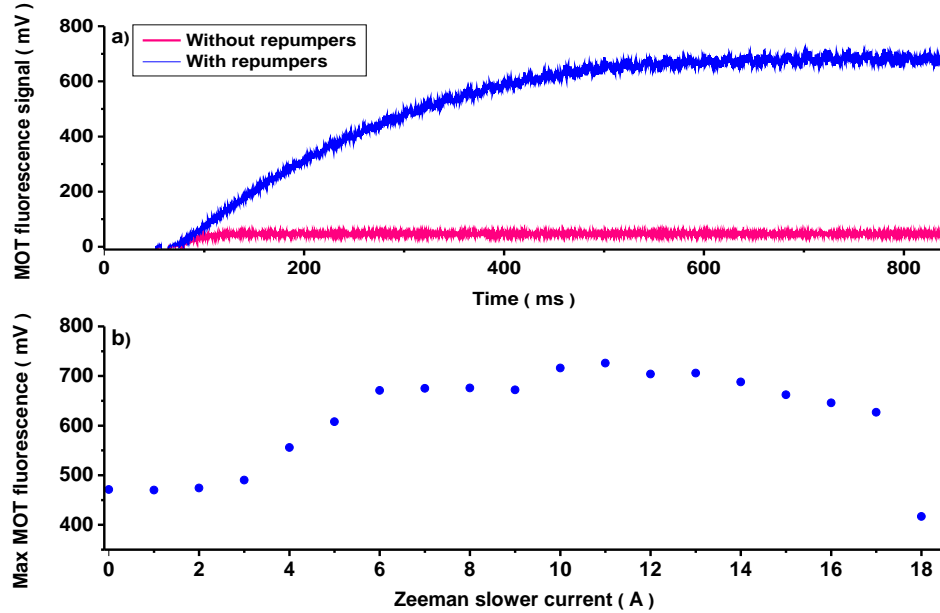


Figure 5.22: a): Typical evolutions of the MOT fluorescence during loading of atoms with and without repumping lasers. The MOT fluorescence with repumping lasers reaches a steady state after about 700 ms. It is assumed that the MOT fluorescence scales with the number of trapped atoms in the MOT. b): The steady state MOT fluorescence as function of currents through the Zeeman slower coil. The Zeeman slower was mostly operated with currents around 11 A.

Figure 5.22a) shows the time dynamics while loading of the MOT used for the main experiments in this work. The vertical axis of Fig. 5.22a) shows the fluorescence from the MOT detected by a photo multiplier. This fluorescence was assumed to scale linear with the number of trapped atoms and it is evaluated that a fluorescence signal of 600 mV corresponds to $5 \cdot 10^8$ trapped atoms. This number of atoms was evaluated based on the power of the detected MOT fluorescence and the light collection angle of the photo multiplier. This evaluation of the number of atoms was also verified by time-of-flight measurements. The above mentioned shelving losses can be eliminated by applying the two repumping lasers at 707 nm and 679 nm (see Sec. 5.1.3) so the atoms in the 3P_2 state can decay to the

shorter lived 3P_1 via the upper 3S_1 . These atomic levels are shown in Fig. 5.1. The loading dynamics are hence shown in Fig. 5.22a) with and without repumping lasers. The measured fluorescence (atom number) evolves as predicted by Eq. (5.1) and a steady state is reached after about 700 ms when repumping lasers are applied. The total data acquisition duration is about 80 ms^{xi} in the spectroscopy experiments presented later in Chap. 6. Hence, the MOT loading time set a lower limit on the total experimental cycling time of about 800 ms. Note, that the maximum number of trapped atoms $N_{\text{Max}} = L/\alpha$ is increased when the repumping lasers are applied, as the shelving loss contribution to the total loss rate α is eliminated. The loading rate L does not depend on the repumping beams and the steady state is hence reached after a much shorter loading time if repumping lasers are not used.

Figure 5.22b) shows the effect of the Zeeman slower on the number of atoms trapped in the MOT. The deceleration applied by the Zeeman slower was evidently not sufficient for Zeeman coil currents of $< 4 \text{ A}$ and no significant effects are seen. The optimal effect of the Zeeman slower is described in Eq. (4.8) and Fig. 5.22b) shows this optimal Zeeman coil current was around 11 A. The effect of the Zeeman slower is degraded for currents $> 11 \text{ A}$ as the deceleration becomes too strong and some of the slowed atoms are sent back in the direction opposite of the beam propagation.

5.2.2 Low finesse cavity

An optical cavity system was constructed, such that the laser cooled strontium atoms were placed inside the cavity mode. This was realized in order to measure the spectroscopic lineshapes predicted in Chap. 3 (these lineshapes are shown in Fig 3.3). It was proposed in Chap. 3 that the phase dispersion lineshape may prove promising as an error signal for laser stabilization. The ideal shot-noise limited linewidths were predicted theoretically for this laser stabilization scheme. Table 3.1 show these predicted linewidths for different system configurations. These predictions were calculated for systems with low ($F = 250$) and higher ($F = 1000$) finesse. Two cavity systems were constructed: A low finesse cavity system outside the main vacuum chamber and an intra-vacuum high finesse cavity. This section describes the low finesse system, while the high finesse cavity is described later in Sec. 5.2.3. The resonance linewidths

^{xi}The data acquisition last for only $100 \mu\text{s}$ but an other reference acquisition is performed after a 80 ms delay.

of both cavity systems are significantly broader than the linewidth of the relevant transition and both cavity systems are hence in the bad-cavity regime.

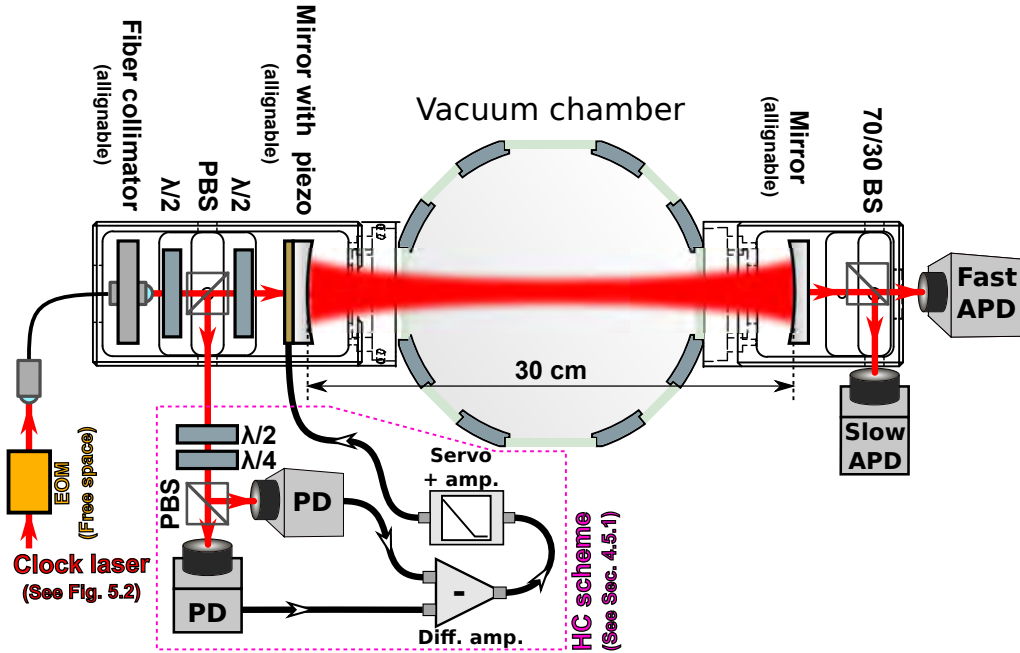


Figure 5.23: Overview of the low finesse cavity system. The cavity mirrors are fixed outside the main vacuum chamber. The probe laser is directed to the cavity through a PM fiber. The cavity length is controlled by a piezo element and the HC locking scheme (described in Sec. 4.5.1) is implemented to keep the cavity on resonance with the probe laser. The cavity transmission is detected by a slow avalanche photo detector (APD) (Thorlabs APD110A) for low frequency detection of the atomic induced absorption and a fast APD (MenloSystems APD210) for detection of higher frequency components for the NICE-OHMS scheme (described in Sec. 4.6).

Figure 5.23 illustrates the low finesse cavity system. Two spherical mirrors with radius of curvature $R_C = 9\text{ m}$ and reflection coefficient $R = 98.3\%$ are placed on both sides of the main vacuum chamber and constitute a Fabry-Perot cavity. The mirrors were mounted on adjustable mirror holders. The cavity length is $L = 30\text{ cm}$ yielding a free spectral range of $FSR = c/2L = 500\text{ MHz}$. Light at 689 nm is transferred to the cavity system through a polarization maintaining optical fiber from the probe laser system described previously in Sec. 5.1.1. The MOT was aligned such

that the atoms were trapped spatially slightly above the center of the anti-Helmholz coils. The atoms were hence exposed to non-zero magnetic field, which split up the magnetic sub-levels $M = 0, \pm 1$ of the 3P_1 level. Only the $M = 0$ level was probed as the linear polarization of the probe laser was adjusted before the light was coupled to the optical cavity, such that the probe polarization matched the magnetic field within the volume of the trapped atomic sample. The relative mechanical vibrations were greatly reduced for the cavity mirrors and the optical components for the probe laser in-coupling by fixing these components on custom made mounts which were fastened tightly on the view-port flanges of the vacuum chamber. These mounts ensured to a great extent that the mechanical vibrations of the cavity were common mode. Technical drawings of these custom made mounts are shown in Fig. A.1 and A.2 in the appendix.

The cavity length was adjustable by using a ring shaped piezo electric element glued between one of the mirrors and the corresponding mirror mount. This piezo element was used to scan the cavity length and a photo detector (*Slow APD* in Fig. 5.23) was set up to monitor the cavity transmitted optical power. Figure 5.24 shows this photo detector signal during a cavity scan. Three transmission peaks are seen in Fig. 5.24: The highest peak is the fundamental transverse TEM_{00} mode of the cavity [Milonni and Eberly, 1988, p.506] with polarization parallel with the magnetic axis of the MOT. The view-port windows placed inside the cavity were anti-reflection coated for 689 nm so reflection and loss in the view ports would not degrade the cavity finesse. However, an unevenly distributed strain was applied to the intra cavity windows during the mounting of the windows on the chamber flanges. This strain induced birefringence in the windows which caused different shifts of the cavity resonances for the two polarizations relative to the MOT axis. The middle peak in Fig. 5.24 is hence the shifted cavity mode for the polarization perpendicular with the MOT axis. The leftmost transmission peak in Fig. 5.24 is a higher transverse order of the cavity due to imperfect mode matching of the input probe laser mode and the fundamental cavity mode.

The intra-cavity windows limit the highest achievable finesse value for the cavity. The cavity finesse was evaluated to be $F = 85$ based on the theoretical fit illustrated with a solid red line in Fig. 5.24. The horizontal axis of Fig. 5.24 was calibrated by scanning over two longitudinal modes and using the $FSR = 500$ MHz as a scale. This calibration assumes a linear behavior of the piezo element, which does not necessarily apply for all conditions. This calibration was confirmed by applying sidebands on the input probe light with a known phase modulation frequency. The cavity finesse was stable during the measurement series presented in Chap. 6.

However, the cavity finesse depended on the cavity alignment and this alignment needed optimization every few days. The optimized cavity finesse was typically within the range of $F = 78\text{--}85$. The overall dynamics of the system were expected to be unchanged within this finesse range.

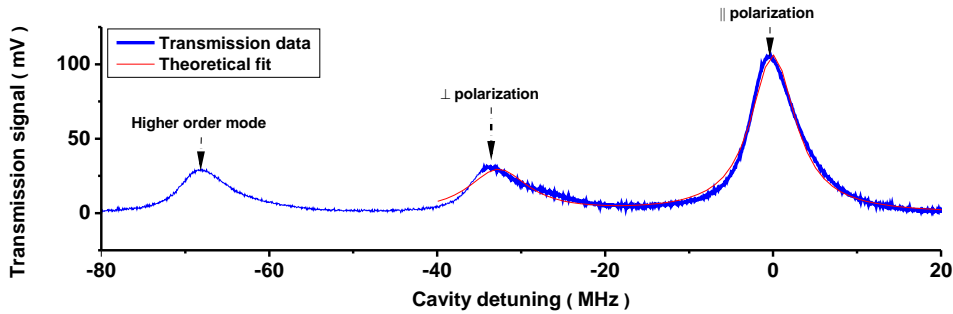


Figure 5.24: *Transmission spectrum of the low finesse cavity during scan of cavity length. Three transmission peaks are seen: The fundamental TEM_{00} modes for the two polarizations (E_{\parallel} and E_{\perp}) and a high order cavity mode due to imperfect modematching of the input probe laser. The horizontal axis is calibrated by scanning over two longitudinal modes and using the $\text{FSR} = 500 \text{ MHz}$ as a scale.*

The piezo element was also used for stabilization of the cavity length. The theoretical model developed in Chap. 3 required that the cavity and the probe laser is forced to be on resonance at all times. This requirement was fulfilled by using the light reflected from the cavity to generate an error signal through the HC stabilization scheme (described in Sec. 4.5.1). The above mentioned birefringence of the chamber windows were exploited as the birefringent intra-cavity element required in the HC stabilization scheme. The control bandwidth of the cavity was limited to about 900 Hz due to a mechanical resonance of the piezo electric element and the movable mirror. The phase response of the piezo system was delayed by 180° for frequencies above this mechanical resonance. This phase delay might amplify the noise components around unity-gain, if this unity gain is near the mechanical resonance frequency. An integrating servo circuit [Riehle, 2004, p.42] was developed to amplify the low frequency components of the error signal. This ensured that only frequency components below this piezo bandwidth were used for error suppression, and that noise components outside the piezo bandwidth were not amplified. Figure 5.25 shows a Bode plot measured for this servo circuit. An integrating servo circuit has an intrinsic phase delay which might add up to the phase

delay of the piezo resonance and limit the bandwidth of the cavity stabilization even more. This phase delay was corrected by extending the integrator characteristics with a proportional amplifier characteristics for higher frequencies. The transition from the integrator characteristic to the proportional characteristic was determined by a corner frequency of a few hundred Hz.

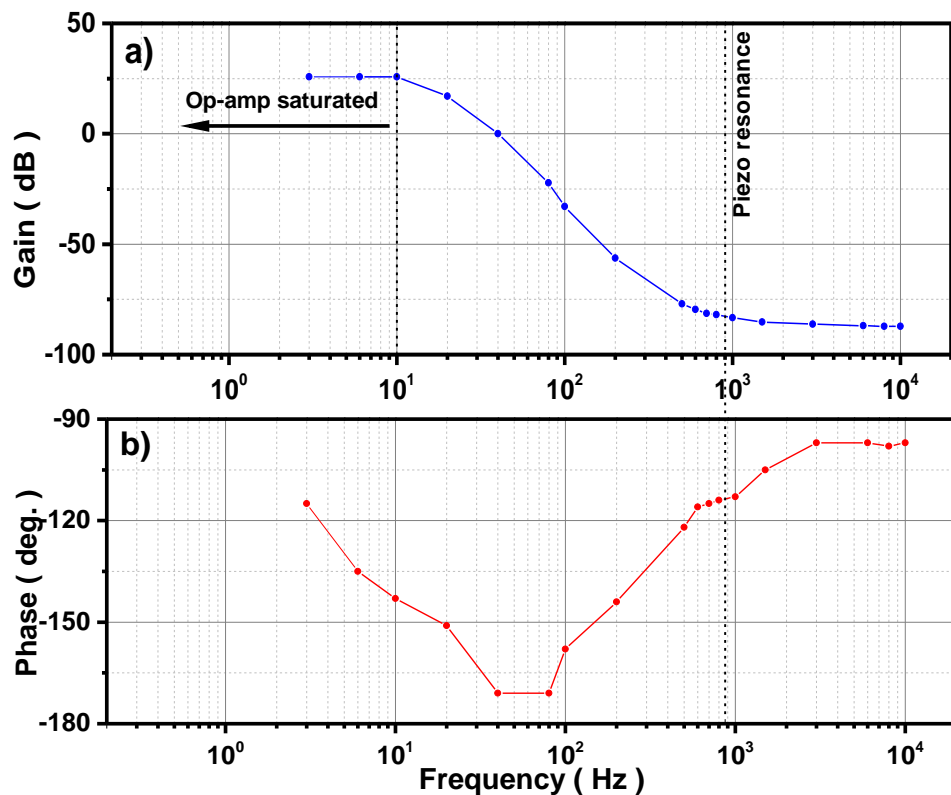


Figure 5.25: *Bode plot of the serve circuit used for locking the cavity on resonance with the input probe laser. Low frequency gain was optimized by setting a corner frequency just below the combined mechanical resonance of the piezo and the moveable mirror. The operational amplifiers used in the servo circuit was saturated for sub 10 Hz components.*

The radius of curvature of the cavity mirrors $R_C = 9$ m and the cavity length $L = 30$ cm yielded a cavity beam waist of $w_0 = 500 \mu\text{m}$. The finite mean velocity of laser cooled atoms imposes a transit time broadening, when spectroscopy is performed with a finite probe beam waist. However,

the relatively large beam waist of this cavity ensured that the majority of the atoms stayed within the cavity mode during the interrogation procedure. This transit time broadening was hence estimated to be about 1–2 kHz, which is significantly smaller than the natural atomic linewidth of the interrogated transition, $\Gamma/2\pi = 7.5$ kHz.

An EOM was used before the optical cavity in order to apply side bands on the probe laser. This EOM is illustrated as a free space EOM in Fig. 5.23. The sidebands are applied primarily for detecting atom-induced phase shifts by using the NICE-OHMS technique. The ratio of the carrier and sideband power can be adjusted in order to optimize the NICE-OHMS signal, which is optimized when the so-called phase modulation index is $x = 1.08$. This modulation index determines the ratio of the carrier and sideband field amplitudes $J_1(1.08)/J_0(1.08)$ in Eq. (4.13). A modulation index of $x = 1.08$ requires high voltage modulation amplitudes for a free space EOM. A fiber based EOM (JenOptik, PM705) was implemented during this work as shown later in Fig. 5.27 in order to optimize the modulation index without high voltage electronics. The majority of the spectroscopic results shown later in Chap. 6 were measured with this fiber based EOM.

Detailed understanding of this modulation index x is required for detailed predictions of the lineshapes measured by the NICE-OHMS technique as correction terms will emerge for high values of x (correction terms are shown in Eq. (4.13)). The modulation index of the fiber EOM used in this work was hence been mapped out for different modulation powers and it is shown in Appendix A.2.

Finally, the different coupling and dissipation rates for this low finesse cavity system are needed to be outlined before an improved vacuum cavity system is presented in the following section. These rates are essential for the predictions calculated by the theoretical model presented in Chap. 3 (see for example Eq. (3.4)–(3.5)). The cavity decay rate for this cavity system was $\kappa/2\pi = 5.8$ MHz. This system was hence within the bad-cavity regime ($\kappa \gg \Gamma$) as the natural linewidth of the relevant transition is $\Gamma/2\pi = 7.5$ kHz. The cavity dimensions and the properties of the relevant transition yielded a single-atom-cavity coupling constant of $g/2\pi = 590$ Hz. The so-called single-atom cooperativity of this system was hence $C_0 = 4g^2/\Gamma\kappa = 3.2 \times 10^{-5}$ [Tanji-Suzuki et al., 2011, p. 31]. This single-atom cooperativity C_0 yielded a collective cooperativity $C = N_{\text{cav}}C_0$ (described in Sec. 2.2) of around $C = 630$. Here, N_{cav} is the number of intra-cavity atoms, which was typically in the $N_{\text{cav}} = 1.0 \times 10^7$ – 2.5×10^7 range (described later in Sec. 6.1.3).

5.2.3 Vacuum cavity

The cavity system described above in Sec. 5.2.2 was improved to an intra-vacuum cavity system during this work. The motivation for this was twofold: Firstly, it was predicted in Chap. 3 that an ideal shot noise limited linewidth down to $< 10 \text{ mHz}$ can be achieved by using the phase dispersion lineshape as an error signal for laser stabilization. This prediction is shown in Table 3.1. This $< 10 \text{ mHz}$ linewidth was predicted for a Finesse of $F = 1000$, which was significantly higher than the finesse of the cavity system described in Sec. 5.2.2. Secondly, the collective emission processes discussed in Chap. 2 scales with the collective cooperativity $C_0 N$ and this will also be enhanced for atom-cavity systems with higher finesse. Absorption and scattering losses in the vacuum chamber windows however limits the finesse of the cavity described previously in Sec. 5.2.2. A finesse of $F = 1000$ is difficult to achieve with mirrors fixed outside the vacuum chamber. Hence a vacuum cavity was developed.

Figure 5.26a) shows a technical sketch of this vacuum cavity. The cavity consisted of two spherical mirrors glued on a monolithic zerodur spacer structure. A ring shaped vacuum compatible piezo electric element (Noliac, NAC2125) was glued (Thorlabs TS10) in between the cavity spacer and one of the mirrors. The electrodes are guided out of the spacer through two holes (See Fig. 5.26a)) and high voltages are applied through an electrical feedthrough. The mirrors were glued while the probe laser transmission was monitored and while the mirror alignment was optimized with a 3D translatable mirror mount developed for this purpose. This alignment process is illustrated in Fig. 5.26b).

The two cavity mirrors have a radius of curvature of $R_C = 9 \text{ m}$ and reflection coefficient of $R = 99.8\%$. The cavity length is $L = 19.2 \text{ cm}$ yielding a free spectral range of $FSR = c/2L = 781.14 \text{ MHz}$. The cavity beam waist is $w_0 = 450 \mu\text{m}$. Whereas this waist is slightly smaller than the cavity waist of the low finesse cavity (described in Sec. 5.2.2), the transit time broadening will be of the same order of magnitude. The transit time broadening will hence not limit the experiment.

The cavity spacer was resting on the inner side of two opposite camber view ports and supported by four vibration isolating Viton strips. Outgassing of the Viton strips can potentially degrade the vacuum level of the main chamber and reduce the number of atoms trapped in the MOT. The viton strips were baked in a separate vacuum chamber at temperatures up to 80°C for a month in order to outgas all the vacuum degrading components before the strips were used for supporting the vacuum cavity [Peacock, 1980]. This outgassing process is described in

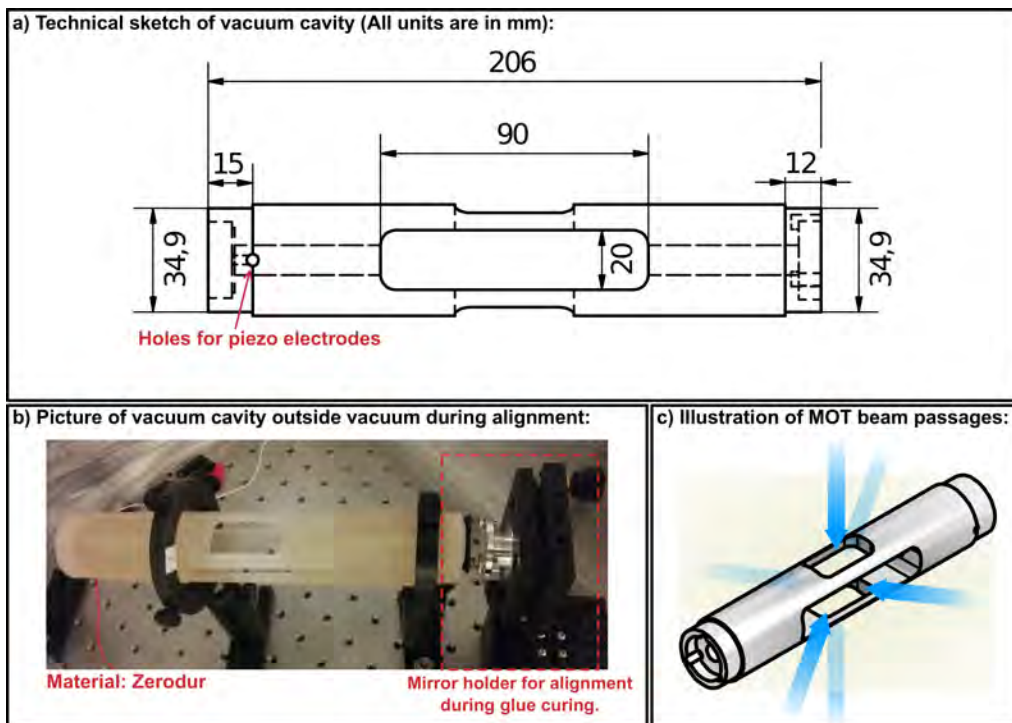


Figure 5.26: Illustrations of the vacuum cavity spacer made of Zerodur glass. a): Technical sketch of the cavity spacer. A more detailed technical drawing is shown in Fig. A.5 in Appendix A.4. b) Picture of the vacuum cavity during preparation. The electrodes can be seen on the left end from the piezo element glued on the movable cavity mirror. A custom mirror holder was developed for keeping the cavity alignment while the cavity mirrors were glued. c): Illustration of the MOT beam passages.

Appendix A.3.

Figure 5.27 illustrates the overall vacuum cavity system. All cavity components were placed within the vacuum chamber and the optical components for cavity in-coupling and transmission detection were fixed on custom made mounts fastened on the vacuum chamber flanges. These mounts were the same mounts as those used for the low finesse cavity system illustrated in Fig 5.23. Detailed drawings of these mounts are also shown in Fig. A.1 and A.2 in appendix A.1. The alignment of the vacuum cavity mirrors are not adjustable and an extra degree of freedom was desired for optimizing the mode matching of the input probe light. A degree of freedom was added by modifying the mount for in-coupling of

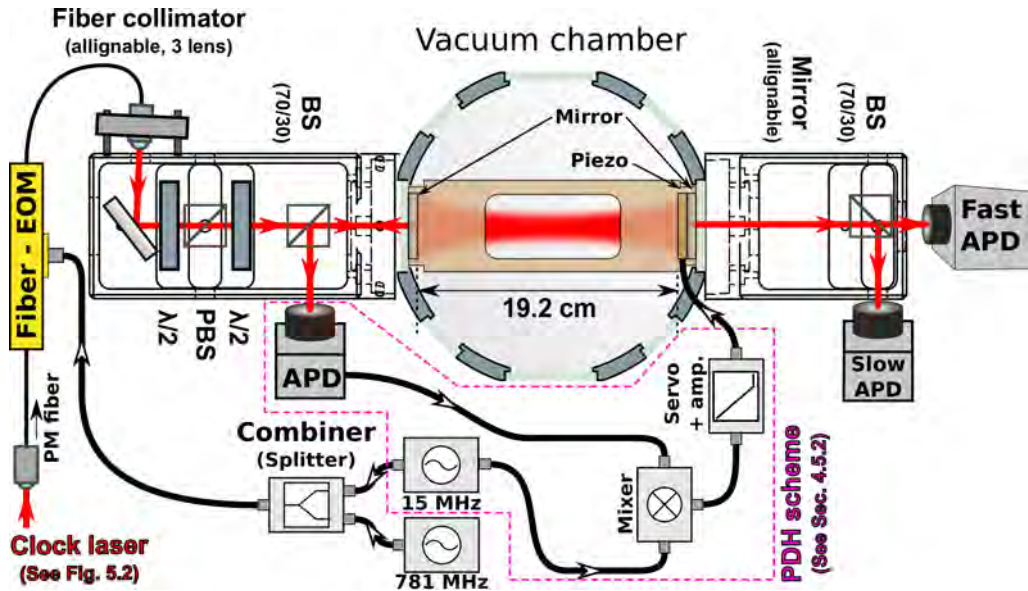


Figure 5.27: Overview of the vacuum finesse cavity system. The cavity structure is placed inside the main vacuum chamber. The probe laser is directed to the cavity through a PM fiber with an integrated waveguide EOM. The cavity length is controlled by a piezo element and the PDH locking scheme (described in Sec. 4.5.2) is implemented to keep the cavity on resonance with the probe laser. The cavity transmission is detected by a slow avalanche photo detector (APD) (Thorlabs APD110A) for low frequency detection of the atomic induced absorption and a fast APD (MenloSystems APD210) for detection of higher frequency components for the NICE-OHMS scheme (described in Sec. 4.6).

the probe light. An adjustable fiber collimator mount was screwed onto the side of the mount and the probe beam was redirected towards the cavity by an adjustable mirror. This added fiber collimator mount is illustrated in the upper left corner in Fig. 5.27. The degrees of freedom were thus sufficient for mode matching the probe laser mode to the vacuum cavity mode.

The probe laser light at 689 nm was transferred to the cavity system through a fiber based EOM (JenOptik, PM705). The output beam profile of the fiber EOM was less symmetrical and Gaussian than the PM fiber used for transferring the probe light to the low finesse cavity setup (See Fig. 5.23). The collimation of the fiber EOM output was optimized by implementing a 3 lens collimator (Thorlabs, TC06FC-633).

The extended degrees of freedom and optimized mode matching

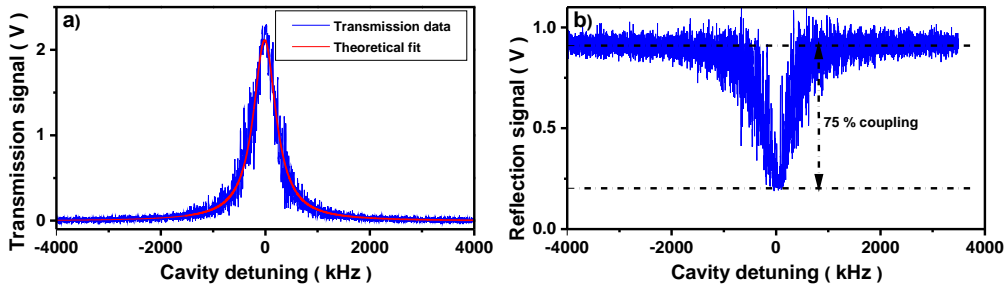


Figure 5.28: *Transmission and reflection spectra of the vacuum cavity. The horizontal axes are calibrated by scanning over two longitudinal modes and using the FSR= 781.15 MHz as a scale. a): The blue line is experimental data while the red line is a theoretical fit used for determining the cavity finesse. b) The reduction of the reflected light around cavity resonance indicates that around 75 % of the input light is coupled to the cavity.*

allowed coupling of the probe light to intra vacuum cavity. The cavity length was scanned using the piezo electric element glued on one of the cavity mirrors and the cavity transmission and reflection were monitored by photo detectors. Figure 5.28 shows the transmission and reflection signals during this cavity scan. Figure 5.28a) shows a transmission peak corresponding to the fundamental TEM_{00} mode of the cavity. The finesse of the cavity was evaluated to be $F = 1452 \pm 95$ based on theoretical fits (shown as the red solid line in Figure 5.28a)) for five cavity scans. Both horizontal axes in Fig. 5.28 were calibrated to cavity detuning by scanning over two longitudinal modes and using the FSR= 781.14 MHz as a scale and by examining the transmission of sidebands during cavity scans with a known phase modulation frequency. Interestingly, the cavity finesse was measured to be about 1200, when the cavity was tested outside the vacuum chamber where the atmospheric air had possibly reduced the cavity finesse. Figure 5.28b) shows the cavity reflection during a scan of the cavity length. It is evaluated that about 75 % of the input light is coupled into the cavity at resonance. Figure 5.28 only shows narrow scans and high order transverse cavity modes are not shown, but the higher modes were greatly reduced compared to the transmission spectrum of the low finesse cavity shown in Fig. 5.24.

Whereas the low finesse cavity described in Sec. 5.2.2 had birefringent windows inside the cavity, the vacuum cavity does not have this. The HC stabilization technique (described in Sec. 4.5.1) was hence not suited

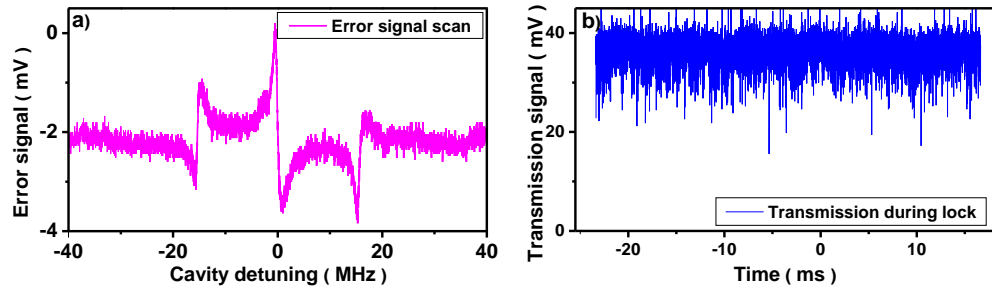


Figure 5.29: *a)*: The PDH error signal during scan of cavity length used for locking the vacuum cavity on resonance with the probe laser. The horizontal axis is calibrated using the known spacing between the probe carrier and the sidebands applied for the PDH scheme. The signal-to-noise ratio of this error signal is suboptimal due to a very limited optical power from the cavity reflection. *b)*: The cavity transmission signal during lock. The fluctuation of this transmission signal is in the order of 25 % relative to the maximum transmission signal. This fluctuation can most likely be reduced by improving the signal-to-noise ratio of the error signal and the servo circuit used in the locking scheme (described in Fig. 5.30).

for stabilizing the length of the vacuum cavity. The PDH stabilization technique (described in Sec. 4.5.2) was implemented instead. A set of sidebands were applied on the probe laser before coupling into the vacuum cavity. The sidebands were generated by periodic phase modulation with modulation frequency of 15 MHz. The PDH error signal was generated by detecting the reflected light from the cavity and demodulating the reflection signal at the same frequency as the modulation frequency. Figure 5.29a) shows this error signal for when the cavity length was scanned. The horizontal axis was calibrated to cavity detuning by using the known frequency spacing between the carrier and the sidebands as a scale.

Ideally, a $\lambda/4$ -plate should be placed before the cavity, in order to redirect the reflected light towards a photo detector through a PBS (This is described in more details in Sec. 4.5.2). The spectroscopy experiments described later in Chap. 6 require however linearly polarized light with polarization parallel with the MOT axis. A $\lambda/4$ -plate would modify the probe laser polarization and result in circular polarized intra cavity

light. A conventional non-polarization BS^{xii} was used instead of a PBS and only about 20 % of the input probe laser power was redirected to the photodetector. This limited optical power of the detected reflection resulted in the relatively small error signal amplitude of $\sim 4\text{ mV}$ shown in Fig. 5.29a).

The error signal shown in Fig. 5.29a) was sent to the cavity piezo through a servo circuit and a high voltage amplifier. The cavity length is thereby locked on the probe light frequency such that standing waves are maintained in the cavity. Figure 5.29b) shows the cavity transmission during this lock. The intensity noise of the transmitted light is about 25 % of the total transmitted intensity. This transmission noise is possibly due to the poor signal-to-noise ratio of the error signal (see Fig 5.29b)) or inadequate frequency response of the servo circuit. Fortunately, this cavity stabilization is found to be sufficient for performing the experiments described later in Sec. 6 and 7.

Figure 5.30 shows the Bode plots of the servo circuit developed for stabilizing the vacuum cavity. A more detailed description of the servo circuit is presented in Appendix A.6. This servo circuit had integrating frequency characteristics for low frequencies and proportional characteristics for higher frequencies. A corner frequency of about 360 Hz was separating the integrating and proportional frequency ranges. The control bandwidth of this servo circuit was hence limited to about 360 Hz. The mechanical resonance of the cavity piezo limits typically the control bandwidth of a piezo controlled cavity length. This mechanical resonance was determined to be about 1.4 kHz for the vacuum cavity. The control bandwidth of the servo circuit should hence ideally be increased to a frequency just below 1.4 kHz. Improvements of this cavity lock can hence be expected by optimizing this control bandwidth. This optimization was, however, not completed during this work due to unidentified phase delays in the feedback loop and leaves such optimization to future works.

Finally, the different coupling and dissipation rates for this vacuum system are needed to be outlined in order to describe collective emission processes presented later in Chap. 7. The cavity decay rate for the vacuum cavity was $\kappa/2\pi = 520\text{ kHz}$. The dimensions of this vacuum cavity yielded a single-atom-cavity coupling constant of $g/2\pi = 825\text{ Hz}$, when probing the ${}^1\text{S}_0 \rightarrow {}^3\text{P}_1$ transition (with natural linewidth $\Gamma/2\pi = 7.5\text{ kHz}$). The single-atom cooperativity of this system was hence $C_0 = 4g^2/\Gamma\kappa = 6.3 \times 10^{-4}$. This C_0 is one order of magnitude larger than the single-atom cooperativity of the low finesse cavity (described in Sec. 5.2.2). Collective emission

^{xii}A 70/30 BS was used in order to increase the optical probe power reaching the cavity.

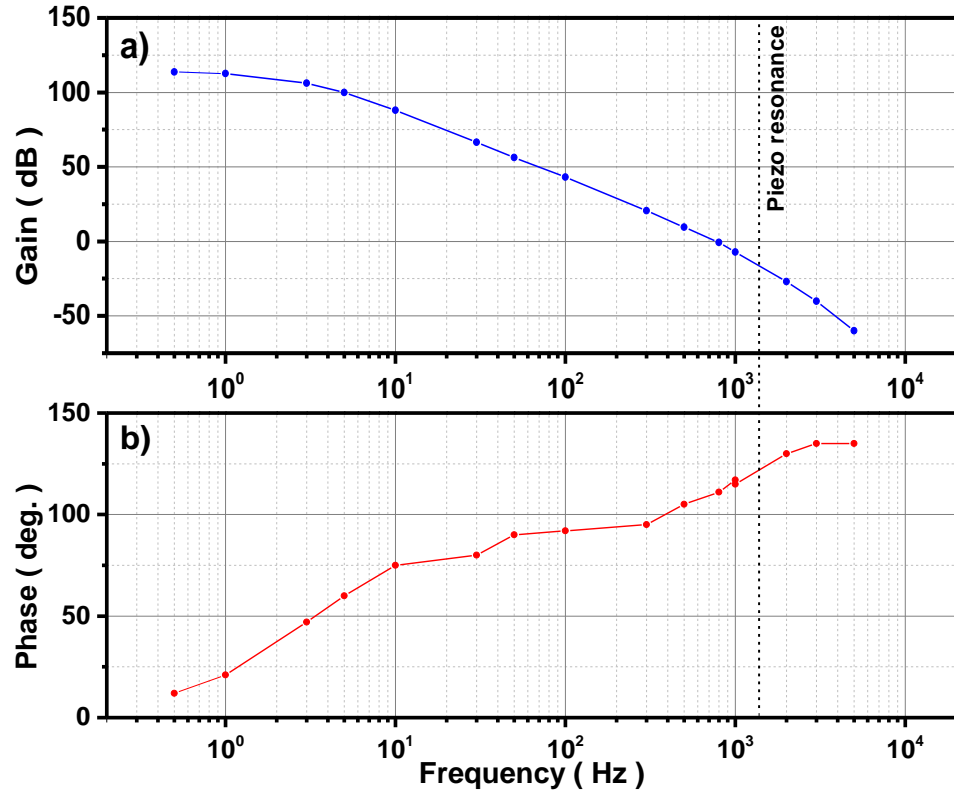


Figure 5.30: Bode plot of the servo circuit used for locking the vacuum cavity on resonance with the input probe laser. The combined mechanical resonance of the piezo element and the movable mirror is identified around 1.4 kHz and a corner frequency should be set near this frequency in order to optimize the servo circuit. A design error increases the phase shift around this mechanical resonance, which most likely limits the bandwidth of the combined feedback system. A detailed description of the servo circuit is presented in Fig A.6 in Appendix A.5.

processes can be expected when the collective cooperativity $C = N_{\text{cav}}C_0$ is higher than 1, $C > 1$ (this is described in Sec. 2.2). Here, N_{cav} is the number of intra-cavity atoms, which typically yielded values in the $N_{\text{cav}} = 1.0 \times 10^7$ – 2.5×10^7 range (described later in Sec. 6.1.3). The collective cooperativity of this vacuum cavity system was hence expected to be in the $C = N_{\text{cav}}C_0 \gg 1$ range, where collective emission processes were expected.

Outlook

The most essential components of the main experimental system in this work were presented in this chapter. ^{88}Sr atoms were cooled down to temperatures around mK and trapped in a standard MOT as described in Sec. 5.2.1. These trapped atoms were placed inside a low finesse cavity ($F = 85$, described in Sec. 5.2.2) and later inside a vacuum cavity with higher finesse ($F = 1450$, described in Sec. 5.2.3). The vacuum cavity system was an upgrade of the low finesse cavity and the two systems were not realized in parallel.

These trapped neutral strontium atoms with temperatures in the mK level coupled to optical cavities with finesse of $F = 85$ and $F = 1450$ are very suited for performing proof-of-principle experiments to study the non-linear spectroscopic lineshapes theoretically predicted in Chap. 3. The results of such studies are presented in the next chapter where detailed studies of the system dynamics relevant for laser stabilization are also presented.

CHAPTER



NONLINEAR SPECTROSCOPY FOR LASER STABILIZATION

The theoretical model established in Chap. 3 predicted that atom-cavity systems with laser cooled atoms could potentially reach sub-10 mHz linewidths when applied as a frequency reference for laser stabilization. The dynamics of the system observables were however predicted to be highly non-linear and the identification of the optimal parameter regime for laser stabilization was non-trivial.

Chapter 5 described two cavity-atom systems prepared in order to verify the predicted dynamics and characteristic features. The first system consisted of laser cooled ^{88}Sr atoms placed inside a low finesse optical cavity. This cavity was mounted outside a vacuum chamber and the cavity finesse was limited to $F = 85$ by the chamber windows. This system was later upgraded to the second system, where the cavity was placed inside the vacuum chamber. The finesse of this cavity was $F = 1450$, which allowed studies of the prospects for sub-10 mHz linewidths predicted in Sec. 3.4.2 and studies of collective spontaneous emission phenomena presented later in Sec. 7.

The two atom-cavity systems were not designed for continuous laser stabilization operation. However, a verification of the dynamics and features of these systems will strongly support the validity of the theoretically predicted sub-Hz linewidths. This will provide great motivation for designing future systems for continuous laser stabilization.

The following sections present the results of the studies of these two cavity-atom systems. The system dynamics were studied most extensively

for the low finesse ($F = 85$) system. Different spectroscopy schemes, such as *overtone demodulation* (presented in Sec. 6.1.2) and *sideband probing* (presented in Sec. 6.2.1) were developed during this work in order to confirm the spectroscopic features of the system. The dynamics of the system was also studied in detail and the optimal system parameters for laser stabilization were identified (presented in Sec. 6.1.3 and 6.1.4). The spectroscopic lineshape of the low finesse cavity system exhibits minor modifications due to multiphoton scattering processes. It was considered based on this, whether observations of recoil shifts from these multiphoton scatterings could be expected. It was attempted to measure these recoil shifts but no conclusive results were achieved (see Sec. 6.2.2).

Finally, the spectroscopic lineshapes of the high finesse system were studied briefly in order to confirm, that the system behavior scales with the cavity finesse as predicted by the theoretical model.

The majority of the results presented in the following sections are published in [Westergaard et al., 2015] and [Christensen et al., 2015a].

6.1 Spectroscopy with low finesse

The spectroscopic dynamics were studied for laser cooled ^{88}Sr coupled to the low finesse optical cavity system described in Sec. 5.2.2. These studies were carried out by studying the cavity transmitted light as illustrated in Fig. 6.1a). The system parameters of the different components of this experimental atom-cavity system are briefly described in the first part of the following section before the spectroscopy experiments are presented in the rest of the section.

Experimental setup

About 5×10^8 laser-cooled ^{88}Sr atoms were trapped in a standard magneto-optical trap (MOT) (described in Sec. 4.4) by using the ${}^1\text{S}_0 \rightarrow {}^1\text{P}_1$ transition at 461 nm and by applying repumping lasers at 707 nm and 679 nm. The two main atomic transitions of interest are shown in Fig. 6.1b)ⁱ. The atomic temperature was in the range of $2 \sim 6$ mK. This temperature depends on experimental conditions such as MOT laser detunings and MOT laser intensities [Xu et al., 2003b] and the temperature was determined from the Doppler broadened absorption width. These temperatures were also verified by time-of-flight measurements.

The laser-cooled atoms were coupled to a single mode of an optical cavity with a finesse of $F = 85$. The radius of curvature of the cavity mirrors

ⁱAll involved transitions are illustrated in more details in Fig. 5.1.

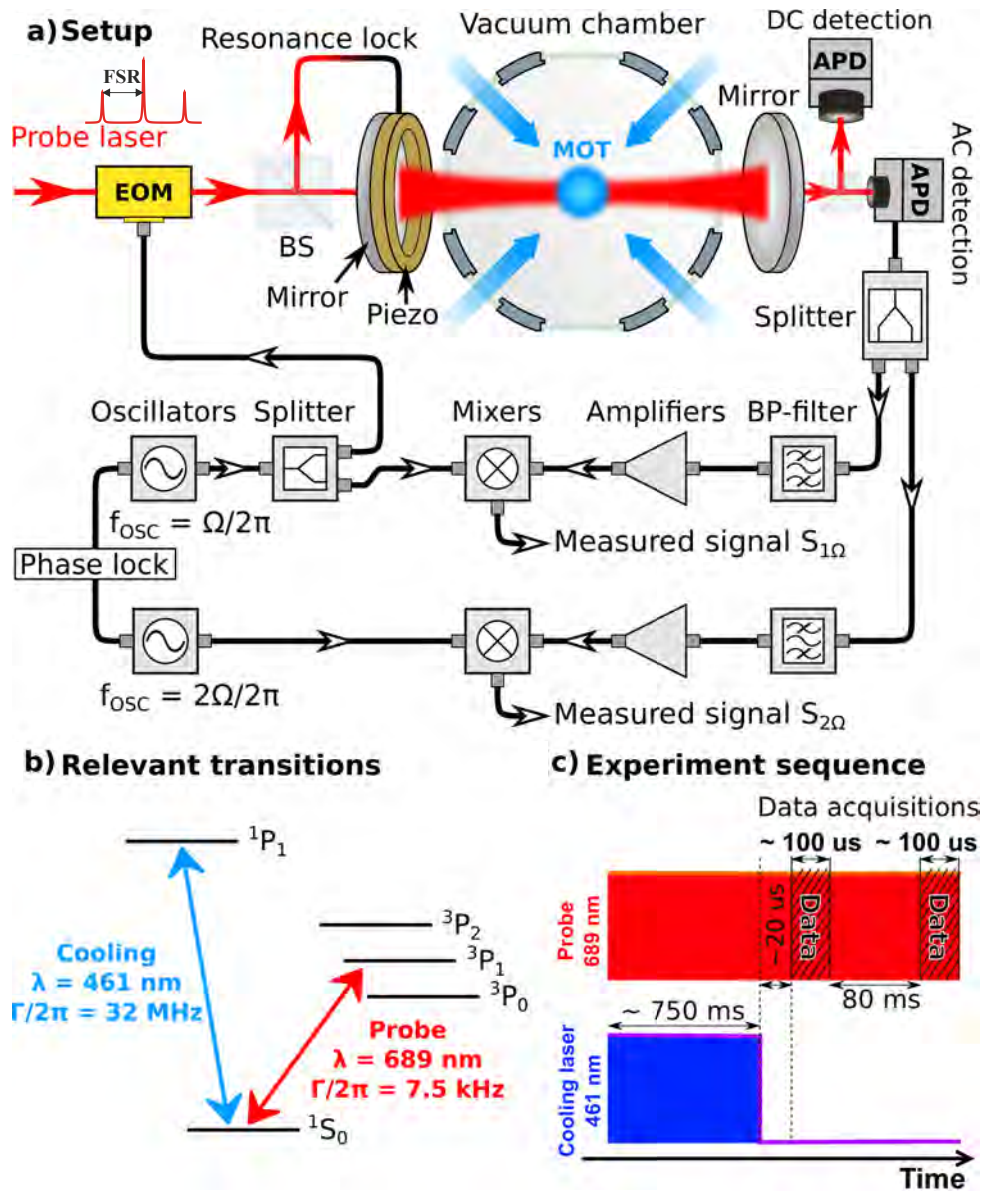


Figure 6.1: a): Experimental setup. A sample of laser cooled ⁸⁸Sr atoms trapped in a standard MOT was located inside a low finesse optical cavity ($F = 85$). The absorption and phase dispersion lineshapes were measured by performing cavity-enhanced FM spectroscopy (NICE-OHMS, described in Sec. 4.6) where the input light is modulated at $\Omega/2\pi = \text{FSR}$ and the cavity output is demodulated at $\Omega/2\pi = \text{FSR}$ or $2\Omega/2\pi = \text{FSR}$. b): Illustration of the energy levels of ⁸⁸Sr relevant for the spectroscopy experiments described in this section. c): Experimental sequence. the MOT was loaded for about 750 ms after which the system was probed for 100 μs . A reference measurement with no atoms was also performed after 80 ms.

are 9 m and the mirrors were displaced 30 cm from each other. These dimensions yielded a cavity waistⁱⁱ of 500 μm and a free spectral range of $FSR = 500 \text{ MHz}$. The maximum number of atoms inside the cavity mode, N_{cav} , was evaluated to be $N_{\text{cav}} = 2.5 \times 10^7$ based on the dimensions of the cavity mode and the volume of the MOT. The narrow $^1\text{S}_0 \rightarrow ^3\text{P}_1$ intercombination transition was probed by a pre-stabilized probe laser at 689 nm (described in Sec. 5.1.1), while a servo system forced the cavity to be on resonance with the probe laser at all times through the Hänsch-Couillaud (HC) stabilization scheme [Hänsch and Couillaud, 1980]. It is described later in this section and in Sec. 6.1.2, that this at first glance harmless resonance requirement implemented by the cavity feedback system turned out to modify the spectroscopy lineshapes significantly.

The time evolution of this atom-cavity system was governed by a number of decay- and dissipation rates, which were essential for predicting the steady-state spectroscopic lineshapes by using the theoretical model presented in Chap. 3. The cavity decay rate κ , which relates to the cavity linewidth, was measured to be $\kappa/2\pi = 5.8 \text{ MHz}$. The spontaneous decay rate Γ of the $^1\text{S}_0 \rightarrow ^3\text{P}_1$ transition is $\Gamma/2\pi = 7.5 \text{ kHz}$. The relation $\kappa \gg \Gamma$ brought this system into the socalled bad-cavity regime (described in Chap. 2), where the atomic spectral properties could potentially dominate the combined system. The transit time broadening was estimated to be $1 \sim 2 \text{ kHz}$ based on the realized MOT temperature and the cavity waist size. This transit time broadening was not limiting our system, as this was much narrower than the natural atomic linewidth of the $^1\text{S}_0 \rightarrow ^3\text{P}_1$ transition, $\Gamma/2\pi$. The system was probed for $100 \mu\text{s}$ during all the experiments presented in this chapter. The linewidth of the pre-stabilized probe laser was evaluated to be 800 Hz during the probing timescale (described in Sec. 5.5b). The transit time broadening and the probe laser linewidth did not affect the system behavior significantly but they were included in the theoretical model as a decoherence term (Γ_p in Eq. (3.5)). The single-atom-cavity coupling rate was found to be $g_0/2\pi = 590 \text{ Hz}$ based on the cavity dimensions and the atomic transition dipole. This yields a single atom cooperativity $C_0 = \frac{4g_0^2}{\kappa\Gamma}$ [Tanji-Suzuki et al., 2011, p. 31] of $C_0 = 3.2 \times 10^{-5}$. This single atom cooperativity represents the ratio of the rate at which a photon is emitted by an atomic decay into the cavity mode and the rate of the dissipation processes in the system. The atomic decay rate into the cavity mode is hence higher than the dissipation rates when $C_0 > 1$ and this parameter regime is often called the *strong coupling* regime. The atom-cavity systems studied in this work are not in this

ⁱⁱRadius of cavity mode waist.

regime. However, one other essential parameter is the so-called collective cooperativity $C = N_{\text{cav}}C_0$, which describes the ratio of the dissipation rates and the total photon decay rate into the cavity mode by all the intra-cavity atoms. This collective cooperative parameter was around $C = 630 \gg 1$ for the low finesse cavity. This brought our system into a regime with high collective cooperativity within the bad-cavity regime.

The experimental sequence shown in Fig. 6.1c) was performed for all spectroscopy experiments presented in this chapter. The MOT was fully loaded within 750 ms. The MOT was then turned off and the trapped atoms were released by using an AOM as a shutter for the cooling laser. The system was probed with the pre-stabilized probe laser at 689 nm during the entire sequence. Multiple orders of sideband components were applied on the probe laser by exposing a periodic phase modulation on the probe light using an *electro optical modulator* (EOM). This phase modulation frequency was $\Omega/2\pi = 500$ MHz resulting in a probe laser spectrum with 500 MHz frequency spacings between the components. Note that all probe laser components were simultaneously resonant with the empty cavity modes as the sideband frequency spacing was equal to the cavity mode spacing, $\Omega/2\pi = FSR$. The cavity transmission was detected by two *avalanche photo detectors* (APD). These transmission signals were acquired as data from 20 μ s after the MOT was turned off and the acquisition lasted for 100 μ s. The 20 μ s delay was implemented to prevent the cooling laser to affect the atoms during the data acquisition because the AOM, used to turn off the MOT, had a small after glow diffraction for up to 3 μ s after the RF signal to the AOM was turned offⁱⁱⁱ. It was evaluated that the released atoms stayed within the cavity mode during the data acquisition^{iv}. A final data acquisition was done 80 ms after the first data acquisition in order to have a reference measurement of the empty cavity.

6.1.1 *Absorption spectroscopy*

The two main observables of interest in this work are the atom induced *absorption* and *phase shift* of the probe laser. The atom induced absorption will be examined first in this section but it will soon be clear, that these two observables are closely interlinked.

ⁱⁱⁱThis afterglow was most likely due to imperfect damping of the phonons in the AOM crystal after the RF signal is turned off.

^{iv}The average atomic velocity in the radial direction of the cavity mode is $\langle v \rangle \sim 0.5$ m/s. The average displacement of the atoms is 0.5 m/s $\times 100$ μ s = 50 μ m, which is considerably less than the cavity waist radius $w_0 = 500$ μ m.

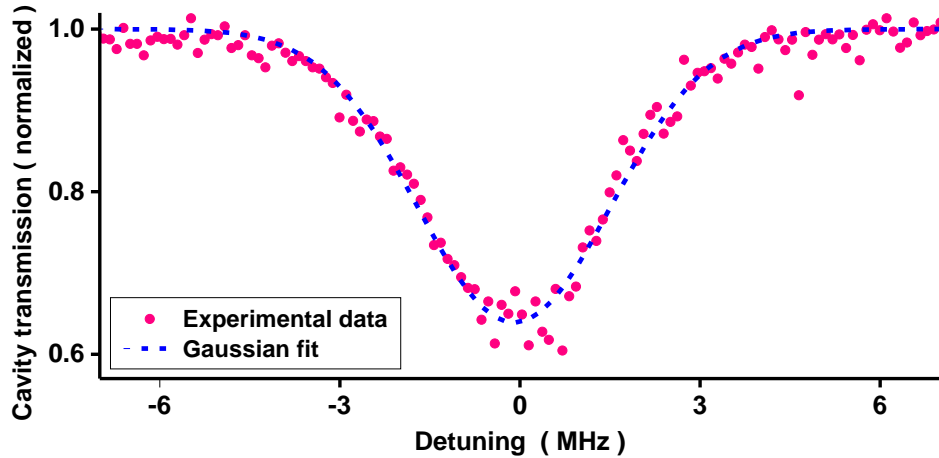


Figure 6.2: The cavity transmission power for different probe laser detunings. The red dots are experimental data, while the dashed blue line is a Gaussian fit yielding a doppler broadened linewidth corresponding to an atomic temperature of $T = 6 \text{ mK}$. The modulation index was ($x < 1$). The transmitted power is clearly reduced due to atomic absorption, when the probe laser is near resonance with the atomic transition. The lineshape details predicted in Fig. 3.3 are however not present as the cavity servo system counteracts the atomic induced phase shift. See Sec. 4.6.1 for details.

The atomic absorption was studied by measuring the optical power transmitted by the atom-cavity system as function of the probe laser detuning, and a single scan is shown in Fig. 6.2. This transmission signal was normalized with respect to the transmission signal for an empty cavity. The FWHM width $\delta\nu_D$ of the Doppler broadened absorption profile can be calculated from the Maxwell-Boltzmann distribution [Milonni and Eberly, 1988, p.103]:

$$\delta\omega_D = \frac{\omega_0}{c} \sqrt{\frac{2k_B T}{m} \ln 2}, \quad (6.1)$$

where ω_0 is the transition frequency, c is the speed of light, k_B is the Boltzmann constant and T and m are the temperature and the mass of the laser cooled ^{88}Sr . The transmission spectrum in Fig. 6.2 shows a clear absorption with a width of $\delta\omega_D/2\pi = 2.7 \text{ MHz}$, which according to Eq. (6.1) corresponds to an sample temperature of $T = 6 \text{ mK}$ for ^{88}Sr .

The transmission lineshape shown in Fig. 6.2 is however strikingly different when compared with the theoretically predicted transmission spectrum shown in Fig. 3.3. This difference is due to the requirement that the atom modified optical cavity was forced to be on resonance with the probe laser at all time during the experiments. The theoretical model described in Chap. 3 required that the *empty* cavity frequency ω_c was on resonance with the probe laser frequency ω_l , $\omega_l = \omega_c$. In the theoretical model, the atom induced phase shifts brought the probe light out of resonance of the combined atom-cavity system and reduced the transmission, which resulted in the lineshape shown in Fig. 3.3. In the experimental system, the cavity servo system counter-acted the atomic induced phase shift such that the $\omega_l = \omega_c$ requirement was no longer valid. Hence, the slightly different requirement inflicted by the cavity servo system was modifying the transmission lineshape shown in Fig. 6.2.

The main purpose of this work is to study the prospects of using the atomic induced phase dispersion as an error signal for high performance laser stabilization. With this in mind, a modification of the absorption lineshape might seem harmless for the laser stabilization prospects. However, it turns out, that the measurements of the phase dispersion is also complicated by the requirement inflicted by the cavity servo system. Hence, the modifications caused by the cavity servo system are described in the following. Note, that whereas the following description is formulated coherently, such that the reader does not need to jump back to previous sections, a part of the following description is repetition from Sec. 4.6.1. The full connection between the measured observables and the theoretically predicted values has been described in more details in Sec. 4.6.1.

Modifications due to the cavity servo system

Any electromagnetic field E_{out} transmitted through an optical cavity is modified according to a complex transmission coefficient described as [Riehle, 2004, p.101]:

$$E_{\text{out}} = \frac{Te^{i\varphi}}{1 - Re^{i2\varphi}} E_{\text{in}} = \chi E_{\text{in}}, \quad (6.2)$$

where φ is the single cavity round-trip phase shift of the electromagnetic field, E_{in} is the input field and T (R) is the power transmission (reflection) coefficient of the cavity mirrors.

This complex single round-trip phase for the probe laser in this work, φ_0 , can be expressed as:

$$\varphi_0 = \phi_{\text{cavity}} + \beta_D + i\beta_A, \quad (6.3)$$

where β_D and β_A describe the single pass dispersion and absorption due to the atoms present in the cavity, and ϕ_{cavity} is the phase shift due to propagation in the empty cavity. The j 'th order sideband component experiences a different single round-trip phase $\varphi_{\pm j}$:

$$\varphi_{\pm j} = \phi_{\text{cavity}} \pm j\pi, \quad (6.4)$$

where $\pm j\pi$ is added by the sideband detuning of $\pm j\Omega$. Equation (6.4) is not affected by the atomic absorption and phase shift, as the sideband frequencies were separated from the carrier frequency by $\Omega/2\pi = 500$ MHz, which was far off resonant with the natural linewidth of the $^1S_0 \rightarrow ^3P_1$ transition, $\Gamma/2\pi = 7.5$ kHz. The cavity servo system controlled ϕ_{cavity} by controlling the cavity length using the piezo electric element attached on one of the mirrors such that a standing wave was present inside the atom modified cavity at all time. This servo system adjusted ϕ_{cavity} such that the following standing wave condition was maintained:

$$\text{Re}(\varphi_0) = \phi_{\text{cavity}} + \beta_D = m\pi, \quad (6.5)$$

where m is an integer. The transmission coefficient χ_0 becomes purely real for this condition:

$$\chi_0 = \frac{Te^{-\beta_A}}{1 - Re^{-2\beta_A}}. \quad (6.6)$$

The theoretical transmission lineshape predicted in Chap. 3 was converted^v to the carrier transmission coefficient χ_0 and shown as the blue dashed line in Fig. 6.3. The reduction in transmission due to the atom induced phase shift, which was seen for large detunings (~ 1 MHz) in Fig. 3.3, is not present in the theoretical plot of χ_0 in Fig. 6.3. This is because χ_0 only describes the atomic absorption, while the transmission lineshape shown in Fig. 3.3 is also modified by the atomic phase shift. The power transmission coefficient for the probe laser is $|\chi_0|^2$. It is however already apparent by considering the lineshape of $|\chi_0|$ in Fig. 6.3 that this lineshape is more consistent with the experimentally observed transmission lineshape shown in Fig. 6.2.

The modifications of the transmission coefficients imposed by the cavity servo system will not only affect the cavity transmitted power.

^vThis conversion was done by following the procedures described in Sec. 4.6.1.

The results from demodulation techniques such as the NICE-OHMS technique (described in Sec. 4.6) will also be modified by the cavity servo system. These modifications are not included in the conventional literature concerning the NICE-OHMS technique [Ye et al., 1998, Ye and Lynn, 2003]. However, it was found during this work, that these modifications are of importance, when the atomic induced phase shifts are large, and when the amplitude of the sideband components are comparable with the carrier.

The following section describes the phase shift and absorption of the atom-cavity system measured by employing the NICE-OHMS technique with great emphasis on the modifications caused by the cavity servo system.

6.1.2 Demodulation spectroscopy

The NICE-OHMS technique (described in Sec. 4.6) was used for measuring the phase dispersion and absorption lineshapes of the atom-cavity system studied in this work. The NICE-OHMS technique involves demodulation of the total cavity transmitted field intensity. It was found in this work, that the modifications of the transmission coefficients described in the previous section also affect the demodulated signals. The first part of this section describes these modifications of the NICE-OHMS signals, while experimental measurements of the NICE-OHMS signals are interpreted in the latter part.

Sideband components were added to the probe laser spectrum as illustrated in Fig. 6.4 in order to employ the NICE-OHMS technique. The transmission coefficient $\chi_{\pm j}$ ($j \neq 0$) for the sidebands is also modified by the cavity servo system. This transmission coefficient turns out to be complex when inserting Eq. (6.5) in Eq. (6.4):

$$\chi_{\pm j} = \frac{Te^{i(\pm j\pi - \beta_D)}}{1 - Re^{2i(\pm p\pi - \beta_D)}}. \quad (6.7)$$

The cavity servo system has transferred the atom induced phase shift β_D onto the sideband transmission coefficient! Hence, $\chi_{\pm j}$ ($j \neq 0$) contains information about the attenuation of the cavity transmission caused by the atomic phase shift bringing the cavity out of resonance. The final cavity transmitted field up to the second order sidebands can now be described as:

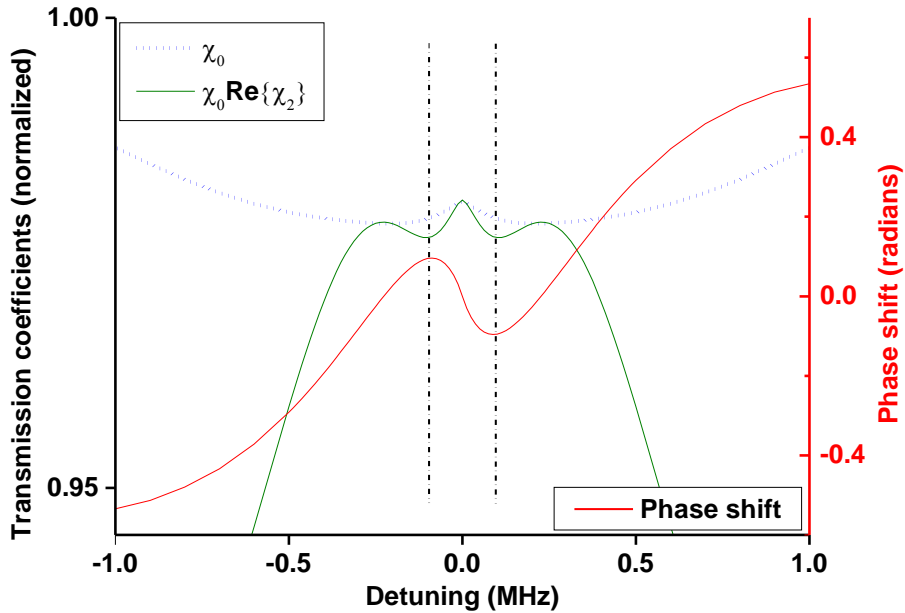


Figure 6.3: From [Christensen et al., 2015a, Appendix]. Theoretical values of the transmission coefficient of the carrier (dashed blue), χ_0 , the combined line shape of the atomic absorption and the attenuation due to atomic dispersion (green), $\chi_0 \text{Re}\{\chi_2\}$, and the total cavity transmitted phase shift (red). The black vertical dashed lines highlight the fact that transmission minima occur at dispersion maxima.

$$\begin{aligned} E_{\text{out}} = & E_0 \left(J_0(x) \chi_0 e^{i\omega_l t} \right. \\ & + J_1(x) \chi_1 e^{i(\omega_l + \Omega)t} - J_1(x) \chi_{-1} e^{i(\omega_l - \Omega)t} \\ & \left. + J_2(x) \chi_2 e^{i(\omega_l + 2\Omega)t} + J_2(x) \chi_{-2} e^{i(\omega_l - 2\Omega)t} \right), \end{aligned} \quad (6.8)$$

where ω_l is the frequency of the probe carrier and $J_j(x)$ is the j 'th order regular Bessel function describing the amount of power transferred from the carrier to the j 'th order sideband when modulated by an EOM with modulation index x . The spectrum of the probe laser components and the relation to the atomic and cavity spectrum are illustrated in Fig. 6.4. The transmitted field power can be detected by a fast photo diode and

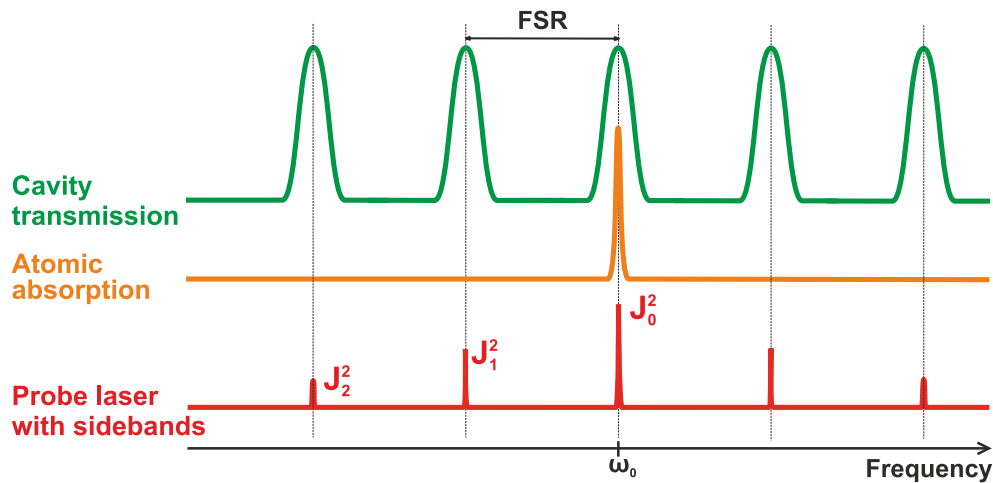


Figure 6.4: Relation between the spectral components relevant for the NICE-OHMS technique. The probe laser spectrum is shown for up to the second order sidebands. J_j is the j 'th order regular Bessel function which illustrate the power ratio of the carrier and sideband components of the probe laser according to Eq. (6.8).

demodulated by $\Omega/2\pi = FSR$ and $2\Omega/2\pi = 2FSR$ as shown in Fig. 6.1. The demodulation with $\Omega/2\pi = FSR$ yield a signal $S_{1\Omega}$ which is proportional to:

$$S_{1\Omega} \propto J_0(x)J_1(x)\chi_0 \cdot \text{Im}(\chi_1) \quad (6.9)$$

$$\left(+J_1(x)J_2(x)(\chi_2\chi_1^* - \chi_1\chi_2^*) + J_2(x)J_3(x)(\chi_2^*\chi_3 - \chi_2\chi_3^*) \right).$$

The first term of Eq. (6.9) is proportional with the atomic induced phase, $S_{1\Omega} \propto \sin(\beta_D)^{\text{vi}}$, and this signal corresponds to the conventional expression (shown in Eq. (4.13)) for the NICE-OHMS technique without modifications from the cavity servo system. Furthermore, $S_{1\Omega} \propto \beta_D$ is valid in the limit of small atomic phase shifts, and this allows a linear relation between the measured $S_{1\Omega}$ signal and the theoretically predicted near resonance phase shifts. The last terms inside the parenthesis in Eq. (6.9) are only small corrections for large phase shifts but they are included for completeness. These corrections do not modify the dispersion signal near resonance and the laser stability performance of the system is not affected.

^{vi}This is shown explicitly in Eq. (4.24).

Information related to the transmission lineshape of the transmitted field can be achieved by demodulating the transmitted field with twice the FSR, $2\Omega/2\pi = 2\text{FSR}$ (here for sidebands up to third order):

$$S_{2\Omega} \propto 2J_0(x)J_2(x)\chi_0 \cdot \text{Re}(\chi_2) - J_1^2(x)|\chi_1|^2 + J_1(x)J_3(x)(\chi_1^*\chi_3 - \chi_1\chi_3^*) \quad (6.10)$$

The green line in Fig. 6.3 corresponds to the first term of Eq. (6.10), $\chi_0 \cdot \text{Re}(\chi_2)$. Whereas χ_0 (blue line in Fig. 6.3) only contains information about the atomic absorption (see Eq. (6.6)), the attenuation due to the atomic phase shift is described by $\text{Re}(\chi_2)$. Hence, this $\chi_0 \cdot \text{Re}(\chi_2)$ -term describes a combination of both the atomic absorption (χ_0) and dispersion ($\text{Re}(\chi_2)$). This variation of the NICE-OHMS technique with demodulation at $2\Omega/2\pi = 2\text{FSR}$ is called *overtone demodulation* henceforth. It is shown in Fig. 6.3 that $\chi_0 \cdot \text{Re}(\chi_2)$ reproduces features similar to the characteristic features already seen in the theoretical transmission lineshape in Fig. 3.3 such as the small *dips* for small detunings and the large reduction of the transmission for larger detuning. These transmission features were theoretically predicted for a system without the restriction imposed by the cavity servo system as previously described in details in Sec. 3.2.1. The total atomic dispersion is also shown in Fig. 6.3, and it is evident that the minima of $\chi_0 \cdot \text{Re}(\chi_2)$ occurs at the dispersion maxima (highlighted with dashed vertical lines). Note however, that $\chi_0 \cdot \text{Re}(\chi_2)$ is not exactly equal to the theoretically predicted transmission and Eq. (6.10) has in addition two other correction terms. These correction terms do modify the line shape but they do not erase the structures. The signal described in Eq. (6.10) is hence only *related* to the transmission lineshape of the transmitted field. Nevertheless, this extended description of the NICE-OHMS technique enables a complete connection^{vii} between the complex transmission coefficients χ_j and the theoretical predictions for the cavity transmission derived in Chap. 3.

Figure 6.5 shows the NICE-OHMS signals for demodulation at $\Omega/2\pi = 1 \times \text{FSR}$ and $2\Omega/2\pi = 2 \times \text{FSR}$, which were obtained experimentally. The solid and dashed lines are predictions based on the theoretical model presented in Chap. 3, where the modifications due to the cavity servo system are included. These theoretical predictions were calculated by inserting the experimentally verified number of atoms, probe laser linewidth, laser input power, cavity dimensions and cavity linewidth in the theoretical

^{vii}This connection is outlined in Eq. (4.26)–(4.27).

model and only a scaling factor was left as a free parameter to scale the measured data to match the theoretical values. The temperature was allowed to vary in the range of $T = 2 - 5$ mK as changes in the reference oven setup for stabilization of the cooling laser frequency had changed the temperature of the trapped atoms during the years these experiments were performed. Both the scaling factor and the temperature were only changed if a relevant experimental configuration had been changed. The $\Omega/2\pi = 1 \times \text{FSR}$ and $2\Omega/2\pi = 2 \times \text{FSR}$ signals shown in Fig. 6.5 are measured separately. However, simultaneous measurements were possible and one example is shown in Fig. A.7 in Appendix A.6.

Figure 6.5a) shows the NICE-OHMS signals obtained by the conventional NICE-OHMS technique with demodulation at $\Omega/2\pi = 1 \times \text{FSR}$, which represents the atomic induced phase shift through Eq. (6.9). The values on the vertical axis are the measured signal values in volts and the theoretical values are scaled to match the measured signals. The measured values and the theoretical predictions agree remarkably well for most detuning values. A sharp dispersion signal with a steep slope is observed around resonance as expected from Fig. 3.3.

This sharp dispersion feature is the saturated absorption feature, which was predicted in Sec. 3.4.2 to be a promising frequency discriminator for laser stabilization. This dispersion feature is examined in details in the inset in Fig. 6.5a) which shows a zoom of the central dispersion curve close to resonance. The vertical axis of this inset corresponds to the atomic phase shift in radians, as it was described earlier in this section. This central part of the NICE-OHMS signal scales linearly with the atom induced phase shift of the cavity transmitted field.

Two theoretical plots are also shown in the inset of 6.5a). The blue solid line displays the full theory including all Fourier components in Eq.(3.13)–(3.15), which corresponds to including multi-photon doppler resonances to all orders. The black dashed line on the other hand is based on a theoretical prediction where only the $l = 0$ Fourier component is included in Eq.(3.13)–(3.15). Hence, this dashed line corresponds to a situation where the velocity dependent doppler resonances are not taken into account. The best agreement is observed for the full theoretical model including all doppler orders. Note that the doppler resonances tend to decrease the phase dispersion slope around resonance slightly as expected from Fig. 3.9. The two theory lines (solid and dashed) are also included in the broad frequency scan shown in Fig. 6.5(a) but the doppler resonances seem to only affect the central dispersion.

It seems reasonable to conclude based on the agreement between data and the full theory, that the doppler resonances affect and degrade the

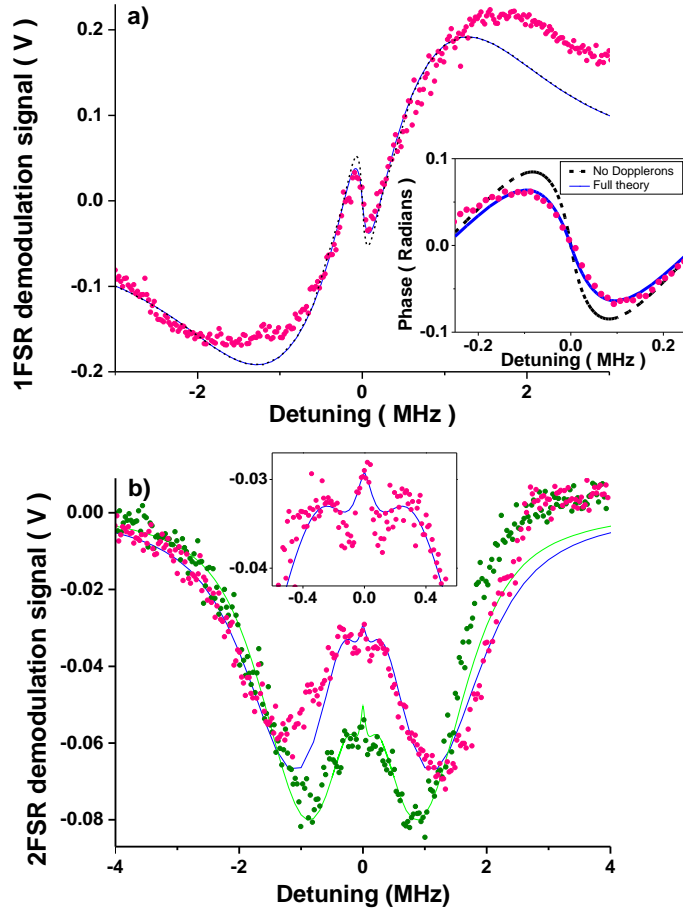


Figure 6.5: From [Christensen et al., 2015a, Fig. 2]. The solid and dashed lines are predictions based on the theoretical model presented in [Westergaard et al., 2015, Tieri et al., 2015]. The dots are data measured by cavity-enhanced FM spectroscopy. All data are averaged values, where approximately five times as many measurements have been performed for data in b) due to the weaker signal compared to data in a). a): Frequency scan of the cavity transmitted phase shift close to resonance for an carrier input power of 240 nW, total number of atoms of $N = 5.0 \cdot 10^8$ and atom temperature of $T = 5.0 \text{ mK}$. The data points are averages of 9 measurements. Theoretical values from Eq. (6.9) are scaled to data. Inset: High resolution scan of the central region. The vertical axis in this central region corresponds to the total atomic phase shift of the transmitted sideband and data is scaled to theory. b): Frequency scans of the absorption lineshape of the cavity transmitted field measured by the NICE-OHMS technique obtained with a demodulation $\Omega/2\pi = 2\text{FSR}$. The total number of atoms is $N = 4.5 \cdot 10^8$, atom temperature of $T = 5.0 \text{ mK}$ and total input power of 310 nW (blue line) and 155 nW (green line). Theoretical values from Eq. (6.10) are scaled to data. Inset: High resolution scans around the central region. The units on the inset axes are the same as in b).

central dispersion feature to some extend. One remaining concern could be, if the dashed theory line excluding doppleron resonances could also agree with the experimental data, if other parameter values (scaling factor, number of atoms etc.) were chosen for the theoretical calculations. This agreement can possibly be achieved, but it will most likely not be possible within the margins of the experimentally verified parameters. More importantly, the non-linear dynamics studied in the following sections would most probably not be reproduced, if the wrong parameters values were used for the theoretical calculations.

The magnitude of the slope of the central dispersion feature and the signal-to-noise-ratio of the measured dispersion signal are ultimately determining the obtainable laser linewidth when this system is used as a frequency discriminator. The dynamics of the dispersion slope was studied experimentally and the results of these studies are presented later in Sec. 6.1.4 and Sec. 6.1.3.

It was shown in Eq. (6.10) that information related to the absorption of the cavity transmitted light could also be obtained by using the NICE-OHMS technique with overtone demodulation at $2\Omega/2\pi = 2 \times \text{FSR}$. The remaining part of this section will address this alternative demodulation signal in details.

This signal was obtained experimentally by demodulating the cavity transmitted field at $2 \times \text{FSR}$ (described in Eq. (6.10)) and Fig. 6.5b) shows this signal for different probe laser detunings. This signal is related to the absorption line shape of the cavity transmitted field. Background transmission signals acquired for an empty cavity were subtracted from the experimental values shown in Fig. 6.5b)^{viii}. A similar background value for an empty cavity has been subtracted from the theoretical values. Finally, the theoretical value has been scaled to match the experimental values. The absolute value of this background corrected signal represents the degree of absorption experienced by the cavity transmitted light. A great agreement is once again observed between the theoretical predictions and the values measured by demodulation at $2\Omega/2\pi = 2 \times \text{FSR}$. A slight asymmetry is, however, present for the experimental data in both Fig. 6.5a) and Fig. 6.5b). This asymmetry is expected to be due to a drift of some relative phase between the light wavefront and the demodulation phase during scan. Measurements from the vacuum cavity system hints that this asymmetry might be linked to the position of the piezo element for controlling the cavity length (described in Sec. 6.3).

^{viii}This background signal was measured in the last data acquisition part of the measurement sequence (after the 80 ms delay) shown in Fig. 6.1c).

The expression for the NICE-OHMS signal for demodulation at $\Omega/2\pi = 2 \times \text{FSR}$ includes some correction terms (shown in parenthesis in Eq. (6.10)). Whereas the correction terms^{ix} for the conventional NICE-OHMS signal with demodulation at $\Omega/2\pi = 1 \times \text{FSR}$ were small, all correction terms were needed to be included in Eq. (6.10) in order to achieve full agreement between the theoretical predictions and the experimental data in Fig. 6.5b). The significance of these higher order corrections are governed by the modulation index x for the Bessel functions $J_{\pm j}(x)$ in Eq. (6.9) and Eq. (6.10). This modulation index x was determined experimentally by measuring the transmission of the cavity while scanning the length of the cavity. The modulation frequency for applying the sidebands was detuned a few MHz from the cavity FSR, such that the sideband components were observed as new transmission components as shown in Fig. 6.6. The Bessel functions $J_{\pm j}(x)$ were then determined by comparing the peak heights of the carrier and sideband transmission components.

The importance of an accurate determination of the modulation index x is expressed in Fig. 6.5b) as the results shown here were measured for two different modulation indices: $x = 0.65$ for the blue theory line and of $x = 0.57$ for the green theory line. The two different modulation values are shown to illustrate that the signal described in Eq. (6.10) takes the optical power ratio of the carrier and the sidebands into account in good agreement with the experimental data.

One final correction included in the theoretical predictions is caused by the presence of several sideband orders, which contributes to the servo error signal when the atomic phase shift is large. This error signal

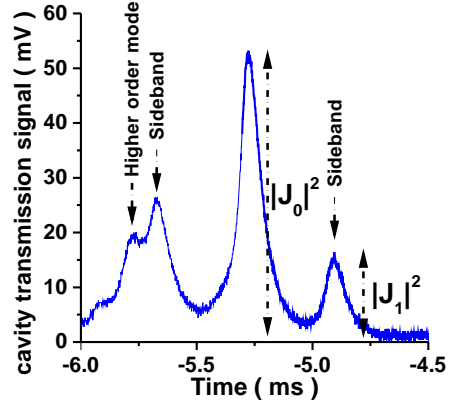


Figure 6.6: Example of cavity transmission while scanning the cavity length. The modulation frequency for sideband generation was set to slightly deviate from the cavity FSR such that the sidebands were visible. The modulation index was determined by comparing the carrier ($|J_0|^2$) and sideband ($|J_1|^2$) heights. The left sideband component seems higher than the right sideband, as this left sideband coincide with a higher order spatial mode of the cavity.

^{ix}Shown in parenthesis in Eq. (6.9).

contribution will slightly offset the cavity resonance relative to the carrier frequency [Ye and Lynn, 2003]. These corrections were described in details in Sec. 4.6.1. Fortunately, these corrections turned out to be small but they are included in the calculated values in Fig. 6.5 for completeness.

The carrier input power dependency of the absorption lineshape is also expressed in Fig. 6.5b) as the two absorption line shapes shown here were measured for two different carrier input powers, 310 nW (red dots) and 155 nW (green dots). It is not shown in Eq. (6.10), but the 2FSR demodulation signal is proportional to the total optical input power $S_{2\Omega} \propto |E_{in}|^2$. A carrier input power of 155 nW should thus in general yield about half of the signal measured for twice as much carrier input power (310 nW). This is indeed confirmed experimentally, however, the data points for carrier input power of 155 nW are normalized to the signal for a carrier input power of 310 nW in Fig. 6.5b). This scaling has been done in order to illustrate the line shape dynamics on the same figure.

The detailed near resonant transmission lineshape structures predicted by the theoretical model (shown in Fig. 3.3) were also observed by using the NICE-OHMS technique with demodulation at $\Omega/2\pi = 2 \times \text{FSR}$. The inset in Fig. 6.5b) shows a zoom of the central region and represents the transmission structures near resonance. This transmission signal was slightly reduced for small detunings and *dips* were formed on both sides of the central saturation peak at around 100 kHz. This transmission reduction was due to the atom induced phase shift, which reduced the sideband transmission coefficient $\text{Re}(\chi_2)$ in Eq. (6.10). The phase shift induced by the atoms decreased eventually for larger detuning and the transmission was increased resulting in two shoulders located next to the dips, when the atomic phase shift was zero again. This *dip* structure is outlined in Fig. 6.3. This detailed transmission structure was hence successfully observed by using the NICE-OHMS technique with demodulation at $\Omega/2\pi = 2 \times \text{FSR}$, even though this structure was not observed initially when the total cavity transmitted power was measured, while the cavity was kept on resonance with the probe carrier (This transmission is shown in Fig. 6.2).

One final comment regarding the inset of Fig. 6.5b) should be added: The structures in the inset of Fig. 6.5b) seem more pronounced in the measured data, than predicted by theory. This might be due to the limited bandwidth of the cavity locking scheme. The data acquisition was started 20 μs after the cooling lasers were turned off. The near resonant atomic phase shift builds up after this and reaches steady state with a rate comparable to the Rabi frequency^x while the cavity bandwidth is only

^xIn the order of $\sim 100 \text{ kHz}$.

about 1 kHz (described in Sec. 5.2.2), which in fact is far from fast enough to react on the atomic phase shift before the data acquisition starts.

In conclusion, great agreement has been observed between the theoretically calculated complex transmission coefficients and the quantities measured experimentally by demodulating the cavity transmitted field at $\Omega/2\pi = 1 \times \text{FSR}$ and $2\Omega/2\pi = 2 \times \text{FSR}$. It was observed that both the atomic induced phase shift and absorption were modified due to the cavity servo system. It was shown in Fig. 6.5a) that a narrow doppler free dispersion feature was observed around the resonance of the broad thermal dispersion. It was predicted earlier in Sec. 3.4.2, that this narrow dispersion has a great potential as an error signal for laser stabilization, even though velocity dependent multiphoton scattering processes seemed to slightly degrade the error signal slope. The two plots in Fig. 6.5b) gave strong indications, that the measurements agreed with the dynamics of the theoretical model. The observation of the central doppler free dispersion allowed detailed studies of the dynamics of this dispersion feature with the purpose of identifying the optimal parameters for laser stabilization. The results of such studies are presented in the following sections, Sec. 6.1.3–6.1.4.

6.1.3 Atom number dependency

The previous section presented, that a sharp dispersion feature was observed for the atom-cavity system studied in this work. In addition, it was predicted in Chap. 3, that this dispersion feature might prove promising as an error signal for laser stabilization. The slope of this narrow dispersion feature is one of the defining system parameters for laser stabilization, as the slope determines the frequency sensitivity of this feature. The dynamics of this dispersion slope was predicted in Chap. 3 to exhibit nonlinear behavior and the determination of the optimal system parameters was not trivial. The following sections present experimental studies of the dynamics of the dispersion slope.

The narrow doppler free phase dispersion was measured for a fixed input probe power and different number of atoms inside the cavity mode, N_{cav} . N_{cav} was changed from $N_{\text{cav}} = 1.2 \times 10^7$ to $N_{\text{cav}} = 2.5 \times 10^7$ by varying the MOT loading time. The measured central dispersion features are shown in Fig. 6.7a)–6.7d). The dispersion slopes at resonance were determined as the resonance slope of theoretical fits performed on the entire dispersion feature.^{x_i}. The resonance slope can in principle be determined by restricting

^{x_i}Note that it was described in the previous Sec. 6.1.2 that these measured slopes at resonances were not modified by the restrictions imposed by the cavity servo system.

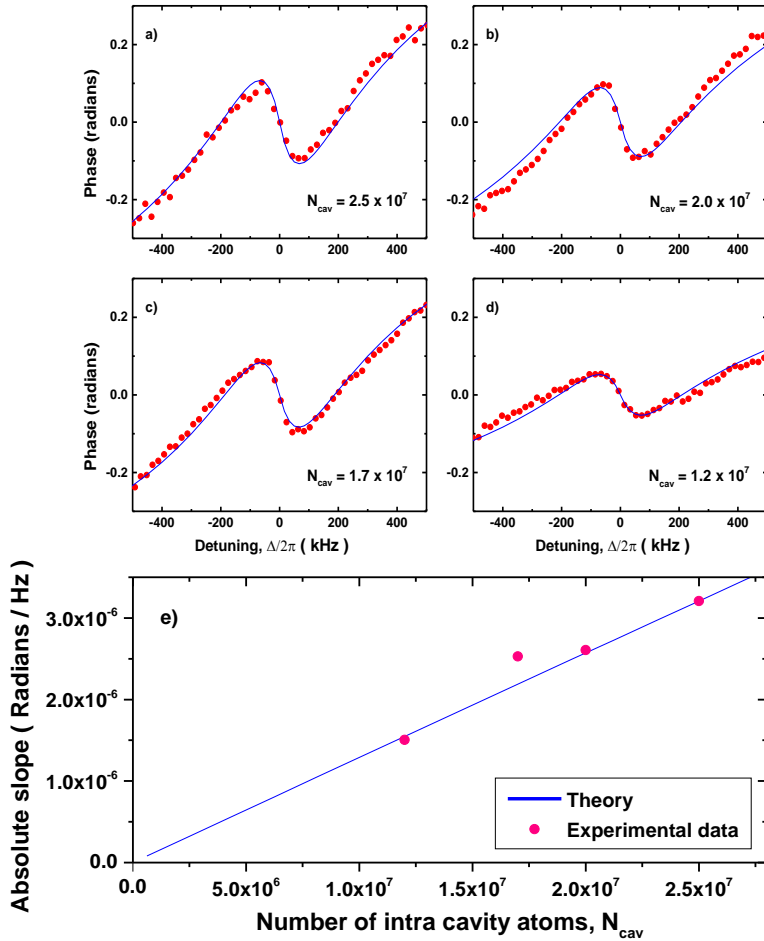


Figure 6.7: a)–d): Near resonant phase dispersion lineshapes. The number of intra-cavity atoms N_{cav} was changed from 2.5×10^7 to 1.2×10^7 , while all other parameters were kept constant ($P_{\text{in}} = 650 \text{ nW}, T = 4 \text{ mK}$). The solid lines are theoretical fits based on our theoretical model described in Sec. 3 and the points are experimentally obtained values. Each point is an average of about 10 separate measurement sequences. e): The dispersion slope at resonance ($\Delta = 0$) is evaluated based on the theoretical fits and shown as a function of the number of atoms. The theoretical slope (blue solid line) scales linearly with the number of atoms in this parameter regime and the experimental slope values (red dots) seem to follow this trend.

such a fit to only the central linear part of the dispersion feature, but the dynamics of the entire dispersion lineshapes were studied by performing the fit to the entire dispersion feature. Figure 6.7a)–6.7d) show great

agreement between the measured dispersion feature and the theoretical fits. This agreement is not just a validation of the theoretical model, but it also allows studies of the experimental dynamics relevant for laser stabilization.

It was predicted in Sec. 3.3 that the slope of the central phase dispersion would depend linearly on the total number of atoms inside the cavity (this is illustrated in Fig. 3.5). The dispersion slopes at resonance were determined from the fits shown in Fig. 6.7a)–6.7d) and these slope values are shown in Fig. 6.7e) as function of the number of intra cavity atoms. A linear trend is seen in Fig. 6.7(e) as expected from the theoretical model. The slope dependency of the number of intra cavity atoms shown in Fig. 3.5 predicted that the slope value will be reduced for very large number of atoms. However, this will only occur for unrealistically large number of atoms. The slope can hence be improved for laser stabilization by straight forwardly increasing the number of atoms. Note, that the number of atoms presented in Fig. 3.5 is the total number of trapped atoms N , while N_{cav} is the number of the trapped atoms which are inside the optical cavity. It is evaluated based on the cavity mode volume and the MOT volume that $N = 5.0 \times 10^8$ corresponds to $N_{\text{cav}} = 2.5 \times 10^7$.

Whereas the atom number dependency of the dispersion slope is linear and simple, the input power dependency is strongly non-linear and the optimal parameters are not trivially determined. Hence, the input power dependency is studied experimentally in the following section.

6.1.4 Input power dependency

The theoretical model described in Chap. 3 predicted that the slope of the doppler free dispersion observed in the previous Sec. 6.1.2 depends strongly non-linearly on the input probe power P_{in} . The theoretical prediction of the optical input power dependency of this dispersion slope was illustrated previously in Fig. 3.10b). It was observed here, that this dependency exhibits an optimal input power, where the absolute slope is maximized.

The narrow dispersion feature was measured experimentally for different input powers and the dispersion slope at resonance was determined by performing theoretical fits following the same procedures as in Sec. 6.1.3. Representative dispersion scans are shown in Fig. 6.8a)–f) in order to illustrate the dynamics. It is clear that the dispersion width is power broadened for large input powers, but an optimal input power cannot be identified by examining only the dispersion slopes.

The experimentally determined dispersion slopes are shown in Fig. 6.9a) for input powers in the range from $P_{\text{in}} = 17 \text{ nW}$ to $P_{\text{in}} = 360 \text{ nW}$. The measurements (dots) and theoretical values (solid lines) are in good agreement and the non-linear input power dependency predicted in Fig. 3.10b) is evident. It is at first glance disappointing that the maximum absolute values of the slope for lower input powers were not measured. However, the prospects for laser stabilization with this system do not depend only on the phase dispersion slope. It was described earlier in Sec. 3.4 that the ideal shot noise limited linewidth is also governed by the input power in accordance with Eq. (3.28). The ideal shot noise limited linewidth for each measured parameter was calculated and shown in Fig. 6.9b). The data sets in Fig. 6.9a) and b) are identical.

It should be stressed that the linewidths shown in Fig. 6.9b) are ideal linewidths theoretically evaluated based on the experimentally measured phase dispersion. Hence, these linewidths have not been realized. Nevertheless, the input powers corresponding to the predicted minimum shot-noise limited linewidth has been realized and measured for a fixed ratio of the optical powers of the probe carrier and sidebands. Interestingly, Fig. 6.9b) shows that the minimum shot-noise limited linewidth occurs

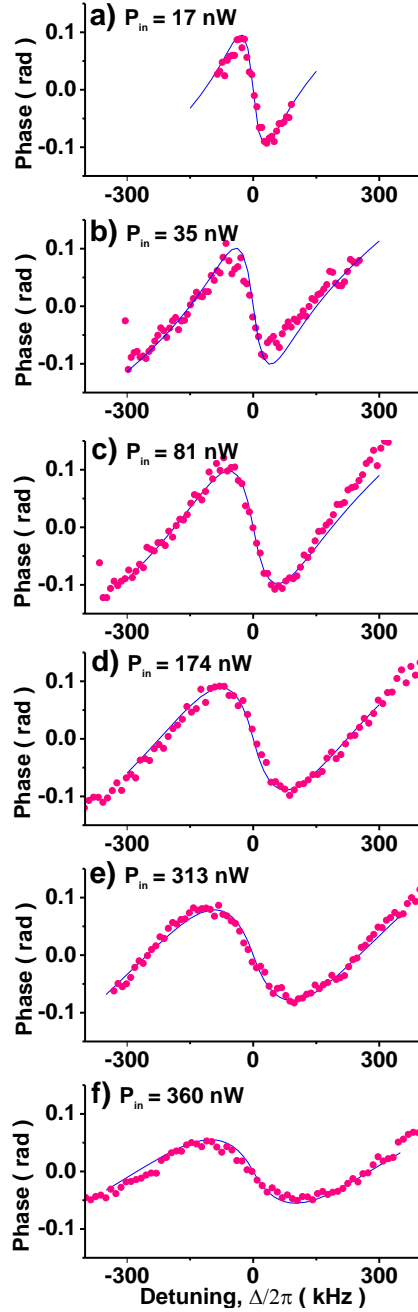


Figure 6.8: a)–f): Near resonant phase dispersion line shapes. The cavity input power P_{in} was changed from 17 nW to 360 nW, while all other parameters were kept constant ($N_{\text{cav}} = 2.0 \times 10^7, T = 5 \text{ mK}$). The solid lines are theoretical fits based on our theoretical model described in Sec. 3 and the points are experimentally obtained values. Each point is an average of about 20–30 separate measurement sequences.

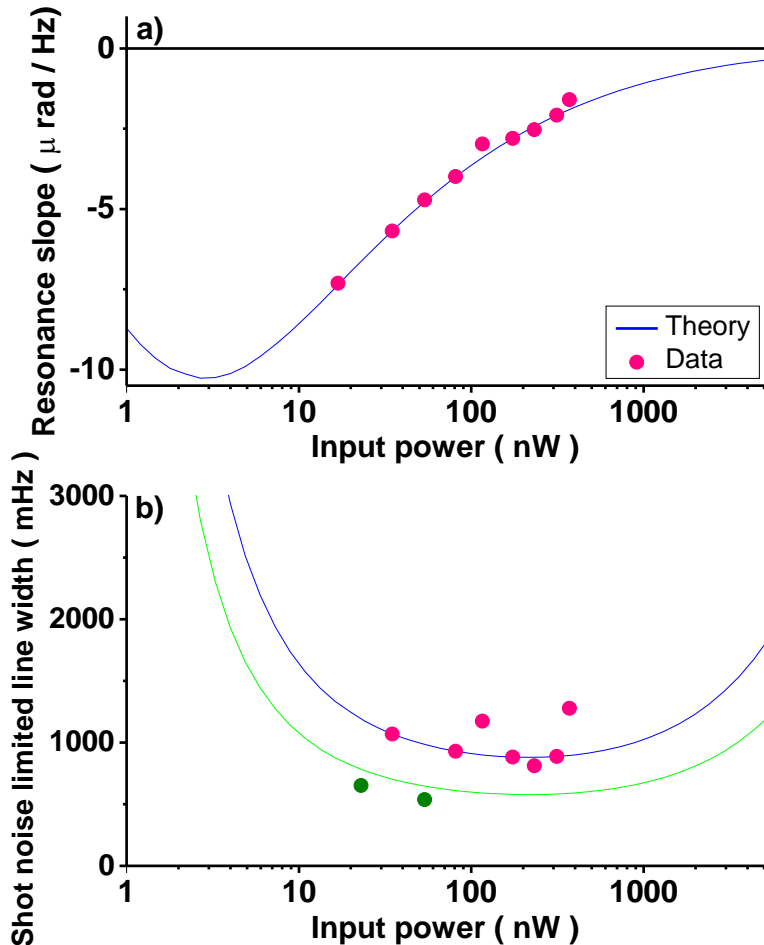


Figure 6.9: From [Christensen et al., 2015a, Fig. 3 (a)–(b)]. a): The near resonant slope of the phase dispersion measured for different input powers. The solid lines are theoretical predictions and the dots are experimental values based on the fits in Fig. 6.8. The data and theory are in excellent accordance and the nonlinear dependence is evident. Notice that the horizontal axes are logarithmic. b): The ideal shot-noise limited linewidth calculated from Eq. (3.43) for the measured parameters in a). The blue theory line corresponds to a ratio of carrier and sideband input powers of $\frac{P_c}{2P_s} = 1.65$ and the green theory line corresponds to $\frac{P_c}{2P_s} = 0.75$ in Eq. (3.43).

for higher input power than the input power for which the maximum absolute slope value occurs.

The carrier-sideband power ratio is governed by the modulation index x of the EOM (described in Eq. (6.8)). The shot-noise linewidth

in Eq. (3.28) is optimized for a carrier-sideband ratio of $\frac{P_{\text{sig}}}{2P_{\text{sideband}}} = 1$. This ratio corresponds to a modulation index of $x \approx 1.16$. However, this optimal carrier-sideband ratio was not optimized for the results shown in Fig. 6.9b). The carrier-sideband ratios for the measurements shown in Fig. 6.9 were determined to be $\frac{P_{\text{sig}}}{2P_{\text{sideband}}} = 1.65$ for the blue theory line and $\frac{P_{\text{sig}}}{2P_{\text{sideband}}} = 0.75$ for the green theory line. These ratios were determined by following the procedure described in Fig. 6.6. The minimum achievable shot-noise limited linewidth for this system was estimated to be as low as 500 mHz, even though the carrier-sideband ratio was not optimized. A line width of 500 mHz is already promising, but it was predicted in Sec. 3.4.2, that this shot-noise limited linewidth can be reduced even further by increasing the collective cooperative $C = C_0N$. C can be increased by increasing the total number of trapped atoms or by increasing the cavity finesse. It is technically difficult to increase the number of atoms by a factor of 10, but it is possible to increase the cavity finesse with several orders of magnitude. An upgraded vacuum cavity system with increased cavity finesse ($F = 1450$) was hence constructed (described in Sec. 5.2.3) during this work. This vacuum system is studied later in Sec. 6.3.

It is worth noting that the horizontal axis in Fig. 6.9b) is logarithmic. This allows a change in input power of one order of magnitude without degrading the shot noise limited linewidth significantly. It is hence not necessary to probe the system with technically challenging low input powers down to < 100 nW. Optimal laser stabilization can be achieved for more convenient higher input powers and the system can operate within a very wide range of input powers.

The measurements presented so far in this section were all performed in a cyclic manner as illustrated in Fig. 6.1c). Continuous laser stabilization on the presented system is hence not currently feasible, as the doppler free dispersion is smeared out when the cooling lasers are turned on. However, it seems within reach of the current technology to implement the techniques presented in this section into beam-line experiments [Chen, 2009, Schaffer et al., 2015], where a beam of cold atoms with high loading rates [Yang et al., 2015] is interrogated in a cavity. This opens the possibilities for a continuous laser stabilization on an atom-cavity system with a narrow optical transition. Another promising approach is to implement the same techniques to interrogate molecular systems with narrow optical transitions placed inside an optical cavity [Schaffer et al., 2015]. The proof-of-concept investigations of the non-linear spectroscopic dynamics of an atom-cavity system presented in this chapter sparked the initiatives

to realize the above mentioned promising systems. These new systems and the prospects for future studies are discussed in Sec. 8.

6.2 Other spectroscopic techniques

A number of different spectroscopic setups were developed during this work. Two of these setups are presented in the following sections: The first setup is the, *Sideband probing* which was a technique developed in an attempt to study the doppler free dispersion feature for probe input powers down to around 1 nW, such that the maximum slope could be measured (see Fig. 6.9). The second setup was developed in an attempt to measure *multi-photon recoils* from velocity dependent multi-photon scatterings.

Both setups did not lead to any conclusive results and the reader can skip forward to Sec. 6.3 if the reader is more interested in spectroscopic studies with the upgraded vacuum cavity system.

6.2.1 Sideband probing

While the input power corresponding to the minimal shot-noise limited linewidth was identified in Fig. 6.9b) the maximum absolute slope was however not realized in Fig. 6.9(a). This maximum absolute slope was not measured as the input carrier power P_{in} was too low for the cavity servo system to keep the cavity-atom system on resonance with the probe laser when $P_{\text{in}} < 10 \text{ nW}$. A variation of the NICE-OHMS technique was developed in order to probe the system with lower optical power. The probe laser frequency was shifted $1 \times \text{FSR}$ such as the atomic transition was probed by one of the sidebands. This technique was able to measure the same dispersion features as the conventional NICE-OHMS technique. This sideband probing technique and the experimental data are described in the following section.

The frequency relations of the involved spectra are as shown in Fig. 6.10 when the probe laser frequency is shifted $\Omega/2\pi = 1 \times \text{FSR}$. Only one of the first order sidebands are resonant with the atomic transition and the output electromagnetic field can be described as:

$$\begin{aligned} E_{\text{out}} = & E_0 \left(J_0(x) e^{i\omega_l t} \right. \\ & + J_1(x) \chi_{1,\text{sideband}} e^{i(\omega_l + \Omega)t} - J_1(x) e^{i(\omega_l - \Omega)t} \\ & \left. + J_2(x) e^{i(\omega_l + 2\Omega)t} + J_2(x) e^{i(\omega_l - 2\Omega)t} \right). \end{aligned} \quad (6.11)$$

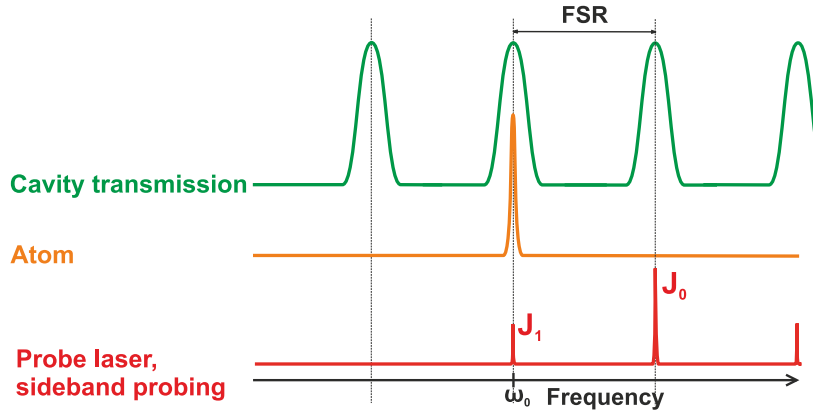


Figure 6.10: Relation between the spectral components relevant for the sideband probing configuration of the NICE-OHMS technique.

Here, $\chi_{1,\text{sideband}} = \frac{Te^{i(\beta_D+i\beta_A)}}{1-Re^{2i(\beta_D+i\beta_A)}}$ is the complex transmission coefficient of the sideband resonant with the atoms. It is assumed, that the optical power of this resonant sideband is significantly smaller than the total power of the carrier and other sideband orders. The atom induced phase shift β_D in $\chi_{1,\text{sideband}}$ is hence not transferred to other probe carrier components as it was the case for the conventional NICE-OHMS technique (described in Eq. (6.6) and (6.7)). The power of this cavity transmitted light can be detected and demodulated with a demodulation signal $\sin(\Omega \cdot t) = \frac{1}{2}(e^{i\Omega \cdot t} - e^{-i\Omega \cdot t})$. This demodulation yields a DC signal S_{sideband} by neglecting all oscillating terms (here with sidebands up to second order):

$$S_{\text{sideband}} \propto -(J_0(x)J_1(x) - J_1(x)J_2(x)) \cdot \text{Im}(\chi_{1,\text{sideband}}) \quad (6.12)$$

It can be shown by straight forward algebra^{xii}, that $\text{Im}(\chi_{1,\text{sideband}}) \propto \beta_D$ for $\beta \rightarrow 0$. The phase dispersion can hence potentially be measured through S_{sideband} .

One essential issue arises for this sideband probing technique. The relative phase between the cavity transmitted field and the demodulation signal, ϕ_{demodul} , turns out to govern the spectroscopic behavior of S_{sideband} . A significantly different signal $S_{\text{sideband},\pi}$ compared to Eq. (6.12) appears when the cavity transmitted light is demodulated with a demodulation signal $\sin(\Omega \cdot t + \pi) = \frac{1}{2}(e^{i\Omega \cdot t} + e^{-i\Omega \cdot t})$ (corresponds to $\phi_{\text{demodul}} = \pi/2$):

^{xii}The exact expression for Im is: $\text{Im}(\chi_{1,\text{sideband}}) = \frac{Te^{-\beta_A(1+Re^{2\beta_A})}\sin(\beta_D)}{1+R^2e^{-4\beta_A}-2e^{-2\beta_A}R\cos(2\beta_D)}$.

$$S_{\text{sideband},\pi/2} \propto (J_0(x)J_1(x) + J_1(x)J_2(x)) \cdot \text{Re}(\chi_{1,\text{sideband}}) - 2(J_0(x)J_1(x) + J_1(x)J_2(x)) \quad (6.13)$$

$\text{Re}(\chi_{1,\text{sideband},\pi/2})$ does in fact depend on the atomic phase shift (β_D) but the β_D dependency is not very intuitive:

$$\text{Re}(\chi_{1,\text{sideband},\pi/2}) = \frac{Te^{-\beta_A(1+R \cdot e^{2\beta_A})} \cos(\beta_D)}{1 - R^2 e^{-4\beta_A} - 2e^{-2\beta_A} R \cdot \cos(2\beta_D)}$$

Furthermore, two constant correction terms $2(J_0(x)J_1(x) + J_1(x)J_2(x))$ are added and $S_{\text{sideband},\pi/2}$ do not reflect the phase shift as clearly as S_{sideband} (described in Eq. (6.12)). The demodulation signal will in fact yield a superposition of Eq. (6.12) and Eq. (6.13) if the relative phase is any other value than $\phi_{\text{demodul}} = 0$ or $\phi_{\text{demodul}} = \pi/2$. This requires the demodulation phase to be adjusted to $\phi_{\text{demodul}} = 0 \pm m \cdot \pi$ (m is any integer) and this imposes strict requirements on the stability of the relative phase. These requirements for the demodulation phase are less strict for the conventional NICE-OHMS technique as a change in ϕ_{demodul} does only results in a change of scaling.

A series of experiments were performed in order to measure S_{sideband} and thereby determine the dispersion slope for very low input power. The probe carrier frequency was shifted by 500 MHz = FSR by implementing the AOM setup shown in Fig. 6.11. The cavity transmitted light is detected by a fast APD following the main experimental setup and cyclic sequence illustrated in Fig. 6.1. This detected signal is demodulated by mixing the signal with demodulation frequency of 500 MHz. The demodulation phase ϕ_{demodul} was controlled by changing cable lengths and by employing a voltage controlled phase shifter (Mini-circuits, JSPHS-661+). A broad frequency scan of this demodulated signal is shown in Fig. 6.12. The signal after the demodulation was in general smaller than the signals detected by the conventional NICE-OHMS technique and additional RF amplifiers were added. This high amplification level caused the amplifiers to saturate for broad frequency scans as can be seen on the left side of Fig. 6.12. The broad and narrow dispersion features (also seen in Fig. 6.5a)) are visible in Fig. 6.12 if the amplifier saturation is disregarded. The central dispersion feature is shown with a higher resolution in the inset in Fig. 6.12. It has hence been proven that this sideband probing technique can map out this central dispersion feature. However, difficulties of optimizing the demodulation phase ϕ_{demodul} and

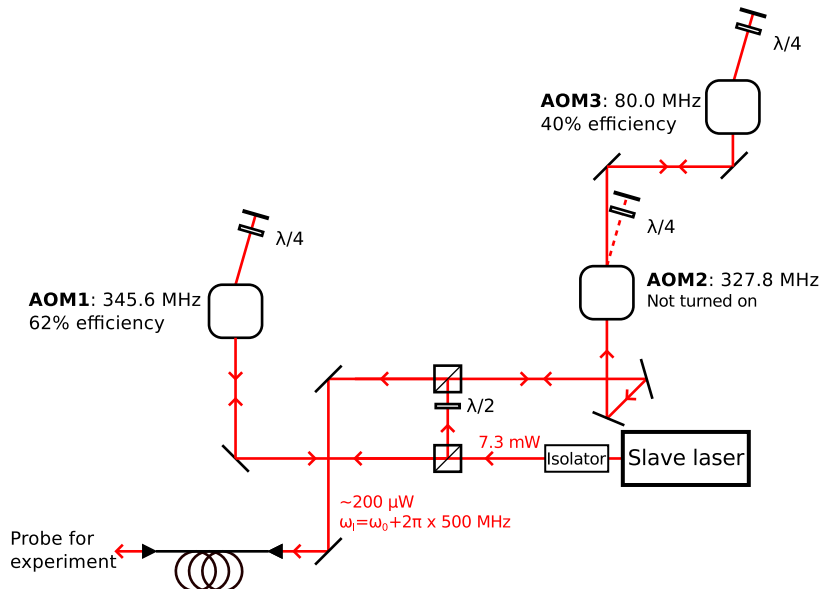


Figure 6.11: Overview of the AOM configuration for sideband probing. The poor AOM efficiencies are due to wrong coatings on the AOMs and astigmatism in the beam modes.

an unidentified drift of this demodulation phase hampered high signal to noise ratio measurements of the dispersion feature. This unoptimized demodulation phase is also evident in both scans shown in Fig. 6.12, as the central dispersion feature is not placed around zero. This indicates that the two correction terms from Eq. (6.13) were most likely included in the signal. A convincing measurement of the maximum absolute dispersion slope was despite numerous attempts not measured with this technique.

One of the suspected causes for the unidentified phase drift was the temperature drifts of the atmospheric air between the cavity mirrors and the vacuum chamber windows. This drift is suspected to be eliminated for the intra-vacuum cavity described later in Sec. 6.3. Implementation of this sideband probing technique on this vacuum cavity may prove promising for future works.

6.2.2 Multi photon recoils

It was shown in the inset of Fig. 6.5b) that the contributions from velocity dependent multiphoton scatterings (Doppleron resonances described in Sec. 3.3.1) reduced the central narrow saturated absorption feature slightly. This modification of the spectroscopic features indicates that multiphoton

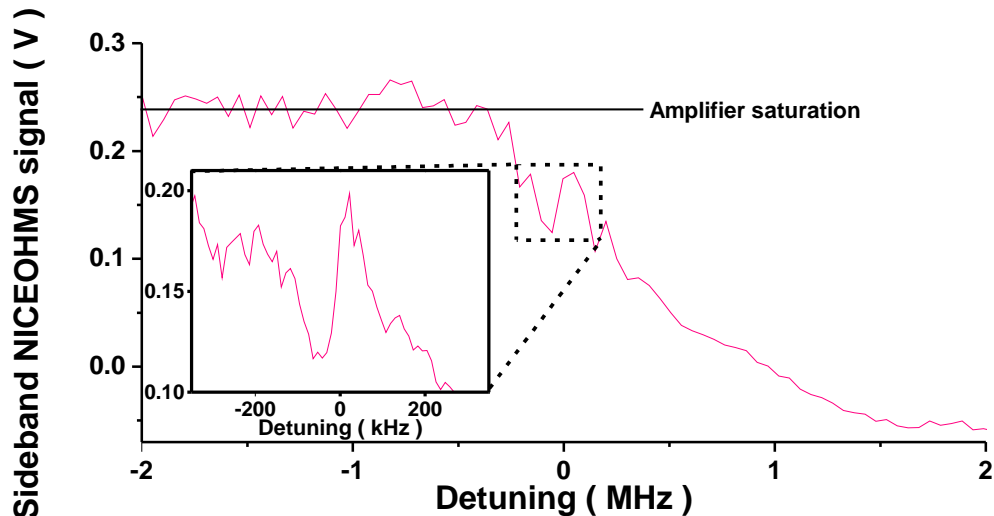


Figure 6.12: *Phase dispersion measurements of the main atom-cavity system by sideband probing. The data points for the broad scan are averages of 2 measurement cycles. Inset: The data points are averages of 6 measurement cycles.*

scatterings occurred to some extent in our system. Such scattering events would potentially cause a non-zero recoil shift of the scattered light.

This recoil shift δ_1 can be calculated straight forwardly through energy- and momentum conservation for the conventional single photon absorption for the $^1S_0 \rightarrow ^3P_1$ transition and $\delta_1 = 4.78 \text{ kHz}$. However, it is shown in the following that the recoil shifts yields different values for the velocity dependent multi photon scatterings.

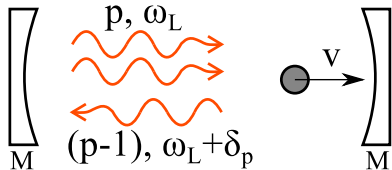


Figure 6.13: *Illustration of the recoil shift δ_p . p photons with frequency ω_l are absorbed and $(p - 1)$ photons with a shifted frequency $\omega_l + \delta_p$ is emitted in the opposite direction. The atom is moving with a velocity v in the positive direction.*

The velocity dependent multi photon resonances were previously in Sec. 3.3.1 described in the rest frame of the atom. Figure 6.13 illustrates a situation, where the multi-photon scattering is considered in the reference

frame of the cavity system. In this case, p photons with frequency ω_l are absorbed and $(p - 1)$ photons with a shifted frequency $\omega_l + \delta_p$ is emitted in the opposite direction. The atom is left excited, but a frequency shift δ_p is applied on the back scattered photons due to recoil and the atomic momentum will also be increased to $m \cdot v'$, where m is the single atom mass. Conservation of energy and momentum leads to the following relations:

$$p\hbar\omega_l + \frac{(m \cdot v)^2}{2m} = \hbar\omega_0 + \frac{(m \cdot v')^2}{2m} + (p - 1)\hbar(\omega_l - \delta_p) \text{ (E. conserv.)}, \quad (6.14)$$

$$m \cdot v + p\hbar\frac{\omega_l}{c} = m \cdot v' - (p - 1)\frac{\hbar}{c}(\omega_l - \delta_p) \quad \text{(M. conserv.)}. \quad (6.15)$$

Equation (6.14) and (6.15) can be solved for δ_p by substituting the Doppler resonance condition (shown in Eq. (3.27)) into Eq. (6.14) and (6.15). Table 6.2.2 shows the calculated recoil shifts δ_p for the first two higher orders of Doppler resonance. These values differ clearly from the conventional single photon recoil shift δ_1 . A series of experiments were hence performed in order to verify these recoil shifts.

Incoming photons	Shift, δ_p
$p = 1$	4.78 kHz
$p = 2$	14.34 kHz
$p = 3$	29.88 kHz

Table 6.1: Recoil shift δ_p for different scattering orders p .

The quest for recoil shifts

The setup shown in Fig. 6.14 was set up in order to investigate the possible recoil shifts from multi photon recoils. The recoil shifts described in Sec. 6.2.2 would apply sidebands on the intra cavity photons if sufficient velocity dependent multiphoton recoils occurred in this system. It was attempted to measure these sidebands by detecting the cavity transmitted light and demodulate this signal with $\delta/2\pi$. The demodulation signal frequency $\delta/2\pi$ was generated by mixing two frequency synthesizers with frequencies $\Omega/2\pi$ and $(\Omega + \delta)/2\pi$ as no low frequency synthesizers were available. This mixer output signal contains frequency components with frequencies $\delta/2\pi$ and $(2\Omega + \delta)/2\pi$, corresponding to the sum and difference of the two mixer input frequencies, and the $\delta/2\pi$ component was selected by implementing a low-pass filter. The power of the cavity transmitted

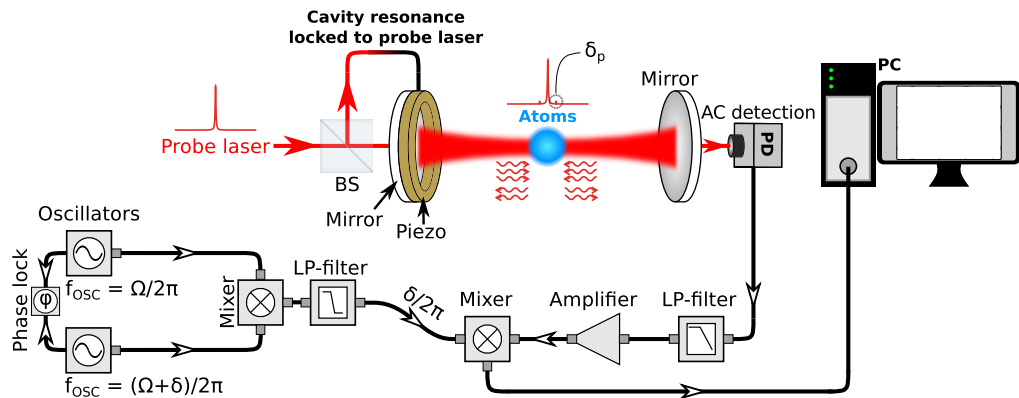


Figure 6.14: Illustration of the setup for measuring recoil shifts. The cavity transmitted light was detected and demodulated at $\delta/2\pi$ in an attempt to measure the recoil shifts.

light would contain frequency components oscillating with the recoil frequency $\delta_p/2\pi$ ^{xiii}. It was attempted to demodulate this oscillation due to the recoil by mixing the cavity transmitted power with $\delta/2\pi$. Figure 6.15 shows the measured demodulation signal as function of the demodulation signal $\delta/2\pi$.

The characteristics of this demodulation signal can be theoretically simulated by considering a probe laser with two small recoil induced sidebands (illustrated in Fig. 6.14). The demodulation signal can be described theoretically by considering the power of the cavity transmitted electromagnetic field components. The power of this transmitted fields consists of static DC components and components oscillating at $\delta_p/2\pi$ and $2\delta_p/2\pi$. The demodulation signal was simulated by multiplying (mix) these components with $\sin(\delta t)$. This theoretically predicted demodulation signal is shown in Fig. 6.16. It was assumed in this theoretical lineshape, that the signal was averaged by a computer with integration time constant $T = 500 \mu s$. The sinc function-like shape of the lineshape in Fig. 6.16 arises mainly due to the fact that a large DC component was multiplied by $\sin(\delta t)$ and averaged with a finite integration time.

Figure 6.16 shows the frequency scan of two theoretically calculated demodulation signals: *with* (red line) and *without* (blue line) recoil induced

^{xiii}Corresponding to the difference between the probe laser frequency and the recoil sidebands.

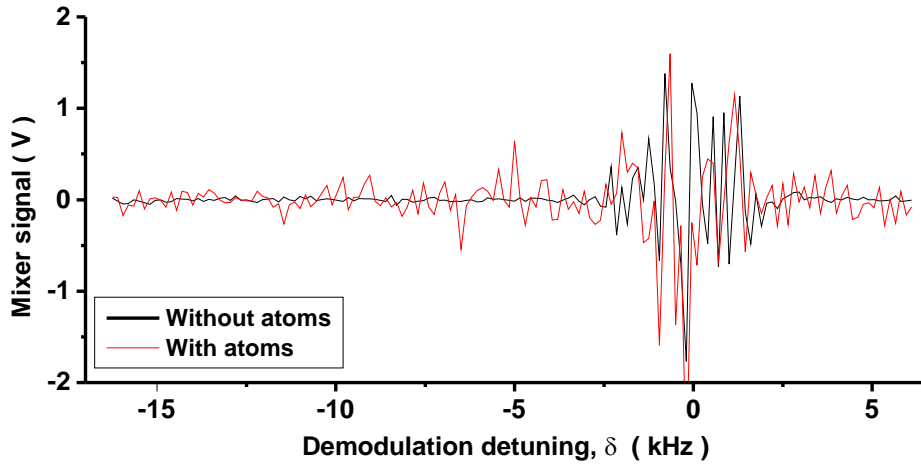


Figure 6.15: Measured signal from demodulation of the cavity transmitted light. Red line is with atoms inside the cavity while the black line is without atoms. The effect of the atoms are clearly seen, however no clear indication of recoil shifts are seen.

sidebands for $\delta_p/2\pi = 14.34$ kHz corresponding to the recoil shift for the 2nd order doppleron resonance ($p = 2$ in table 6.2.2). The theoretically calculated lineshape with multi-photon recoils shows that these recoils have a minor effect on the lineshape. The relative magnitude of the recoil induced sidebands used in these calculations were evaluated based on the ratio of the photon rates of the probe laser I_{probe} and the rate of the coherent scattering I_{coh} for the $^1\text{S}_0 \rightarrow ^3\text{P}_1$ transition for an given intra-cavity saturation parameter [Cohen-Tannoudji et al., 1992, p.383]. This ratio was evaluated to be $I_{\text{coh}}/I_{\text{probe}} \approx 5 \times 10^{-5}$ for a probe input power of around 300 nW^{xiv}.

Comparison of Fig. 6.15 and Fig. 6.16 reveals an agreement of the overall lineshapes of the measured data and the theoretical prediction. The signal-to-noise ratio in Fig. 6.15 is however too poor to show the oscillations predicted in Fig. 6.16. The signal-to-noise ratio in Fig. 6.15 are also far too poor for enabling verification of the recoil induced modifications of the linesapes predicted in Fig. 6.16. An improvement of this signal-to-noise ratio is most likely needed for further investigations of the possible recoil shifts.

^{xiv}corresponding to a saturation parameter of $s = 750$

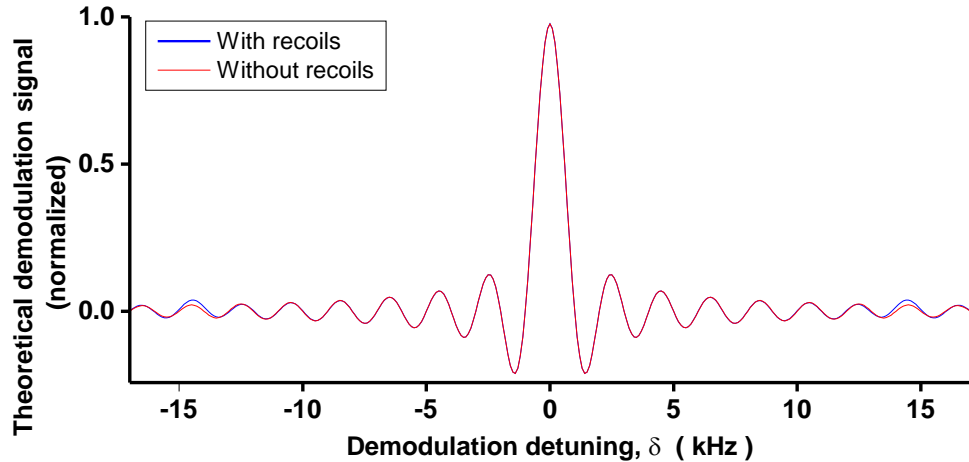


Figure 6.16: *Theoretically predicted lineshape of the signal acquired by demodulating the cavity transmitted light. An integration time of 500 μ s was assumed for the data acquisition. The blue line shows that the signal is expected to be modified slightly if recoil shifts are present. The magnitude of this modification is however most likely too small to be resolved with the signal-to-noise ratio in Fig. 6.15*

There are also indications that the above description does not provide a sufficient description of the performed experiment. Fig. 6.15 shows the demodulation signal with and without atoms coupled to the cavity. Whereas it is reassuring that the atoms do affect the signal, the atoms affect the signal in an unexpected manner. It was expected that the presence of the atoms would reduce the demodulation signal in general as the atomic absorption would reduce the total cavity transmitted optical power. The demodulation signal is however larger when the atoms are present. The underlying explanation has not yet been fully identified for this behavior.

While the recoil shifts were not verified experimentally, it is theoretically indicated that the velocity dependent multi photon scatterings are only a minor effect in this system. This is based on the very small contribution of the recoil shift predicted in Fig. 6.16 and the theoretically evaluated very small coherent scattering rate I_{coh} . It was also indicated previously in Fig. 6.5 that the higher order multi photon scatterings do not significantly affect the spectroscopic characteristics. The higher order multi photon scatterings only slightly attenuate the saturation degree of the central saturated absorption peak in Fig. 6.5. This is most likely caused as the multi

photon scatterings scatter photons that would otherwise have contributed to the saturation.

6.3 Spectroscopy with high finesse

A detailed understanding was obtained in Sec. 6.1 for the characteristics and the dynamics of cavity enhanced spectroscopy with a low finesse cavity. Whereas this low finesse system served as a proof of principle experiment, a higher finesse is required in order to achieve laser stabilization performance in line with the current state-of-the-art laser stabilization [Kessler et al., 2012a, Häfner et al., 2015, Bishof et al., 2013]. It was predicted in Sec. 3.4.2 that a cavity finesse of the order of $F = 1000$ is needed for an ideal shot noise limited feedback system to achieve a linewidth competitive with the current state-of-the-art.



Figure 6.17: Picture of a MOT inside the cavity structure inside the main vacuum chamber. The fluorescence from the trapped atoms is seen as the central blue dot.

It was described in details in Sec. 5.2.3 that a monolithic cavity system was developed and placed inside the main vacuum chamber of this experiment. The cavity spacer design allowed passage of all the MOT beams and a sample of laser cooled ^{88}Sr atoms was trapped inside the cavity structure and in between the cavity mirrors. Figure 6.17 shows a picture of the trapped atoms inside the cavity structure. This section presents preliminary results of cavity enhanced spectroscopy performed with this vacuum cavity system.

The atom induced absorption and phase shift of the cavity transmitted light were detected experimentally. This detection was performed in a setup very similar to the setup used for the spectroscopy experiments with the low finesse cavity described previously in Sec. 6.1 and illustrated in Fig. 6.1a). The primary change of the system is that the original optical

cavity fixed outside the main vacuum chamber is replaced by a new intra-vacuum cavity.

The DC transmission power and a NICE-OHMS signal were detected for different probe laser detunings and representative data are shown in Fig. 6.18 as red dots. The DC transmission was normalized relative to the transmitted power when no atoms were trapped inside the cavity. The NICE-OHMS signal was demodulated by a demodulation frequency $\Omega/2\pi = \text{FSR}$. This corresponds to the conventional NICE-OHMS technique described in Sec. 4.6 and represents the lineshape of the atom induced dispersion. The solid blue lines show the theoretically predicted lineshapes corresponding to the experimental parameters during the data acquisition: The total number of atoms $N = 4.5 \times 10^8$ (corresponding to around $N_{\text{cav}} = 2.25 \times 10^7$ intra-cavity atoms), cavity input power $P_{\text{in}} = 70 \text{ nW}$ and temperature of the trapped atoms is $T = 9.4 \text{ mK}$. This relatively high temperature was due to an improper detuning of the cooling light for the MOT. These experimental parameters are rough estimates and a more thorough determination of these parameters is required for future detailed studies of these lineshapes. The cavity length was controlled during this experiment such that the combined cavity-atom system was kept on resonance with the probe laser in the same manner as for the low finesse cavity. The lineshape modifications imposed by this resonance condition are included in the theoretical predictions in Fig. 6.18 in the same manner as described in Sec. 4.6.1.

At first glance, the experimental data reproduces roughly the same features as the theoretical predictions. This indicates that the theoretical model described in Chap. 3 can be scaled to cavity systems with finesse in the order of $F = 1450$. The degree of agreement between the experimental and theoretical values are however not as significant as for the similar results for the low finesse cavity (shown in Fig. 6.5). The deviation between the experimental data and the theoretical values are particularly pronounced for large probe laser detuning. Part of this is most likely due to insufficient measurement statistics and less thorough determination of the experimental parameters.

Most likely, the dispersion lineshape of this system presented here is not optimized for laser stabilization purposes. For example the central dispersion slope can be improved by increasing the number of intra cavity atoms and by reducing the input probe power. A lower input probe power can narrow the entire spectroscopic lineshapes, which were most likely power broadened due to the increased intra cavity power build up in this vacuum cavity. Hence, detailed studies of the experimental parameters and the system dynamics similar to the studies presented in

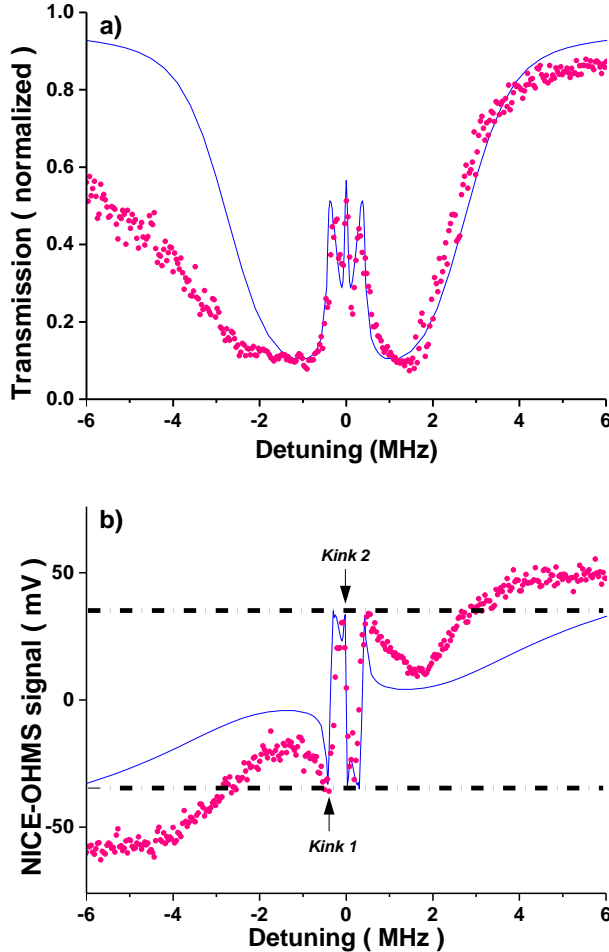


Figure 6.18: Frequency scan of the atom induced phase dispersion and the cavity transmitted optical power. The dots are measured data, while the solid and dashed lines are predictions based on the theoretical model presented in Chap. 3. All data are averaged values of 6 separate measurement cycles. The total number of atoms is $N = 4.5 \cdot 10^8$, the cavity input power is $P_{in} = 70 \text{ nW}$ and the temperature of the trapped atoms is $T = 9.4 \text{ mK}$. a): Frequency scan of the cavity transmitted phase shift. Theoretical values from Eq. (6.9) are scaled to data. b): Frequency scans of the cavity transmission. The horizontal axis is normalized to the transmission power without intra-cavity atoms.

Sec. 6.1.3–6.1.4, are needed for future works in order to evaluate the laser stabilization prospects of this system.

Two interesting and surprising new features are observed in Fig. 6.18. The first feature is the *kinks* of the NICE-OHMS lineshapes seen around detuning values of $\pm 0.5 \text{ MHz}$ in Fig. 6.18b). These kinks are observed both

in the theoretical and experimental values (marked as *Kink 1* in Fig. 6.18b)). An additional kink is also observed in the theoretical lineshape (marked as *Kink 2* in Fig. 6.18b)), while this was not observed in the experimental values. All kinks occurred around the same value of the NICE-OHMS signal (marked with dashed lines). It is hence suspected, that these kinks happen when the atom induced phase shift β_D (presented in Eq. (4.24)) reaches a value where the NICE-OHMS signal is maximized after which the signal is reduced for further increase of the phase shift^{xv}.

The second surprising feature is, that both the experimental and theoretical transmission lineshapes in Fig. 6.18a) show the characteristic detailed shape caused by the atom induced phase shift on the intra cavity light (shown in Fig. 3.3). This is surprising as the similar DC transmission for the low finesse cavity shown in Fig. 6.2 yielded a more simple Gaussian lineshape without these detailed structures. The interpretation^{xvi} for this simple lineshape was that the cavity servo system canceled out the atom induced phase shift and effectively transferred the atom induced phase shift to the sideband components of the probe laser. The transmission lineshape is, however, clearly reduced in both the experimental and theoretical results for large detunings in Fig. 6.18a) and the detailed structures (*dips* described in Sec. 6.1.2) near resonance are also seen clearly. These unexpected details in the transmission lineshape might be an indication of the limitations of the semi-classical description of this system where the atom induced absorption and dispersion are extracted from the values calculated by the theoretical model described in Chap. 3 (see also for details Eq. (4.26)–(4.27)). Further studies of the connection between the theoretically modeled system and the influence of the cavity servo system are most likely needed in order to establish a detailed description of the above mentioned two new features. The asymmetry seen in the transmission lineshape (shown in Fig. 6.18a)) can possibly be due to technical conditions such as an unidentified drift of the relative phase of the cavity transmitted light and the demodulation phase or due to more intrinsic properties of the physical system such as a detuning dependent dipole forces caused by the intra-cavity field. Further studies are needed in order to identify the cause of this asymmetry.

^{xv}Similar to when the slope of $\sin(\varphi)$ changes around $\varphi = \pi/2$.

^{xvi}This interpretation was presented in details in Sec. 6.1.2) and illustrated in Fig. 6.3

6.4 Outlook

This chapter presented results from cavity enhanced non-linear spectroscopy of laser cooled ^{88}Sr placed inside optical cavity systems. The first and most comprehensively studied system was a low finesse cavity with mirrors fixed outside the main vacuum chamber of the experiment. It was discovered in Fig. 6.2 that the transmission lineshape was significantly modified by the cavity servo system which adjusted the cavity length such that the atomic induced phase shifts were counter-acted and standing waves were present inside the cavity at all times. The modifications imposed by this standing-wave requirement on the NICE-OHMS signal were studied in details in Sec. 6.1.2. These modifications were included in the theoretical predictions such that the theoretically predicted values were in great accordance with the experimentally acquired experimentally measured NICE-OHMS signal values. The detailed spectroscopic features of the transmission lineshape predicted previously in Sec. 3.2 were also observed by developing an overtone demodulation technique also presented in Sec. 6.1.2.

The system dynamics were studied in details and the optimal input power of the probe laser was identified. Based on the system parameters, the ideal shot-noise limited linewidth achievable with this system was evaluated to be as low as 500 mHz which already makes this system interesting for laser stabilization. However, it was predicted previously in Sec. 3.4.2, that shot-noise-limited linewidths in the sub 10 mHz level could be achieved for a similar system with cavity finesse in the order of $F = 1000$. A vacuum cavity system with a finesse of $F = 1450$ was hence realized (described in Sec. 5.2.3).

Preliminary spectroscopic experiments performed with this vacuum cavity system confirmed roughly the theoretically predicted dispersion and absorption lineshape characteristics for an atom-cavity system with cavity finesse of this order of magnitude ($F = 1450$). Detailed studies of the system parameters are however needed to evaluate the laser stabilization performance of this system. It should however be mentioned that both the low finesse cavity system and the vacuum cavity system were designed for cyclic operation where the atoms are only interrogated by the probe laser in a minor fraction of the cycle time. Continuous laser stabilization is hence not feasible with the current system. The results presented in this chapter have however established motivation for realizing different cavity-atom systems for continuous laser stabilization. Experimental setups for continuous laser stabilization on a beam of strontium atoms or molecular cells have been initiated during this work and these systems

are presented briefly in the final Chap. 8.

In addition, the vacuum cavity system brings the system into a parameter regime with high collective cooperativity $C \gg 1$, where collective emission phenomena can be expected and the system will act as a so-called active light source. Collective spontaneous emission was presented in Sec. 2.2 as a promising strategy to achieve highly stable light sources. Observations of collective emission phenomena in simple systems with laser cooled narrow line atoms would prove very valuable for the development of compact active light source systems. Hence, the following chapter investigates the prospects for achieving collective spontaneous emission with the vacuum cavity system.

CHAPTER



COLLECTIVE SPONTANEOUS EMISSION

The main purpose of the experimental systems developed in this work is to exploit narrow line atomic transitions for achieving ultra stable lasers. These experimental systems are described in Chap. 5. It was presented in Chap. 2 that ultra stable lasers could be achieved by using an atom-cavity system in two different ways: By performing *laser stabilization on passive atomic systems* and by using *active light sources*.

So far, this work has studied the prospects for performing laser stabilization using a passive atomic systems as frequency reference. This was studied in details in Chap. 6 and a system of laser cooled ^{88}Sr atoms coupled to an optical cavity was found to be promising for laser stabilization. This following chapter investigates the possibilities for using the same experimental system for achieving an active light source.

Active light sources are an alternative approach to achieve ultra stable light sources by exploiting collective emission phenomena in atom-cavity systems. One collective emission phenomena of particular interest is *superradiance*. Theoretical studies predict, that spectral linewidths in the sub mHz-level can be achieved for super radiant light emitted from systems based on strontium atoms trapped in optical lattices and coupled to an optical cavity in the so-called bad-cavity regime [Chen, 2009, Meiser et al., 2009]. Pioneering experiments have shown linewidth narrowing effects in similar cavity-atom systems with alkali elements other than strontium [Bohnet et al., 2012, Zhi-Chao et al., 2015]. Most recently, atom-cavity systems with strontium atoms trapped in optical lattices have

also been realized [Norcia and Thompson, 2016a, Norcia and Thompson, 2016c, Norcia et al., 2016] and the studies of collection emission from such systems are ongoing.

An ensemble of excited atoms can emit light collectively in a variety of ways and different collective emission phenomena have been observed in a number of very different atomic systems [Kwong et al., 2015a, Baudouin et al., 2013, Noe II et al., 2012], showing the diversity of collective emission phenomena. Hence, the variety of collective emission phenomena are described in the following Sec. 7.1.

The experimental system realized in this work does not include complex experimental systems such as optical lattices, which makes this system much more simple than the systems investigated in other works [Norcia and Thompson, 2016a, Norcia and Thompson, 2016c, Norcia et al., 2016]. It would prove promising for future compact out-of-lab laser systems if linewidth narrowing effects could be studied in such simple systems. Hence, preliminary experimental studies has been conducted in order to investigate the possibility of observing collective emission for the vacuum cavity system developed in this work (described in Sec. 5.2.3). A variant of collective emission is observed in this system and the results of these studies are presented in Sec. 7.2, where the origin and dynamics of this collective emission phenomena is discussed.

7.1 Super radiance, Super Fluorescence and Amplified Spontaneous Emission

A collection of coherently prepared two-level atoms can decay collectively in a flash with enhanced decay rate. This is known as Dicke *Superradiance* (SR) [Dicke, 1954], which is illustrated in Fig. 7.1a). The atomic transition linewidth will dominate the spectral linewidth of this super radiant light as previously described in Chap. 2. Hence, SR based on ultra narrow atomic transitions is an interesting candidate for surpassing the precision of the current state-of-the-art clock lasers [Kessler et al., 2012a, Bishof et al., 2013, Häfner et al., 2015], which are currently limited by thermal noise of the passive reference cavities. An other enhanced decay process can also occur from uncorrelated incoherently excited atoms. This is called *Super Fluorescence* (SF), which is illustrated in Fig. 7.1b). SF is initiated quantum mechanically by spontaneous emission after which the system gets correlated giving rise to a coherent light pulse with a characteristic delay time τ_D [Bonifacio and Lugiato, 1975]. Both SR and SF

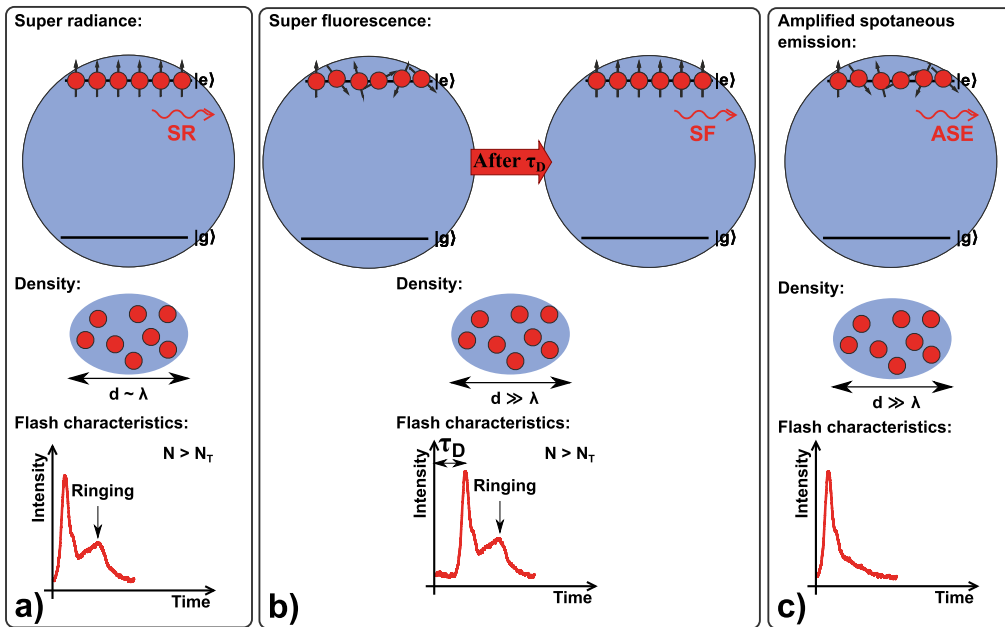


Figure 7.1: Illustration of superradiance (SR), superfluorescence (SF) and amplified spontaneous emission (ASE) in a two-level system.

exhibit interference effects such as ringing (shown in Fig. 7.1a)–b)), which are characteristic for emission from coherent states. Finally, collective emission from an incoherent system can also occur without developing coherence in the system and without a delay. This is called *Amplified Spontaneous Emission* (ASE), which is illustrated in Fig. 7.1c). All possible spontaneous emission modes are amplified by stimulated emission in ASE and the atomic excitation is in general incoherent, yet the emission mode with maximum gain can outmatch the other modes and result in some degree of coherent output [Dai, 2011].

While SR can be identified by its requirements for an external source to establish the coherence, the difference between SF and ASE can be challenging to distinguish and the transition between these two regimes has been studied in previous works [Malcuit et al., 1987, Kumarakrishnan and Han, 1998]. The intensity of the collectively emitted light for SR and SF scales in general with the number of excited atoms N as $\propto N^2$, while the intensity of ASE scales as $\propto N$. However, SF is a robust phenomena and it has been reported, that the super fluorescent light can be emitted collectively even under unfavorable conditions with high decoherence,

resulting in SF intensity scaling as $\propto N$ [Kumarakrishnan and Han, 1998].

In addition to the atom number dependencies, SF and ASE are separated by the coherent ringing of the emission and the characteristic emission delay time τ_D . The parameter regimes of SF and ASE are, in fact, determined by a number of characteristic time scales, which are presented in the following section.

7.1.1 Characteristic time scales

A number of characteristic time scales determine the collective emission behaviors [Kumarakrishnan and Han, 1998]. The radiative coupling time, τ_R , is the time in which spontaneously emitted photons are coupled into the cavity mode.

$$\tau_R = \frac{1}{C_0 N_{\text{cav}} \Gamma}, \quad (7.1)$$

where C_0 is the single atom-cavity cooperativity described in Sec. 2.2, N_{cav} is the number of intra-cavity atoms and Γ_{12} is the spontaneous emission rate for the radiating transition. This coupling time τ_R is the time scale in which coherence builds up in the system. This coherence is, however, destroyed by decoherence mechanisms such as the Doppler broadening with the characteristic time scale T_2 . Thus, the threshold for SF generally occurs when $\tau_R = T_2$ which yields a threshold number of intra-cavity atoms N_T (derived from Eq. (7.1)):

$$N_T = \frac{1}{C_0 T_2 \Gamma}. \quad (7.2)$$

This threshold atom number N_T can be calculated for the parameters of the vacuum cavity system realized in this work (described in Sec. 5.2.3). The parameters for this system are $C_0 = 6.3 \times 10^{-4}$ and $\Gamma/2\pi = 7.5$ kHz for the $^1S_0 \rightarrow ^3P_1$ transition. According to Eq. (7.2), the threshold intra-cavity atom number for this system is $N_T = 6.3 \times 10^5$ for a decoherence time $T_2 = \frac{1}{\Gamma_{\text{Dop}}}$ caused by a Doppler broadening of $\Gamma_{\text{Dop}}/2\pi = 1.5$ MHz. This Doppler broadening corresponds to an atomic sample temperature of around $T = 9.8$ mK, which was evaluated based on the spectroscopic lineshape shown in Fig. 6.18.

Furthermore, atomic systems interacting with light are characterized by the propagation time $\tau_E = l/c$ for the light propagating through the atomic system with a length l . All emitted photons can stimulate all atoms

in the sample volume when $\tau_E < \tau_R$, and pure SF can occur. Geometric effects become important when $\tau_E > \tau_R$ as emitted photons can only stimulate closely adjacent atoms and this modifies the dynamics of the SF. One example of this modification is, that the atom number dependency of SF intensity might become $\propto N$ instead of $\propto N^2$ [Kumarakrishnan and Han, 1998]. The $\propto N$ and $\propto N^2$ dependencies were one of the characteristics which distinguished SF and ASE. This complicates the separation of SF and ASE. It should also be added that the systems described in the previous works [Kumarakrishnan and Han, 1998, Bonifacio and Lugiato, 1975] mentioned here are atomic systems without cavities. However, the main system studied in this work had an optical cavity, where the intra-cavity photons have a round-trip time. Thorough considerations of τ_E for an atom-cavity system are most likely needed for future works.

Finally, the most significant quantity for SF is the delay time τ_D for which the intensity maximum occurs for the collective emission flash. This delay depends as $\tau_D \propto \frac{1}{N}$ for pure SF [Kumarakrishnan and Han, 1998]. This dynamics of the delay is once again expected for free space systems without an optical cavity and further development of the theoretical description is most likely needed.

The emitted light from uncorrelated incoherently excited atoms is SF if most of the excitation energy is radiated coherently. It has been shown, that coherent emission dominates whenⁱ [Schuurmans, 1980]:

$$T_2 > \sqrt{\tau_R \tau_D}. \quad (7.3)$$

On the other hand, incoherent emission through ASE dominates when:

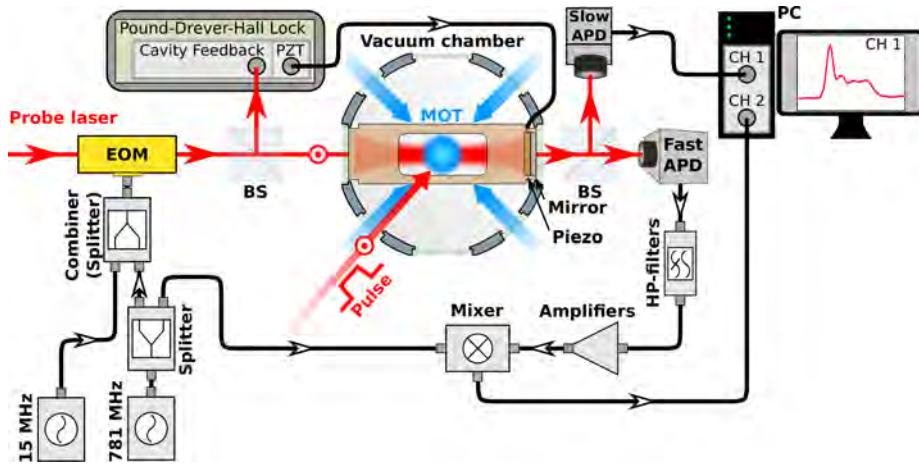
$$T_2 < \sqrt{\tau_R \tau_D}. \quad (7.4)$$

The characteristic times in the experiment studied later in this chapter (and described in Sec. 5.2.3) are $\tau_R = \frac{1}{C_0 N_{\text{cav}} \Gamma_{12}} \approx 3.3 \text{ ns}$, $\tau_D \approx 500 \text{ ns}^{\text{ii}}$, which yields $\sqrt{\tau_R \tau_D} \approx 40 \text{ ns}$ and $T_2 = \frac{1}{\Gamma_{\text{Dop}}} \approx 160 \text{ ns}$. These characteristic time scales just bring the system into the SF regime $T_2 > \sqrt{\tau_R \tau_D}$ while leaning close against the transition regime $T_2 \approx \sqrt{\tau_R \tau_D}$.

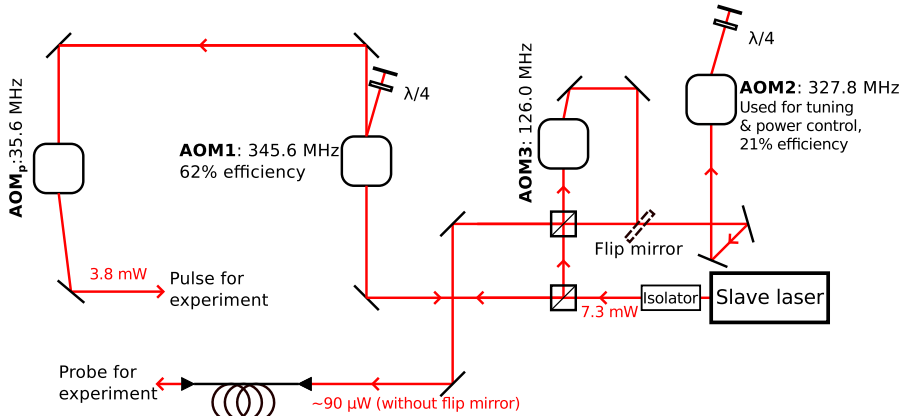
ⁱEq. (7.3) is presented as $T_2 > \sqrt{\tau_R T_D}$ in [Schuurmans, 1980], where T_D is the delay time τ_D in the absence of decoherence. Here, the experimentally more accessible τ_D is written in Eq. (7.3)-(7.4), as $\tau_D > T_D$ and $T_2 > \sqrt{\tau_R \tau_D} > \sqrt{\tau_R T_D}$.

ⁱⁱThis delay time τ_D is determined experimentally later in Sec. 7.2.

7.2 Experimental investigations



(a) Overview of pulse experiments for studies of collective emission.



(b) Overview of AOM configuration for pulse experiments.

Figure 7.2: a): Experimental overview for pulse experiments. A fraction of a sample of laser cooled ^{88}Sr atoms were placed inside an optical cavity and prepared in an excited state by sending a pulse resonant with the $^1\text{S}_0 \rightarrow ^3\text{P}_1$ transition into the atomic sample. A likewise resonant probe laser was coupled to the cavity and the cavity was kept on resonance with this probe laser by using the PDH locking scheme (described in Sec. 4.5.2). An increase in cavity transmission in the form of a flash was observed by direct measurement of the transmitted intensity (Slow APD) and by using the NICE-OHMS technique (Fast APD) (described in Sec. 4.6). Two sets of sidebands were applied on the probe laser by periodic phase modulation at 15 MHz for the PDH scheme and at 781.14 MHz for the NICE-OHMS technique. b): Overview of the AOM configuration used for preparing light resonant with the $^1\text{S}_0 \rightarrow ^3\text{P}_1$ transition for the probe laser and for the pulse.

The possibility to observe collective emission processes was investigated for thermal ^{88}Sr atoms coupled to an optical cavity.

About 5×10^8 ^{88}Sr atoms were trapped in a single stage MOT (described

in Section 4.4 and 5.2.1) and coupled to the vacuum cavity described in Sec. 5.2.3. Figure 7.2(a) illustrates the overall experimental setup. The total number of intra-cavity atoms was evaluated to be about 1×10^7 , which was lower than the number of intra-cavity atoms in the low finesse cavity experiments presented previously in Sec. 6.1. This difference in the number of intra-cavity atoms was due to improper alignment of the MOT relative to the vacuum cavity mode. The finesse of the cavity was $F = 1450$. A pulse of light with frequency ω_0 resonant with the ${}^1S_0 \rightarrow {}^3P_1$ transition was sent in parallel with one of the MOT beams. The angle between the pulse direction and the cavity axis was around 45° . The polarizations of the pulse and the intracavity probe were linear and parallel with the magnetic field within the volume of the trapped atomic sampleⁱⁱⁱ. This system was in the bad-cavity regime as the ${}^1S_0 \rightarrow {}^3P_1$ transition linewidth ($\Gamma/2\pi = 7.5$ kHz) was much narrower than the cavity linewidth ($\kappa/2\pi = 520$ kHz). It can hence be studied whether the spectral linewidth of a potential collective emission from this system can potentially be dominated by the narrow atomic transition linewidth in accordance with the description of the bad cavity regime presented in Chap. 2.

Figure 7.2(b) shows the AOM configuration for preparing the probe laser and resonant pulse. This AOM configuration was modified compared to the setup already shown in Fig. 5.2. Two new AOMs were added: Firstly, AOM_P was added to prepare light for the pulse mentioned above. The slave laser frequency ω_l and was shifted up to 3.8 mW light was prepared with frequency $\omega_l - 2\pi \times 35.6$ MHz = ω_0 . Here, ω_0 is the resonance frequency of the ${}^1S_0 \rightarrow {}^3P_1$ transition. Secondly, AOM3 (shown in Fig. 7.2(b)) was added to prepare light with frequency $\omega_l - 2\pi \times (2 \times 345.6 + 126.6)$ MHz = $\omega_0 - 2\pi \times \text{FSR}$, which was one *free spectral range* (FSR = 781.14 MHz) off-resonant with the atomic resonance. This off-resonant light was used to stabilize the cavity without probing the atomic transition continuously. The main focus in this chapter will be results obtained with a probe laser resonant with the atomic transition, while the setup with the one FSR off-resonant probe laser is described in the end of this chapter.

An ensemble of excited atoms had to be prepared in order to study collective emission. This is done by applying a so-called π -pulse to the atoms. The population of the excited level P_e of a stationary two-level atom exposed to monochromatic radiation evolves in the most simple case as:

ⁱⁱⁱThe atoms were trapped slightly above the center of the MOT yielding a non-zero magnetic field. This is also described in Sec. 5.2.2.

$$P_e = \sin^2\left(\frac{\Omega_{\text{Rabi}} t}{2}\right), \quad (7.5)$$

when probed by resonant radiation [Foot, 2005, p. 128]. Here, Ω_{Rabi} is the Rabi-frequency and the monochromatic radiation is resonant with the atomic transition.

The generalized Rabi frequency $\sqrt{\Omega_{\text{Rabi}}^2 + \Delta^2}$ will be modified if the atoms have finite velocities v causing the pulse to be detuned by a Doppler shift $\Delta = kv$. In this case, the excitation level can be described as the following if the atomic velocities follow a Maxwell-Boltzmann distribution $f(v)$:

$$P_{e,\text{Doppler}} = \int_{-\infty}^{\infty} \left(\frac{\Omega_{\text{Rabi}}^2}{\Omega_{\text{Rabi}}^2 + (kv)^2} \right) \sin^2\left(\frac{\sqrt{\Omega_{\text{Rabi}}^2 + (kv)^2} t}{2}\right) f(v) dv. \quad (7.6)$$

This modification from the atomic velocities will affect the effective excitation level $P_{e,\text{Doppler}}$ and reduce the maximum achievable excitation level.

It can be seen from Eq. (7.5), that the population of stationary atoms can in principle be completely transferred from one state to another with a so-called π -pulse of radiation with duration $t_\pi = \pi/\Omega_{\text{Rabi}}$. The duration t_π depends on the Rabi frequency $\Omega_{\text{Rabi}} = \Gamma \sqrt{\frac{I}{2I_0}}$. Here Γ is the transition linewidth, I_0 is the saturation intensity of the transition, and I is the probing intensity. The relation of pulse duration t_π and probing power P for a π -pulse is hence:

$$P = \frac{2I_0\pi^2 A}{\Gamma^2 \cdot t_\pi^2}. \quad (7.7)$$

Here, A is the pulse beam cross-section which was shaped as an oval to optimize the overlap between the pulse beam and the cavity mode. This area was thus optimized to $A = 1.25 \text{ mm}^2$. The relevant transitions parameters are $\Gamma = 7.5 \text{ kHz}$ and $I_0 = 3 \mu\text{W}/\text{cm}^2$. The maximum optical power realized for the pulse was 3.8 mW which yielded an ideal π -pulse durations of $t_\pi = 1.8 \mu\text{s}$. The π -pulse duration t_π is however influenced by decoherence from homogeneous and inhomogeneous couplings such

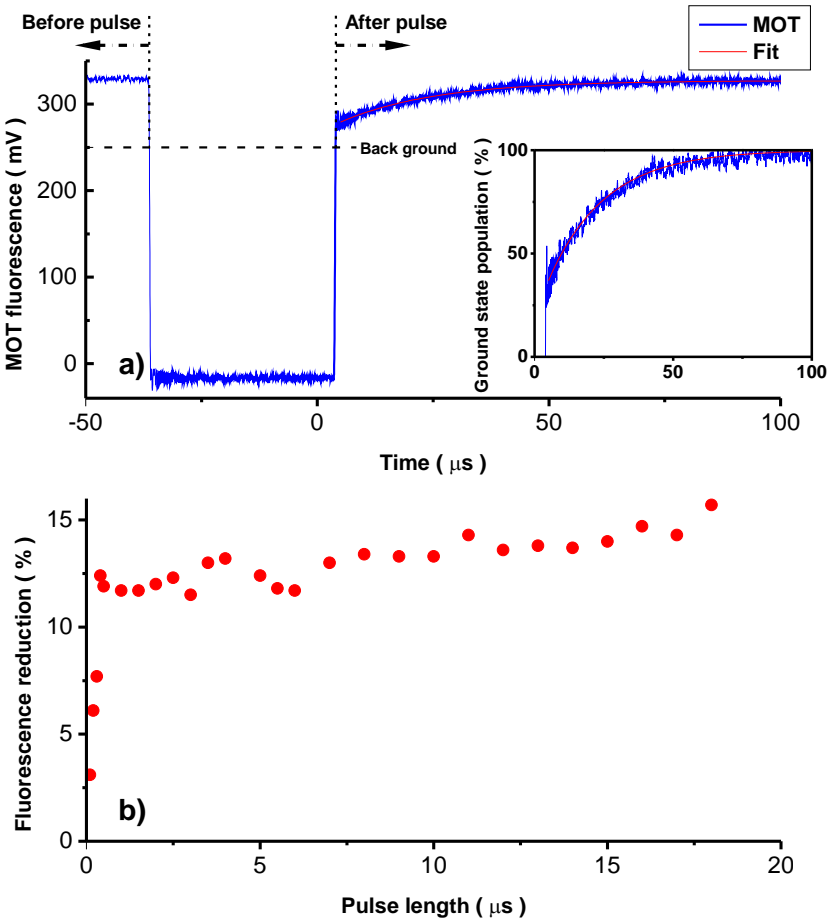


Figure 7.3: a): Illustration of the MOT fluorescence before and after a fraction of the laser cooled ^{88}Sr atoms were excited by a resonant pulse. The blue line is the experimental data, while the red line is a theoretical fit. The fluorescence reduction was only around 15 %. However, a larger fraction of the atoms exposed to the pulse were expected to be excited as a large background fluorescence (marked with horizontal dashed line) was caused by the part of the cooled atoms, which were not exposed to the pulse. Inset: Zoom of the reduced fluorescence. The vertical axis is calibrated to show the ground state population. This calibration is based on the geometry of the pulse beam volume and the MOT volume. b): Maximum fluorescence reduction as function of the duration of the resonant pulse.

as the Doppler broadening as indicated in Eq. (7.6) and the optimal t_π is investigated later in this section.

Figure 7.3 shows the fluorescence from the MOT measured with a

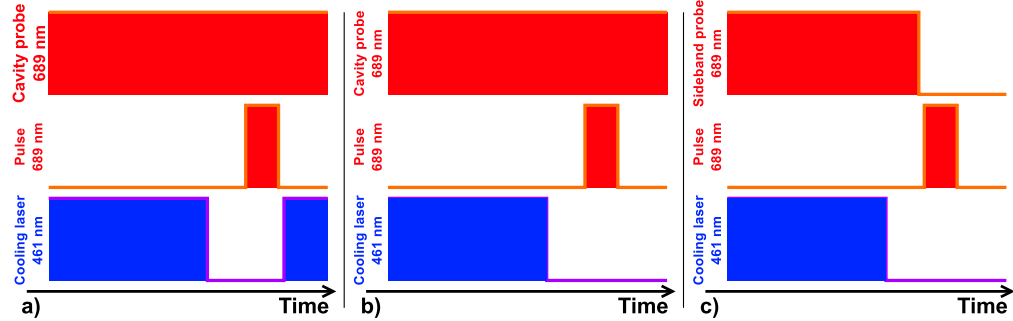


Figure 7.4: Illustration of the experimental sequences presented in Chap. 7. a): Sequence for testing the amount of excited atoms investigated in Fig. 7.3. b): Sequence used for investigations of collective emission flash in this work. This sequence was used for acquiring the majority of the results shown in Sec. 7.2.1. c): Sequence used for investigation of collective emission without continuous seeding by the intra-cavity probe laser.

photo multiplier during the following experimental sequence: Firstly, the 461 nm cooling light (described in Sec. 5.1.2) was tuned off and the fluorescence dropped to near zero. Then, the resonant pulse with variable duration was sent in such that this pulse was turned off 2 μs before the cooling light was turned on again 40 μs after the cooling light was tuned off. This sequence is illustrated in details in Fig. 7.4a). The repumping lasers were tuned on during the whole sequence but the resonant cavity probe was not present (The probe and repumping lasers are described in Chap. 5). It is shown in Fig. 7.3, that the fluorescence signal was lower after the pulse, as a fraction of the atoms were excited by the pulse and the ground state population was reduced. The photo multiplier detected fluorescence from the entire MOT, while only a fraction of the MOT was exposed by the pulse. This introduces a large and constant background signal in Fig. 7.3a) and the total reduction of fluorescence after the pulse is only around $\sim 10\%$. This reduction in fluorescence is evaluated to correspond to an total excitation level of $P_c \sim 43\%$ ^{iv} for the intra-cavity atoms. This was evaluated by taking into account the ratio between the MOT volume, the volume of the pulse mode and the overlapping cavity volume. The relation of these volumes is illustrated in

^{iv}Around 60 % of the atoms interacting with the pulse was excited and around 72 % of the cavity mode was exposed to the pulse yielding a total excitation level of $0.60 \cdot 0.72 = 43\%$

Fig. 7.5. Furthermore, the interpretation of this fluorescence reduction as excitation of the $^1S_0 \rightarrow ^3P_1$ transition is supported by the rate at which the fluorescence level returns exponentially to its initial level. The solid red line in Fig. 7.3 is a theoretical fit yielding a time constant corresponding to a decay rate of 7.73 ± 0.04 kHz which agrees well with the natural decay rate of the $^1S_0 \rightarrow ^3P_1$ transition ($\Gamma/2\pi = 7.5$ kHz).

Equation (7.5) indicates that one might expect oscillation of the excitation probability P_e as function of pulse duration time. Figure 7.3b) shows the pulse duration time dependency of the measured MOT fluorescence reduction, which scales with the excitation probability P_e . An oscillation of the MOT fluorescence reduction was not observed. Instead, the fluorescence reduction was rapidly increasing for short pulse durations ($< 0.5 \mu s$) and steadily increasing for longer pulse durations. This behavior is most likely due to the modification from averaging the effects of the atomic velocities described in Eq. (7.6).

Some level of population inversion is now expected to be established and observations of enhanced cavity transmission due to collective emission was attempted with this setup.

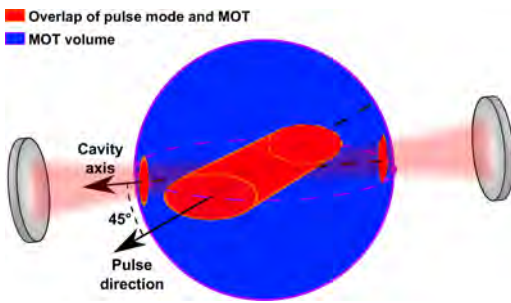


Figure 7.5: Illustration of the spatial overlap of the pulse mode, cavity mode and the MOT volume. The dimensions are exaggerated for clarity.

7.2.1 Dynamics of the collectively enhanced transmission

A fraction of a sample of laser cooled ^{88}Sr atoms were excited as described in the section above. These excited atoms were coupled to the vacuum cavity realized in this work (described in Sec. 5.2.3) and studies of collective emission phenomena transmitted through this cavity are presented in this section.

The cooled atoms were released from the MOT by turning the MOT beams off and a resonant pulse with adjustable duration was sent in $20 \mu s$ later alongside one of the MOT beams in order to study possible collective emissions transmitted out of the vacuum cavity. This sequence is illustrated in Fig. 7.4b). The cavity length was locked on resonance with a continuous 689 nm probe laser using the PDH locking scheme (described in Sec. 4.5.2). This probe laser was resonant with the narrow $^1S_0 \rightarrow ^3P_1$ transition and a standing wave field resonant with the atomic transition

was hence present inside the optical cavity during the experiments. This resonant intra cavity field is henceforth referred to as a continuous *seed*. The overall experimental setup is described in Fig. 7.4. The transmission of the vacuum cavity was monitored during this sequence and an example of the transmission dynamics is shown in Fig. 7.6.

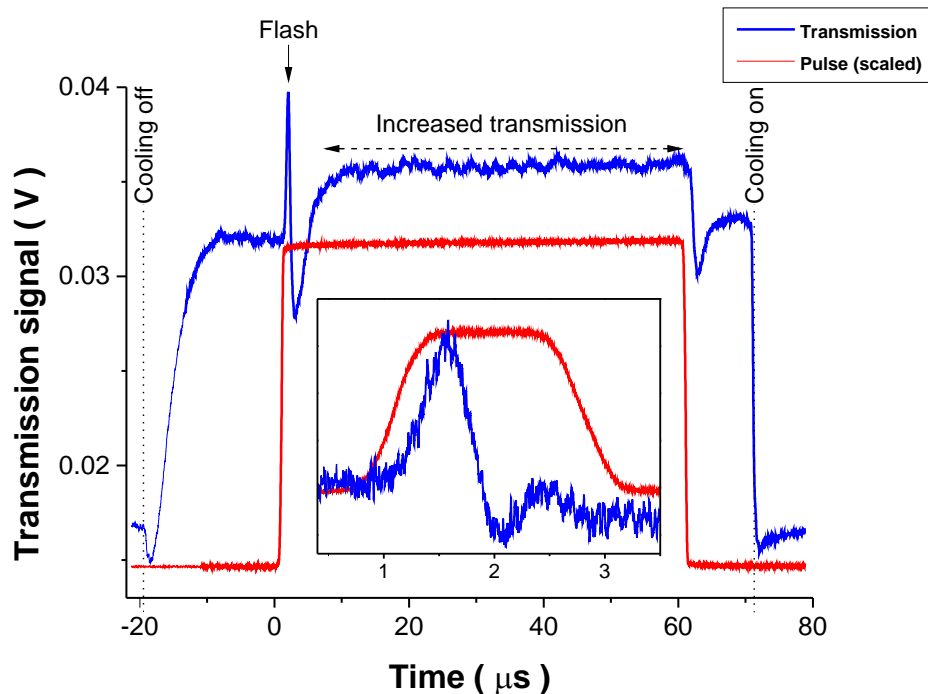


Figure 7.6: *Transmission signal of the vacuum cavity during the pulse sequence illustrated in Fig. 7.4b).* A series of processes were identified: Firstly, the cooling lasers were turned off and a new steady state was reached for the transmission signal within 20 μ s. Secondly, a resonant pulse was sent into the atomic sample and a flash is observed. The inset shows a zoom of this flash for a pulse duration of 2 μ s. The units on the inset axes are the same as in the main figure. This flash exhibits a coherent ringing in the form of a decrease of the transmission below the steady state level or subsequent peaks after the first flash as shown in the inset. Thirdly, a quasi-continuous increase of the cavity transmission is observed for longer pulse lengths. Finally, the cooling lasers are turned on again and the cavity transmission is returned to the original steady state level. This final steady state is reached much more rapid than when the cooling lasers were tuned off.

Different physical processes can be identified when considering the

transmission shown in Fig. 7.6: First, the cooling lasers were turned off. The AC Stark shift caused by the cooling lasers was now canceled and the absorption spectrum of the resonant probe light inside the cavity was changed. This caused the transmission level to reach a new steady state during the first $10\ \mu\text{s}$. This time scale corresponds to the order of magnitude of the Rabi frequency, which is expected to be in the order of $\sim 100\ \text{kHz}$ when the narrow ${}^1\text{S}_0 \rightarrow {}^3\text{P}_1$ transition is interrogated by the resonant intra-cavity seed. Secondly, the pulse with a duration of t_{pulse} ($t_{\text{pulse}} = 60\ \mu\text{s}$ in Fig. 7.6 and $t_{\text{pulse}} = 2\ \mu\text{s}$ in inset) is turned on when the new steady state was established after the cooling lasers were turned off. A sudden increase in the cavity transmission (henceforth called *the flash*) occurs with a $\sim 500\ \text{ns}$ delay after the onset of the pulse. The duration of this flash is in the order of $\sim 1\ \mu\text{s}$, which is far faster than the decay time of the ${}^1\text{S}_0 \rightarrow {}^3\text{P}_1$ transition. This fast flash duration indicates that some sort of collective decay process was observed. A continuous increase of the cavity transmission was also seen after the flash, when the pulse duration was long ($> 5\ \mu\text{s}$). Thirdly, the pulse is switched off and the cavity transmission returns to the steady state with no cooling. Finally, the cooling lasers were turned on and the cavity transmission returned to the original steady state far more rapidly than when the cooling lasers were tuned off. This is suspected to be due to a higher Rabi-frequency when the strong cooling transition is interrogated. The mean velocity of the laser cooled atoms is around $\langle v \rangle = 0.6\ \text{m/s}$ and the majority of the atoms will stay within the cavity mode during this sequence. Figure 7.7 shows that the flash reached an intensity maximum corresponding to up to a $15\ \text{mV}$ signal on the photo detector, which was used for measuring the cavity transmission (see CH1 in Fig. 7.2(a)). The optical power at this intensity maximum corresponds to around $\sim 23\ \text{nW}$ which also corresponds to a total intra-cavity photon number of $\sim 2.0 \times 10^7$. This indicate that every atom inside the cavity roughly contribute with 1–2 photons per flash, as the intra cavity number of atoms here is evaluated to be around $N_{\text{cav}} = 1 \times 10^7$.

Figure 7.7b) shows simulated values for the intra cavity photon number for a system with similar parameters as the experimental system realized in this work. These theoretical values were achieved by solving the so-called *optical Bloch equations* (OBE) which are equations of motions describing the time evolution of the population and the coherence of a two-level atom-cavity system^v. This theoretical procedure followed the procedure presented in [Bohnet et al., 2014] and the values shown in Fig. 7.7b) are

^vThese ODE are very similar to Eq. (3.6)-(3.8)).

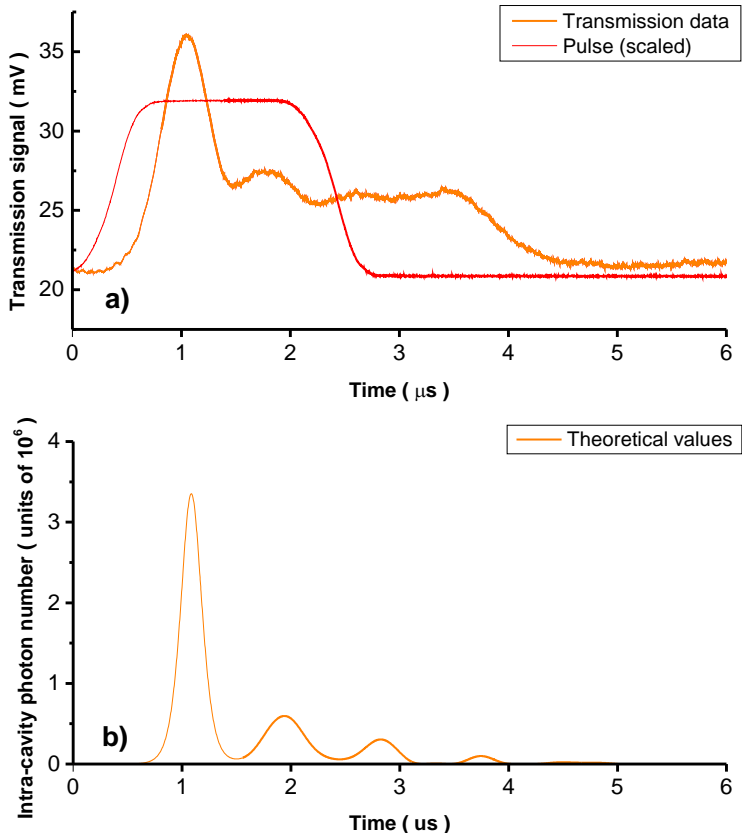


Figure 7.7: a): Example of the observed cavity transmitted flash shape. b): Theoretically predicted flash shape for a system with system parameters similar to the experimental parameters for the flash shown in a). This theoretical model did, however, not take a continuous intra cavity seed laser into account and a direct comparison is not feasible.

provided with the courtesy of Matthew Norcia^{vi} from JILA at University of Colorado, Boulder. The Doppler broadening due to the finite temperature of the atoms are taken into account by modifying the atom-cavity coupling rate $g(t) = g_0 \cos(vkt)$ (also seen in Eq. (3.6)-(3.8)) according to an atomic velocity v from the Maxwell-Boltzmann distribution corresponding to the sample temperature. Here, g_0 is the maximum atom-cavity coupling rate and k is the wave number for the radiation resonant with the atomic transition.

^{vi}e-mail: matthew.norcia@colorado.edu

The theoretical results shown in Fig. 7.7b) are preliminary and the continuous resonant seed needs to be implemented in the theoretical model before direct comparison with the experimental results shown in Fig. 7.7a). However, the overall shape and timescales of the theoretically predicted flash seems to resemble the experimentally observed flash and further development of this theoretical model might result in a convincing description of the flash shown in Fig. 7.7a).

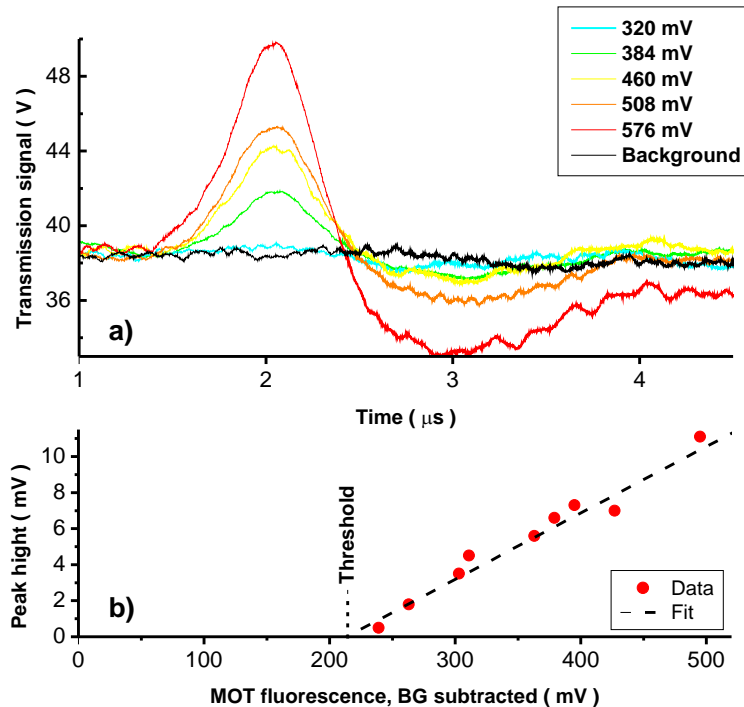


Figure 7.8: a): Atom number dependency of the flash shape. The flash shapes are shown for different MOT fluorescence representing different atom numbers. b): Atom number dependency of the flash peak height. The red dots are experimental data, while the dashed line is a linear fit. The background fluorescence signal is subtracted such that zero MOT fluorescence corresponds to zero atoms.

The parameter dynamics were investigated for the observed cavity transmission flash. The lineshape of the flash is shown in Fig. 7.8a) for different numbers of intra cavity atoms, N_{cav} . In addition, the transmission signal values for the intensity maxima are presented for different N in Fig. 7.8b). The total number of intra cavity atoms N_{cav} were varied by varying the loading time of the MOT and the total number of atoms in the MOT is evaluated to scale linearly with the MOT fluorescence. Whereas

$a \propto N_{\text{cav}}^2$ dependence of the intensity maximum was expected from a pure SF flash according to theory [Kumarakrishnan and Han, 1998], a clear $\propto N_{\text{cav}}$ is seen in Fig. 7.8b). The intensity maximum of SF flash can however, show $\propto N$ dependency [Kumarakrishnan and Han, 1998] in some specific parameter regimes as mentioned previously in Sec. 7.1. This makes it difficult to determine whether the observed phenomena is SF or something else.

Two other interesting characteristics which deviates from the behavior expected for SF are observed: Firstly, a $\tau_D \propto N^{-1}$ dependency is expected for the pulse delay [Kumarakrishnan and Han, 1998]. However, this pulse delay t_D seems independent of N in Fig. 7.8. The second interesting characteristic in Fig. 7.8b) is the threshold observed for a MOT fluorescence corresponding to $N_{\text{cav}} = 8.5 \times 10^6$ atoms (of which only around 36 % are excited as discussed in the previous section). This observed threshold intra-cavity atom number is far above the threshold $N_T = 6.3 \times 10^5$ calculated from Eq. (7.2). These characteristics suggest once again that an improved theoretical model is needed in order to describe this observed flash.

Whereas the above mentioned observations from Fig 7.8 suggest that the observed flash is something else than SF, the observation of a non-zero flash delay t_D is also not consistent with ASE even though the expected $\propto N^{-1}$ dependency of t_D was not observed. It was on the other hand observed, that this flash delay t_D depends on the power of the pulse power P_{pulse} . Figure 7.9a) shows that the flash delay t_D have a $\propto P_{\text{pulse}}^{-1}$ -like dependency. The pulse power dependency of the flash delay t_D was measured and is presented in Fig. 7.9b) and t_D is defined as the time between the onset of the excitation pulse to the intensity maximum of the flash. This behavior is not predicted by theory [Bonifacio and Lugiato, 1975, Bohnet et al., 2014], however this theory takes neither the optical cavity or the continuous driving from the resonant intra-cavity seed into account. Ideally, the π -pulse duration should also be infinitesimally small, $\tau_p < \tau_R$, for pure SF [Kumarakrishnan and Han, 1998], while the pulse durations in the order of few μs are far longer than the $\tau_R \approx 20\text{ ns}$ in the presented experiments. The physical situation in the experiments presented in this section are altogether very different from the situations studied in the previous theoretical works and a direct comparison with the these theoretical models might not be allowed. Hence, a further development of the theoretical model seems once again to be needed to describe this flash in more details.

However, the most interesting characteristics for realizing active frequency standards are in fact the coherence and the frequency stability of

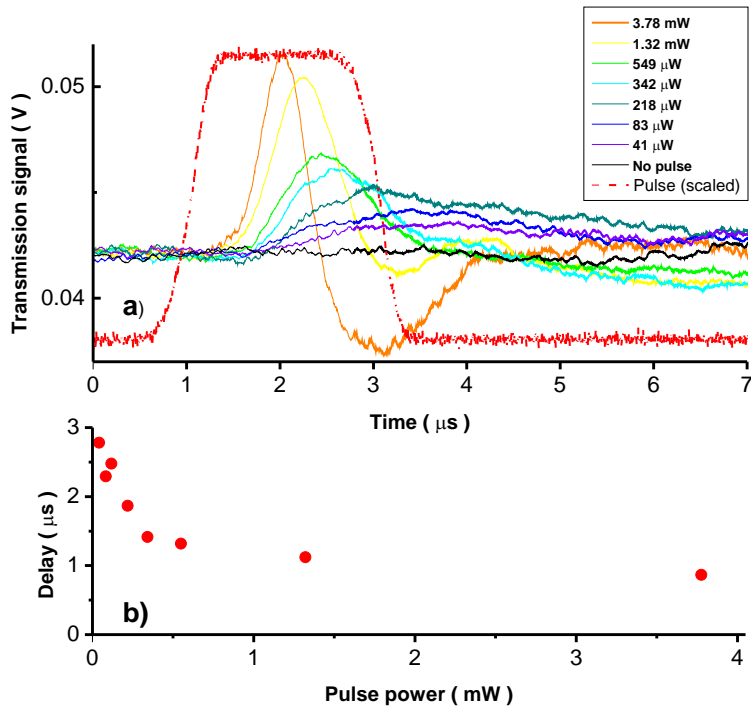


Figure 7.9: a): Pulse power dependency of the flash shape. b): The pulse power dependency of the delay of the flash peak maximum after the pulse initiation. The pulse duration was set to $2\text{ }\mu\text{s}$ in all cases.

this flash. It would be of particular interest for continuous clock operations to study the continuous enhanced transmission after the flash observed in Fig. 7.7 (marked with an arrow). Figures 7.6–7.9 have all shown *ringing* after the flash in the form of a subsequent smaller flash or a decrease of the transmission around the steady state transmission level. This ringing is possibly an indication of some degree of coherence in the system and indicates a SF-like behavior. Figure 7.10 shows the flash lineshapes for different pulse detunings and this ringing is seen very clearly in all cases. It is also very apparent, that the shape of this ringing is very sensitive to the pulse detuning.

The NICE-OHMS technique should also be able to measure this flash and determine if the light has some level of coherence, as the NICE-OHMS signal (described in Eq. (4.13)) will only yield non-zero values, if the measured light has a well defined atom induced phase. The flash was hence measured simultaneously by a slow and a fast APD (Shown in Fig. 7.2(a)), where the signal from the fast a photo detector

was demodulated in the same manner as in the NICE-OHMS technique. Figure 7.11 shows the results of these two simultaneous measurements. We see that the flash is measured convincingly for both detection techniques in Fig. 7.11, which indicates some level of coherence during the flash. However, the NICE-OHMS signal is not mirroring the features of the direct transmission as convincingly during the continuous enhancement of the cavity transmission after the flash. This indicates that two different physical processes might be occurring during the flash and during the continuous cavity transmission enhancement. It should be mentioned, that the frequency of the continuous seed beam was shifted one free spectral range $FSR = 781.14 \text{ MHz}$ (by using the flip mirror in Fig. 7.2(b)) during the measurements shown in Fig. 7.11^{vii}. This was done in order to investigate the possibility to observe the flash without having a continuous resonant seed inside the cavity. These investigations are presented in the following.

The presence of the intra-cavity continuous resonant seed used for stabilizing the optical cavity raises a number of concerns for the prospect of using collectively emitted light as an active frequency standard: Firstly, the observed flash might be light emitted primarily due to stimulation by the seed. The spectral properties of the flash will then be dominated by the seed and possible linewidth narrowing effects from the collective spontaneous emission might be corrupted. Secondly, it is important to be able to separate the collectively emitted light and the seed light used for stabilizing the optical cavity in order to exploit a potential coherence of the collectively emitted light. One approach among many to separate the involved light components is by using a seed off-resonant with the atomic transition for stabilizing the cavity and then apply narrow band interference filters or applying heterodyne demodulation measurement techniques such as the NICE OHMS technique (described in Sec. 4.6).

The frequency of the continuous probe laser was shifted one free spectral range ($FSR = 781.14 \text{ MHz}$) from the atomic resonance as described previously in this section. By doing this, the probe laser could be used for stabilizing the vacuum cavity and at the same time be far detuned from the $^1S_0 \rightarrow ^3P_1$ transition. The atomic transition could still be probed resonantly by adding sidebands on the probe laser by applying phase modulation on the probe light with modulation frequency $\omega_m/2\pi = FSR$. The intra cavity sideband-seed power can be varied by varying the amplitude of this phase modulation, and it is shown in Fig. 7.12 that the flash intensity depends significantly on the seed power. The flash seemed to disappear,

^{vii}This setup is very similar to the setup described in Sec. 6.2.1

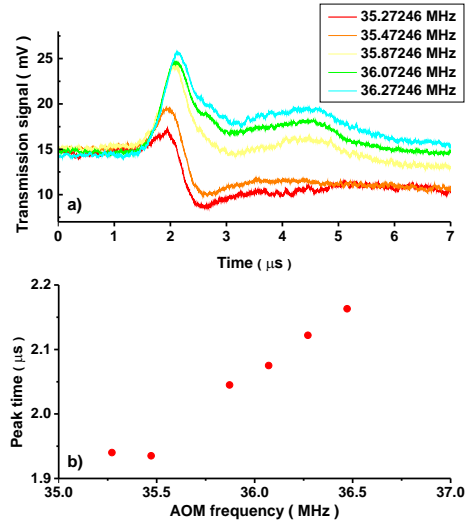


Figure 7.10: *a)*: Pulse detuning dependency of the flash shape. *b)*: The delay of flash peak maximum as function of pulse detuning. The pulse duration was set to $2\ \mu\text{s}$ in all cases. The detuning is presented in terms of the modulation frequency of AOM_p shown in Fig. 7.2(*a*).

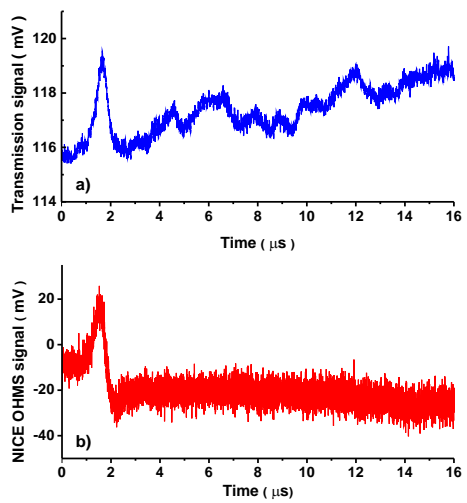


Figure 7.11: *The cavity transmitted flash measured by measuring the direct transmission power (shown in *a*) and by using the NICE-OHMS technique (shown in *b*).* The pulse length was $> 16\ \mu\text{s}$ and the quasi continuous transmission increase was seen in *a*) while this was not as pronounced in *b*).

when there was no resonant sideband-seed, and a seed power threshold was also observed.

It appears that the observed flash only occurs when a strong resonant seed is present. The probe carrier was hence prepared detuned one FSR from the atomic resonance while a side band was resonant with the atomic resonance. The pulse sequence shown in Fig. 7.4(*c*) was performed. In this sequence, the seed laser was turned off $2\ \mu\text{s}$ before the pulse. The vacuum cavity was kept on resonance with the atomic transition under the entire sequence because the carrier component of the probe was resonant with a cavity mode, which was one FSR off resonant with the atomic transition. No significant flash-like behavior was observed in the cavity transmission in this setup and more thorough studies of the flash without a continuous seed are left for future studies.

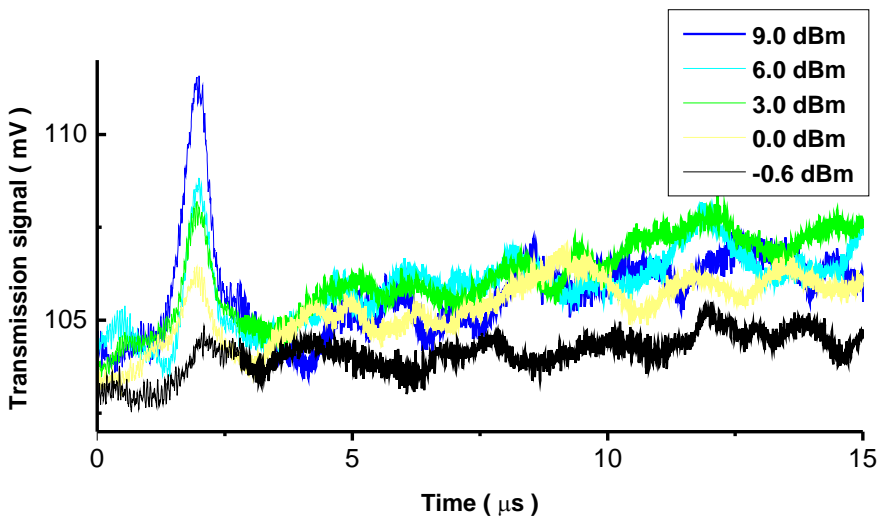


Figure 7.12: Flash lineshapes for different intra cavity seed powers. The probe laser frequency was shifted by one FSR and the atomic resonance was probed by a sideband. The seed power was controlled by adjusting the modulation amplitudes shown in the figure legend, which represents the amount of optical probe laser power transferred to the resonant sideband.

Outlook

In this chapter, collective emission phenomena were studied experimentally for an atom-cavity system consisting of laser cooled ^{88}Sr atoms coupled to a vacuum cavity with a finesse of $F = 1450$. The collective cooperativity of this system is expected to be around $C = 6.3 \times 10^3 \gg 1$. This value of C brings the system into the regime of strong collective cooperativity, where collective emission phenomena can be expected as described earlier in Sec. 2.2.

Collective emission was observed in the form of a flash of enhanced cavity transmission shortly after a fraction of the atomic sample was excited by a resonant pulse. Whereas signs of coherence was observed for the flash, detailed studies of the spectral properties of the flash was not yet performed. Studies of these spectral properties are ideal topics for future works, as observations of linewidth narrowing processes with thermal atoms would pave the way for many interesting applications for compact clock systems.

The characteristic time scales of this system suggested that the observed flash might be superfluorescence. The optical power of the observed flash was consistent with the number of atoms inside the cavity mode, but

the peak heights and the delay of this flash did not depend on the system parameters as expected for pure superfluorescence described in the literature [Kumarakrishnan and Han, 1998, Bonifacio and Lugiato, 1975]. The experimentally determined threshold number of intra-cavity atoms was also far above the theoretically expected threshold number N_T described in Eq. (7.2).

A continuous resonant seed intra-cavity field was present in the experimentally studied system and the flash was only observed when this seed was present. This continuous seed makes this system significantly different from the systems described in previous works [Kumarakrishnan and Han, 1998, Bonifacio and Lugiato, 1975]. It is hence appropriate to suspect the observed flash differs quite radically from the conventional superfluorescence and a new theoretical description is most likely needed to describe this phenomena. A new theoretical description is also necessary for detailed studies of the prospects for applying this collective emission for active frequency standards. A simple theoretical model following the procedures presented in [Bohnet et al., 2014] predicted collective emission processes qualitative similar to the experimentally observed flash (presented in Fig. 7.7). Further development of this model might be a promising topic for future theoretical works.

OUTLOOK

In this final chapter, the general content of this work is summarized. The general motivations, which initiated this work, and the main results of this work are presented. The novel results and understanding has given rise to new questions and motivations, which will be discussed in comparison with the works of other research groups within the topic of this work. Finally, the theoretical understanding and experimental techniques developed in this work has spawned a new generation of experimental setups with great diversity, which will be presented as a possible glimpse into the future works.

8.1 This work

This work was initiated based on the encouraging prospects of achieving ultra stable lasers by exploiting systems, where a sample of atoms with narrow atomic transitions are trapped inside an optical cavity. It was predicted that the spectral properties of the narrow atomic transitions could be exploited advantageously by operating in the so-called bad cavity regime, where the atomic transition would dominate the spectral properties of the combined atom-cavity system.

The main theoretical works, which initiated the motivation for this work were produced by incredibly skilled physicists at JILA, University of Colorado, Boulder [Martin et al., 2011, Meiser et al., 2009] and at Peking University, Beijing [Chen, 2009]. In all these theoretical works, great focus was put on using ultra cold neutral strontium atoms due to their

the ultra narrow $^1S_0 \rightarrow ^3P_0$ transition. Neutral strontium was most likely also considered as a promising candidate due to the availability of the required laser wavelengths, the maturity of the current laser and trapping techniques and due to the great number of research groups working with ultra cold strontium atomsⁱ. Hence, laser cooled ^{88}Sr strontium isotope was also chosen as the element of interest in this work.

The first theoretical works studied the prospects for using strontium atoms tightly trapped in optical lattices, such that the atomic temperatures corresponds essentially to $T = 0\text{ K}$. Whereas such conditions are realized in a great number of atomic clock research groups around the world, a much simpler system with atomic temperatures in the mK level was studied in this work. This choice of atomic temperature was motivated by a wish to realize simple and compact systems. The theoretical model developed for atomic temperatures of $T = 0\text{ K}$ [Martin et al., 2011] were not directly compatible with atomic temperatures in the mK level. A new theoretical model was hence developed in this work by taking the effects of the finite atomic velocities into account. This new model was developed in collaboration with theorists at JILA, University of Colorado, Boulder and published in [Tieri et al., 2015]. This new model predicted that laser linewidths in the sub 10 mHz level could potentially be achieved by using atom-cavity systems with very realizable experimental parameters. This predicted linewidth may compete with the current state-of-the-art ultra stable lasers.

A proof-of-concept experimental setup was developed in parallel with the development of the above mentioned theoretical model. A sample of laser cooled ^{88}Sr were prepared inside a low finesse cavity and the atomic induced phase dispersion signal was mapped out as a potential error signal, which could be used for laser stabilization. The temperature of the laser cooled atoms were in the mK level and a convincing agreement was observed between the experimental data and the values predicted by the new theoretical model developed in this work. The preliminary results from this proof-of-concept experiment was published in [Westergaard et al., 2015].

The proof-of-concept atom-cavity system studied theoretically and experimentally in this work was in a so-called strongly saturated regime where highly non-linear dynamics were expected. This non-linear dynamics regime made it non-trivial to determine the optimal system parameters

ⁱSimilar experiments can most likely also be performed with a large number of trapped ions. However, perturbations from different micro motion effects will most likely be difficult to control.

for laser stabilization. A detailed study of the non-linear system dynamics were performed and a number of new experimental techniques were developed in order to carry out this study. The results of these studies and the technical details concerning the experimental techniques were published in [Christensen et al., 2015a].

The proof-of-concept experiment showed that such a system can be realized. However, the experimental and theoretical studies of the system dynamics revealed that a higher finesse was needed for the optical cavity of the atom-cavity system in order to achieve the predicted sub 10 mHz linewidths. The optical cavity in the first proof-of-concept experiment had a finesse of around $F = 85$. These cavity mirrors were placed outside a vacuum chamber and the intra cavity vacuum windows limited the value of the corresponding cavity finesse. However, the theoretical model predicted that a finesse around $F = 1000$ was required in order to reach the sub 10 mHz linewidths. A vacuum cavity was hence designed and realized inside the vacuum chamber. The finesse of this cavity was evaluated to be $F = 1450$, which brought the system into the parameter regime interesting for laser stabilization.

An other approach for achieving ultra stable lasers is to exploit collective emission processes in atom-cavity systems as active frequency standards. Active frequency standards are atom-cavity systems which directly emit radiation with low phase noise. Theoretical prediction had estimated that the realized vacuum cavity and the laser cooled ^{88}Sr atoms could constitute an atom-cavity system in a parameter regime, where collective emission can occur. A variant of collective emission was observed in the form of a flash of light transmitted out of the cavity. Preliminary studies of the characteristics of this flash were performed but further studies are needed in order to describe the phenomena in details and in order to evaluate the spectral purity of this flash.

8.1.1 Other similar works

The prospects for achieving ultra stable lasers by exploiting ultra narrow atomic transitions are under study in many other research groups other than at the Niels Bohr Institute, where this work was performed.

The developments in this field has accelerated rapidly and a great number of pioneering works have been reported during the years, where this work was carried out. This rapid development is for example reflected in the fact that a new separate presentation session on *Atomic Laser Stabilization* was introduced at the 2015 Joint Conference of IEEE

IFCS&EFTF in Denver, where this work was also presented [Christensen et al., 2015b].

The main focus for many groups have been to achieve collective emission processes such as superradiance or superfluorescence for ultra narrow transitions in strontium based systems. Particularly, the group of James K. Thomsen at JILA, University of Colorado, Boulder has achieved tremendous progress the recent years. This group has reported observations of collective emission for both the narrow $^1S_0 \rightarrow ^3P_1$ 7.5 kHz transition of ^{88}Sr and the ultra narrow $^1S_0 \rightarrow ^3P_0$ 1 mHz transition of ^{87}Sr [Norcia and Thompson, 2016a, Norcia et al., 2016]. Similar collective emission phenomena has been observed for systems with high atomic density and without an optical cavity in the group of David Wilkowski at Nanyang Technological University, Singapore [Kwong et al., 2015b]. Collective processes leading to linewidth narrowing of the collectively emitted light have been reported for different other alkali elements [Zhi-Chao et al., 2015, Bohnet et al., 2012]. This enhances the motivations for pursuing further research in collective emission processes with ultra narrow transitions for applications in frequency standards.

The application of narrow line transitions for continuous laser stabilization have also been pursued with many atomic systems [Fox et al., 2012, Cook et al., 2015]. Continuous laser stabilization on the narrow transitions of strontium atoms has, to the best knowledge of the author of this work, not yet been realized. This is thus a promising topic for future studies.

8.1.2 Future studies

The studies carried out in this work has led to achievements towards frequency stabilization with laser cooled strontium atoms. However, these studies have also given rise to new topics for future studies.

First of all, actual laser stabilization on the $^1S_0 \rightarrow ^3P_1$ 7.5 kHz transition of ^{88}Sr should be realized in order to confirm the promising laser stabilization performances predicted by the theoretical model developed in this work. The experimental systems developed in this work operate with cyclic sequences, which are not very suited for continuous laser stabilization. Hence, the preparation of a beam-line setup for continuous laser stabilization was initiated in parallel with this work and further development of this system is a promising topic for future studies. A beam of transversely cooled and longitudinally slowed strontium atoms will be interrogated continuously in this beam-line setup, which allows continuous laser stabilization. A number of technical challenges are most

likely needed to be overcome for this beam-line setup. Fortunately, a large part of the experimental techniques developed in this work can be transferred to the beam-line setup and prove valuable for the realization continuous laser stabilization.

Cavity enhanced laser stabilization on the ${}^1\text{S}_0 \rightarrow {}^3\text{P}_1$ 7.5 kHz transition of ${}^{88}\text{Sr}$ will require cavity finesse similar to or higher than the finesse of the vacuum cavity developed in this work. The system dynamics of this vacuum cavity system was not studied as detailed in this work as the dynamics of the low finesse cavity. Some peculiar and not fully understood features were observed in the spectroscopic transmission and phase dispersion lineshapes. Detailed studies of these features and the dynamics of the system are needed in future studies in order to optimize the performance of future systems for continuous laser stabilization on atom-cavity systems with similar finesse values.

Finally, a wide range of topics for studies are opened up by the preliminary observations of collective emission phenomena in an thermal atom-cavity system with atomic temperatures in the relatively high mK level. An improved theoretical model needs to be developed in order to gain understanding of the observed phenomena. Detailed investigations of the spectral properties of the collectively emitted light is also needed in order to study the prospects for realizing a simple active frequency standard system. It will also be very interesting to study continuous collective emission in the above mentioned beam-line setup.

8.2 On the horizon

The understanding of the cavity enhanced spectroscopy of atoms with narrow line transitions achieved in this work has spawned a new generation of experimental systems, which consists of three different systems.

The first system is the strontium beam-line experiment already presented in the section above. Figure 8.1a) shows the realized system where a thermal beam of strontium atoms are released from an oven. The atoms in this beam are slowed down in a Zeeman slower and the atoms are cooled transversely in the dimensions perpendicular to the beam propagation axis by using a 2D MOT. The beam of cold atoms is sent through an optical cavity and cavity enhanced interrogation of the atoms can be performed continuously. This setup allows studies of both continuous laser stabilization and continuous collective emission phenomena.

The development of two molecular setups were also initiated during this work. Both of these systems consist of a gas cell placed inside

an optical cavity. Here, narrow line molecular transitions are used as the frequency references instead of an atomic transition. Figure 8.1b)–c) shows two realized molecular systems based on narrow molecular transitions of iodine (I_2) and acetylene (ethyne). The target transitions are the $^{127}I_2 P(13)43-0:a3$ transition at $\lambda = 514.6$ nm for the iodine with a transition width of $\Gamma_I = 2\pi \times 284$ kHz and the $^{13}C_2H_2 P(16):\nu_1 + \nu_3$ transition at $\lambda = 1542.4$ nm for acetylene with a transition linewidth in the Hz level [Schaffer et al., 2015]. The transition wavelength of acetylene is of particular interest, as this is in the telecommunication wavelength band. A stable frequency standard in this wavelength band can hence be easily implemented in telecommunication systems.

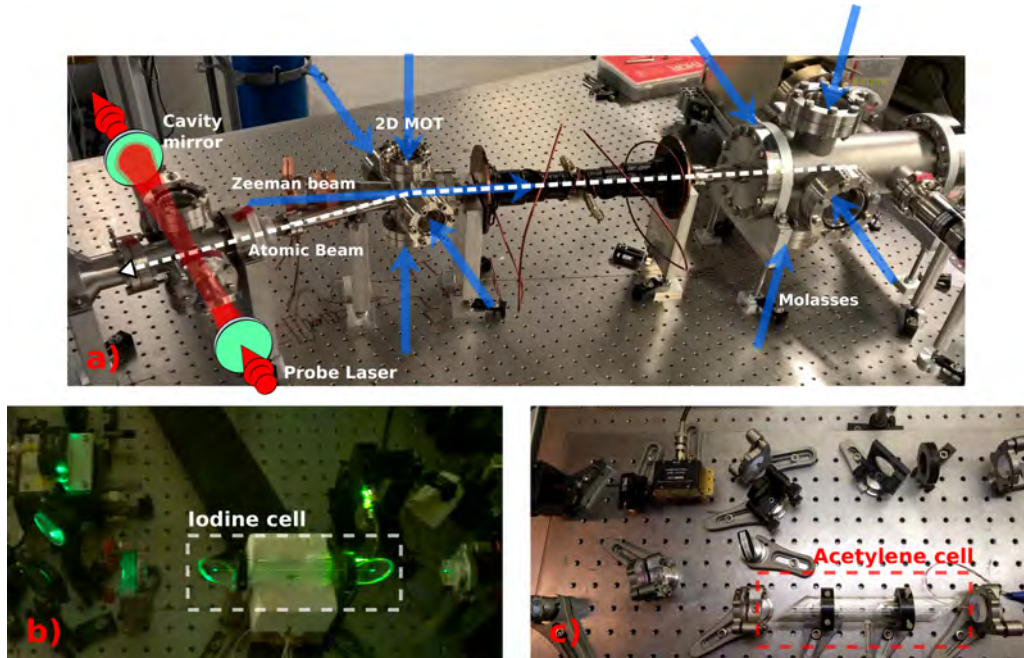


Figure 8.1: *Pictures of the new generation of laser stabilization systems inspired by this work.* a): Picture of strontium beam-line experiment setup for studies of continuous laser stabilization and continuous collective emission. b): Picture of setup for cavity enhanced spectroscopy of iodine. c): Picture of setup for cavity enhanced spectroscopy of acetylene.

The ultimate linewidths predicted for atom-cavity systems with atoms trapped in an optical lattice or in a MOT cannot be achieved for these molecular systems. However, these systems do not require laser cooling or trapping techniques and can operate near room temperatures. Hence,

these molecular systems are promising for realizing simple and compact molecular systems relevant for out-of-lab operation under more noisy environments.

It is the hope of the author of this work, that the physical understanding and experimental techniques developed in this work might push this next generation of experiments up to new stabilization levels.



APPENDIX

A.1 Vacuum chamber mounts

Figure A.1–A.2 show the two mounts used for fixing the optical components used for coupling the probe laser to the two cavity systems described in Sec. 5.2.2–5.2.3 and for detecting the light transmitted by these two cavities. All components on these mounts were either fastened by screws or glued.

The cavity mirrors of the low finesse cavity (described in Sec. 5.2.2) were also fixed on these mounts. These mounts were fastened tightly on the view port flanges of the main vacuum chamber, which ensured to a great extent that the mechanical vibrations of the low finesse cavity mirrors were common mode. Hence, the relative mechanical vibrations were greatly reduced.

The mount on the input side was modified significantly for the vacuum cavity system, as the mode matching of the input beam required an extra degree of freedom. These modifications are unfortunately not shown in Fig. A.2.

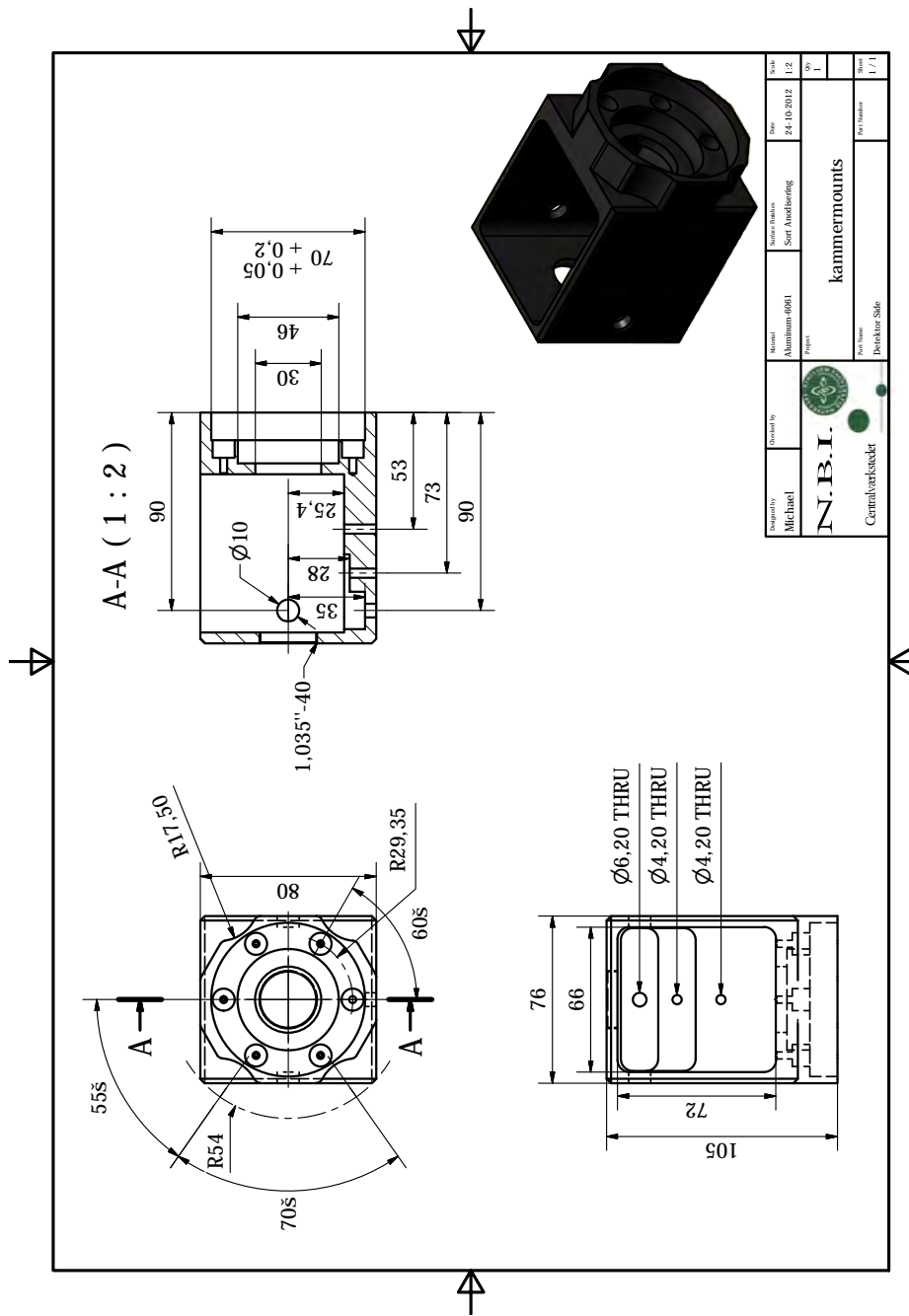


Figure A.1: Technical drawing of the mounting structure used to fix the output mirror of the low finesse cavity described in Sec. 5.2.2. The optical components used for detection of the cavity transmitted light were also fixed on the same mount.

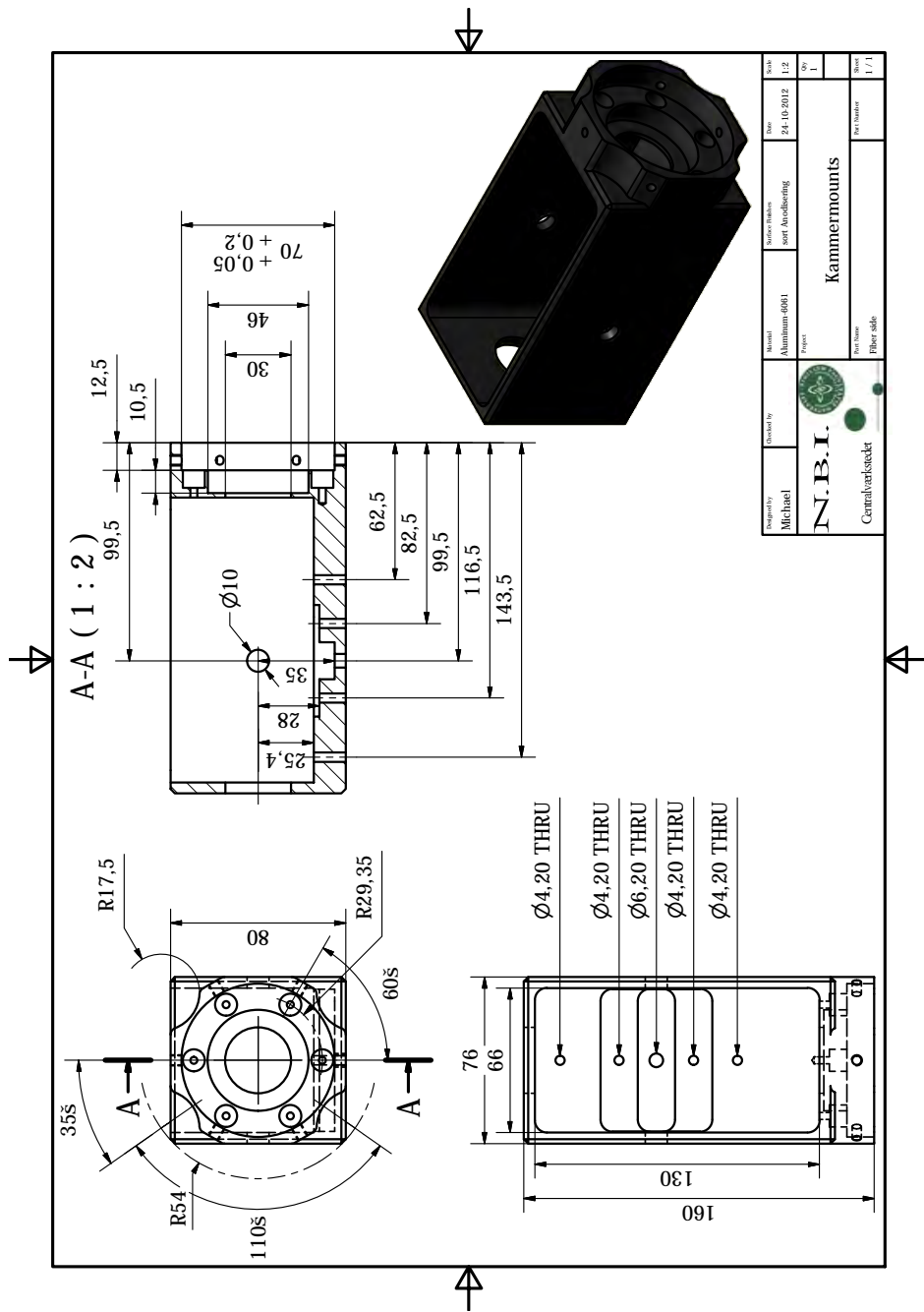


Figure A.2: Technical drawing of the mounting structure used to fix the input mirror of the low finesse mirror cavity in Sec. 5.2.2. This mount did also fix the optical components used for controlling the input polarization and for mode matching of the cavity mode and the input beam mode.

A.2 Modulation index for fiber EOM

Figure A.3 shows the dependency of sideband generation for different phase modulation powers. The sidebands are applied on the probe laser used in this work (described in Sec. 5.1.1) by using an EOM to apply a periodic phase modulation. The so-called modulation index x is determined by coupling the probe laser to an optical cavity and detecting the peak values of the transmission signal while scanning the cavity length. An example of such a transmission scan is shown in Fig. 6.6.

The optical power ratio of the carrier component and one of the sideband components are shown in Fig. A.3a). This ratio corresponds to $(J_1(x)/J_0(x))^2$, where $J_j(x)$ is the j 'th order regular Bessel function describing the amount of power transferred from the carrier to the j 'th order sideband when modulated by an EOM with modulation index x .

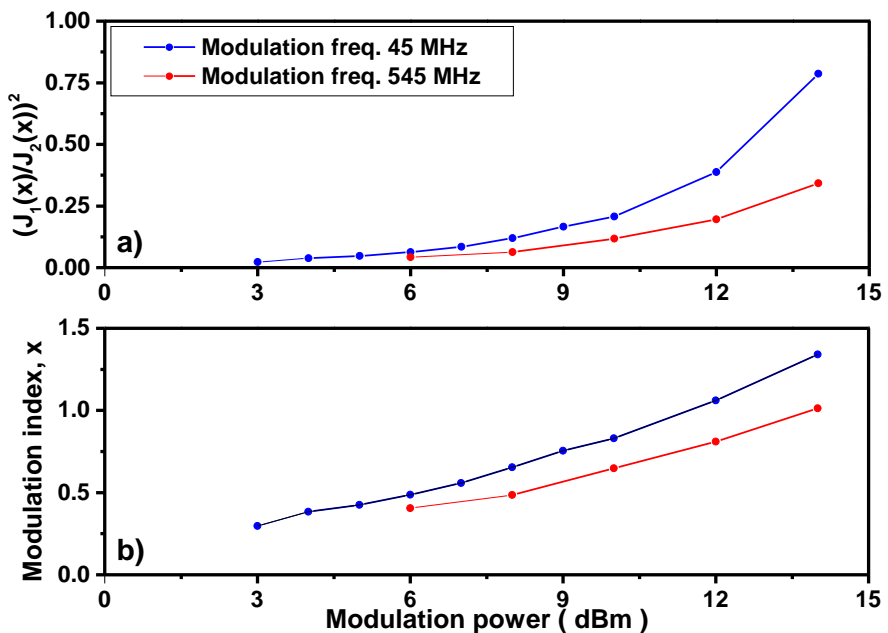


Figure A.3: Dependency of sideband generation for different phase modulation powers in terms of dBm. The blue line is for phase modulation frequency of 45 MHz, while the blue line is for phase modulation at 545 MHz. a): Ratio of the optical power of the carrier component and the optical power transferred to one of the first order sidebands. b): Modulation index x as function of the phase modulation power. x is a measure of the amplitude of the phase modulation. All values of x shown in b) are calculated from the results shown in a).

A.3 Outgassing of viton

Viton strips were used for supporting the vacuum cavity structure described in Sec. 5.2.3. Outgassing of the viton strips can potentially degrade the vacuum level of the main chamber. This outgassing can increase the background pressure in the main vacuum chamber and reduce the number of atoms trapped in the MOT. Hence, the vacuum degrading components in the viton strips were outgassed in a separate test vacuum chamber at temperatures up to 80 °C for a month before the strips were used for supporting the vacuum cavity [Peacock, 1980]. Figure A.4 shows the pressure level inside the test vacuum chamber during this outgassing processes. The viton strips were put into the main vacuum chamber when pressure levels in the low 10^{-9} mBar were confirmed.

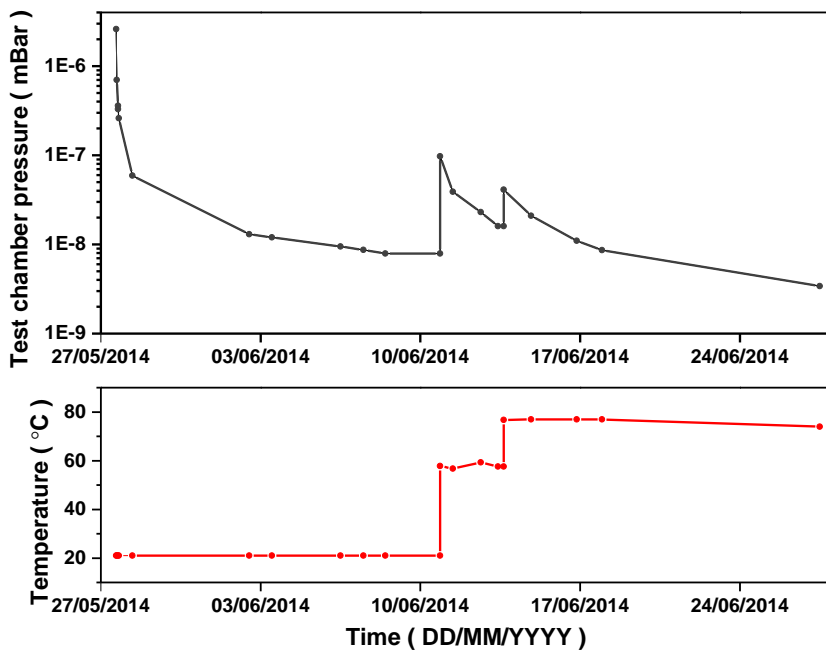


Figure A.4: Pressure level and temperature of the test vacuum chamber during the outgassing process of Viton strips. The horizontal axis shows the dates where this outgassing process was carried out.

A.4 Vacuum cavity drawing

Figure A.5 shows the technical drawings of the cavity spacer for the vacuum cavity system designed in this work (described in Sec. 5.2.3).

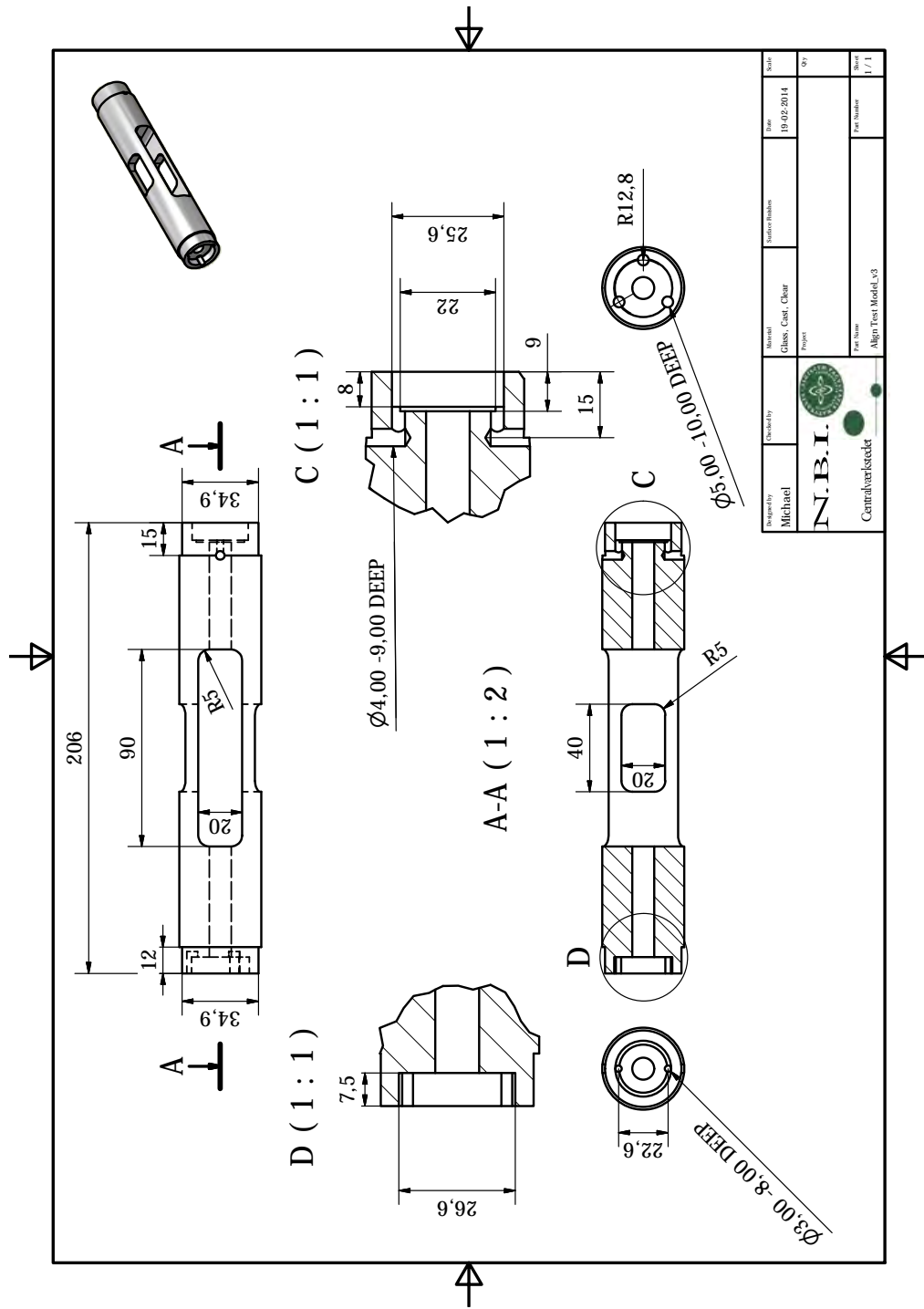


Figure A.5: Technical drawings of the cavity spacer for the vacuum cavity described in Sec. 5.2.3. The spacer material is Zerodur and all length units are in mm.

A.5 Servo circuit for vacuum cavity

Figure A.5 shows the servo circuit developed for stabilizing the length of the vacuum cavity (described in Sec. 5.2.3), such that the cavity is resonant with the probe laser at all times. The Bode plot of this servo circuit (shown in Fig. 5.30) reveals that the corner frequencies are all far from the mechanical resonance of the cavity mirror. This servo circuit can hence most probably be improved.

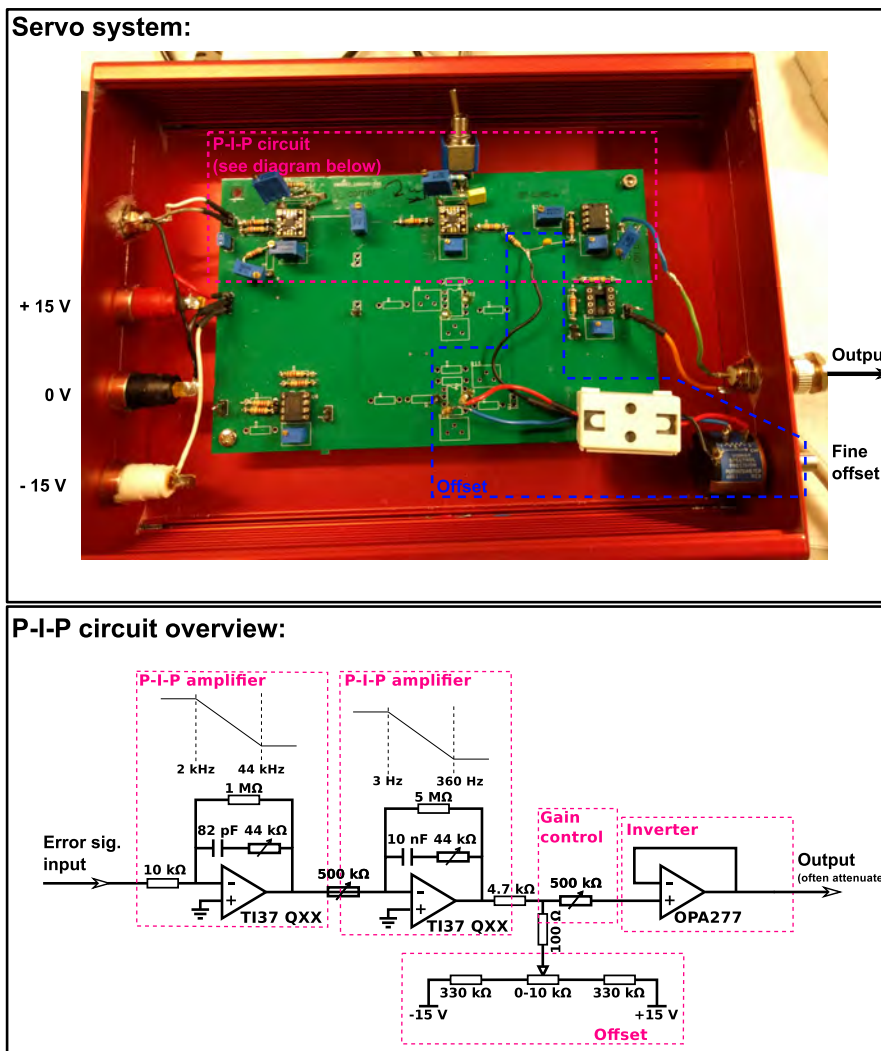


Figure A.6: Picture and circuit diagram of the servo circuit used for stabilizing the length of the vacuum cavity described in Sec. 5.2.3. The circuit is placed inside a metal box in order to shield it from electro magnetic radiation from the surroundings.

A.6 Simultaneous NICEOHMS

Figure 6.5 shows the NICE-OHMS signals obtained by demodulation at $\Omega/2\pi = 1 \times \text{FSR}$ (see Eq. (6.10)) and $2\Omega/2\pi = 2 \times \text{FSR}$ (see Eq. (6.9)). These two signals are measured separately, as the signal-to-noise ratio was greatly degraded, when the detected AC signal power was split into two channels as shown in Fig. 6.1a). However, simultaneous measurements are possible and one example is shown in Fig. A.7.

Simultaneous scans

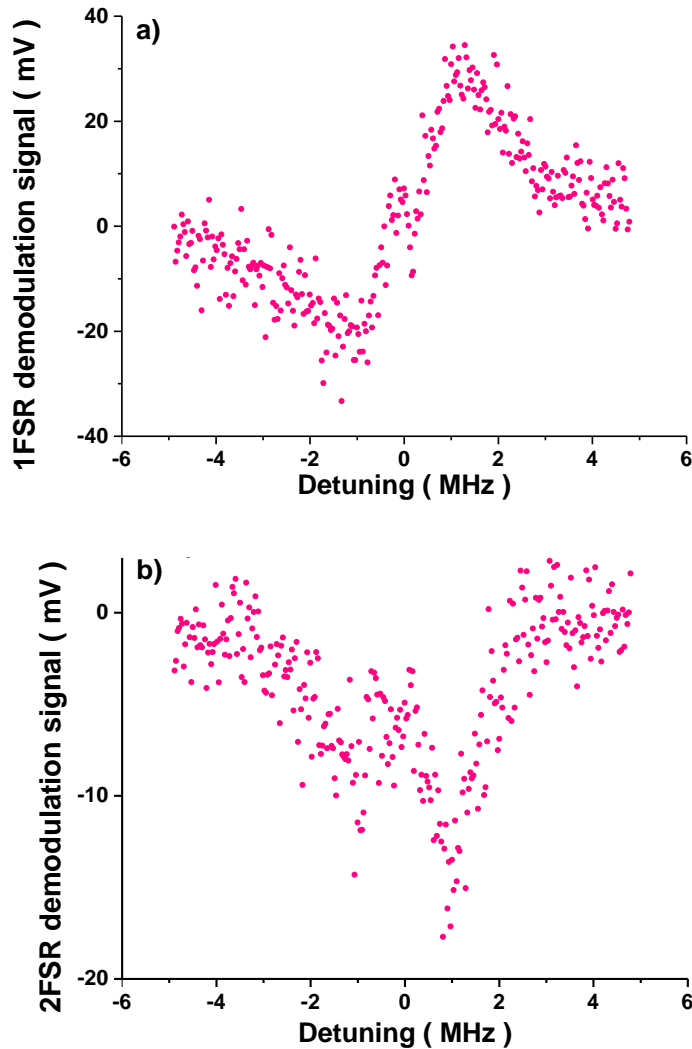
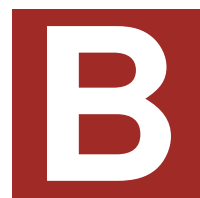


Figure A.7: *Simultaneous measurements of the NICE-OHMS signals for demodulation at 1FSR or 2FSR. The signal-to-noise ratio is poor because the AC signal power is split into two channels. (see Fig. 6.1a) for details.)*



MAIN PUBLICATIONS

B.1 Non-linear Spectroscopy of Sr Atoms in an Optical Cavity for Laser Stabilization

Bjarke T. R. Christensen, Martin R. Henriksen, Stefan A. Schäffer, Philip G. Westergaard, Jun Ye, Murray J. Holland & Jan W. Thomsen, *Non-linear Spectroscopy of Sr Atoms in an Optical Cavity for Laser Stabilization*, *Phys. Rev. A*, **92**, 053820 (2015).

Nonlinear spectroscopy of Sr atoms in an optical cavity for laser stabilization

Bjarke T. R. Christensen,^{1,*} Martin R. Henriksen,¹ Stefan A. Schäffer,¹ Philip G. Westergaard,² David Tieri,³ Jun Ye,³ Murray J. Holland,³ and Jan W. Thomsen¹

¹*Niels Bohr Institute, University of Copenhagen, Blegdamsvej 17, 2100 Copenhagen, Denmark*

²*Danish Fundamental Metrology, Matematiktorvet 307, 1. sal, 2800 Kgs. Lyngby, Denmark*

³*JILA, National Institute of Standards and Technology and University of Colorado, Boulder, Colorado 80309-0440, USA*

(Received 21 July 2015; published 6 November 2015)

We study the nonlinear interaction of a cold sample of ^{88}Sr atoms coupled to a single mode of a low finesse optical cavity in the so-called bad cavity limit, and we investigate the implications for applications to laser stabilization. The atoms are probed on the weak intercombination line $|5s^2 \ ^1S_0\rangle - |5s5p \ ^3P_1\rangle$ at 689 nm in a strongly saturated regime. Our measured observables include the atomic induced phase shift and absorption of the light field transmitted through the cavity represented by the complex cavity transmission coefficient. We demonstrate high signal-to-noise-ratio measurements of both quadratures—the cavity transmitted phase and absorption—by employing frequency modulation (FM) spectroscopy (noise-immune cavity-enhanced optical-heterodyne molecular spectroscopy). We also show that when FM spectroscopy is employed in connection with a cavity locked to the probe light, observables are substantially modified compared to the free-space situation in which no cavity is present. Furthermore, the nonlinear dynamics of the phase dispersion slope is experimentally investigated, and the optimal conditions for laser stabilization are established. Our experimental results are compared to state-of-the-art cavity QED theoretical calculations.

DOI: [10.1103/PhysRevA.92.053820](https://doi.org/10.1103/PhysRevA.92.053820)

PACS number(s): 37.30.+i, 32.80.Wr, 42.50.Ct, 42.62.Fi

I. INTRODUCTION

Lasers with exceedingly pure spectral features are a key element in the interrogation of ultranarrow atomic transitions applied in, for example, optical atomic clocks [1–5], condensed-matter simulations with cold atoms [6], and relativistic geodesy [7,8]. Such pure spectral instruments with high-phase stability and long coherence times are essential to investigations of physics beyond the standard model, e.g., the drift of fundamental physical constants [9,10] or the detection of gravitational waves [11] as predicted by the general theory of relativity. The stability of the current state-of-the-art lasers is limited by Brownian motions of the reference cavity mirror substrates and coatings [12–14], and the emergence of new technologies [15–17] seems necessary if further improvements are to be made commonly available.

Recent studies have proposed a new scheme for laser stabilization to a mK thermal sample of atoms placed in a low finesse optical cavity [18–21]. By placing the atoms inside the optical cavity, atom-light interactions are enhanced by order of the finesse of the cavity, and nonlinear effects are brought into play, which enhance the spectral sensitivity of the detected photocurrent used for stabilization. Interestingly, the first proposals considered atoms trapped in an optical lattice or systems with a sample temperature equivalent to zero degrees Kelvin [19]. Further studies have extended these results to also include the finite temperature of the sample [20,21]. At finite temperatures, the bistability regime, present at the optimal locking point for zero-Kelvin systems, turns out to be effectively removed. Since there is no bistability at the optimal locking point for finite-temperature systems, this sparks renewed interest for stabilization to samples of atoms with finite temperatures.

In this work, we investigate the nonlinear coupling of laser-cooled ^{88}Sr atoms to a single mode of an optical cavity. During experiments, the atom-modified cavity mode is forced to be on-resonance with the carrier of the probe laser and thus a standing wave will be present at all times in the cavity. As a result, significant changes appear in the observables of the system due to reaction of the atoms on the cavity servo system.

This has major consequences: the phase and absorption information is altered compared to conventional free-space frequency modulation (FM) spectroscopy, but may be recovered under special conditions of laser detuning and demodulation frequency. In the following, we also explore the nonlinear cavity-atom dynamics and identify optimal parameters relevant for laser stabilization to our cavity system. The experiments are performed in a cyclic manner, but the understanding of the nonlinear dynamics and the optimal experimental parameters obtained here will prove valuable for continuous laser stabilization to future noncyclic systems [22].

II. EXPERIMENTAL SETUP

Experimentally, our cavity system consists of a sample of laser-cooled ^{88}Sr atoms with a temperature of 5 mK coupled to an optical cavity with finesse $F = 85$; see Fig. 1(a). We operate a standard magneto-optical trap (MOT) and trap about 5×10^8 Sr atoms using the strong $^1S_0 \rightarrow ^1P_1$ transition at 461 nm; see Fig. 1(b). The system is probed on the $^1S_0 \rightarrow ^3P_1$ intercombination transition at 689 nm while the cavity is forced to be on resonance with the probe laser at all times. The cavity mirrors have a radius of curvature of 9 m yielding a cavity waist diameter of about 1 mm, which is comparable to the size of the MOT. At our current MOT temperature, we estimate the transit time broadening to be 1–2 kHz, which is significantly smaller than the natural atomic linewidth of $\Gamma/2\pi = 7.5$ kHz. The 30 cm cavity, with a free spectral range (FSR) of 500 MHz, is placed outside the vacuum chamber

*bjarkesan@nbi.ku.dk

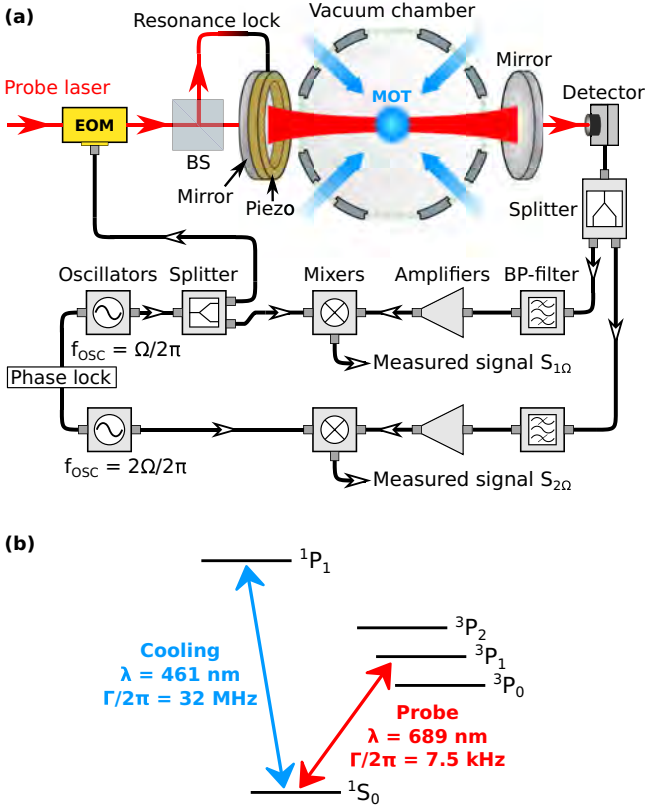


FIG. 1. (Color online) (a) Experimental setup. A sample of cold ^{88}Sr atoms trapped in a standard magneto-optical trap (MOT) is located inside a low finesse optical cavity ($F = 85$). The cavity is locked to resonance with the light using the Hänisch-Couillaud [25] scheme. We perform cavity-enhanced FM spectroscopy (NICE-OHMS) where the light is modulated at $\Omega/2\pi = \text{FSR}$ (free spectral range of the cavity). The detected signal is split into two arms where the Ω and 2Ω components are selected by band-pass filters and separately demodulated using rf mixers. One part of the signal is demodulated at Ω giving a phase signal, and the other part is demodulated at 2Ω giving an attenuation signal. Both the phase shift and the absorption line shape of the transmitted probe light are recorded simultaneously with this scheme. (b) Energy levels of the ^{88}Sr atom important for this work. The singlet transition $|5s^2\ 1S_0\rangle - |5s5p\ 1P_1\rangle$ at 461 nm is used to trap and cool the atoms. The narrow intercombination line transition $|5s^2\ 1S_0\rangle - |5s5p\ 3P_1\rangle$ at 689 nm is used to probe the atoms.

thereby limiting the obtainable finesse. We measure a cavity linewidth of $\kappa/2\pi = 5.8$ MHz placing our system in the bad-cavity regime $\kappa \gg \Gamma$. We probe the atoms for 100 μs and the 461 nm light is turned off during this probing period. At the probing time scale, our prestabilized laser has an estimated linewidth of 800 Hz.

We employ cavity-enhanced FM spectroscopy [noise-immune cavity-enhanced optical-heterodyne molecular spectroscopy (NICE-OHMS)] [23,24]; see Fig. 1, where the probe carrier is modulated at the FSR to create sidebands, in our case separated from the carrier by multiples of 500 MHz. The cavity-transmitted signal is detected by a high bandwidth photodetector recording the beat note between the carrier

and the sidebands. This signal contains information about the cavity-transmitted field amplitude and nonlinear phase shifts due to the atoms present in the cavity. These contributions are recovered with a high signal-to-noise ratio by demodulating at FSR and multiple FSRs.

Our cavity system supports a single-atom cooperativity $C_0 = 4g^2/\Gamma\kappa$ of $C_0 = 3 \times 10^{-5}$, where g is the single-atom-cavity coupling constant. For our cavity setup, we find $g/2\pi = 590$ Hz. The C_0 parameter is a measure of the rate at which an atom emits a photon into the cavity mode compared to all other dissipation rates in the system. For the collective cooperativity, we find $C = N_{\text{cav}}C_0 = 630$, where N_{cav} is the total number of atoms in the cavity mode volume. With a MOT atom number of 5×10^8 , we find $N_{\text{cav}} = 2.5 \times 10^7$.

III. THEORY OF MEASUREMENT

In this section, we establish a connection between our measured cavity-transmitted quantities and the complex transmission coefficient of the input field χ . Our input probe field can be written in terms of a carrier and multiple orders of sidebands induced by phase modulation. By neglecting residual amplitude modulation, the total input probe field, E_{in} , with sidebands can be given as

$$E_{\text{in}} = E_0 \sum_{p=-\infty}^{\infty} J_p(x) e^{i(\omega_c + p\Omega)t}, \quad (1)$$

where $J_p(x)$ is the p th-order regular Bessel function describing the amount of power transferred from the carrier ($p = 0$) to the sidebands ($|p| > 0$), x is the electro-optic modulator (EOM) modulation index, ω_c is the carrier frequency, which is close to the atomic resonance, and Ω is the EOM modulation frequency equal to the free spectral range of the cavity. Each transmitted component of the cavity field is modified by the cavity according to the well-known expression [26]

$$E_{\text{out}} = \frac{T e^{i\varphi}}{1 - R e^{i2\varphi}} E_{\text{in}} = \chi E_{\text{in}}, \quad (2)$$

where χ is the complex transmission coefficient describing the phase change and the absorption of the field, T (R) is the power transmission (reflection) coefficient of the cavity mirrors, and φ is the single round-trip complex phase picked up by the intracavity field.

The carrier frequency is used to probe the atomic transition and is close to the atomic resonance, while the sidebands at $\Omega/2\pi = 500$ MHz are far off resonance compared to the natural linewidth, $\Gamma/2\pi = 7.5$ kHz. Each of the field's phase components—carrier (φ_0) and sidebands ($\varphi_{\pm p}$ for $p = 1, 2$)—experiences identical phase shifts due to the cavity assembly ϕ_{cavity} , but only the carrier interacts with the atoms,

$$\varphi_0 = \phi_{\text{cavity}} + \beta_D + i\beta_A, \quad \varphi_{\pm p} = \phi_{\text{cavity}} \pm p\pi, \quad (3)$$

where β_D and β_A denote the single pass dispersion and absorption due to the atoms present in the cavity, and the sideband frequency detuning of $\pm p\Omega$ introduces additional phase factors of $\pm p\pi$ if the cavity is on resonance with the carrier and the sidebands. During experiments, the cavity is forced to be on resonance with the probe laser, a requirement that generally imposes restrictions on measured quantities

in cavity experiments. Enforcing the resonance condition by locking the cavity to the probe carrier implies

$$\text{Re}(\varphi_0) = \theta_0 = \phi_{\text{cavity}} + \beta_D = m\pi, \quad (4)$$

where θ_0 is the real part of φ_0 and m is an integer. This imposes restrictions on the sideband phases, which become

$$\varphi_{\pm p} = \phi_{\text{cavity}} - \theta_0 \pm p\pi = -\beta_D \pm p\pi. \quad (5)$$

For the carrier, the complex transmission coefficient χ_0 becomes purely real,

$$\chi_0 = \frac{Te^{-\beta_A}}{1 - Re^{-2\beta_A}}, \quad (6)$$

while the sideband complex transmission coefficients $\chi_{\pm p}$ become

$$\chi_{\pm p} = \frac{Te^{i(\pm p\pi - \beta_D)}}{1 - Re^{2i(\pm p\pi - \beta_D)}}, \quad (7)$$

and the atomic phase shift β_D is transferred onto the sideband transmission coefficients. As the cavity is kept on resonance with the carrier at all times, we obtain the final output field to second order, E_{out} :

$$\begin{aligned} E_{\text{out}} = & E_0(J_0(x)\chi_0 e^{i\omega_c t} \\ & + J_1(x)\chi_1 e^{i(\omega_c + \Omega)t} - J_1(x)\chi_{-1} e^{i(\omega_c - \Omega)t} \\ & + J_2(x)\chi_2 e^{i(\omega_c + 2\Omega)t} + J_2(x)\chi_{-2} e^{i(\omega_c - 2\Omega)t}). \end{aligned} \quad (8)$$

Detecting this signal on a fast photodiode and demodulating at $\Omega/2\pi = \text{FSR}$ gives a photocurrent signal $S_{1\Omega}$ proportional to

$$S_{1\Omega} \propto J_0(x)J_1(x)\chi_0 \text{Im}(\chi_1), \quad (9)$$

where $\text{Im}(\chi_1)$ is the imaginary part of the χ_1 coefficient.

In the limit $R \rightarrow 0$, corresponding to the free space case in which no cavity is used, we recover from Eq. (9) the well-known expression from FM spectroscopy $S_{1\Omega} \propto e^{-\beta_A} \sin(\beta_D)$. On the other hand, in the limit where the complex phase shift due to the atoms is very small, i.e., $\beta_D \rightarrow 0$ and a cavity is present, we find $S_{1\Omega} \propto \beta_D$, which is also proportional to the total atomic phase shift of the transmitted sideband field. In our case, this approximation is satisfied very close to resonance.

Information related to the absorption of the transmitted light may be obtained by demodulating the transmitted field at twice the FSR, i.e., 2Ω , where one obtains (here with sidebands up to second order)

$$S_{2\Omega} \propto [2J_0(x)J_2(x)\chi_0 \text{Re}(\chi_2) - J_1^2(x)|\chi_1|^2], \quad (10)$$

where $\text{Re}(\chi_2)$ is the real part of the χ_2 coefficient. This signal is related to the absorption line shape of the transmitted field (see Appendix). The complete information about the complex transmission coefficients, χ_j , can now be found by combining the quantities obtained from demodulating at FSR and 2FSR via Eqs. (9) and (10).

In conclusion, the demodulating of the cavity-transmitted field by $\Omega/2\pi = \text{FSR}$ [Eq. (9)] provides a signal proportional to the atomically induced phase shift for small detunings. The high signal-to-noise-ratio of this signal makes it promising for applications in laser stabilization. The absorption line shape, on the other hand, can be obtained by demodulating the cavity-transmitted field by 2FSR [Eq. (10)]. This technique can

also be applied to molecular systems at ambient temperatures coupled to optical cavities, and it is not only limited to laser-cooled neutral atoms.

IV. RESULTS AND DISCUSSION

In our system, the energy scale associated with the mK Doppler temperature is several orders of magnitude larger than the energy scale associated with the narrow linewidth of the optical transition. In this limit, the nonzero velocities of the atoms bring additional multiphoton resonance phenomena into play, so-called doppler resonances, which modify the complex transmission coefficient of the cavity field close to the atomic resonance [21].

Doppler resonances are multiphoton processes in which $l + 1$ photons from one direction are resonantly absorbed by an atom with a velocity v , and l photons are emitted in the reverse direction leaving the atom in the excited state [27,28]. Energy conservation demands the doppler resonances to be located approximately at [27]

$$kv = \frac{\pm(\Delta^2 + 2g^2)^{1/2}}{2l + 1}, \quad (11)$$

where k is the wave vector of the laser light, v is the resonant atom velocity, Δ is the detuning, l is the number of emitted photons, i.e., the order of the doppler resonance, and g is the single-atom-cavity coupling constant.

NICE-OHMS signals obtained by demodulation at $\Omega/2\pi = \text{FSR}$, see Eq. (9), are shown in Fig. 2(a). Those values represent the total phase dispersion induced by the atom-cavity system. A sharp dispersion signal with a steep slope can be seen around resonance. The magnitude of this slope, as well as the signal-to-noise ratio, ultimately determines the obtainable frequency stability of the system when used as a frequency discriminator for laser stabilization. The inset in Fig. 2(a) shows a zoom of the central dispersion curve close to resonance. This NICE-OHMS signal is proportional to the cavity-transmitted phase shift. Two theoretical plots are also shown. The blue solid line displays the full theory, i.e., including doppler resonances to all orders, while the black dashed line is based on a theoretical prediction where the velocity-dependent doppler resonances are not taken into account. We observe very good agreement with the full theoretical model including all doppler orders, and we notice that the doppler resonances tend to decrease the phase dispersion slope around resonance slightly. The two theory lines are also included in the broad frequency scan shown in Fig. 2(a). For the dashed theory line excluding doppler resonances, the agreement with the data is always worse than that including the doppler resonances.

Whereas the results presented in Fig. 2(a) have already been understood in previous works [21], the corresponding absorption line shape has not yet been fully understood. The signal obtained by demodulating the cavity-transmitted field at 2FSR [Eq. (10)] is shown in Fig. 2(b) and is related to the absorption line shape of the cavity-transmitted field. A background signal corresponding to the empty cavity signal (no atoms) is subtracted. A similar background value has been subtracted from the theoretical values. The absolute value of this background-corrected signal represents the degree of

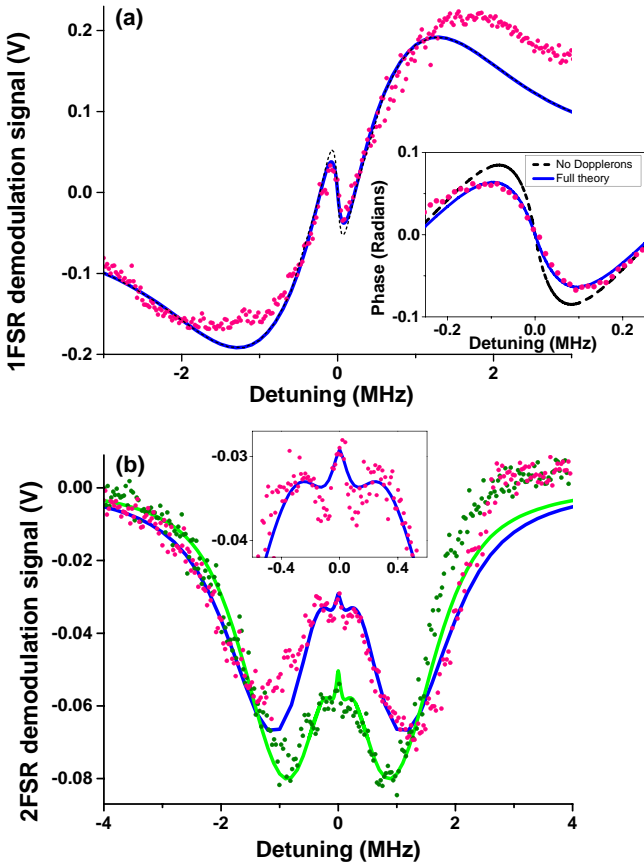


FIG. 2. (Color online) The solid and dashed lines are predictions based on the theoretical model presented in [20,21]. The dots are data measured by cavity-enhanced FM spectroscopy. All data are averaged values, where approximately five times as many measurements have been performed for data in (b) due to the weaker signal compared to data in (a). The slight asymmetry of the experimental data in both plots is expected to be due to a drift of the relative phase between the light wavefront and the demodulation phase during scan. (a) Frequency scan of the cavity-transmitted phase shift close to resonance for a carrier input power of 240 nW, a total number of atoms of $N = 5.0 \times 10^8$, and an atom temperature of $T = 5.0$ mK. The data points are averages of nine measurements. Theoretical values from Eq. (9) are scaled to data. Inset: high-resolution scan of the central region. The vertical axis in this central region corresponds to the total atomic phase shift of the transmitted sideband, and data are scaled to theory. (b) Frequency scans of the absorption line shape of the cavity-transmitted field measured by the NICE-OHMS technique obtained with a demodulation $\Omega/2\pi = 2\text{FSR}$. The total number of atoms is $N = 4.5 \times 10^8$, an atom temperature of $T = 5.0$ mK, and a total input power of 310 nW (blue line) and 155 nW (green line). Theoretical values from Eq. (10) are scaled to data. Inset: high-resolution scans around the central region. The units on the inset axes are the same as in (b).

field absorption experienced by light transmitted through the cavity. To reproduce the detailed features of the absorption line shape, we must include contributions from sidebands up to the third order in the theoretical model. These higher-order contributions modify the line shape. Different modulation indices of $x = 0.65$ for the blue theory line and of $x = 0.57$

for the green theory line are chosen to show that the signal described in Eq. (10) takes the optical power ratio of the carrier and the sidebands into account, in good agreement with the data.

The absorption line shapes in Fig. 2(b) are shown for two different carrier input powers: 310 nW (red dots) and 155 nW (green dots). The 2FSR demodulation signal is proportional to the total optical input power. A carrier input power of 155 nW should thus yield about half of the signal measured for a carrier input power of 310 nW. This is indeed observed experimentally, however in the presented figure the signal for a carrier input power of 155 nW has been normalized to the signal for a carrier input power of 310 nW in order to illustrate the line-shape dynamics on the same figure.

As mentioned earlier, the cavity is forced on resonance with the probe carrier by the cavity lock feedback loop such that the combined atom-cavity system is kept on resonance. However, the presence of several sideband orders contributes to the servo error signal for large atomic phase shifts and will slightly offset the cavity resonance compared to the carrier frequency [29]. Corrections due to these shifts are small, but they are included in the theoretical model for completeness.

The central region of Fig. 2(b) shows a small central peak with reduced absorption (increased transmission) due to saturation. Insets show a zoom of the phase and the cavity-transmitted signal in Figs. 2(a) and 2(b), respectively. A reduction in transmission occurs for small detunings and forms dips on both sides of the central saturation peak at around 100 kHz. This reduction is due to atom-induced cavity response, where a nonzero atomic phase shifts the sidebands out of cavity resonance and reduces the transmitted power. As the detuning increases to larger values, the phase shift induced by the atoms eventually decreases to zero again, bringing the sidebands back into resonance with the cavity mode and thus increasing the amount of transmitted light. This corresponds to the two shoulders located next to the dips. This structure is less pronounced when measuring the total cavity transmitted power as a function of the detuning because the carrier, which is kept on resonance, accounts for most of the transmitted power for low modulation indices ($x < 1$). On the other hand, this structure is significantly more pronounced when the cavity-transmitted field is demodulated with 2FSR [Eq. (10)]. A detailed account of this structure can be found in Appendix. The atom-induced cavity response seems even more pronounced in the data [see the inset in Fig. 2(b)] than predicted by theory, which might be due to an imperfect cavity-locking scheme.

The shot-noise limited linewidth of the system, $\Delta\nu$, can be estimated by assuming a perfect locking scheme that is of infinite bandwidth, and detectors with unity quantum efficiencies as [19]

$$\Delta\nu = \frac{\pi\hbar\nu}{2P_{\text{sig}}\left(\frac{d\phi}{d\nu}\right)^2} \left(1 + \frac{P_{\text{sig}}}{2P_{\text{sideband}}}\right), \quad (12)$$

where P_{sig} is the input carrier power, P_{sideband} is the first-order sideband power, and $\frac{d\phi}{d\nu}$ is the dispersion slope at resonance. The minimum achievable shot-noise limited linewidth of the current system is estimated from Eq. (12) to be 500 mHz. The minimum shot-noise limited linewidth will be further reduced

for higher values of $C = NC_0$. Hence, it can be optimized by increasing the atom number or the cavity finesse.

A system with improved finesse ($F = 1000$) and intracavity atom number (N_{cav}) increased by a factor 2 is estimated to have a shot-noise limited linewidth of $\Delta\nu < 10 \text{ mHz}$ [20], which is already comparable to state-of-the-art laser stabilization [13,30,31], and even narrower linewidths can be expected for a higher cavity finesse realized for intravacuum cavities in similar works [15]. Furthermore, the theoretical model shows that the gain, in terms of dispersion slope $\frac{d\phi}{d\nu}$, by further cooling of the atomic sample is minimal [21]. Experimentally, the reduction of the sample temperature by one or two orders of magnitude in temperature is usually accompanied by a reduction in atom number by similar orders of magnitude. In this regime with lower temperature, the optimum input power is reduced to technically challenging values ($< n\text{W}$). Therefore, the overall gain from reducing the sample temperature and thereby increasing the complexity of the system is comparatively small, and operating the system at relatively high temperature is more desirable. This may pave the way for implementations of thermal atoms in a simple and compact transportable optical atomic clock with high phase stability.

The phase dispersion slope depends nonlinearly on the optical intracavity power, which makes the optimal choice of parameters for laser stabilization nontrivial. The nonlinear input power dependence of the phase dispersion slope is measured and shown in Fig. 3(a). The slope values are evaluated by performing theoretical fits on phase dispersion scans, shown in Figs. 3(c)–3(e), for different input powers. The measurements and theory are in good agreement, and the nonlinear input power dependency predicted in [20] is evident. The theoretical curve predicts a maximum absolute value of the slope for lower input powers than measured. However, the shot-noise limited linewidth does not depend solely on the phase dispersion slope. It is also governed by the input power in accordance with Eq. (12). The shot-noise limited linewidth for each measured parameter is calculated and shown in Fig. 3(b), where data sets in Figs. 3(a) and 3(b) are identical. Figure 3(b) shows that a system with input powers corresponding to the predicted minimum shot-noise limited linewidth has been realized and measured for a fixed carrier-sideband ratio. Note that the horizontal axis is logarithmic, allowing a change in input power of one order of magnitude without degrading the shot-noise limited linewidth significantly. This indicates that probing with technically challenging low input powers down to $< 100 \text{ nW}$ is not necessary, and that the system is robust to changes in the input power. The ratio of carrier and sideband powers is governed by the modulation index x of the EOM, and it optimizes the linewidth in Eq. (12) for a carrier-sideband ratio of $\frac{P_{\text{sig}}}{2P_{\text{sideband}}} = 1$. The measurements presented in this work are performed in a cyclic manner, and continuous laser stabilization on the presented system is not currently feasible. However, the implementation of the techniques presented in this work into beamline experiments [22], where a beam of cold atoms with high loading rates [32] is interrogated in a cavity, seems realizable. This paves the way for a continuous laser stabilization on an atom-cavity system with a narrow optical transition.

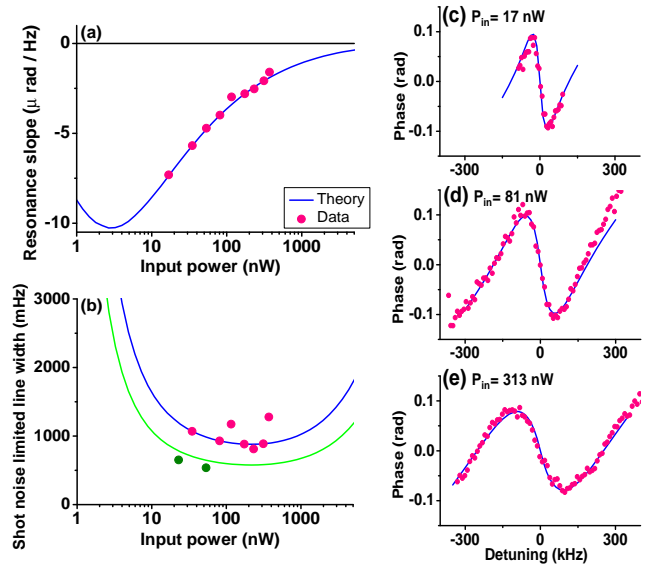


FIG. 3. (Color online) The input power dependence of the slope of the phase dispersion around resonance and the corresponding shot-noise limited linewidth for a total number of atoms of $N = 4.0 \times 10^8$ and MOT temperature of $T = 5.0 \text{ mK}$. The solid lines are theoretical predictions and the dots are experimental data. (a) The slope of the phase dispersion around resonance measured for different input powers. The data and theory are in excellent accordance and the nonlinear dependence is evident. Notice that the power axis is logarithmic. (b) The shot-noise limited linewidth from Eq. (12) for different input powers corresponding to the measured parameters in (a). The solid lines are theoretical predictions and the dots are experimental values. The blue theory line corresponds to a ratio of carrier and sideband input powers of $\frac{P_{\text{sig}}}{2P_{\text{sideband}}} = 1.65$ and the green theory line corresponds to $\frac{P_{\text{sig}}}{2P_{\text{sideband}}} = 0.75$. (c)–(e) Frequency scans of the phase dispersion for different input powers. All experimental values in (a) and (b) are evaluated by fitting theoretical curves to frequency scans of the phase dispersion around resonance. The nonlinear dynamics of the overall dispersion shape is in very good accordance with the theory.

V. CONCLUSION

We have experimentally investigated the velocity-dependent spectroscopic features and nonlinear dynamics of a cavity-atom system in the bad-cavity limit consisting of laser-cooled ^{88}Sr atoms coupled to a low finesse optical cavity.

The NICE-OHMS technique has been applied to perform FM spectroscopy, and a complete connection is established between the measured quantities and the complex transmission coefficient of the input field. The cavity-transmitted phase shift and the absorption of the cavity-transmitted field are measured, and both quantities show significant modifications due to velocity-dependent processes and atom-induced cavity response in accordance with the theoretical model.

The ideal shot-noise limited linewidth of a laser stabilized to our system depends on the phase dispersion slope around resonance. The nonlinear input power dependence of the phase

dispersion slope is measured, and the optimal input power for the minimum shot-noise limited linewidth is determined. Parameters corresponding to a shot-noise limited linewidth down to 500 mHz are measured.

The understanding of relevant velocity-dependent effects presented here has direct relevance for atomic clocks and superradiant laser sources [18] involving ultranarrow transitions. Specifically, the understanding of the dynamics of a cavity-atom system with single-stage MOT temperatures obtained in this work will prove valuable for future transportable stable lasers and atomic clocks employing thermal atoms for out-of-lab operation under more noisy environments.

ACKNOWLEDGMENTS

The authors would like to acknowledge support from the Danish research council and ESA Contract No. 4000108303/13/NL/PA-NPI272-2012. J.Y. and M.H. also wish to thank the DARPA QuASAR program, the NIST, and the NSF for financial support.

APPENDIX: LINE SHAPE OF ABSORPTION

The absorption dips shown in the inset of Fig. 2(b) are predicted from our theoretical model [20,21], where the empty cavity frequency is kept on resonance with the probe field. The standing-wave condition inside the cavity is, however, unfulfilled when a strong atomic dispersion is introduced, and the transmission will be reduced for all detunings with nonzero atomic phase shifts. Hence the large enhancement of the absorption for large detunings (\sim MHz) is also due to the broad thermal dispersion.

Experimentally, the cavity servo system ensures that the combined resonance of the cavity and the atoms is kept on resonance with the probe field. The standing-wave condition is hence maintained and the atomic phase shift is canceled out for the carrier, as shown in Eq. (4). A measurement of the transmission power of the system will be dominated by the complex transmission coefficient of the carrier, χ_0 [see Eq. (6)], and the change in the transmission power due to

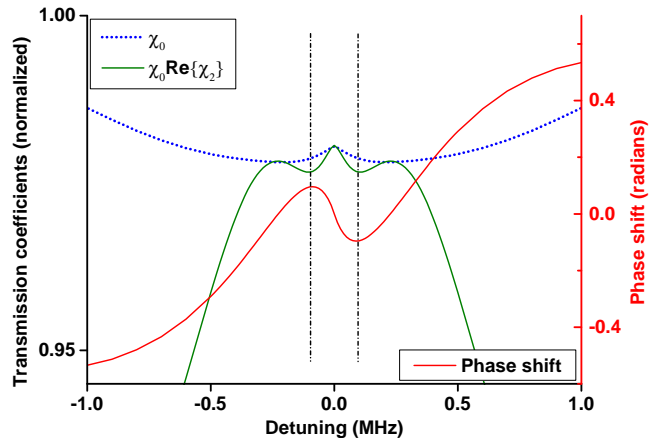


FIG. 4. (Color online) Theoretical values of the transmission coefficient of the carrier (dashed blue), χ_0 , the combined line shape of the atomic absorption and the attenuation due to atomic dispersion (green), $\chi_0\text{Re}(\chi_2)$, and the total cavity transmitted phase shift (red). The black vertical dashed lines highlight the fact that transmission minima occur at dispersion maxima.

the atomic phase shift is not evident. The signal demodulated with 2FSR [Eq. (10)], on the other hand, contains information about the atomic absorption (χ_0) and the attenuation due to the atomic phase shift [$\text{Re}(\chi_2)$]. Hence, the detailed absorption structure is evident in this signal.

Theoretical values of some relevant transmission coefficients are shown in Fig. 4. χ_0 (blue line) describes only the atomic absorption of the carrier [see Eq. (6)], and $\chi_0\text{Re}(\chi_2)$ describes the combined line shape from the atomic absorption (χ_0) and the attenuation due to the atomic phase shift [$\text{Re}(\chi_2)$]. $\chi_0\text{Re}(\chi_2)$ corresponds to the first term of Eq. (10) measured using the NICE-OHMS technique with demodulation of 2FSR. The second term in Eq. (10) and the additional contributions from the higher-order sidebands included in the theoretical description modify the line shape without erasing the structures. The corresponding total dispersion of the system is also shown in Fig. 4, and it is evident that the transmission minima occur at the dispersion maxima (highlighted with dashed vertical lines).

-
- [1] B. J. Bloom *et al.*, An optical lattice clock with accuracy and stability at the 10^{-18} level, *Nature (London)* **506**, 71 (2014).
 - [2] T. L. Nicholson *et al.*, Systematic evaluation of an atomic clock at 2×10^{-18} total uncertainty, *Nat. Commun.* **6**, 6896 (2015).
 - [3] I. Ushijima *et al.*, Cryogenic optical lattice clocks, *Nat. Phot.* **9**, 185 (2015).
 - [4] N. Hinkley *et al.*, An atomic clock with 10^{-18} instability, *Science* **341**, 1215 (2013).
 - [5] R. Le Targat *et al.*, Experimental realization of an optical second with strontium lattice clocks, *Nat. Commun.* **4**, 2109 (2013).
 - [6] M. J. Martin *et al.*, A quantum many-body spin system in an optical lattice clock, *Science* **341**, 632 (2013).
 - [7] R. Bondarescu *et al.*, Geophysical applicability of atomic clocks: direct continental geoid mapping, *Geophys. J. Int.* **191**, 78 (2012).
 - [8] J. Guéna, M. Abgrall, D. Rovera, P. Rosenbusch, M. E. Tobar, P. Laurent, A. Clairon, and S. Bize, Improved Tests of Local Position Invariance Using ^{87}Rb and ^{133}Cs Fountains, *Phys. Rev. Lett.* **109**, 080801 (2012).
 - [9] T. Rosenband *et al.*, Frequency ratio of Al^+ and Hg^+ single-ion optical clocks; Metrology at the 17th decimal place, *Science* **319**, 1808 (2008).
 - [10] R. M. Godun, P. B. R. Nisbet-Jones, J. M. Jones, S. A. King, L. A. M. Johnson, H. S. Margolis, K. Szymaniec, S. N. Lea, K. Bongs, and P. Gill, Frequency Ratio of Two Optical Clock Transitions in $^{171}\text{Yb}^+$ and Constraints on the Time Variation

- of Fundamental Constants, *Phys. Rev. Lett.* **113**, 210801 (2014).
- [11] P. W. Graham, J. M. Hogan, M. A. Kasevich, and S. Rajendran, New Method for Gravitational Wave Detection with Atomic Sensors, *Phys. Rev. Lett.* **110**, 171102 (2013).
- [12] T. Kessler, T. Legero, and U. Sterr, Thermal noise in optical cavities revisited, *J. Opt. Soc. Am. B* **29**, 178 (2012).
- [13] T. Kessler *et al.*, A sub-40-mHz-linewidth laser based on a silicon single-crystal optical cavity, *Nat. Photon.* **6**, 687 (2012).
- [14] G. D. Cole *et al.*, Tenfold reduction of Brownian noise in high-reflectivity optical coatings, *Nat. Photon.* **7**, 644 (2013).
- [15] M. A. Norcia and J. K. Thompson, Strong Coupling on a Forbidden Transition in Strontium and Nondestructive Atom Counting, [arXiv:1506.02297](https://arxiv.org/abs/1506.02297).
- [16] J. G. Bohnet *et al.*, A steady-state superradiant laser with less than one intracavity photon, *Nature (London)* **484**, 78 (2012).
- [17] R. Kohlhaas, A. Bertoldi, E. Cantin, A. Aspect, A. Landragin, and P. Bouyer, Phase Locking a Clock Oscillator to a Coherent Atomic Ensemble, *Phys. Rev. X* **5**, 021011 (2015).
- [18] D. Meiser, J. Ye, D. R. Carlson, and M. J. Holland, Prospects for a Millihertz-Linewidth Laser, *Phys. Rev. Lett.* **102**, 163601 (2009).
- [19] M. J. Martin, D. Meiser, J. W. Thomsen, J. Ye, and M. J. Holland, Extreme nonlinear response of ultranarrow optical transitions in cavity QED for laser stabilization, *Phys. Rev. A* **84**, 063813 (2011).
- [20] D. A. Tieri, J. Cooper, B. T. R. Christensen, J. W. Thomsen, and M. J. Holland, Laser stabilization using saturated absorption in a cavity-QED system, *Phys. Rev. A* **92**, 013817 (2015).
- [21] P. G. Westergaard, B. T. R. Christensen, D. Tieri, R. Matin, J. Cooper, M. Holland, J. Ye, and J. W. Thomsen, Observation of Motion-Dependent Nonlinear Dispersion with Narrow-Linewidth Atoms in an Optical Cavity, *Phys. Rev. Lett.* **114**, 093002 (2015).
- [22] J. Chen, Active optical clock, *Chin. Sci. Bull.* **54**, 348 (2009).
- [23] J. Ye, L.-S. Ma, and J. L. Hall, Ultrasensitive detections in atomic and molecular physics: demonstration in molecular overtone spectroscopy, *J. Opt. Soc. Am. B* **15**, 6 (1998).
- [24] L.-S. Ma, J. Ye, P. Dubé, and J. L. Hall, Ultrasensitive frequency-modulation spectroscopy enhanced by a high-finesse optical cavity: theory and application to overtone transitions of C_2H_2 and C_2HD , *J. Opt. Soc. Am. B* **16**, 2255 (1999).
- [25] T. W. Hänsch and B. Couillaud, Laser frequency stabilization by polarization spectroscopy of a reflecting reference cavity, *Opt. Commun.* **35**, 441 (1980).
- [26] F. Riehle, *Frequency Standards: Basics and Applications* (Wiley-VCH, Weinheim, 2004).
- [27] A. Tallet, Raman emission versus dopplerons in a two-level atomic cell, *Soc. Am. B* **11**, 1336 (1994).
- [28] E. Kyrölä and S. Stenholm, Velocity tuned resonances as multi-doppleron processes, *Opt. Commun.* **22**, 123 (1977).
- [29] J. Ye and T. W. Lynn, Applications of optical cavities in modern atomic, molecular, and optical physics, *Adv. At., Mol., Opt. Phys.* **49**, 1 (2003).
- [30] M. Bishop, X. Zhang, M. J. Martin, and J. Ye, Optical Spectrum Analyzer with Quantum-Limited Noise Floor, *Phys. Rev. Lett.* **111**, 093604 (2013).
- [31] S. Häfner *et al.*, 8×10^{-17} fractional laser frequency instability with a long room-temperature cavity, *Opt. Lett.* **40**, 2112 (2015).
- [32] T. Yang *et al.*, A high flux source of cold strontium atoms, *Eur. Phys. J. D* **69**, 226 (2015).

B.2 Laser stabilization using saturated absorption in a cavity-QED system

David A. Tieri, John Cooper, Bjarke T. R. Christensen, Jan W. Thomsen, & Murray J. Holland, *Phys. Rev. A*, **92**, 013817 (2015).

Laser stabilization using saturated absorption in a cavity-QED system

D. A. Tieri,¹ J. Cooper,¹ Bjarke T. R. Christensen,² J. W. Thomsen,² and M. J. Holland¹

¹JILA, National Institute of Standards and Technology and University of Colorado, Boulder, Colorado 80309-0440, USA

²Niels Bohr Institute, University of Copenhagen, Blegdamsvej 17, 2100 Copenhagen, Denmark

(Received 18 March 2015; published 10 July 2015)

We consider the phase stability of a local oscillator (or laser) locked to a cavity-QED system composed of atoms with an ultranarrow optical transition. The atoms are cooled to milli-Kelvin temperatures and then released into the optical cavity. Although the atomic motion introduces Doppler broadening, the standing-wave nature of the cavity causes saturated absorption features to appear, which are much narrower than the Doppler width. These features can be used to achieve an extremely high degree of phase stabilization, competitive with the current state of the art. Furthermore, the inhomogeneity introduced by finite atomic velocities can cause optical bistability to disappear, resulting in no regions of dynamic instability and thus enabling a new regime accessible to experiments where optimum stabilization may be achieved.

DOI: 10.1103/PhysRevA.92.013817

PACS number(s): 42.62.Fi, 32.80.Wr, 37.30.+i, 42.50.Ct

I. INTRODUCTION

Today's ultraprecise and accurate atomic clocks continue to make important contributions to fundamental physics as well as applied technology. Atomic clocks have imposed significant constraints on the drift of fundamental constants [1–3], may have the potential to enhance the sensitivity of gravitational wave detectors, and have provided ultimate tests of the general theory of relativity [4]. With the current stability of optical clocks at the 1×10^{-18} level, there are prospects for applying atomic clocks for the detailed mapping of the Earth's gravity field [5,6].

A highly stabilized laser is an integral component of high-precision measurements, such as optical atomic clocks and precision spectroscopy. Current technology for achieving highly phase stable laser sources relies on locking a laser to a high- Q reference ultra-low expansion glass cavity [7–9]. The phase stability of this method is currently limited by the thermal noise induced in the mirrors, spacers, and coatings of the reference cavity [10], but has been significantly reduced over the past few years with new engineered materials [11,12].

As an alternative approach to overcoming the thermal noise problem, it was recently proposed [13] to lock the laser to the saturated resonance feature exhibited by a collection of atoms with an ultranarrow electronic transition trapped in an optical cavity. Here, the atoms were assumed to be trapped in an optical lattice inside the cavity. Due to the narrow atomic line, such a system would typically operate in the parameter region corresponding to the bad cavity limit of cavity QED. There, the atomic linewidth is significantly narrower than the cavity linewidth. In contrast to the reference cavity stabilization method described above, the cavity-QED method offers a distinct advantage since no drift compensation is needed.

The cavity-QED system exhibits optical bistability in the intracavity intensity [14,15] where several solutions exist for the steady-state intracavity field. Working at an input intensity in the region where bistability is present would in principle allow the greatest degree of stabilization [13]. However, it is not practical to work in the bistable region since quantum and classical fluctuations between the semiclassical eigenmodes cause the system to be dynamically unstable.

Therefore, one is restricted to working at input intensities above the bistability, where the achievable stabilization is orders of magnitude worse. Still, it was shown [13] that phase stability corresponding to the sub-milli-hertz level should be achievable.

Recently [16], an experimental effort to demonstrate the cavity-QED system was made by probing the $|^1S_0\rangle - |^3P_1\rangle$ intercombination line of ^{88}Sr atoms (i.e., $\gamma_a/2\pi = 7.6$ kHz) inside an optical cavity. There, however, the atoms were not trapped in an optical lattice, but loaded into the center of the cavity using a magneto-optical trap (MOT), which was then turned off during probing. Typical MOT temperatures correspond to a few milli-Kelvin, which is equivalent to a Doppler width of several megahertz. Considering the narrow 7.6-kHz line of the optical transition, this implies that motional effects will be important.

In this paper, we extend the many-atom cavity-QED theory of [13] to include atomic motion, and study its effect on the stabilization precision. In spite of the large Doppler effect, the standing-wave nature of the cavity field induces sharp saturated absorption and dispersion features to appear in the considered observables. These features are nestled in the center of the overall Doppler broadened features [17–20]. The stabilization that is achievable by utilizing these sharp features is impeded by multiphoton scattering processes that occur when an atom's velocity matches one of its Doppler resonances [21,22]. The dependence of the stabilization on the number of atoms and the temperature due to the Dopplerons is discussed. We demonstrate that the motion of the atoms causes the bistability region to disappear, so that no restrictions on input power are necessary to avoid the dynamic instability that would otherwise result.

II. MODEL

We model our system as a collection of N two-level atoms inside a single mode optical cavity using the quantum Born-Markov master equation to describe the open quantum system:

$$\frac{d}{dt} \hat{\rho} = \frac{1}{i\hbar} [\hat{H}, \hat{\rho}] + \hat{\mathcal{L}}[\hat{\rho}], \quad (1)$$

where

$$\hat{H} = \frac{\hbar\Delta}{2} \sum_{j=1}^N \hat{\sigma}_j^z + \hbar\eta(\hat{a}^\dagger + \hat{a}) + \hbar \sum_{j=1}^N g_j(t)(\hat{a}^\dagger \hat{\sigma}_j^- + \hat{\sigma}_j^+ \hat{a}), \quad (2)$$

and $\hat{L}[\hat{\rho}]$ denotes the Liouvillian.

The Hamiltonian H describes the coherent evolution of the coupled atom cavity system in an interaction picture which rotates at the frequency of the cavity, and Δ is the atom-cavity detuning. The Pauli spin matrices for the atoms are $\hat{\sigma}_j^+$, $\hat{\sigma}_j^-$, and $\hat{\sigma}_j^z$, and \hat{a} is the annihilation operator of the cavity mode. Furthermore, $\eta = \sqrt{(\kappa P_{\text{in}})/(\hbar\omega)}$ is the classical drive amplitude, where κ is the decay rate of the cavity, P_{in} is the input power, and ω is the frequency of the cavity mode. The atom-cavity coupling rate is $g_j(t) = g_0 \cos(\delta_j t)$, where g_0 is the maximum coupling amplitude, and $\delta_j = kv_j$ is the Doppler shift in terms of the velocity v_j of the j th atom and wave number k of the light.

The incoherent evolution describes the various forms of dissipation in this system and is described by the Liouvillian $\hat{L}[\hat{\rho}]$:

$$\begin{aligned} \hat{L}[\hat{\rho}] = & -\frac{\kappa}{2}\{\hat{a}^\dagger \hat{a} \hat{\rho} + \hat{\rho} \hat{a}^\dagger \hat{a} - 2\hat{a} \hat{\rho} \hat{a}^\dagger\} \\ & - \frac{\gamma}{2} \sum_{j=1}^N \{\hat{\sigma}_j^+ \hat{\sigma}_j^- \hat{\rho} + \hat{\rho} \hat{\sigma}_j^+ \hat{\sigma}_j^- - 2\hat{\sigma}_j^- \hat{\rho} \hat{\sigma}_j^+\} \\ & + \frac{\gamma_p}{2} \sum_{j=1}^N \{\hat{\sigma}_j^z \hat{\rho} \hat{\sigma}_j^z - \hat{\rho}\}, \end{aligned} \quad (3)$$

where $\hat{\rho}$ is the system's density matrix, γ is the spontaneous emission rate for the atoms, and γ_p is the total decay rate of the atomic dipole.

We derive Langevin equations corresponding to Eq. (1). Assuming that the classical drive η is sufficiently strong, a mean-field description provides an accurate representation [23]. We define the mean values for the field $\alpha = -i\langle\hat{a}\rangle$, and for the atoms, $\sigma_j^- = \langle\hat{\sigma}_j^-\rangle$, $\sigma_j^+ = \langle\hat{\sigma}_j^+\rangle$, $\sigma_j^z = \langle\hat{\sigma}_j^z\rangle$, which evolve according to the semiclassical evolution:

$$\dot{\alpha} = -\kappa\alpha + \eta + \sum_{j=1}^N g_j(t)\sigma_j^-, \quad (4)$$

$$\dot{\sigma}_j^- = -(\gamma_p + i\Delta)\sigma_j^- + g_j(t)\alpha\sigma_j^z, \quad (5)$$

$$\dot{\sigma}_j^z = -\gamma(\sigma_j^z + 1) - 2g_j(t)(\alpha\sigma_j^+ + \alpha^*\sigma_j^-). \quad (6)$$

In the moving frame of reference of the j th atom, the cavity field appears as a traveling wave, containing two frequencies shifted above and below the cavity frequency by the Doppler shift δ_j (refer to Fig. 1).

It is convenient to approximate Eqs. (4)–(6) as a function of the continuous variable $\delta = kv$:

$$\dot{\alpha} = -\kappa\alpha + \eta + g_0 \int d\delta P(\delta) \cos(\delta t)\sigma^-, \quad (7)$$

$$\dot{\sigma}^- = -(\gamma_p + i\Delta)\sigma^- + g_0 \cos(\delta t)\alpha\sigma^z, \quad (8)$$

$$\dot{\sigma}^z = -\gamma(\sigma^z + 1) - 2g_0 \cos(\delta t)(\alpha\sigma^+ + \alpha^*\sigma^-), \quad (9)$$

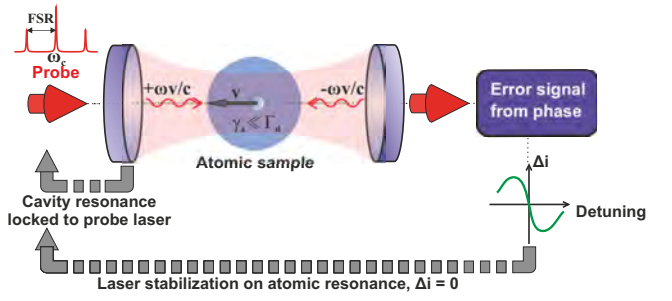


FIG. 1. (Color online) Schematic of the cavity-QED experiment with a thermal sample of atoms with Doppler width Γ_d , each of which have a narrow optical transition of width $\gamma_a \ll \Gamma_d$. The atoms are probed with a carrier with frequency ω_c , and two sidebands located at $\omega_c \pm \text{FSR}$, where FSR is the free spectral range of the cavity. The carrier frequency ω_c , which is close to the atomic frequency ω_a , is locked on the cavity mode frequency ω , while the sidebands are assumed far off resonance, typically $\sim 10^4$ atomic linewidths. By demodulating the light transmitted through the cavity at the FSR, detection of the nonlinear phase response of the transmitted light is achieved. This phase response results in a photocurrent that serves as a frequency discriminating error signal that stabilizes the laser frequency through the requirement $\Delta i = 0$.

where $P(\delta)$ is the Maxwell velocity distribution of width δ_0 , which is related to the temperature by the equipartition theorem.

To solve this problem that intrinsically contains a bichromatic drive, we proceed in two ways. Our first approach is to numerically integrate Eqs. (7)–(9), partitioning the integral into finite-size velocity bins. The velocity partition must be chosen with care, since the system exhibits Doppler resonances, which have a strong dependence on the atomic velocity. Specifically, at lower velocity, more resolution in the partition is required.

Our second approach is semianalytic, and involves a Floquet analysis [24,25], in which we expand σ^- , σ^+ , and σ^z in terms of their Fourier components:

$$\begin{aligned} \sigma^- &= \sum_l e^{il\delta t} x_1^{(l)}, \\ \sigma^+ &= \sum_l e^{il\delta t} x_2^{(l)}, \\ \sigma^z &= \sum_l e^{il\delta t} x_3^{(l)}, \end{aligned} \quad (10)$$

where $x_1^{(l)}$, $x_2^{(l)}$, and $x_3^{(l)}$ are the amplitudes of the l th Fourier component. Upon substitution of Eqs. (10) into Eqs. (7)–(9), equations for the amplitudes are found:

$$\dot{x}_1^{(l)} = -(i(\Delta + l\delta) + \gamma_p)x_1^{(l)} + \frac{g_0\alpha}{2}(x_3^{(l+1)} + x_3^{(l-1)}), \quad (11)$$

$$\dot{x}_2^{(l)} = (i(\Delta + l\delta) - \gamma_p)x_2^{(l)} + \frac{g_0\alpha^*}{2}(x_3^{(l+1)} + x_3^{(l-1)}), \quad (12)$$

$$\dot{x}_3^{(l)} = -\gamma \delta_{l,0} - (il\delta + \gamma)x_3^{(l)} - g_0(\alpha x_2^{(l+1)} + \alpha^* x_1^{(l+1)} + \alpha x_2^{(l-1)} + \alpha^* x_1^{(l-1)}). \quad (13)$$

In order to find a steady-state solution, we set the time derivatives in Eqs. (11)–(13) to zero, and substitute Eqs. (11) and (12) into Eq. (13), yielding

$$0 = \gamma \delta_{l,0} + a_l x_3^{(l)} + d_l x_3^{(l+2)} + b_l x_3^{(l-2)}, \quad (14)$$

where $\delta_{l,0}$ is a Kronecker delta, and

$$a_l \equiv il\delta + \gamma + \frac{g_0^2 |\alpha|^2}{2} \left(\frac{1}{Q_{l+1}} + \frac{1}{P_{l+1}} + \frac{1}{Q_{l-1}} + \frac{1}{P_{l-1}} \right), \quad (15)$$

$$b_l = d_{l-2} \equiv \frac{g_0^2 |\alpha|^2}{2} \left(\frac{1}{Q_{l-1}} + \frac{1}{P_{l-1}} \right), \quad (16)$$

where

$$P_l = i(l\delta + \Delta) + \gamma_p, \quad (17)$$

$$Q_l = i(l\delta - \Delta) + \gamma_p. \quad (18)$$

For a given α , Eq. (14) defines a tridiagonal linear system that can be solved by truncating l at some finite value, and applying the Thomas algorithm for matrix inversion [26].

Since the atoms have motion, the condition for resonance between an atom and photon is achieved when the atomic frequency and photon frequency are offset by δ . However, higher-order multiphoton processes, known as Doppler resonances, involving $2n + 1$ photons where n is an integer, are also possible. The n th-order Doppler resonance corresponds to the terms of order $l/2$ in the Floquet theory [21,22]. This correspondence is why only even values of l can couple into Eq. (14).

In steady state, Eq. (7) simplifies to

$$\alpha = \frac{\eta}{\kappa} + \frac{g_0^2 N}{2\kappa} \int d\delta P(\delta) (x_1^{(-1)} + x_1^{(1)}). \quad (19)$$

Since x_1^{-1} and x_1^1 depend on α , the self-consistent field amplitude α that solves Eq. (19) is found numerically by applying Newton's method for root finding [26].

We have seen excellent agreement between the two previously described solution methods, and for the remainder of the paper we focus our attention on the Floquet solution, which most transparently illuminates the underlying physics.

III. DISCUSSION OF STEADY-STATE SOLUTIONS

We first consider the lowest-order solution to Eq. (19), by truncating at $l = 0$, which means we have not included higher-order Doppler resonances. We have verified that this solution displays the correct physics qualitatively by comparing to higher-order solutions that are truncated at increasing values of l . We define scaled intracavity and input field amplitudes $x \equiv \alpha/\sqrt{n_0}$, $y \equiv \eta/(\kappa\sqrt{n_0})$, where $n_0 = (\gamma\gamma_p)/(4g_0^2)$ is the

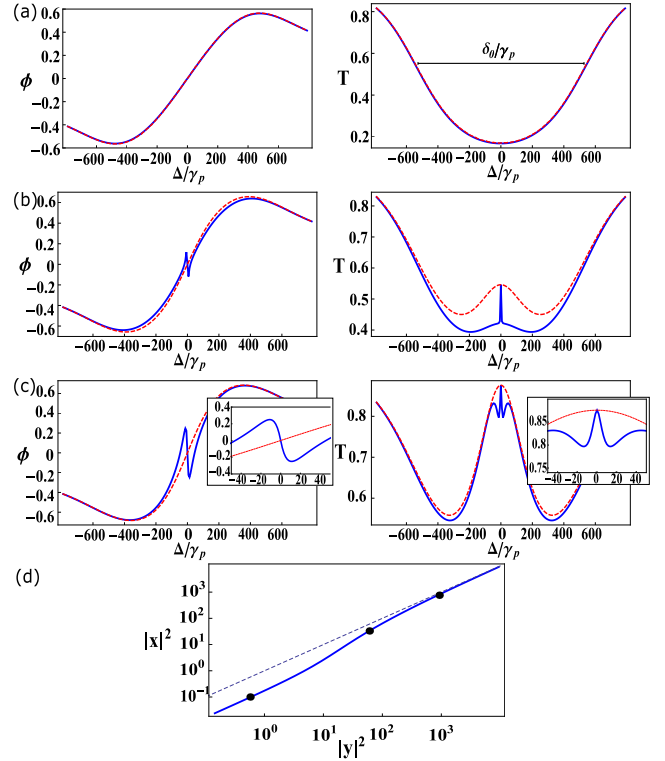


FIG. 2. (Color online) Development of the extra absorption and dispersion features in the transmission (T) and phase shift (ϕ), as the input intensity is increased. Blue (dark gray) solid curves are for a standing wave cavity; red (light gray) dashed curves are for a traveling wave cavity. For all plots, $NC_0 = 600$ and $\delta_0/\gamma_p = 260$, which in the case of ^{88}Sr corresponds to a temperature of ~ 15 mK. (a) $|y|^2 = 5 \times 10^{-1}$. (b) $|y|^2 = 6 \times 10^1$. (c) $|y|^2 = 9 \times 10^2$. The inset is zoomed in to emphasize the central features. (d) Input vs intracavity intensity at resonance. The black dots label the input and intracavity intensities of (a)–(c), and the dashed line is $|y|^2 = |x|^2$ for reference. Note that there is no bistability.

saturation photon number. Equation (19) then becomes

$$y = x \left(1 + \frac{NC_0}{4} \int d\delta P(\delta) \left\{ \frac{1 - i(\Delta + \delta)/\gamma_p}{1 + \frac{(\Delta + \delta)^2}{\gamma_p^2} + \frac{|x|^2}{4}(1 + \xi^+)} \right. \right. \\ \left. \left. + \frac{1 - i(\Delta - \delta)/\gamma_p}{1 + \frac{(\Delta - \delta)^2}{\gamma_p^2} + \frac{|x|^2}{4}(1 + \xi^-)} \right\} \right), \quad (20)$$

where $C_0 \equiv \frac{\delta_0^2}{\kappa\gamma_p}$, and $\xi^\pm = \frac{\gamma_p^2 + (\Delta \mp \delta)^2}{\gamma_p^2 + (\Delta \mp \delta)^2}$.

It is interesting to consider the relation corresponding to Eq. (20) for a ring cavity system that has a field traveling in only one direction, assuming equal intracavity power. The corresponding expression is given by

$$y = x \left(1 + \frac{NC_0}{2} \int d\delta P(\delta) \frac{1 - i(\Delta + \delta)/\gamma_p}{1 + \frac{(\Delta + \delta)^2}{\gamma_p^2} + \frac{|x|^2}{2}} \right). \quad (21)$$

In the experiment described in [16], the measured observables are the cavity transmitted power $T \equiv |x/y|^2$ and transmitted phase shift $\phi \equiv \arg(x/y)$ of the intracavity light

relative to the input light. Figure 2 shows that the presence of ξ^\pm in Eq. (20) results in extra absorption and dispersive features (blue solid line) around resonance in the transmission and phase shift, as compared to a ring cavity field (red dashed line) where $\xi^\pm = 0$.

These extra absorption and dispersive features are caused by the following: The distribution of atomic velocities results in a different Doppler frequency shift of the light for each atomic velocity class, so that each velocity class will be resonant at a different detuning Δ . When $|\Delta| \ll \gamma_p|x|$, the resonant velocity class of the atoms is interrogated by both components of the standing-wave field, whereas when $|\Delta| \gg \gamma_p|x|$ the resonant velocity class of atoms is interrogated by only one component of the standing-wave field. Thus, there is an increased saturation in atomic absorption, with a corresponding saturated dispersive feature, for $|\Delta| \ll \gamma_p|x|$. These sharp features are absent from the traveling-wave cavity situation where there is only one propagating field.

As seen in Fig. 2(a), for low input intensities, there is no atomic saturation at any detuning. In Fig. 2(b), the atoms in the velocity class around resonance are saturated by both components of the field, and the velocity classes away from resonance are saturated by only a single component of the standing-wave field. Therefore, the features caused by the two component saturation and the features caused by the single component saturation are clearly able to be distinguished. It can be seen in Fig. 2(c) that as the amount of saturation becomes large the central feature becomes power broadened, but is still identifiable. Figure 2(d) shows the intracavity intensity for a given input intensity with the values used in Figs. 2(a)–2(c) labeled by black dots.

IV. SHOT-NOISE LIMITED LASER STABILIZATION

For laser stabilization, the central part of the phase response close to the atomic resonance serves as an error signal, see Fig. 2(c), and allows for the generation of a feedback signal to the laser frequency. Through the photodetector, the error signal is converted to a measurable photocurrent. Any photocurrent measured by the photodetector should, in principle, be zeroed by an ideal feedback loop of infinite bandwidth to the laser frequency.

To determine the potential phase stability that could be achievable using our system, we consider the shot-noise limited stabilization linewidth assuming a strong local oscillator, as derived in [13]:

$$\Delta\nu = \frac{\hbar\omega}{8\pi\varepsilon P_{\text{sig}}\left(\frac{\partial\phi}{\partial\Delta}\right)^2} = \frac{C_0}{4\pi\varepsilon\gamma|x|^2\left(\frac{\partial\phi}{\partial\Delta}\right)^2}, \quad (22)$$

where P_{sig} is the signal power, ε is the photodetector efficiency, and $\left(\frac{\partial\phi}{\partial\Delta}\right)$ is the dimensionless phase slope at resonance $\Delta = 0$. In the case that FM spectroscopy, such as NICEOHMS [16], is used for the detection of the absorption or cavity transmitted phase, Eq. (22) must be modified as follows. In general, in a configuration where sidebands are applied at the free spectral range of the cavity, Eq. (22) must be multiplied with $(1 + P_{\text{sig}}/2P_{\text{sideband}})$, where P_{sideband} is the sideband power.

Equation (22) is the smallest, and hence the phase is most stable, when the product of the slope around resonance and the

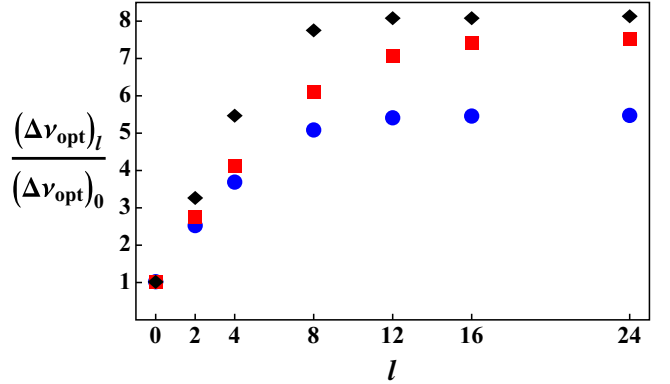


FIG. 3. (Color online) Linewidth at the optimum $|y|^2$, which gives the smallest linewidth, as a function of included orders of l , normalized by the $l = 0$ linewidth. Blue circles: $NC_0 = 600$, $\delta_0/\gamma_p = 260$, $|y|^2 = 1270$. Red squares: $NC_0 = 6000$, $\delta_0/\gamma_p = 260$, $|y|^2 = 7700$. Black diamonds: $NC_0 = 600$, $\delta_0/\gamma_p = 80$, $|y|^2 = 850$.

intracavity intensity is as large as possible. The optimal input intensity, which allows this product to be as large as possible, is the value used in Fig. 2(c) and is labeled by the black dot at $|y|^2 \approx 10^3$ in Fig. 2(d).

To achieve a quantitative agreement between theory and experiment [16], higher orders in l in Eq. (19) must be included. These higher-order terms correspond to Doppler resonances, i.e., multiphoton scattering processes between the atoms and cavity mode.

To study the importance of these higher-order Dopplerons, we calculate the linewidth from Eq. (22) at the optimum input power while varying the order of l at which the truncation occurs.

Figure 3 shows the dependence of the linewidth at the optimum input intensity on the order of l at which the truncation occurs for three different sets of parameters. The first set, shown in blue circles, converges by $l = 12$. The linewidth calculated with up to $l = 12$ included before truncation is around five times larger than the linewidth with only $l = 0$ included. This shows that Doppler resonances are crucial to include for a correct quantitative analysis of this system.

Shown in red squares, we increase the number of atoms by a factor of 10, and again calculate the linewidth as a function of the order of l at which the truncation occurs. As a result of N being increased, the optimum value of $|y|^2$ is also increased. Convergence occurs around $l = 16$. Now, the difference between the converged linewidth and the linewidth with only $l = 0$ included has increased by a factor of around 2. This demonstrates that as N is increased higher-order Dopplerons play an increasing role.

We also decrease the temperature by a factor of 10, and again calculate the linewidth at the new optimum value of $|y|^2$, as shown by the black diamonds. Even though the optimum $|y|^2$ occurs at a lower value, there is still an increase in the difference between the converged linewidth and the $l = 0$ linewidth. Convergence occurs around $l = 12$. This shows that as the temperature is decreased higher-order Dopplerons also play an increasing role.

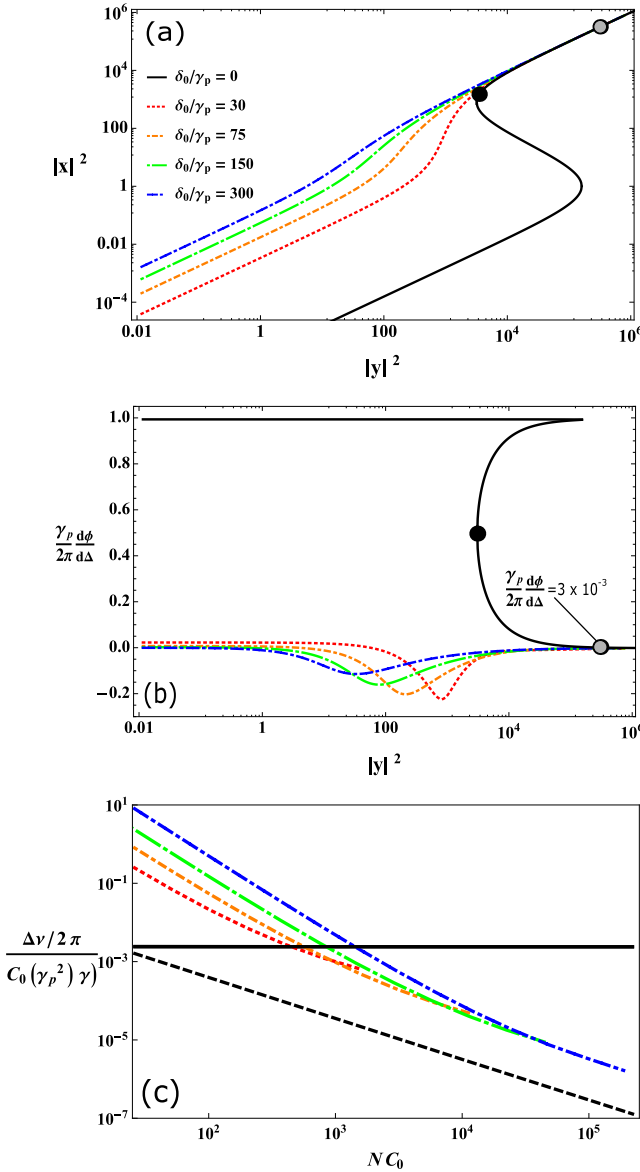


FIG. 4. (Color online) (a) Scaled input ($|x|^2$) vs intracavity ($|y|^2$) intensities for several temperatures with $NC_0 = 800$. (b) Slope at resonance for several temperatures with $NC_0 = 800$. (c) Stabilization linewidth as a function of NC_0 for several temperatures. For $\delta_0/\gamma_p = 0$, the black dashed line is calculated at the fixed input intensity $|y|^2 = 4NC_0$; the black solid line is calculated at the fixed input intensity $|y|^2 = (NC_0)^2/4$. For $\delta_0/\gamma_p \neq 0$, the linewidth is calculated with the input intensity fixed to the optimum value that gives the smallest linewidth. In the case of ^{88}Sr , $\delta_0/\gamma_p = 150$ corresponds to a temperature of ~ 5 mK.

We next study the effect of optical bistability, and its effects on the optimum input intensity. As can be seen in Fig. 4(a), when $\delta_0/\gamma_p = 0$ there is a bistability in input ($|y|^2$) versus intracavity ($|x|^2$) intensities. As the temperature is increased, the bistability becomes less pronounced, until eventually it disappears entirely, which can be seen in the $\delta_0/\gamma_p = 30$ curve.

The slope at resonance, which can be seen in Fig. 4(b), has a very different behavior for the zero and nonzero temperature cases. For $\delta_0/\gamma_p = 0$, the slope is largest on the lower branch,

decreases slightly in the bistable region, and then drops exponentially to zero as the intensity is increased on the upper branch. When the temperature is increased, the bistability disappears, and a dispersion feature with negative slope appears. Then the slope goes to a maximally negative value before power broadening eventually causes it to increase to zero.

The disappearance of the bistability is important for achieving the highest possible degree of stabilization. In the zero-temperature case, the optimal combination of $|x|^2$ and $\frac{\partial\phi}{\partial\Delta}$ to give the smallest $\Delta\nu$ occurs on the far left side of the upper branch, when the input intensity has the fixed value $|y|^2 = 4NC_0$, labeled with the black dot in Figs. 4(a) and 4(b). However, this value of intensity is in the bistable region, so the system is dynamically unstable when the full quantum dynamics are accounted for. If the tunneling rate between the different branches is not small, we are constrained to work at input intensities that are above the bistable region where the achievable frequency precision is much less. The gray dot in Figs. 4(a) and 4(b) is at the far right side of the bistable region, at the fixed input intensity value $|y|^2 = (NC_0)^2/4$. The stabilization linewidth is orders of magnitude worse here, because the slope is so small. Nonetheless, working above the bistability allows for shot-noise limited stabilization line widths of ~ 1 mHz [13].

Figure 4(c) shows the stabilization linewidth as a function of NC_0 for several temperatures. In the $\delta_0/\gamma_p = 0$ limit of zero temperature, the black dashed curve corresponds to the input intensity corresponding to the black dot, and the black solid curve corresponds to the input intensity of the gray dot. When the temperature is increased sufficiently, the bistability disappears. Then, there are no longer any regions of dynamic instability and therefore no restrictions on input intensity. Each of the $\delta_0/\gamma_p \neq 0$ cases in this plot is calculated at its respective optimal input intensity and stops at a critical value of NC_0 , where the bistability reappears. It follows as reciprocal information that for a given value of NC_0 there exists a critical temperature at which the bistability disappears. Therefore, by using Fig. 4(c) to note the values of temperature and NC_0 at which the bistability disappears for the different curves, it is seen that the critical temperature increases as NC_0 increases.

In general, a lower temperature will yield a smaller linewidth. However, because one must avoid working in a region of optical bistability, the optimal shot-noise limited linewidth for certain values of NC_0 and δ_0/γ_p in which there is no bistability can actually be smaller than the $\delta_0/\gamma_p = 0$ linewidth which is constrained above the bistability.

V. ATOMIC SYSTEMS

In order to evaluate the performance of the cavity-QED stabilization method presented in this work, we have estimated the shot-noise limited linewidth using Eq. (22) for a number of different atomic systems. For each element we assume the atomic sample laser to be cooled close to the Doppler limit with reference to temperatures obtained experimentally in [16,27–29] (see Table I). These temperatures are all above the critical temperature where bistability disappears by at least an order of magnitude.

TABLE I. Shot-noise limited linewidths $\Delta\nu$ estimated theoretically for a number of $^1S_0 \rightarrow ^3P_1$ intercombination lines at experimentally realizable parameters: transition wavelength λ , natural linewidth γ , atomic sample temperature as reported in [27–29], and optimal cavity input power $P_{\text{in, opt}}$. The critical temperature at which bistability disappears for $NC_0 = 4593$, the largest value of NC_0 here considered, is $60 \mu\text{K}$, which is well below any temperatures considered. The ratio of the carrier and sideband power is chosen to $\frac{P_{\text{sig}}}{2P_{\text{sideband}}} = 1$ in all cases. Throughout the calculation we have assumed a prestabilized probe laser decoherence of $\gamma_{\text{laser}}/2\pi = 2.0 \text{ kHz}$. The shot-noise limited linewidths are calculated for systems with empty cavity finesse of $F = 250$ and $N = 2.5 \times 10^7$ atoms overlapping the cavity mode, and an improved system with $F = 1000$ and $N = 5.0 \times 10^7$.

Transition	λ	$\gamma/2\pi$	F	N	NC_0	Temperature	$P_{\text{in, opt}}$	$\Delta\nu$
$^{171}\text{Yb } ^1S_0 \rightarrow ^3P_1$	556 nm	182 kHz	250	2.5×10^7	374	6.5 mK	$128 \mu\text{W}$	3.3 Hz
			1000	5.0×10^7	2991		$312 \mu\text{W}$	207 mHz
$^{40}\text{Ca } ^1S_0 \rightarrow ^3P_1$	657 nm	400 Hz	250	2.5×10^7	522	1.7 mK	5.5nW	322 mHz
			1000	5.0×10^7	4176		2.2nW	20 mHz
$^{24}\text{Mg } ^1S_0 \rightarrow ^3P_1$	457 nm	34 Hz	250	2.5×10^7	253	3.0 mK	0.5nW	8.1 Hz
			1000	5.0×10^7	2021		0.2nW	500 mHz
$^{88}\text{Sr } ^1S_0 \rightarrow ^3P_1$	689 nm	7.6 kHz	250	2.5×10^7	574	3.0 mK	47nW	102 mHz
			1000	5.0×10^7	4593		84nW	6.8 mHz

A realistic atom number overlapping the cavity mode has been estimated to be $N = 2.5 \times 10^7$ and has been used for all the elements. For several elements, larger atom numbers have been reported in the literature, which makes our estimates somewhat conservative [16,27–29]. Cavity dimensions are based on the experimental values obtained in [16]. The cavity waist diameter is chosen to be 1.0 mm and the empty cavity finesse is chosen to be $F = 250$ and 1000, corresponding to an empty cavity decay rate of $\kappa/2\pi = 2.0 \times 10^6$ and $0.5 \times 10^6 \text{ Hz}$, respectively. In each case, the laser decoherence has been assumed to be $\gamma_{\text{laser}} = 2\pi \times 2.0 \text{ kHz}$. For each element in Table I, we have used the laser power that corresponds to the minimum shot-noise limited linewidth.

Whereas stabilizing a probe laser on the $^1S_0 \rightarrow ^3P_1$ transition of ^{24}Mg may be slightly more experimentally challenging compared to the other elements in Table I, the stabilization of a probe laser on the $^1S_0 \rightarrow ^3P_1$ transition of ^{88}Sr with cavity finesse $F = 250$ and $N = 2.5 \times 10^7$ promises a shot-noise limited linewidth of 107 mHz. This linewidth is already comparable with the linewidths of the current state-of-the-art frequency stabilized lasers [12,16].

The shot-noise limited linewidth may be reduced further by increasing the value of NC_0 . This can be achieved by increasing the atom number or the cavity finesse. The shot-noise limited linewidth, $\Delta\nu$, is inversely proportional to the square of the atom number according to Eq. (22), as the phase slope at resonance, $\frac{\partial\phi}{\partial\Delta}$, depends linearly on the atom number N . A similar scaling can be achieved by increasing the finesse while keeping the classical drive amplitude η constant. For ^{88}Sr , the laser linewidth may be reduced to $\Delta\nu = 6.8 \text{ mHz}$ by only increasing the cavity finesse to $F = 1000$ and increasing the atom number by a factor of 2 to $N = 5.0 \times 10^7$ (see Table I).

A cavity imposes a delay on the error signal possibly degrading the feedback to the laser. Generally, the optical cavity effectively acts as a low pass filter with a cutoff frequency given by $f_{\text{cut}} = c/(4LF)$ [30], where c is the speed of light, L is the cavity length, and F is the finesse of the cavity. In the case studied in this paper we find the cavity belonging to the so-called bad cavity limit, where the cavity linewidth Γ_c is significantly larger than the the atomic linewidth γ_a .

For a typical cavity of length 10 cm, operated in this domain, the finesse ranges from 100 to 1000 and corresponds to cutoff frequencies in the megahertz range. For practical purposes this will not pose any significant delay in the servo loop.

The experimental proof of principle demonstrated in [16] is operated in a cyclic fashion, on a time scale similar to that of state-of-the-art optical lattice clocks. In these clocks, the preparation of cold atoms takes of order 0.5–1 s, before they are interrogated by the clock laser. This leaves the probe (clock) laser uncorrected during the dead time period. All such systems suffer from the so-called optical Dick effect [31,32] where the frequency noise of the clock laser is aliased into the sampled signal and ends up contaminating the clock stability. Possible ways to decrease the Dick effect are to increase the probe period by transferring the atoms to an optical lattice or by reducing the initial clock laser instability. With a laser noise level similar to that achieved by optical lattice clocks, and a duty cycle of about 1 s, we would be limited to stability at the 10^{-15} level [33]. Compared to the estimated shot-noise limited linewidths presented in Table I, this corresponds to the low-finesse cases. Pushing the limit, as shown by the slightly higher finesse of 1000, would require the atoms to be loaded into an optical lattice, or require a reduction of the duty cycle by a factor 10 to 100 ms in the experiment presented in [16]. This may be achieved with an optimized experimental loading rate as shown in [34].

Alternatively, one may use a cold bright atomic beam as a source of atoms to be interrogated in the cavity, rather than atoms prepared in a MOT and then released. Using experimentally achieved numbers from [34], we have estimated signals comparable to that achieved in [16], but now allowing for a continuous interrogation. This seems to be a very tantalizing and promising approach for these systems.

VI. CONCLUSION

We have seen that thermal atoms in a standing-wave cavity field exhibit additional phenomena that were not observed when considering a frozen arrangement of atoms. Specifically, when the detuning of the laser and atoms is less than the power broadened linewidth, the system interacts with both

components of the standing-wave field. This causes new absorptive and dispersive features in the observables, which are the features that can be used as an error signal for frequency stabilization. Multiphoton scattering processes due to Doppler resonances cause the stabilization linewidth to increase. This effect becomes more dominant as the collective cooperativity NC_0 is increased, and as the temperature is decreased. A system with sufficient NC_0 and no atomic motion will exhibit optical bistability. Atomic motion may cause this bistability to disappear. When optical bistability occurs, one is generally restricted to using an input intensity that lies outside of the bistable region in order to prevent hopping between semiclassical solutions. When there is no optical bistability, there are no dynamically unstable regions, so that

no such restrictions on input intensity are necessary, allowing the optimally smallest stabilization linewidth to be achieved.

ACKNOWLEDGMENTS

The authors acknowledge valuable conversations with G. S. Agarwal. This work has been supported by JILA Grant No. NSF-PFC-1125844, Defense Advanced Research Projects Agency (DARPA), Quantum-Assisted Sensing and Readout (QASR), National Institute of Standards and Technology (NIST), The Danish Research Council (DRC), and European Space Agency (ESA) Contract No. 4000108303/13/NL/PANPI272-2012.

-
- [1] R. Le Targat, L. Lorini, Y. Le Coq, M. Zawada, J. Guéna, M. Abgrall, M. Gurov, P. Rosenbusch, D. G. Rovera, B. Nagórny, R. Gartman, P. G. Westergaard, M. E. Tobar, M. Lours, G. Santarelli, A. Clairon, S. Bize, P. Laurent, P. Lemonde, and J. Lodewyck, *Nat. Commun.* **4**, 2109 (2013).
 - [2] N. Huntemann, B. Lipphardt, C. Tamm, V. Gerginov, S. Weyers, and E. Peik, *Phys. Rev. Lett.* **113**, 210802 (2014).
 - [3] R. M. Godun, P. B. R. Nisbet-Jones, J. M. Jones, S. A. King, L. A. M. Johnson, H. S. Margolis, K. Szymaniec, S. N. Lea, K. Bongs, and P. Gill, *Phys. Rev. Lett.* **113**, 210801 (2014).
 - [4] S. Schiller, G. M. Tino, P. Gill, C. Salomon, U. Sterr, E. Peik, A. Neovsky, A. Görlitz, D. Svehla, G. Ferrari, N. Poli, L. Lusanna, H. Klein, H. Margolis, P. Lemonde, P. Laurent, G. Santarelli, A. Clairon, W. Ertmer, E. Rasel, J. Müller, L. Iorio, C. Lämmerzahl, H. Dittus, E. Gill, M. Rothacher, F. Flechner, U. Schreiber, V. Flambaum, W.-T. Ni, L. Liu, X. Chen, J. Chen, K. Gao, L. Cacciapuoti, R. Holzwarth, M. P. Heß, and W. Schäfer, *Einstein Gravity Explorer—a Medium-Class Fundamental Physics Mission* (Springer, The Netherlands, 2009), Vol. 23, pp. 573–610.
 - [5] J. Guéna, M. Abgrall, D. Rovera, P. Rosenbusch, M. E. Tobar, P. Laurent, A. Clairon, and S. Bize, *Phys. Rev. Lett.* **109**, 080801 (2012).
 - [6] R. Bondarescu, M. Bondarescu, G. Hetényi, L. Boschi, P. Jetzer, and J. Balakrishna, *Geophys. J. Int.* **191**, 78 (2012).
 - [7] R. Drever, J. L. Hall, F. Kowalski, J. Hough, G. Ford, A. Munley, and H. Ward, *Appl. Phys. B* **31**, 97 (1983).
 - [8] B. C. Young, F. C. Cruz, W. M. Itano, and J. C. Bergquist, *Phys. Rev. Lett.* **82**, 3799 (1999).
 - [9] Y. Jiang, A. Ludlow, N. Lemke, R. Fox, J. Sherman, L.-S. Ma, and C. Oates, *Nat. Photon.* **5**, 158 (2011).
 - [10] K. Numata, A. Kemery, and J. Camp, *Phys. Rev. Lett.* **93**, 250602 (2004).
 - [11] T. Kessler, C. Hagemann, C. Grebing, T. Legero, U. Sterr, F. Riehle, M. J. Martin, L. Chen, and J. Ye, *Nat. Photon.* **6**, 687 (2012).
 - [12] M. J. Martin, M. Bishof, M. D. Swallows, X. Zhang, C. Benko, J. von Stecher, A. V. Gorshkov, A. M. Rey, and J. Ye, *Science* **341**, 632 (2013).
 - [13] M. J. Martin, D. Meiser, J. W. Thomsen, J. Ye, and M. J. Holland, *Phys. Rev. A* **84**, 063813 (2011).
 - [14] R. Bonifacio and L. A. Lugiato, *Phys. Rev. A* **18**, 1129 (1978).
 - [15] P. D. Drummond and D. F. Walls, *J. Phys. A* **13**, 725 (1980).
 - [16] P. G. Westergaard, B. T. R. Christensen, D. Tieri, R. Matin, J. Cooper, M. Holland, J. Ye, and J. W. Thomsen, *Phys. Rev. Lett.* **114**, 093002 (2015).
 - [17] S. Stenholm and W. E. Lamb, Jr., *Phys. Rev.* **181**, 618 (1969).
 - [18] C. Freed and A. Javan, *Appl. Phys. Lett.* **17**, 53 (1970).
 - [19] S. Stenholm, *Foundations of Laser Spectroscopy* (Dover, New York, 2005).
 - [20] M. Levenson, *Introduction to Nonlinear Laser Spectroscopy* (Elsevier, New York, 2012).
 - [21] G. S. Agarwal and Y. Zhu, *Phys. Rev. A* **46**, 479 (1992).
 - [22] A. Tallet, *J. Opt. Soc. Am. B* **11**, 1336 (1994).
 - [23] J. Gripp, S. L. Mielke, and L. A. Orozco, *Phys. Rev. A* **56**, 3262 (1997).
 - [24] Z. Ficek and H. S. Freedhoff, *Phys. Rev. A* **48**, 3092 (1993).
 - [25] G. S. Agarwal, Y. Zhu, D. J. Gauthier, and T. W. Mossberg, *J. Opt. Soc. Am. B* **8**, 1163 (1991).
 - [26] W. H. Press, S. A. Teukolsky, W. T. Vetterling, and B. P. Flannery, *Numerical Recipes 3rd Edition: The Art of Scientific Computing*, 3rd ed. (Cambridge University, New York, 2007).
 - [27] M. Riedmann, H. Kelkar, T. Wübbena, A. Pape, A. Kulosa, K. Zipfel, D. Fim, S. Rühmann, J. Fribe, W. Ertmer, and E. Rasel, *Phys. Rev. A* **86**, 043416 (2012).
 - [28] T. Kohno, M. Yasuda, K. Hosaka, H. Inaba, Y. Nakajima, and F.-L. Hong, *Appl. Phys. Express* **2**, 072501 (2009).
 - [29] U. Dammalapati, I. Norris, L. Maguire, M. Borkowski, and E. Riis, *Meas. Sci. Technol.* **20**, 095303 (2009).
 - [30] M. Rakhamanov, R. L. Savage, D. H. Reitze, and D. B. Tanner, *Phys. Lett. A* **305**, 239 (2002).
 - [31] G. J. Dick, in Proceedings of Precise Time and Time Interval Meeting, 1987 (unpublished), Vol. 133.
 - [32] P. Westergaard, J. Lodewyck, and P. Lemonde, *IEEE Trans. Ultrason. Ferroelectr. Frequ. Control* **57**, 623 (2010).
 - [33] Y. Jiang, A. Ludlow, N. Lemke, J. Sherman, J. Von Stecher, R. Fox, L.-S. Ma, A. Rey, and C. Oates, in Frequency Control and the European Frequency and Time Forum (FCS), 2011 Joint Conference of the IEEE International, 2011 (unpublished), pp. 1–3.
 - [34] D. Chruściński and A. Kossakowski, *Phys. Lett. A* **373**, 2301 (2009).

B.3 Observation of Motion-Dependent Nonlinear Dispersion with Narrow-Linewidth Atoms in an Optical Cavity

Philip G. Westergaard, Bjarke T. R. Christensen, David A. Tieri, Rastin Matin, John Cooper, Murray J. Holland, Jun Ye & Jan W. Thomsen, *Phys. Rev. Lett.* **114**, 093002 (2015).

Observation of Motion-Dependent Nonlinear Dispersion with Narrow-Linewidth Atoms in an Optical Cavity

Philip G. Westergaard,^{1,2,*} Bjarke T. R. Christensen,¹ David Tieri,³ Rastin Matin,¹ John Cooper,³ Murray Holland,³ Jun Ye,³ and Jan W. Thomsen¹

¹*Niels Bohr Institute, University of Copenhagen, Blegdamsvej 17, 2100 Copenhagen, Denmark*

²*Danish Fundamental Metrology, Matematiktorvet 307, 1 sal, 2800 Kongens Lyngby, Denmark*

³*JILA, National Institute of Standards and Technology and University of Colorado, Boulder, Colorado 80309-0440, USA*

(Received 15 August 2014; revised manuscript received 26 January 2015; published 4 March 2015)

As an alternative to state-of-the-art laser frequency stabilization using ultrastable cavities, it has been proposed to exploit the nonlinear effects from coupling of atoms with a narrow transition to an optical cavity. Here, we have constructed such a system and observed nonlinear phase shifts of a narrow optical line by a strong coupling of a sample of strontium-88 atoms to an optical cavity. The sample temperature of a few mK provides a domain where the Doppler energy scale is several orders of magnitude larger than the narrow linewidth of the optical transition. This makes the system sensitive to velocity dependent multiphoton scattering events (Dopplerons) that affect the cavity field transmission and phase. By varying the number of atoms and the intracavity power, we systematically study this nonlinear phase signature which displays roughly the same features as for much lower temperature samples. This demonstration in a relatively simple system opens new possibilities for alternative routes to laser stabilization at the sub-100 mHz level and superradiant laser sources involving narrow-line atoms. The understanding of relevant motional effects obtained here has direct implications for other atomic clocks when used in relation to ultranarrow clock transitions.

DOI: [10.1103/PhysRevLett.114.093002](https://doi.org/10.1103/PhysRevLett.114.093002)

PACS numbers: 32.80.Wr, 37.30.+i, 42.50.Ct, 42.62.Fi

State-of-the-art atomic clocks rely on highly coherent light sources to probe narrow optical transitions [1–5]. However, these clocks are limited by the frequency noise of the interrogation oscillator through the Dick effect [6]. Only recently, multiatom optical clocks have surpassed single ion clocks in stability owing to enhanced laser stability [1,2,7]. Achieving a better stability has, so far, been hampered by thermal noise in the reference cavity used for laser stabilization [8–10]. Recent proposals suggest an alternative approach to laser stabilization [11–13] where atoms in an optical lattice are probed on the narrow clock transition inside an optical cavity. This brings nonlinear effects into the system dynamics that could considerably enhance the spectral sensitivity and could potentially lead to laser stability comparable to or better than the current state of the art. However, for finite temperature samples of atoms, the principal mechanisms that are relevant to this physical domain have not been investigated in detail.

In such systems with highly nonlinear phase response, *a priori* unpredictable effects such as bistability [13] and the finite temperature of the atomic ensemble can change the phase response in an undesirable way, which could reduce the performance of the stabilization scheme for all practical implementations. To achieve a better understanding of cavity-mediated effects with a narrow optical transition, we have constructed a system with ⁸⁸Sr atoms probed on the $|^1S_0\rangle - |^3P_1\rangle$ transition at 689 nm inside an optical cavity (see Fig. 1). To capture the basic physics of

the strong nonlinear phenomena, one can consider N atomic dipoles strongly coupled to a single mode of the cavity field. The dipole moment associated with this narrow transition is around 5 orders of magnitude smaller than that for a typical dipole-allowed transition in an alkaline element. Also, at finite temperature only a small fraction of the atomic sample is probed due to Doppler broadening. Here, the role of the cavity is to enhance the weak interaction by order of the finesse of the cavity.

Experimentally we operate in the so-called bad cavity regime, where the atomic dipole decay rate is a factor of 1000 smaller than the cavity decay rate κ . In our experiment we use the ${}^{88}\text{Sr}|5s^21S_0\rangle - |5s5p^1P_1\rangle$ transition at 461 nm to cool and trap atoms in a magneto-optical trap (MOT). We load about 5×10^8 atoms in the MOT at a temperature of 2–4 mK inside an optical cavity prepared for light at 689 nm. The cavity waist of $w_0 = 500 \mu\text{m}$ ensures a good overlap with the MOT and negligible transit time broadening ($\sim 2 \text{ kHz}$) compared to the natural linewidth ($\Gamma/2\pi = 7.6 \text{ kHz}$) of the probe transition. The dimensionless number $C = C_0 N$, where $C_0 = 4g^2/\Gamma\kappa$ depends on the single atom–cavity coupling constant g , is known as the collective cooperativity and is a measure of how strong the coherent atom-cavity coupling is with respect to the dissipation channels. In our configuration ($g/2\pi = 590 \text{ Hz}$, $\kappa/2\pi = 5.8 \text{ MHz}$) we are able to generate a collective cooperativity of about $C = 630$, thus placing our system in the regime of high collective cooperativity in the bad cavity limit, but

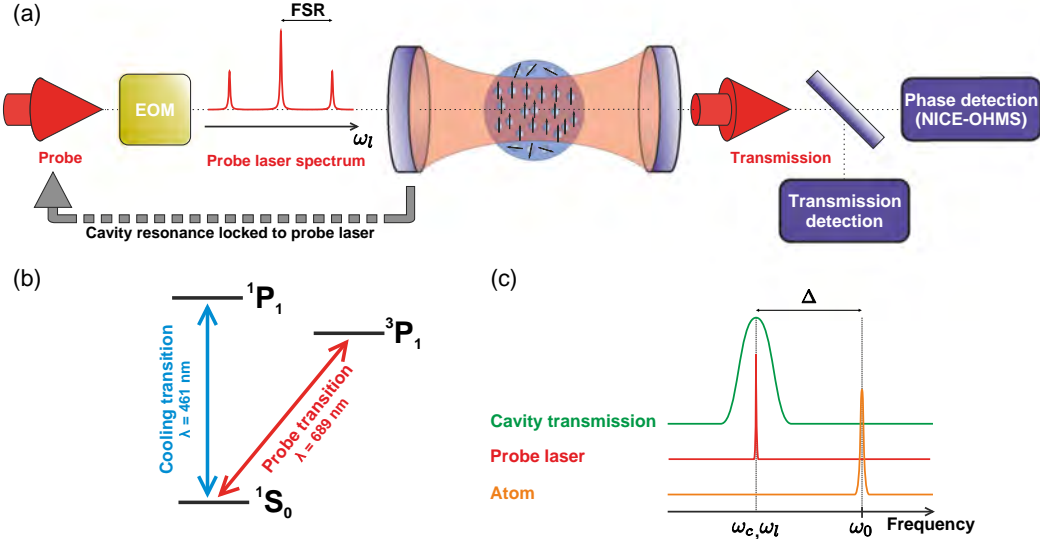


FIG. 1 (color online). (a) Experimental setup. A sample of cold atoms (MOT) is prepared inside a low finesse cavity ($F = 85$) which is held at resonance with the probe laser. We probe the atoms on the intercombination line $|5s^2 1S_0\rangle - |5s5p^3 P_1\rangle$ at 689 nm ($\Gamma/2\pi = 7.6 \text{ kHz}$). Both intensity and phase shift of the transmitted probe light are recorded. The phase is measured relative to the input field by employing cavity-enhanced heterodyne spectroscopy (NICE-OHMS). (b) Energy levels of the ^{88}Sr atom and transitions relevant to this work. (c) Relation between the spectral components in the experiment. The probe laser frequency ω_l (and consequently the cavity resonance ω_c) is detuned a variable amount Δ with respect to the atomic resonance ω_0 .

outside the more restrictive cavity QED strongly coupled regime [14,15].

Our experiment is operated in a cyclic fashion. We start each cycle preparing the atomic sample by loading a MOT inside the optical cavity. After loading we shut off the MOT beams and probe the atoms at 689 nm while recording both the intensity and the phase shift of the transmitted probe light via two detectors (see Fig. 1). The total cycle time is typically around 0.5–1 s. For the phase measurement we employ cavity-enhanced FM spectroscopy by using the so-called noise-immune cavity-enhanced optical-heterodyne molecular spectroscopy (NICE-OHMS) technique [19,20] (see the Supplemental Material [15]). This technique has a clear advantage over heterodyne signals generated, for example, from interferometric methods in terms of superior noise reduction and simplicity. During experiments we lock the cavity resonance to the 689 nm laser frequency using a Hänsch-Couillaud scheme [21]. The standing wave generated in the cavity will thus be present at all times while the 689 nm laser frequency is scanned.

In the limit of $T = 0$ and for very low cavity field intensities several solutions exist for the steady-state intracavity field [13]. This is known as optical bistability, which would render the system unsuited for frequency stabilization. However, at finite temperatures when motional effects are included, this picture changes. In this case, there is a critical temperature T_{crit} above which only one solution for the steady-state intracavity field exists. For our parameters, T_{crit} is of the order of a few hundred nK, while experiments are typically performed at mK temperatures.

The nonzero velocity of the atoms brings additional photon resonance phenomena into play, which changes the complex amplitude of the cavity field around the atomic resonance ω_0 . In the rest frame of an atom moving with velocity v_j the atom experiences a bichromatic light field given by $\omega_+ = \omega_l(1 + v_j/c)$ and $\omega_- = \omega_l(1 - v_j/c)$, where ω_l is the laser frequency and c is the speed of light. Resonant scattering events will take place if the atom is Doppler tuned into resonance at ω_0 , e.g., $\omega_- = \omega_0$, such that the atom may absorb a photon from a given direction of the cavity field. Higher order resonances are also possible where, e.g., the atom absorbs two photons from one direction at ω_- and emits one photon in the other direction at ω_+ . Generally, the resonance condition for $p+1$ absorbed and p emitted photons becomes $(p+1)\omega_- = \omega_0 + p\omega_+$ for $p = 0, 1, 2, \dots$ [22]. The process is illustrated in Fig. 2(a). These nonlinear multiphoton scattering effects are known as Doppleron and give rise to a series of velocity dependent resonances [23] which change the transmitted field amplitude around resonance.

In Figs. 2(b) and 2(c) we show typical results for a frequency scan across the $|^1\text{S}_0\rangle - |^3\text{P}_1\rangle$ line resonance (red circles). The input power was 975 nW, corresponding to an average saturation parameter of $S_0 = 618$. It is clear that the phase signal in Fig. 2(c) has a significantly higher signal-to-noise ratio (SNR = 70) than the transmitted power signal in Fig. 2(b) (SNR ~ 4), demonstrating the effectiveness of the NICE-OHMS technique. Currently, the factor limiting the signal-to-noise ratio of the phase signal is the shot-to-shot atom number fluctuations and

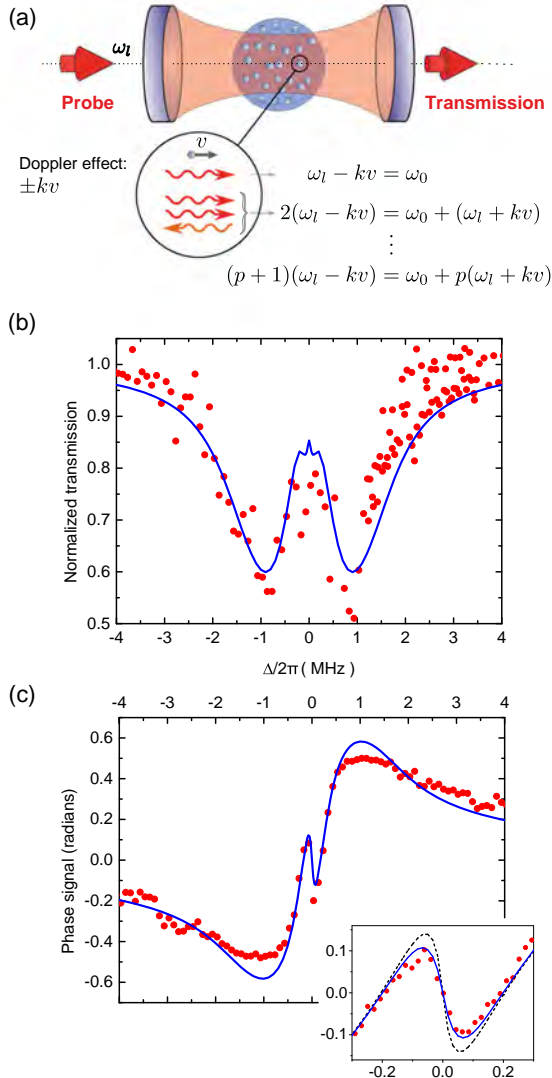


FIG. 2 (color online). (a) Illustration of the Doppleron multiphoton processes that take place in our system. We consider a given atom with velocity component v in the direction of the cavity axis. The first resonance condition (the top equation) involves only one photon and corresponds to the usual Doppler effect. The next resonance involves two photons absorbed and one photon emitted, and so forth. (b),(c) Typical frequency scan without any averaging across the atomic resonance for an input power of 975 nW and a total number of atoms in the MOT of $N = 4.4 \times 10^8$. The data in (b) display the transmission of the probe light through the cavity normalized to a signal with no atoms in the cavity. The data in (c) is the phase shift of the cavity-transmitted field obtained using the NICE-OHMS method. The solid lines are theoretical predictions based on our theoretical model, which includes the Doppler effect and the spatial overlap of the thermal cloud (here with temperature $T = 2.3$ mK) with the cavity field. At maximum phase shift (around detunings of $\Delta = \pm 1$ MHz), our detection system starts to saturate, giving a slightly flatter appearance of the phase data. (Inset) Zoom on central phase feature with similar experimental parameters [data are identical to Fig. 4(a)]. Here, we have included a theoretical plot that does not take the Dopplerons into account (black, dashed curve). The effect of the Dopplerons is readily apparent. Units on axes are the same as in (c).

residual amplitude modulation from the electro-optic modulator (EOM).

We model the dynamics of the system by a Hamiltonian describing the coherent time evolution of an ensemble of atoms, where each atom with a given velocity is coupled to a single mode of the optical cavity. Solving the corresponding optical Bloch equations yields the cavity-transmitted intensity and phase as a function of detuning, number of atoms, and temperature. Our model is also adapted to take into account the spatial extent of the cavity field and the atomic density profile. The blue solid curves in Figs. 2(b) and 2(c) represent the theoretical prediction based on the Hamiltonian presented in Eq. 2 of the Supplemental Material [15]. In our theoretical model we fix the number of atoms, laser input power, laser linewidth, cavity waist, and cavity finesse based on experimental values, but allow a scaling factor for the absolute phase. The temperature is allowed to vary in the range of 2–4 mK, in accordance with the experimental condition.

Considering the transmission in Fig. 2(b), we can identify three spectral features: (1) the broad (~ 3 MHz wide) Doppler absorption feature consistent with the sample temperature of a few mK; (2) a central region (~ 1 MHz wide) with enhanced transmission due to saturation, affected by the Doppler resonances which lead to enhanced backscattering (or reduced forward transmission), limiting the height of the saturated absorption peak; (3) finally, in the central region around zero velocity (i.e., on resonance), the Doppler mechanism breaks down and the saturated absorption takes place again with increased transmission as a result.

The Dopplerons also have an effect in the phase signal [Fig. 2(c)], although the effect is negligible for large laser detunings corresponding to larger atom velocities. In the inset of Fig. 2(c), we zoom in on the phase of the central saturated absorption feature where we have plotted experimental data [with parameters corresponding to Fig. 4(a)] and theoretical curves without Dopplerons (black, dashed line) and with Dopplerons (blue line). Here, the effect of Dopplerons becomes clear and there is an observable effect on the phase signature which is a decrease in slope around resonance, showing consistency between our theoretical model and the experimental data. This decrease in slope is important in the determination of the frequency stability that is achievable using this system since the stability depends inversely on the square of the slope around resonance, and reducing the temperature further does not significantly improve this slope [15].

To evaluate and characterize our physical system experimentally and test it against the theoretical model, we have mapped out the central phase feature as a function of probe input power with a fixed atom number. In addition to a validation of the theoretical model, this will provide an understanding of the behavior and sensitivity of the phase signal to typical experimental variables relevant to, e.g.,

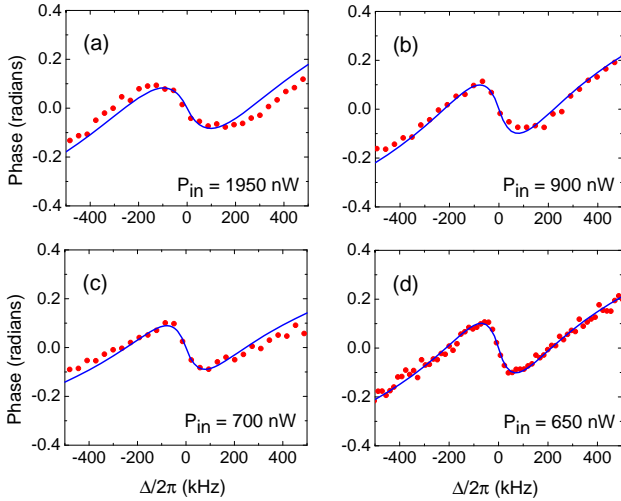


FIG. 3 (color online). Measured phase shift of the cavity-transmitted field when scanned across the atomic resonance. The input probe laser power P_{in} is progressively decreased from 1950 nW (a), 900 nW (b), 700 nW (c) to 650 nW (d). The number of atoms is about $N_{\text{cavity}} = 2.5 \times 10^7$. Each point is an average of three data points. The solid lines are theoretical predictions based on our theoretical model.

laser stabilization. In Fig. 3 we show the phase signal for a fixed number of atoms as a function of laser detuning for different input powers in the range 650–1950 nW. For high input powers we strongly saturate the dipole and power broaden the central saturated absorption peak. As we gradually lower the input power, the power broadening is reduced, leaving the central phase feature with a larger slope without reducing the signal-to-noise ratio.

Figs. 4(a)–4(d) show the evolution of the phase signal for fixed probe power as the number of atoms inside the cavity mode is changed from $N_{\text{cavity}} = 2.5 \times 10^7$ in (a) to $N_{\text{cavity}} = 1.2 \times 10^7$ in (d). We observe a strong dependence on atom number with increasing phase response and increasing slope on resonance for increasing atom numbers, as expected, and the slope can straightforwardly be improved by increasing the number of atoms. However, our system is strongly nonlinear and other optimal parameters, such as input power, for a given number of atoms, may not be trivially assigned to our experiment, but must be found numerically or experimentally.

Using the central phase slope for laser frequency locking, we estimate a shot noise limited linewidth of 1000 mHz, based on our experimental parameters. This number can be improved by at least a factor of 20 with realistic improvements in the experimental parameters, e.g., by optimizing the EOM modulation index (a factor 15) and increasing the atom number and the cavity finesse (both a factor 10), which would render the system comparable to state-of-the-art frequency stabilization Refs. [9,24–26] (see the Supplemental Material [15] for details).

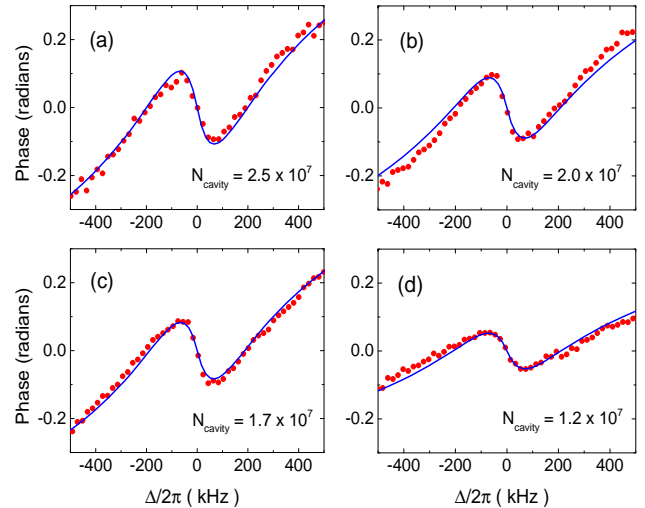


FIG. 4 (color online). Measured phase shift of the probe light when scanned across the atomic resonance. The number of atoms in the cavity is progressively decreased from 2.5×10^7 (a), 2.0×10^7 (b), 1.7×10^7 (c) to 1.2×10^7 (d). The input power used for all plots was 650 nW. Each point is an average of three data points. The solid lines are theoretical predictions based on our theoretical model. The central slope scales linearly with atom number.

In conclusion, we have constructed a system dominated by highly saturated multiphoton absorption with laser-cooled strontium atoms coupled to a low finesse optical cavity. The transmission through the cavity is altered by thermal effects but, apart from a small decrease in slope, the central phase response of the atoms remains relatively immune to these effects while displaying a high SNR owing to the cavity and detection technique. The atomic phase signature was observed via cavity-enhanced FM spectroscopy (NICE-OHMS) on the narrow optical $|^1S_0\rangle - |^3P_1\rangle$ intercombination line of ^{88}Sr , providing a SNR exceeding 7000 for one second of integration. The understanding obtained here of the “bad cavity” physics lends promise to further development in this area, such as a new generation of frequency stabilization [11,13] or superradiant laser sources [27,28]. Specifically, the physical understanding of a “warm” system (MOT temperature) obtained in this work will prove valuable when future atomic clocks, stable lasers, or both will be operated under more noisy and compact environments—e.g., in vehicles and space crafts—where the size, ruggedness, and convenience of the setup might dictate higher atomic temperatures than what is currently used for state-of-the-art systems. In this situation, this work will serve as an important piece of technical understanding for out-of-lab clocks employing warm atoms.

We would like to acknowledge support from the Danish Research Council and ESA Contract No. 4000108303/13/NL/PA-NPI272-2012. D. T., M. H., and J. Y. also wish to thank the DARPA QuASAR program, NIST, and the NSF Physics Frontier Center at JILA for financial support.

*pgw@dfm.dk

- [1] B. J. Bloom, T. L. Nicholson, J. R. Williams, S. L. Campbell, M. Bishop, X. Zhang, W. Zhang, S. L. Bromley, and J. Ye, *Nature (London)* **506**, 71 (2014).
- [2] N. Hinkley, J. A. Sherman, N. B. Phillips, M. Schioppo, N. D. Lemke, K. Beloy, M. Pizzocaro, C. W. Oates, and A. D. Ludlow, *Science* **341**, 1215 (2013).
- [3] R. Le Targat *et al.*, *Nat. Commun.* **4**, 2109 (2013).
- [4] M. Takamoto, F.-L. Hong, R. Higashi, and H. Katori, *Nature (London)* **435**, 321 (2005).
- [5] C. W. Chou, D. B. Hume, J. C. J. Koelemeij, D. J. Wineland, and T. Rosenband, *Phys. Rev. Lett.* **104**, 070802 (2010).
- [6] G. Santarelli, C. Audoin, A. Makdissi, P. Laurent, G. J. Dick, and A. Clairon, *IEEE Trans. Ultrason. Ferroelectr. Freq. Control* **45**, 887 (1998).
- [7] T. L. Nicholson, M. J. Martin, J. R. Williams, B. J. Bloom, M. Bishop, M. D. Swallows, S. L. Campbell, and J. Ye, *Phys. Rev. Lett.* **109**, 230801 (2012).
- [8] T. Kessler, T. Legero, and U. Sterr, *J. Opt. Soc. Am. B* **29**, 178 (2012).
- [9] T. Kessler, C. Hagemann, C. Grebing, T. Legero, U. Sterr, F. Riehle, M. J. Martin, L. Chen, and J. Ye, *Nat. Photonics* **6**, 687 (2012).
- [10] M. J. Martin, M. Bishop, M. D. Swallows, X. Zhang, C. Benko, J. von-Stecher, A. V. Gorshkov, A. M. Rey, and J. Ye, *Science* **341**, 632 (2013).
- [11] D. Meiser, J. Ye, D. R. Carlson, and M. J. Holland, *Phys. Rev. Lett.* **102**, 163601 (2009).
- [12] D. Meiser and M. J. Holland, *Phys. Rev. A* **81**, 033847 (2010).
- [13] M. J. Martin, D. Meiser, J. W. Thomsen, J. Ye, and M. J. Holland, *Phys. Rev. A* **84**, 063813 (2011).
- [14] H. Tanji-Suzuki, I. D. Leroux, M. H. Schleier-Smith, M. Cetina, A. Grier, J. Simon, and V. Vuletic, *Adv. At. Mol. Opt. Phys.* **60**, 201 (2011).
- [15] See Supplemental Material at <http://link.aps.org/supplemental/10.1103/PhysRevLett.114.093002>, which includes Refs. [16–18], for details on experimental parameters, the theoretical model, and a calculation of the shot noise limited linewidth.
- [16] R. W. P. Drever, J. L. Hall, F. V. Kowalski, J. Hough, G. M. Ford, A. J. Munley, and H. Ward, *Appl. Phys. B* **31**, 97 (1983).
- [17] Z. Ficek and H. S. Freedhoff, *Phys. Rev. A* **48**, 3092 (1993).
- [18] S. Stellmer, R. Grimm, and F. Schreck, *Phys. Rev. A* **87**, 013611 (2013).
- [19] J. Ye, L.-S. Ma, and J. L. Hall, *J. Opt. Soc. Am. B* **15**, 6 (1998).
- [20] L.-S. Ma, J. Ye, P. Dubé, and J. L. Hall, *J. Opt. Soc. Am. B* **16**, 2255 (1999).
- [21] T. W. Hänsch and B. Couillaud, *Opt. Commun.* **35**, 441 (1980).
- [22] A. Tallet, *J. Opt. Soc. Am. B* **11**, 1336 (1994).
- [23] E. Kyrölä and S. Stenholm, *Opt. Commun.* **22**, 123 (1977).
- [24] M. Bishop, X. Zhang, M. J. Martin, and J. Ye, *Phys. Rev. Lett.* **111**, 093604 (2013).
- [25] Y. Y. Jiang, A. D. Ludlow, N. D. Lemke, R. W. Fox, J. A. Sherman, L.-S. Ma, and C. W. Oates, *Nat. Photonics* **5**, 158 (2011).
- [26] J. Millo, D. V. Magalhães, C. Mandache, Y. Le Coq, E. M. L. English, P. G. Westergaard, J. Lodewyck, S. Bize, P. Lemonde, and G. Santarelli, *Phys. Rev. A* **79**, 053829 (2009).
- [27] J. G. Bohnet, Z. Chen, J. M. Weiner, D. Meiser, M. J. Holland, and J. K. Thompson, *Nature (London)* **484**, 78 (2012).
- [28] T. Maier, S. Kraemer, L. Ostermann, and H. Ritsch, *Opt. Express* **22**, 13269 (2014).

BIBLIOGRAPHY

- [Abbott et al., 2016] Abbott, B. P. et al. (2016). Observation of gravitational waves from a binary black hole merger. *Phys. Rev. Lett.*, 116:061102.
- [Abgrall et al., 2015] Abgrall, M., Chupin, B., Sarlo, L. D., Guéna, J., Laurent, P., Coq, Y. L., Targat, R. L., Lodewyck, J., Lours, M., Rosenbusch, P., Rovera, G. D., and Bize, S. (2015). Atomic fountains and optical clocks at syrte: Status and perspectives. *Comptes Rendus Physique*, 16(5):461 – 470. The measurement of time / La mesure du temps.
- [Baudouin et al., 2013] Baudouin, Q., Mercadier, N., Guarrera, V., Guerin, W., and Kaiser, R. (2013). A cold-atom random laser. *Nature Physics*, 9(6):357–360.
- [Bergquist et al., 1982] Bergquist, J. C., Hemmati, H., and Itano, W. M. (1982). High power second harmonic generation of 257 nm radiation in an external ring cavity. *Optics Communications*, 43:437–442.
- [Bishof et al., 2013] Bishof, M., Zhang, X., Martin, M. J., and Ye, J. (2013). Optical spectrum analyzer with quantum-limited noise floor. *Phys. Rev. Lett.*, 111:093604.
- [Bloom et al., 2014] Bloom, B. J., Nicholson, T. L., Williams, J. R., Campbell, S. L., Bishof, M., Zhang, X., Zhang, W., Bromley, S. L., and Ye, J. (2014). An optical lattice clock with accuracy and stability at the 10-18 level. *Nature*, 506:71–75.
- [Bohnet et al., 2014] Bohnet, J. G., Chen, Z., Weiner, J. M., Cox, K. C., and Thompson, J. K. (2014). Linear-response theory for superradiant lasers. *Phys. Rev. A*, 89:013806.
- [Bohnet et al., 2012] Bohnet, J. G., Chen, Z., Weiner, J. M., Meiser, D., Holland, M. J., and Thompson, J. K. (2012). A steady-state superradiant laser with less than one intracavity photon. *Nature*, 484(3):78–81.

- [Bohr, 1913] Bohr, N. (1913). I. on the constitution of atoms and molecules. *Philosophical Magazine Series 6*, 26(151):1–25.
- [Bondarescu et al., 2012] Bondarescu, R., Bondarescu, M., Hetényi, G., Boschi, L., Jetzer, P., and Balakrishna, J. (2012). Geophysical applicability of atomic clocks: direct continental geoid mapping. *Geophysical Journal International*, 191(1):78–82.
- [Bongs et al., 2015] Bongs, K., Singh, Y., Smith, L., He, W., Kock, O., Świerad, D., Hughes, J., Schiller, S., Alighanbari, S., Origlia, S., Vogt, S., Sterr, U., Lisdat, C., Targat, R. L., Lodewyck, J., Holleville, D., Venon, B., Bize, S., Barwood, G. P., Gill, P., Hill, I. R., Ovchinnikov, Y. B., Poli, N., Tino, G. M., Stuhler, J., and Kaenders, W. (2015). Development of a strontium optical lattice clock for the {SOC} mission on the {ISS}. *Comptes Rendus Physique*, 16(5):553 – 564. The measurement of time / La mesure du temps.
- [Bonifacio and Lugiato, 1975] Bonifacio, R. and Lugiato, L. A. (1975). Co-operative radiation processes in two-level systems: Superfluorescence. *Phys. Rev. A*, 11:1507–1521.
- [Boyd and Kleinman, 1968] Boyd, G. D. and Kleinman, D. A. (1968). Parametric Interaction of Focused Gaussian Light Beams. *Journal of Applied Physics*, 39(8):3597–3639.
- [Boyd, 2007] Boyd, M. M. (2007). *High Precision Spectroscopy of Strontium in an Optical Lattice: Towards a New Standard for Frequency and Time*. PhD thesis, University of Colorado.
- [Bureau International des Poids et Measures, 2014] Bureau International des Poids et Measures (2014). Bipm annual report on time activities. http://www.bipm.org/utils/en/pdf/time_ann_rep/Time_annual_report_2014.pdf. [Accessed March 30th 2016].
- [Castagna et al., 2013] Castagna, N., Chiodo, N., Lours, M., Holleville, D., Lecoq, Y., Acef, O., and Burck, F. D. (2013). Iodine stabilized ir laser sources. In *European Frequency and Time Forum International Frequency Control Symposium (EFTF/IFC), 2013 Joint*, pages 405–408.
- [Chen, 2009] Chen, J. (2009). Active optical clock. *Chinese Science Bulletin*, 54(3):348–352.
- [Chou et al., 2010a] Chou, C. W., Hume, D. B., Koelemeij, J. C. J., Wineland, D. J., and Rosenband, T. (2010a). Frequency comparison of two high-accuracy al^+ optical clocks. *Phys. Rev. Lett.*, 104:070802.

- [Chou et al., 2010b] Chou, C. W., Hume, D. B., Rosenband, T., and Wineland, D. J. (2010b). Optical clocks and relativity. *Science*, 329(5999):1630–1633.
- [Christensen, 2012] Christensen, B. T. (2012). *Clock laser system for a Hg optical lattice clock*. PhD thesis, Niels Bohr Institute, University of Copenhagen.
- [Christensen et al., 2015a] Christensen, B. T. R., Henriksen, M. R., Schäffer, S. A., Westergaard, P. G., Tieri, D., Ye, J., Holland, M. J., and Thomsen, J. W. (2015a). Nonlinear spectroscopy of sr atoms in an optical cavity for laser stabilization. *Phys. Rev. A*, 92:053820.
- [Christensen et al., 2015b] Christensen, B. T. R., Schäffer, S. A., Henriksen, M. R., Westergaard, P. G., Ye, J., and Thomsen, J. W. (2015b). Laser stabilization on velocity dependent nonlinear dispersion of sr atoms in an optical cavity. In *2015 Joint Conference of the IEEE International Frequency Control Symposium the European Frequency and Time Forum*, pages 357–362.
- [Cohen-Tannoudji et al., 1992] Cohen-Tannoudji, C., Dupont-Roc, J., and Grynberg, G. (1992). *Atom-photon interactions: basic processes and applications*. Wiley-Interscience publication. J. Wiley.
- [Cohen-Tannoudji, 1998] Cohen-Tannoudji, C. N. (1998). Nobel lecture: Manipulating atoms with photons. *Rev. Mod. Phys.*, 70:707–719.
- [Cole et al., 2013] Cole, G. D., Zhang, W., Martin, M. J., Ye, J., and Aspelmeier, M. (2013). Tenfold reduction of brownian noise in high-reflectivity optical coatings. *Nature Photonics*, 7(8):644–650.
- [Cook et al., 2015] Cook, S., Rosenband, T., and Leibrandt, D. R. (2015). Laser-frequency stabilization based on steady-state spectral-hole burning in $\text{eu}^{3+} : \text{y}_2\text{sio}_5$. *Phys. Rev. Lett.*, 114:253902.
- [Courtillot, 2003] Courtillot, I. (2003). *Première observation de la transition fortement interdite 1S0-3P0 du strontium, pour une horloge optique à atomes piégés*. Theses, Université Pierre et Marie Curie - Paris VI.
- [Dai, 2011] Dai, D. (2011). Brief comment: Dicke superradiance and superfluorescence find application for remote sensing in air. <http://arxiv.org/abs/1108.5360>. Arxiv preprint, arXiv:1108.5360.

- [Dammalapati et al., 2009] Dammalapati, U., Norris, I., Maguire, L., Borkowski, M., and Riis, E. (2009). A compact magneto-optical trap apparatus for calcium. *Measurement Science and Technology*, 20(9):095303.
- [Dicke, 1954] Dicke, R. H. (1954). Coherence in spontaneous radiation processes. *Phys. Rev.*, 93:99–110.
- [Diddams et al., 2000] Diddams, S. A., Jones, D. J., Ye, J., Cundiff, S. T., Hall, J. L., Ranka, J. K., Windeler, R. S., Holzwarth, R., Udem, T., and Hänsch, T. W. (2000). Direct link between microwave and optical frequencies with a 300 thz femtosecond laser comb. *Phys. Rev. Lett.*, 84:5102–5105.
- [Dinesan et al., 2015] Dinesan, H., Fasci, E., D’Addio, A., Castrillo, A., and Gianfrani, L. (2015). Characterization of the frequency stability of an optical frequency standard at $1.39\text{ }\mu\text{m}$ based upon noise-immune cavity-enhanced optical heterodyne molecular spectroscopy. *Opt. Express*, 23(2):1757–1766.
- [Dinneen et al., 1999] Dinneen, T. P., Vogel, K. R., Arimondo, E., Hall, J. L., and Gallagher, A. (1999). Cold collisions of sr^* – Sr in a magneto-optical trap. *Phys. Rev. A*, 59:1216–1222.
- [Ficek and Freedhoff, 1993] Ficek, Z. and Freedhoff, H. S. (1993). Resonance-fluorescence and absorption spectra of a two-level atom driven by a strong bichromatic field. *Phys. Rev. A*, 48:3092–3104.
- [Foot, 2005] Foot, C. J. (2005). *Atomic Physics (Oxford Master Series in Atomic, Optical and Laser Physics)*. Oxford University Press, USA, 1 edition.
- [Fox et al., 2012] Fox, R., Sherman, J., Douglas, W., Olson, J., Ludlow, A., and Oates, C. (2012). A high stability optical frequency reference based on thermal calcium atoms. In *Frequency Control Symposium (FCS), 2012 IEEE International*, pages 1–3.
- [Godun et al., 2014] Godun, R. M., Nisbet-Jones, P. B. R., Jones, J. M., King, S. A., Johnson, L. A. M., Margolis, H. S., Szymaniec, K., Lea, S. N., Bongs, K., and Gill, P. (2014). Frequency ratio of two optical clock transitions in $^{171}\text{yb}^+$ and constraints on the time variation of fundamental constants. *Phys. Rev. Lett.*, 113:210801.
- [Graham et al., 2013] Graham, P. W., Hogan, J. M., Kasevich, M. A., and Rajendran, S. (2013). New method for gravitational wave detection with atomic sensors. *Phys. Rev. Lett.*, 110:171102.

- [Guéna et al., 2012] Guéna, J., Abgrall, M., Rovera, D., Rosenbusch, P., Tobar, M. E., Laurent, P., Clairon, A., and Bize, S. (2012). Improved tests of local position invariance using ^{87}Rb and ^{133}Cs fountains. *Phys. Rev. Lett.*, 109:080801.
- [Häfner et al., 2015] Häfner, S., Falke, S., Grebing, C., Vogt, S., Legero, T., Merimaa, M., Lisdat, C., and Sterr, U. (2015). 8×10^{-17} fractional laser frequency instability with a long room-temperature cavity. *Opt. Lett.*, 40(9):2112–2115.
- [Hansch and Couillaud, 1980] Hansch, T. and Couillaud, B. (1980). Laser frequency stabilization by polarization spectroscopy of a reflecting reference cavity. *Optics Communications*, 35(3):441 – 444.
- [Hänsch and Hall, 2006] Hänsch, T. W. and Hall, J. (2006). Nobel lecture: Passion for precision*. *Rev. Mod. Phys.*, 78:1297–1309.
- [Henriksen, 2014] Henriksen, M. R. (2014). *Cavity Enhanced Spectroscopy on Ultra Cold Atoms*. PhD thesis, Niels Bohr Institute, University of Copenhagen.
- [Hinkley et al., 2013] Hinkley, N., Sherman, J. A., Phillips, N. B., Schioppo, M., Lemke, N. D., Beloy, K., Pizzocaro, M., Oates, C. W., and Ludlow, A. D. (2013). An atomic clock with 10^{-18} instability. *Science*, 341(6151):1215–1218.
- [Huntemann et al., 2016] Huntemann, N., Sanner, C., Lipphardt, B., Tamm, C., and Peik, E. (2016). Single-ion atomic clock with 3×10^{-18} systematic uncertainty. *Phys. Rev. Lett.*, 116:063001.
- [Katori, 2001] Katori, H. (2001). Spectroscopy of strontium atoms in the lamb-dicke confinement. In Gill, P., editor, *Proceedings of the 6th Symposium on Frequency Standards and Metrology*, page 323. World Scientific.
- [Kessler et al., 2012a] Kessler, T., Hagemann, C., Grebing, C., Legero, T., Sterr, U., Riehle, F., Martin, M. J., Chen, L., and Ye, J. (2012a). A sub-40-mhz-linewidth laser based on a silicon single-crystal optical cavity. *Nature Photonics*, 6(10):687–692.
- [Kessler et al., 2012b] Kessler, T., Legero, T., and Sterr, U. (2012b). Thermal noise in optical cavities revisited. *J. Opt. Soc. Am. B*, 29(1):178–184.

- [Kohno et al., 2009] Kohno, T., Yasuda, M., Hosaka, K., Inaba, H., Nakajima, Y., and Hong, F.-L. (2009). One-dimensional optical lattice clock with a fermionic ^{171}yb isotope. *Applied Physics Express*, 2(7):072501.
- [Kulosa et al., 2015] Kulosa, A. P., Fim, D., Zipfel, K. H., Rühmann, S., Sauer, S., Jha, N., Gibble, K., Ertmer, W., Rasel, E. M., Safronova, M. S., Safronova, U. I., and Porsev, S. G. (2015). Towards a mg lattice clock: Observation of the 1S_0 - 3P_0 transition and determination of the magic wavelength. *Phys. Rev. Lett.*, 115:240801.
- [Kumarakrishnan and Han, 1998] Kumarakrishnan, A. and Han, X. L. (1998). Superfluorescence from optically trapped calcium atoms. *Phys. Rev. A*, 58:4153–4162.
- [Kuppens et al., 1994] Kuppens, S. J. M., van Exter, M. P., and Woerdman, J. P. (1994). Quantum-limited linewidth of a bad-cavity laser. *Phys. Rev. Lett.*, 72:3815–3818.
- [Kwong et al., 2015a] Kwong, C. C., Yang, T., Delande, D., Pierrat, R., and Wilkowski, D. (2015a). Cooperative emission of a pulse train in an optically thick scattering medium. *Phys. Rev. Lett.*, 115:223601.
- [Kwong et al., 2015b] Kwong, C. C., Yang, T., Delande, D., Pierrat, R., and Wilkowski, D. (2015b). Cooperative emission of a pulse train in an optically thick scattering medium. *Phys. Rev. Lett.*, 115:223601.
- [Kyrölä and Stenholm, 1977] Kyrölä, E. and Stenholm, S. (1977). Velocity tuned resonances as multi-doppleron processes. *Optics Communications*, 22(2):123 – 126.
- [Le Targat et al., 2013] Le Targat, R., Lorini, L., Le Coq, Y., Zawada, M., Guéna, J., Abgrall, M., Gurov, M., Rosenbusch, P., Rovera, D. G., Nagórny, B., Gartman, R., Westergaard, P. G., Tobar, M. E., Lours, M., Santarelli, G., Clairon, A., Bize, S., Laurent, P., Lemonde, P., and Lodewyck, J. (2013). Experimental realization of an optical second with strontium lattice clocks. *Nat Commun*, 4.
- [Lisdat et al., 2015] Lisdat, C., Grosche, G., Quintin, N., Shi, C., Raupach, S., Grebing, C., Nicolodi, D., Stefani, F., Al-Masoudi, A., Dörscher, S., Häfner, S., Robyr, J.-L., Chiodo, N. an Bilicki, S., Bookjans, E., Koczwara, A., Koke, S., Kuhl, A., Wiotte, F., Meynadier, F., Camisard, E., Abgrall, M., Lours, M., Legero, T., Schnatz, H., Sterr, U., Denker, H., Chardonnet, C., Le Coq, Y., Santarelli, G., Amy-Klein, A., Le Targat, R., Lodewyck, J.,

- Lopez, O., and Pottie, P.-E. (2015). A clock network for geodesy and fundamental science. <http://arxiv.org/pdf/1511.07735.pdf>. Arxiv preprint, arXiv:1511.07735.
- [Ma et al., 1999] Ma, L.-S., Ye, J., Dubé, P., and Hall, J. L. (1999). Ultrasensitive frequency-modulation spectroscopy enhanced by a high-finesse optical cavity: theory and application to overtone transitions of c₂h₂ and c₂hd. *J. Opt. Soc. Am. B*, 16(12):2255–2268.
- [Malcuit et al., 1987] Malcuit, M. S., Maki, J. J., Simkin, D. J., Boyd, and W., R. (1987). Transition from superfluorescence to amplified spontaneous emission. *Phys. Rev. Lett.*, 59:1189–1192.
- [Martin et al., 2013] Martin, M. J., Bishof, M., Swallows, M. D., Zhang, X., Benko, C., von Stecher, J., Gorshkov, A. V., Rey, A. M., and Ye, J. (2013). A quantum many-body spin system in an optical lattice clock. *Science*, 341(6146):632–636.
- [Martin et al., 2011] Martin, M. J., Meiser, D., Thomsen, J. W., Ye, J., and Holland, M. J. (2011). Extreme nonlinear response of ultranarrow optical transitions in cavity qed for laser stabilization. *Phys. Rev. A*, 84:063813.
- [Matin, 2013] Matin, R. (2013). *Towards Continuous Cavity-Enhanced Nonlinear Spectroscopy in Strontium*. PhD thesis, Niels Bohr Institute, University of Copenhagen.
- [Meiser et al., 2009] Meiser, D., Ye, J., Carlson, D. R., and Holland, M. J. (2009). Prospects for a millihertz-linewidth laser. *Phys. Rev. Lett.*, 102:163601.
- [Metcalf and van der Straten, 2001] Metcalf, H. and van der Straten, P. (2001). *Laser Cooling and Trapping*. Graduate Texts in Contemporary Physics. Springer New York.
- [Meystre et al., 2007] Meystre, P., Sargent, M., and Sargent, M. (2007). *Elements of Quantum Optics*. Springer-Verlag Berlin and Heidelberg GmbH & Co. K, 4nd edition.
- [Milonni and Eberly, 1988] Milonni, P. W. and Eberly, J. H. (1988). *Lasers*. Wiley-Interscience.
- [Nagourney, 2014] Nagourney, W. (2014). *Quantum Electronics for Atomic Physics and Telecommunication*. Oxford graduate texts. Oxford University Press.

- [Nemitz et al., 2016] Nemitz, N., Ohkubo, T., Takamoto, M., Ushijima, I., Das, M., Ohmae, N., and Katori, H. (2016). Frequency ratio of y_b and sr clocks with 5×10^{-17} uncertainty at 150 s averaging time. <http://arxiv.org/abs/1601.04582>. Arxiv preprint, arXiv:1601.04582.
- [Nicholson et al., 2015] Nicholson, T., Campbell, S., Hutson, R., Marti, G., McNally, R., Zhang, W., Barrett, M., Safranova, M., Strouse, G., Tew, W., and Ye, J. (2015). Systematic evaluation of an atomic clock at 2×10^{-18} total uncertainty. *Nat Commun*, 6.
- [Noe II et al., 2012] Noe II, G. T., Kim, J.-H., Lee, J., Wang, Y., Wójcik, A. K., McGill, S. A., Reitze, D. H., Belyanin, A. A., and Kono, J. (2012). Giant superfluorescent bursts from a semiconductor magneto-plasma. *Nature Physics*, 8(3):219–224.
- [Norcia et al., 2016] Norcia, M. A., M. N. Winchester, M. N., Cline, J. R. K., and Thompson, J. K. (2016). Superradiance on the millihertz linewidth strontium clock transition. <http://arxiv.org/abs/1603.05671>. Arxiv preprint, arXiv:1603.05671.
- [Norcia and Thompson, 2016a] Norcia, M. A. and Thompson, J. K. (2016a). Cold-strontium laser in the superradiant crossover regime. *Phys. Rev. X*, 6:011025.
- [Norcia and Thompson, 2016b] Norcia, M. A. and Thompson, J. K. (2016b). Simple laser stabilization to the strontium 88sr transition at 707 nm. *Review of Scientific Instruments*, 87(2).
- [Norcia and Thompson, 2016c] Norcia, M. A. and Thompson, J. K. (2016c). Strong coupling on a forbidden transition in strontium and nondestructive atom counting. *Phys. Rev. A*, 93:023804.
- [Peacock, 1980] Peacock, R. N. (1980). Practical selection of elastomer materials for vacuum seals. *Journal of Vacuum Science and Technology*, 17(1):330–336.
- [Predehl et al., 2012] Predehl, K., Grosche, G., Raupach, S. M. F., Droste, S., Terra, O., Alnis, J., Legero, T., Hänsch, T. W., Udem, T., Holzwarth, R., and Schnatz, H. (2012). A 920-kilometer optical fiber link for frequency metrology at the 19th decimal place. *Science*, 336(6080):441–444.
- [Prestage et al., 2008] Prestage, J. D., Tu, M., Chung, S. K., and MacNeal, P. (2008). Compact microwave mercury ion clock for space applications. In *Frequency Control Symposium, 2008 IEEE International*, pages 651–654.

- [Riedmann et al., 2012] Riedmann, M., Kelkar, H., Wübbena, T., Pape, A., Kulosa, A., Zipfel, K., Fim, D., Rühmann, S., Friebel, J., Ertmer, W., and Rasel, E. (2012). Beating the density limit by continuously loading a dipole trap from millikelvin-hot magnesium atoms. *Phys. Rev. A*, 86:043416.
- [Riehle, 2004] Riehle, F. (2004). *Frequency Standards: Basics and Applications*. Wiley-VCH.
- [Riehle, 2015] Riehle, F. (2015). Towards a re-definition of the second based on optical atomic clocks. <http://arxiv.org/pdf/1501.02068v2.pdf>. Arxiv preprint, arXiv:1501.02068.
- [Rosenband et al., 2008] Rosenband, T., Hume, D. B., Schmidt, P. O., Chou, C. W., Brusch, A., Lorini, L., Oskay, W. H., Drullinger, R. E., Fortier, T. M., Stalnaker, J. E., Diddams, S. A., Swann, W. C., Newbury, N. R., Itano, W. M., Wineland, D. J., and Bergquist, J. C. (2008). Frequency ratio of Al^+ and Hg^+ single-ion optical clocks; metrology at the 17th decimal place. *Science*, 319(5871):1808–1812.
- [Schaffer et al., 2015] Schaffer, S., Adsersen, S., Christensen, B., and Thomassen, J. (2015). Large waist cavity for ultra-narrow transition spectroscopy. In *Frequency Control Symposium the European Frequency and Time Forum (FCS), 2015 Joint Conference of the IEEE International*, pages 625–629.
- [Schäffer, 2015] Schäffer, S. A. (2015). *Studies of Collective Effects in Atoic Strontium*. PhD thesis, Niels Bohr Institute, University of Copenhagen.
- [Schawlow and Townes, 1958] Schawlow, A. L. and Townes, C. H. (1958). Infrared and optical masers. *Phys. Rev.*, 112:1940–1949.
- [Schuurmans, 1980] Schuurmans, M. (1980). Superfluorescence and amplified spontaneous emission in an inhomogeneously broadened medium. *Optics Communications*, 34(2):185 – 189.
- [Schwindt et al., 2015] Schwindt, P. D. D., Jau, Y. Y., Partner, H. L., Serkland, D. K., Ison, A., McCants, A., Winrow, E., Prestage, J., Kellogg, J., Yu, N., Boschen, C. D., Kosvin, I., Mailloux, D., Scherer, D., Nelson, C., Hati, A., and Howe, D. A. (2015). Miniature trapped-ion frequency standard with $^{171}\text{yb}^+$. In *Frequency Control Symposium the European Frequency and Time Forum (FCS), 2015 Joint Conference of the IEEE International*, pages 752–757.

- [Shimada et al., 2013] Shimada, Y., Chida, Y., Ohtsubo, N., Aoki, T., Takeuchi, M., Kuga, T., and Torii, Y. (2013). A simplified 461-nm laser system using blue laser diodes and a hollow cathode lamp for laser cooling of sr. *Review of Scientific Instruments*, 84(6).
- [Takamoto et al., 2015] Takamoto, M., Ushijima, I., Das, M., Nemitz, N., Ohkubo, T., Yamanaka, K., Ohmae, N., Takano, T., Akatsuka, T., Yamaguchi, A., and Katori, H. (2015). Frequency ratios of sr, yb, and hg based optical lattice clocks and their applications. *Comptes Rendus Physique*, 16(5):489 – 498. The measurement of time / La mesure du temps.
- [Tallet, 1994] Tallet, A. (1994). Raman emission versus dopplerons in a two-level atomic cell. *J. Opt. Soc. Am. B*, 11(8):1336–1349.
- [Tanji-Suzuki et al., 2011] Tanji-Suzuki, H., Leroux, I. D., Schleier-Smith, M. H., Cetina, M., Grier, A. T., Simon, J., and Vuletić, V. (2011). Ch. 4 - interaction between atomic ensembles and optical resonators: Classical description. In E. Arimondo, P. B. and Lin, C., editors, *Advances in Atomic, Molecular, and Optical Physics*, volume 60 of *Advances In Atomic, Molecular, and Optical Physics*, pages 201 – 237. Academic Press.
- [Targat et al., 2005] Targat, R. L., Zondy, J.-J., and Lemonde, P. (2005). 75%-efficiency blue generation from an intracavity {PPKTP} frequency doubler. *Optics Communications*, 247(4–6):471 – 481.
- [Tieri et al., 2015] Tieri, D. A., Cooper, J., Christensen, B. T. R., Thomsen, J. W., and Holland, M. J. (2015). Laser stabilization using saturated absorption in a cavity-qed system. *Phys. Rev. A*, 92:013817.
- [Tyumenev et al., 2016] Tyumenev, R., Favier, M., Bilicki, S., Bookjans, E., Le Targat, R., Lodewyck, J., Nicolodi, D., Le Coq, Y., Abgrall, M., Guéna, J., De Sarlo, L., and Bize, S. (2016). Comparing a mercury optical lattice clock with microwave and optical frequency standards. <http://arxiv.org/abs/1603.02026v1>. Arxiv preprint, arXiv:1603.02026.
- [Ushijima et al., 2015] Ushijima, I., Takamoto, M., Das, M., Ohkubo, T., and Katori, H. (2015). Cryogenic optical lattice clocks. *Nature Photonics*, 9(3):185–189.
- [Westergaard et al., 2015] Westergaard, P. G., Christensen, B. T. R., Tieri, D., Matin, R., Cooper, J., Holland, M., Ye, J., and Thomsen, J. W. (2015). Observation of motion-dependent nonlinear dispersion with narrow-linewidth atoms in an optical cavity. *Phys. Rev. Lett.*, 114:093002.

- [Xu et al., 2003a] Xu, X., Loftus, T. H., Dunn, J. W., Greene, C. H., Hall, J. L., Gallagher, A., and Ye, J. (2003a). Single-stage sub-doppler cooling of alkaline earth atoms. *Phys. Rev. Lett.*, 90:193002.
- [Xu et al., 2003b] Xu, X., Loftus, T. H., Hall, J. L., Gallagher, A., and Ye, J. (2003b). Cooling and trapping of atomic strontium. *J. Opt. Soc. Am. B*, 20(5):968–976.
- [Yamaguchi et al., 2011] Yamaguchi, A., Fujieda, M., Kumagai, M., Hachisu, H., Nagano, S., Li, Y., Ido, T., Takano, T., Takamoto, M., and Katori, H. (2011). Direct comparison of distant optical lattice clocks at the 10^{-16} uncertainty. *Applied Physics Express*, 4(8):082203.
- [Yamanaka et al., 2015] Yamanaka, K., Ohmae, N., Ushijima, I., Takamoto, M., and Katori, H. (2015). Frequency ratio of ^{199}Hg and ^{87}Sr optical lattice clocks beyond the si limit. *Phys. Rev. Lett.*, 114:230801.
- [Yang et al., 2015] Yang, T., Pandey, K., Pramod, M., Leroux, F., Kwong, C., Hajiyev, E., Chia, Z., Fang, B., and Wilkowski, D. (2015). A high flux source of cold strontium atoms. *Eur. Phys. J. D*, 69.
- [Yasuda and Katori, 2004] Yasuda, M. and Katori, H. (2004). Lifetime measurement of the 3p_2 metastable state of strontium atoms. *Phys. Rev. Lett.*, 92:153004.
- [Ye and Lynn, 2003] Ye, J. and Lynn, T. W. (2003). Applications of optical cavities in modern atomic, molecular, and optical physics. volume 49 of *Advances In Atomic, Molecular, and Optical Physics*, pages 1 – 83. Academic Press.
- [Ye et al., 1998] Ye, J., Ma, L.-S., and Hall, J. L. (1998). Ultrasensitive detections in atomic and molecular physics: demonstration in molecular overtone spectroscopy. *J. Opt. Soc. Am. B*, 15(1):6–15.
- [Zhang et al., 2014] Zhang, W., Martin, M. J., Benko, C., Hall, J. L., Ye, J., Hagemann, C., Legero, T., Sterr, U., Riehle, F., Cole, G. D., and Aspelmeyer, M. (2014). Reduction of residual amplitude modulation to 1×10^{-6} for frequency modulation and laser stabilization. *Opt. Lett.*, 39(7):1980–1983.
- [Zhi-Chao et al., 2015] Zhi-Chao, X., Duo, P., Wei, Z., and Jing-Biao, C. (2015). Dual-wavelength bad cavity laser as potential active optical frequency standard. *Chinese Physics Letters*, 32(9):093201.

- [Zhu et al., 1990] Zhu, Y., Gauthier, D. J., Morin, S. E., Wu, Q., Carmichael, H. J., and Mossberg, T. W. (1990). Vacuum rabi splitting as a feature of linear-dispersion theory: Analysis and experimental observations. *Phys. Rev. Lett.*, 64:2499–2502.